The Effects of Electrical and Mechanical Modulation on the Chemical Reactivity of Graphene

by

Min A Kim

Bachelor of Science, La Roche College, 2013

Submitted to the Graduate Faculty of the

Dietrich School of Arts and Sciences in partial fulfillment

of the requirements for the degree of

Doctor of Philosophy

University of Pittsburgh

2021

UNIVERSITY OF PITTSBURGH

DIETRICH SCHOOL OF ARTS AND SCIENCES

This dissertation was presented

by

Min A Kim

It was defended on

July 21, 2021

and approved by

Alexander Star, Professor, Department of Chemistry

Jill Millstone, Associate Professor, Department of Chemistry

Lei Li, Associate Professor, Department of Chemical and Petroleum Engineering

Dissertation Director: Haitao Liu, Professor, Department of Chemistry

The Effects of Electrical and Mechanical Modulation on the Chemical Reactivity of Graphene

Min A Kim, PhD

University of Pittsburgh, 2021

Extreme surface to volume ratio of graphene makes graphene widely open to various reactions; chemistry of graphene is of great interest to fine-tune electronic, chemical, and mechanical properties of graphene, and a better understanding of the factors that impact its chemical reactivity is an invaluable part of graphene chemistry. In this dissertation, dynamic modulation of graphene properties and their effects on the chemical reactivity of graphene are investigated.

A brief background on the history, synthesis, and characterization methods of graphene is summarized in chapter 1. In chapter 2, how graphene interacts with ambient-found species under electrical doping was studied. Electrical doping has significant advantage over chemical doping with in-situ controllability. Static back gating resulted doping hysteresis, which we explained using a charge trapping/de-trapping mechanism.

Efficient electrical doping method was developed to further investigate its effects on the reactivity of graphene in chapter 3. Graphene was heated photothermally in air to ca. 240 ºC and monitored using Raman spectroscopy. Electrically doped graphene showed increased rate in the oxidation reaction. Density functional theory (DFT) calculations indicate that the activation barriers for O_2 insertion and CO_2 desorption decrease with an electric field. This is the first

example of charge-doping induced reactivity enhancement in macroscopic-sized solid-state material.

In chapter 4, the mechanical modulation of graphene and its effects were investigated. Preliminary results suggested an enhanced electrochemical catalytic activity of graphene as well as the electrochemical oxidation itself. The catalytic role of graphene was further investigated and found that applied tensile strain of 0.2 % on a graphene electrode led to a 1~3 % increase of hydrogen evolution reaction (HER) current. Tensile strain increases HER activity while compressive strain decreases it. DFT calculations show increasing H atom adsorption energy with growing tensile strain, leading to a corresponding enhancement of current density in HER.

Table of Contents

Dedication xv

Preface xvi

1.0 Introduction 1

1.1 Why graphene? 2

1.1.1 Before the breakthrough 3

1.1.2 General properties of graphene 6

1.1.3 The electronic structure of graphene 7

1.2 Making graphene 9

1.2.1 Top-down approach: mechanical exfoliation 9

1.2.2 Bottom-up approach: synthesis 11

1.3 Characterization of graphene 13

1.3.1 Optical microscopy 14

1.3.2 Atomic force microscopy (AFM) 14

1.3.3 Raman spectroscopy 16

1.3.4 Other surface analysis techniques 23

1.4 Chemistry of graphene 25

2.0 Environmental Effects on Graphene Doping via Static Gate Voltage 27

2.1 Introduction 27

2.2 Experimental 31

2.2.1 Graphene synthesis 31

2.2.2 Graphene transfer 32

2.2.3 Graphene device fabrication 33

2.2.4 Raman spectroscopy 34

2.2.5 Atomic force microscopy 35

2.2.6 Electrical modulation of graphene 35

2.3 Results and discussion 35

2.3.1 CVD grown single layer graphene 35

2.3.2 Electrical doping in air and early N_2 environment 37

2.3.3 Electrical doping in N_2 42

2.3.4 Long term effect 48

2.4 Conclusion and future directions 50

3.0 Electric Field Effects on the Reactivity of Graphene 52

3.1 Introduction 52

3.2 Experimental 54

3.2.1 Graphene synthesis 54

3.2.2 Graphene transfer 55

3.2.3 Fabrication of back-gated graphene samples 56

3.2.4 Raman spectroscopy 56

3.2.5 Back-gating of graphene 57

3.3 Results and discussion 58

3.3.1 Preliminary results 58

3.3.2 Electric field effect on the photothermal oxidation of graphene 63

3.3.3 Magnitude of the back-gate voltage 66

3.3.4 Frequency of back-gate modulation 68

3.3.5 Theoretical study of the oxidation mechanism 69

3.3.6 Alternative mechanisms 74

3.4 Conclusion 76

4.0 Enhanced Hydrogen Evolution Activity on Strained Graphene 77

4.1 Introduction 77

4.2 Experimental 78

4.2.1 Graphene synthesis and transfer 78

4.2.2 Raman spectroscopy 80

4.2.3 Electrochemical measurements 80

4.3 Results and discussion 81

4.3.1 Preliminary study 81

4.3.1.1 The transfer of graphene on the flexible substrates 82

4.3.1.2 Devices for the mechanical strain application 84

4.3.1.3 Stretching behavior of graphene on PDMS 86

4.3.1.4 Electrochemical oxidative etching of graphene/PDMS 91

4.3.1.5 Effects of PDMS uniaxial stretching on graphene EOE 94

4.3.1.6 Location and mechanical modulation effects 96

4.3.1.7 EOE under tensile strain – multi-axial stretching of PDMS 97

4.3.1.8 EOE under compressive strain – multi-axial stretching of PDMS . 102

4.3.1.9 EOE under tensile strain – bending of PET 104

4.3.1.10 Summary and future directions 106

4.3.2 Mechanical strain on graphene 108

4.3.3 The effects of strain on graphene hydrogen evolution reaction (HER) 110

4.3.4 Theoretical results 115

4.4 Conclusion 124

Appendix A Supplementary Information on Effect of Electric Field on Graphene Oxidation 125

Appendix A.1 Additional experimental data 125

Appendix A.1.1 Effect of back gating after 1 hour oxidation of graphene 125

Appendix A.1.2 The effect of back gating on I(D)/I(G) 126

Appendix A.1.3 Laser absorbance test under back gating 127

Appendix A.1.4 The effect of Joule heating 128

Appendix A.1.5 Additional data on the effect of magnitude of back-gating on the oxidation kinetics 129

Appendix A.1.6 Effect of frequency of the back-gate 130

Appendix A.1.7 Contribution of electrochemical based reactions 131

Appendix A.2 Density functional theory (DFT) calculation 133

Appendix A.3 Micro kinetic model for O_2 oxidation on graphene 134

Appendix A.4 Additional reaction pathways surveyed by DFT calculations 140

Appendix A.5 Effect of electric field on the transition states 144

Appendix B Supplementary Information on Enhanced Hydrogen Evolution Activity on Strained Graphene 148

Appendix B.1 Additional experimental data 148

Appendix B.2 Computational methods 150

Appendix B.3 Additional computational data 151

Bibliography 157

List of Tables

Table 2.1 Time constants of counter doping..... 46

Table 3.1 Effect of electric field on the rate of graphene oxidation 73

Table A.1 O-O bond lengths (l_{O-O} (Å)) and mulliken atomic charges (Q_{O2} (*e*)) 144

Table A.2 Effect of electric field on the oxidation rate of graphene..... 146

Table B.1 List of Monkhorst-Pack k-point grids 152

Table B.2 Calculated free energies of H adsorption reaction 155

List of Figures

Figure 1.1 Publication of graphene related research articles from 2000 to 2020 3

Figure 1.2 Electronic dispersion in the honeycomb lattice 8

Figure 1.3 Raman spectra of graphene and graphite 18

Figure 1.4 Raman spectrum evolution of the graphene disorder 19

Figure 1.5 Raman spectra of graphene as a function of a gate voltage 21

Figure 1.6 Raman spectra of graphene with uniaxial strain 22

Figure 2.1 The CVD process of graphene synthesis 32

Figure 2.2 Schematic image of experimental setup 34

Figure 2.3 CVD grown single layer graphene 37

Figure 2.4 The G peak position of graphene under various electric field 38

Figure 2.5 Schematic diagram of the electrochemical electron transfer doping process of graphene 40

Figure 2.6 The G peak postion in dry and wet environment 43

Figure 2.7 Schematic diagram of the dynamic Fermi level of graphene 44

Figure 2.8 The kinetic of G peak position under applied electric field in N_2 45

Figure 2.9 Diagram of water induced dipoles forming on the top surface of graphene 48

Figure 2.10 Long term effects of electrical modulation on graphene 49

Figure 3.1 Experimental setup of laser induced oxidation of graphene with electrical modulation 57

Figure 3.2 The development of I(D)/I(G) upon laser oxidation 60

Figure 3.3 *in-situ* Raman spectra of laser induced graphene oxidation with gate voltage ... 61

Figure 3.4 The Raman Spectrum of graphene with 1h oxidation 64

Figure 3.5 The photothermal oxidation of graphene as a function of time 65

Figure 3.6 The change in the oxidation kinetic of graphene with the magnitude of back gate voltage 67

Figure 3.7 The effect of back gating frequency on the oxidation kinetic..... 69

Figure 3.8 Band filling of graphene as a function of electrical charge doping..... 70

Figure 3.9 DFT calculation of the oxidation of graphene..... 71

Figure 4.1 Graphene transfer process on PDMS 83

Figure 4.2 Devise designs for mechanical strain application 85

Figure 4.3 Raman spectrum of graphene on PDMS 87

Figure 4.4 The G and 2D peak under multi-directional stretching strain..... 88

Figure 4.5 The 2D Raman map of graphene under multi-directional stretching strain 89

Figure 4.6 The D to G peak ratio under different strain conditions 91

Figure 4.7 The electrochemical oxidative etching (EOE) of graphene 92

Figure 4.8 The regeneration of graphene electrode..... 93

Figure 4.9 EOE of graphene on PDMS under uniaxial strain..... 95

Figure 4.10 Locational control of graphene EOE 96

Figure 4.11 EOE of graphene with multi-directional strain 98

Figure 4.12 EOE of graphene under various amount of tensile strain 100

Figure 4.13 Reproduced graphene EOE trend..... 101

Figure 4.14 EOE of graphene using bubble-up method to apply tensile strain 102

Figure 4.15 EOE of graphene under compressive strain 103

Figure 4.16 EOE of graphene under compressive strain duplicated 104

Figure 4.17 EOE of graphene on PET with tensile strain via bending PET substrate 105

Figure 4.18 Schematics of strain application on a graphene/PET sample..... 108

Figure 4.19 Raman spectra of graphene/PET 109

Figure 4.20 Measured current density of HER vs. time 110

Figure 4.21 The average change in current density..... 111

Figure 4.22 Cyclic voltammetry on graphene/PET 113

Figure 4.23 The dependence of the H adsorption energy on the surface coverage..... 116

Figure 4.24 Variation of the H adsorption energy on graphene lattice elongation..... 119

Figure 4.25 Projected density of states (PDOS) of C and H atom 120

Figure 4.26 Variation of free energy ΔG_{H^*} (eV) 122

Figure A.1 The I(D)/I(G) value comparison after the 1h oxidation 125

Figure A.2 The waveform gate voltage effect on Raman spectroscopy 126

Figure A.3 The waveform gate voltage effect on the laser absorbance..... 128

Figure A.4 The change in the oxidation kinetic of graphene with various back gate voltage magnitudes..... 129

Figure A.5 The effects of static electric field on the graphene and its oxidation 131

Figure A.6 The effect of square waveform modulation on graphene..... 132

Figure A.7 Three alternative reaction pathways 140

Figure A.8 Seven possible reaction pathways of P2 reacting with the second O_2..... 141

Figure A.9 Five possible reaction pathways of P3 reacting with the second O_2..... 142

Figure A.10 Four other reaction pathways of P6 reacting with the second O_2..... 143

Figure A.11 Projected density of states (PDOS) of O and C atoms 145

Figure A.12 Projected DOS and integrated DOS of O atoms and C atoms 145

Figure B.1 Measured current density of HER with negligible background..... 148

Figure B.2 Measured current density of HER under compressive strain 149

Figure B.3 Cyclic voltammetry (CV) on graphene electrode..... 149

Figure B.4 Variation with coverage of H adsorption energy on graphene..... 151

Figure B.5 Supercell cells used in calculations..... 152

Figure B.6 Variation of C-H bond under lattice expansion..... 153

Figure B.7 Variation of the workfunction for adsorbed H 154

Figure B.8 Variation of C p-band center..... 154

Figure B.9 Variation of free energy ΔG_{H^*} at equilibrium (U=0) 156

Figure B.10 Variation of the free energy ΔG_{H^*} with corresponding p-band center 156

Dedication

To Wansu Kim, my loving father who will always be with us in our hearts.

Preface

All the works presented here could not be done without tremendous supports from the people I have met throughout my PhD. Foremost, my dissertation director, Professor Haitao Liu, had been my inspiration, admiration, and encouragement. The creative working environment that Haitao cultures allowed me to learn how to be a scientist. I am sincerely grateful of his patience; without his support and insightful advice along the way, I could not be here where I am.

I would like to express my sincere gratitude to my committee members, Prof. Alexander Star, Prof. Jill Millstone, and Prof. Lei Li for their time and support. I would like to also express my sincere appreciation to collaborators, Prof. Shigeru Amemiya, Prof. Shiyu Du, Prof. Kenneth D. Jordan, Prof. Lei Li, and Prof. Tevis Jacobs for their insightful comments and suggestions.

I would like to offer my special thanks to my colleagues, Dr. Justin Hurst, Dr. Muhammad Salim, Dr. Anqin Xu, and Nathan Tolman for all of our brainstorm sessions and helpful assistants. To Tom Gasmire, Lori Neu, and David Emala, thank you for amazing technical shop support. To all my scientist friends, too numerous to mention here, thank you and it was my pleasure to work with all of you.

Finally, to my dearest parent Wansu Kim and Kangja Seo, and my sister Jinsun Kim, thank you for your bottomless support for all my life.

1.0 Introduction

We have thousands of chemical reactions going on inside of us every second. While it might seem abundant and mundane, discovery of some chemical reactions changed trajectory of the human history. Alloying bronze and iron transformed the human pre-history that we named the historical period after it, the Haber-Bosch process gave us industrial agriculture, and the Czochralski method gave us silicon chips for microelectronics that now we cannot live without. Chemical reaction is a transformation of a reactant that is in the heart of chemistry. When the new material of interest emerges, chemists try to understand how reactions take place with the material and what various factors influences the course of reactions.

Since the visionary hypothesis of Richard Feynman in 1959,[1] nanotechnology have made significant breakthroughs in many fields of science. Now we know that nano-scale can give materials interesting new properties apart from their bulk properties; whole new class of materials suddenly available to us to explore. Development of characterization and synthesis methods of nanomaterials opened the new era of nanotechnology. Among many exciting discoveries, carbon nanomaterials are one of major branches that left historic footprints in nanoscience. In mid 1980s, nanoscale characterization methods such as atomic force microscope (AFM) and scanning probe microscopes (SPM) were in rapid development. At the same time, the "new forms of the element carbon" called fullerenes were discovered which eventually gave Robert Curl, Harold Kroto, and Richard Smalley the Nobel Prize in chemistry in 1996. The sphere-shaped carbon cage made of 60 carbons may only have a diameter of 0.7 nm, but it opened a whole new field of chemistry devoted to fullerene. Soon after the discovery of C_{60}: Buckminsterfullerene in 1985,[2] another exciting fullerene-related structure emerged subsequently, hollow graphitic tubes (carbon

nanotubes, CNTs).[3] The unique properties of CNTs as a one-dimensional material captured great interest of scientists across the field. Then another new carbon nanostructure emerged in 2004. Graphene, similar to singe walled CNT but unzipped, has unique properties now in two-dimensional plane instead of one-dimensional axial direction. With the ignited interest from scientific communities, the Nobel Prize in Physics in 2010 was awarded to Andre Geim and Konstantin Novoselov for their graphene work.[4]

After more than a decade later, still many researchers are exploring graphene and graphene related materials for their exceptional properties and the best route to connect their surprising properties found in lab to groundbreaking everyday life applications. Chemical reactivity of graphene is a great interest since the dawn of graphene rush, and one of critical puzzle pieces to be understood in order to employ graphene and their related materials in those applications. In this dissertation, the chemical reactivity of graphene under different conditions were of interest as well as the reactivity of surroundings in contact with graphene. First, in this chapter, a brief background of graphene is provided; the general properties of graphene, common methods of graphene synthesis and characterization are reviewed.

1.1 Why graphene?

Graphene is a two-dimensional sheet of carbons arranged in honeycomb structure. Each carbon atom is bonded to three neighboring carbon atoms to form a sp^2-hybridized hexagonal network in a planer lattice. Because of this planer structure, one can look at graphene as a building block of other carbon allotropes occupying three dimensions. For example, graphene can be wrapped into a sphere shape of fullerenes, rolled into cylinder shape of carbon nanotubes, and

stacked into bulk graphite. Even though graphene was recognized in 19th century,[5] active graphene research truly began in 2004 when Novoselov and Geim reported isolation of single layer graphene and its surprising electronic properties.[4] Since then, graphene and graphene-based materials have been studied intensively further revealing many interesting properties and applications.

1.1.1 Before the breakthrough

On October 5th 2010, the Nobel Prize in Physics was awarded to Andre Geim and Konstantin Novoselov for "ground breaking experiments regarding the two dimensional material graphene". This was not a huge surprise based on how much graphene was under the spotlight among scientific research topics. The Science paper in 2004 by Geim and Novoselov attracted great attentions from many disciplinaries as reflected in the steep increase of the publications on graphene and its derivatives. According to Web of Science, research articles related to graphene increased dramatically since 2004, and as of today, 17 years after the initial rush, the topic of graphene is still widely studied all over the world.

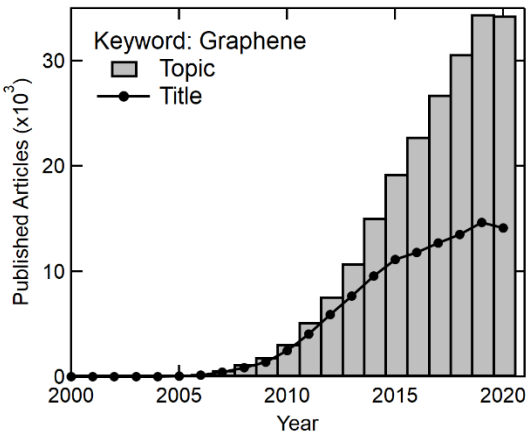

Figure 1.1 Publication of graphene related research articles from 2000 to 2020 Number of published articles having graphene related topic (gray bars) or having title containing word graphene (black dots) is shown for each year based on Web of Science record.

Geim's Science paper in 2004 attracted incredible attentions from the scientific communities, but it was not the first report of the discovery or isolation of graphene. In fact, we can go back more than a century for the discovery of graphene related material. The British chemist Benjamin Brodie is often recognized to report the first graphene-like material in 1859.[5] Brodie obtained "graphon" by exposing graphite to strong acids, and believed it is a new form of carbon (graphite) having an atomic weight of 33. Today, we know Brodie's graphon is a graphite oxide flakes formerly known as graphitic acid, stack of graphene sheets covered with oxygen containing functional groups such as hydroxyl and epoxides. Nearly 90 years later, the physical structure of this graphitic acid was finally visualized using transmission electron microscopy (TEM). Ruess and Vogt observed flake-like "highly lamellar" structure of graphite oxide by depositing graphite oxide suspension on a TEM grid in 1948.[6] Then in 1962, the monolayer of "carbon foil" (reduced graphite oxide) were identified by Boehm *et al.* via the contrast of TEM images of different flake thickness.[7] The TEM contrast cannot be reliably used to identify number of layers of graphene or graphite oxide; nonetheless, this Boehm's work could well be the first observation of the monolayer graphene sheet. More importantly, it showed potential use of TEM in identifying monolayer graphene. In 1986, Boehm and his colleagues suggested the use of the term "graphene" or "graphene layer".[8, 9] A single planer sheet of carbon layer in graphite can be classified in the group of fused polycyclic aromatic hydrocarbons using the suffix of *-ene*, and therefore the term "graphene" was recommended to be used for the individual carbon layers in graphite.

The structure of graphite crystal having stacked planes with hexagonal cleavage face had been generally accepted long before it was confirmed in early 20th century with the development of X-ray crystallography. Often Geim's work in 2004 is quoted with the simple Scotch tape method. However, cleaving the surface of material was already familiar practice in surface and

vacuum science community, and layered structure of graphite made the cleavage easier than other materials. In 1990, Kurz *et al.* prepared thin highly oriented pyrolytic graphite (HOPG) film by peeling optically thin layers from a bulk HOPG with transparent tape and studied carrier dynamics in thin film graphite.[10] Folding graphene into three-dimensional structure, "graphite origami" was already envisioned using HOPG and atomic force microscopy (AFM) by Ebbesen and Hiura in 1995.[11] Ruoff used shearing motion to fan out thin graphite plates and suggested further extensive rubbing of HOPG against other flat surface could result in "single atomic layer of graphite plates" while demonstrating fabrication of graphite sheets via AFM tips.[12] The observation of monolayer graphene via stanning tunneling microscopy (STM) was reported in 2003 by Gan using repeated tip interaction at the step of a terrace on the graphite.[13] By early 2000s, TEM imaging of graphene monolayer was also confirmed by counting the number of folding lines in "carbon nanoscrolls" or "carbon nanofilm" which were exfoliated rolled up graphene sheets.[14-16]

Instead of shaving down graphite into a thin layer, bottom-up approach has been also progressed before the boom of graphene research, eventually leading to the growth of epitaxial graphene and vapor deposition of graphene. Thin films are of interest for a long time from many areas of research such as optics, coatings, and semiconductor. Combined with the progress in crystal growth techniques, growth of thin layer materials such as metals and semiconductors on bulk substrate have been advancing since 1930s.[17, 18] For graphite, thin layer of graphitic film was grown on various substrate as early as 1970. Blakely *et al.* and Grant and Hass reported the segregation of carbon layer on the surface of metals using auger electron spectroscopy in 1970.[19, 20] Potential of epitaxial carbon layer growth on SiC was reported in 1975.[21] Throughout 80s and 90s, the growth of thin carbon layer progressed to several layers of single-crystalline graphite and

even monolayer graphene, and their physical and electronic structure were studied suggesting the potential of graphene electronics.[22-27]

1.1.2 General properties of graphene

The 2004 Science paper reported the astonishing electronic properties of graphene. Since then, intensive efforts on graphene research across the field have revealed many unique properties of graphene, some reaching theoretically predicted limits. Similar to CNTs, graphene also showed remarkable mechanical strength. Despite being the thinnest 2D atomic crystal in its free state, the breaking strength of graphene has been measured to be 42 $N \cdot m^{-1}$ which corresponds to 1.0 TPa Young's modulus.[28] This is comparable to the Young's modulus of in-plane graphite (~1000 GPa) and single-walled and multiwalled CNTs ranging from 0.27 TPa to 1.47 TPa,[29-31] confirming graphene to be one of strongest material available. The optical absorbance of graphene is 2.3 ± 0.2 % and spectrally flat (which is in a great agreement of predicted $\pi\alpha$) over photon energies between 0.5 eV to 1.2 eV.[32, 33] This was in a good agreement with the predicted theory.[34] Graphene is impermeable to any standard gases including helium.[35] Graphene has high thermal conductivity at room temperature, $(5.30 \pm 0.48) \times 10^3$ $W \cdot m^{-1} \cdot K^{-1}$, comparable to single-wall CNT bundles.[36, 37]

Graphene also has remarkable high electron mobility. At room temperature, the electron mobility has been measured in excess of 200,000 $cm^2 \cdot V^{-1} \cdot s^{-1}$ (theoretical limit) using suspended graphene.[38] When graphene is in contact with a substrate, the mobility can be significantly reduced to 15,000 $cm^2 \cdot V^{-1} \cdot s^{-1}$ due to the substrate-graphene interactions.[4, 39] However, even with a substrate, the corresponding sheet resistivity is around 10^{-6} $\Omega \cdot cm$, still less than silver at room temperature. Graphene can also carry extremely high densities of electric currents, several orders of magnitude larger than copper without sustaining damage.[40] The astonishing electronic quality

of graphene has attracted significant interest from the condensed-matter physics community. There had been previous theoretical studies and predictions on graphene's exceptional electronic properties before the rise of graphene in 21st century. It is beyond the scope of this introduction to cover the details, but excellent review papers can be found for additional read.[41-43] Needless to say, graphene research in experimental physics has been advancing spectacularly from the observation of vanishing mass at the Dirac point to the fractional quantum Hall effect.[39, 46] Exiting experimental findings are still actively being reported after a decade of exploration and proved that graphene is a great experimental tool for quantum electrodynamic studies.

1.1.3 The electronic structure of graphene

Experimental studies on semi-metallic characteristics of graphene bloomed with the easily accessible mechanical exfoliation method in early 2000s. However, the electronic band structure of graphene was studied theoretically more than 60 years ago through the development of the band theory of graphite.[44] In graphene, carbon atoms are arranged in a hexagonal 2D lattice with two carbon atoms per unit cell. Each carbon atom has four valence states consisting of three sp^2 orbitals and one p orbital. Those sp^2 orbitals form σ bonds with their neighboring carbon atoms, and p orbitals form π and π^* states. In the lattice structure, π states become the highest occupied valence band (HOVB) and π^* states become the lowest unoccupied conduction band (LUCB). The HOVB is completely filled since graphene has exactly one electron per atom for those π and π^*states. The energy dispersion of those two bands is shown in Figure 1.2. The energy of those two bands meets at points, called Dirac points, providing interesting characteristics. The zoomed in picture in Figure 1.2 shows the HOVB (bottom cone), the LUCB (upper cone), and a linear dispersion near the Dirac points. Therefore, graphene is not a metal because the Fermi level of graphene does not lie within

the bands, nor is it a semiconductor because there is no band gap. This unique band structure makes graphene a true semimetal with a point-like metallic Fermi surface.

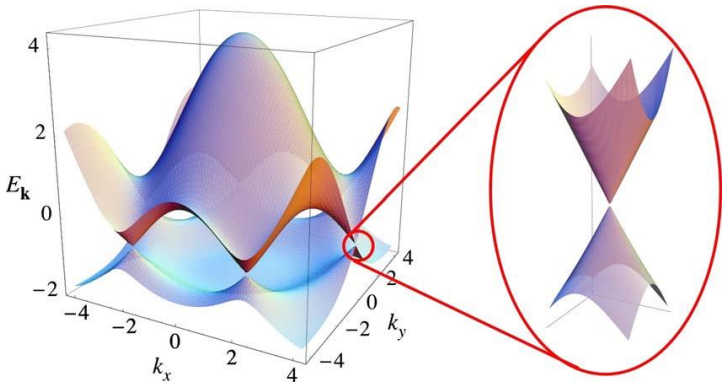

Figure 1.2 Electronic dispersion in the honeycomb lattice Energy dispersion is plotted with the reciprocal lattice vector k. Zoom in of the energy band close to one of the Dirac points is on the right. Reprinted with permission from ref 42. Copyright 2008 by the American Physical Society.

The band structure of graphene makes its properties very sensitive to charge density. Since graphene has a completely filled valence band, any type of doping from charge transfer of adsorbates to external electric field always induces a doping effect by introducing electrons into the conduction band or holes into the valence band.[42] This pronounced ambipolar electric field effect enables charge carriers to be continuously modulated between electrons and holes with high charge density and high mobilities. Graphene doping can be achieved electrically where gate voltage is applied externally, or chemically using various chemical dopants. With the electrical doping, only Fermi level changes in response to the gate voltages, while chemical doping induces the shift of the Dirac point or further collapse of the conical shape of the band structure.[45]

1.2 Making graphene

The first reported free-standing graphene was prepared by the mechanical exfoliation of highly oriented pyrolytic graphite (HOPG).[4] The technique is reliable and easy to perform and therefore has been used by many researchers. However, the limitations of mechanical exfoliation such as lack of scalability lead to the rapid development of new efficient synthesis route to produce high quality and large area graphene. In this section, different synthesis methods of graphene are reviewed.

1.2.1 Top-down approach: mechanical exfoliation

Graphene can be produced from high purity graphite since graphite is simply stacked layers of graphene sheet held together by weak van der Waals forces. The exfoliation of HOPG demonstrated by Geim and Novoselov is widely adopted by many researchers to produce high quality graphene. In their paper,[4] HOPG was attached to a photoresist layer. Then, they used scotch tape to repeatedly peel off the graphite flakes from the photoresist layer. The thin flakes left on the photoresist were released in acetone and captured on Si wafer. Mechanical separation of graphite layers can be done with many other variations such as SiO_2 stamp[46] and PDMS stamp[47]. Graphene obtained from mechanical exfoliation can be high quality compared to that of many different synthesis methods thanks to the inherited quality from high grade HOPG. Especially considering the low cost and simplicity of the process makes the mechanical exfoliation widely used method of choice among researchers. However, low yield and scalability are critical disadvantages of the mechanical exfoliation method. The process produces flakes of graphene in limited size (in micrometers), and it is hard to control the number of graphene layers. Larger variability on the

skill level of researchers is also not ideal for the repeatability and training of new researchers. Overall, such process is limited to the laboratory research due to labor-intensive and time-consuming nature. Efforts in large production of graphene via mechanical exfoliation had been reported. For example, Jayasena *et al.* used lathe-like setup to shave off graphene flakes from HOPG crystal,[48] and Chen *et al.* used a three-roll mill machine with a polymer adhesive to mimic the peeling off motion continuously.[49] However, quality of graphene flakes such as thickness of exfoliated flakes and contamination from adhesives remains to be a challenge to overcome.

Large scale production of graphene at a low cost is a critical step for the commercialization of graphene applications. Graphite exfoliation in liquids has a great advantage in scalability. Generally, in liquid phase exfoliation, graphite is dispersed in various exfoliation media, solvents with or without the presence of surfactants, and sonicated to induce the exfoliation. The liquid exfoliation of layered materials has a long history with the production of graphite oxide that expends back through many decades,[50] but recent interest in graphene stimulated some newer developments. Using an organic solvent having a similar surface energy as that of graphene, such as N-methyl-pyrrolidone, monolayer graphene was produced from graphite using liquid exfoliation method.[51, 52] More details on the recent developments in liquid assisted exfoliation of graphene and graphene related materials can be found in the related review articles.[53, 54] While mass production engineering is much more feasible, quality of graphene product remains to be a major obstacle in liquid phase exfoliation. During the sonication, cavitation induces micro-jects and shock waves which are critical for the exfoliation mechanism, but also creates extreme conditions such as high local temperature, rapid temperature change, and high pressure.[55-57] Those sonication environment can introduce additional defects as well as resulting in high oxygen content in exfoliated graphene sheets.[58, 59]

There are also other mechanical exfoliation processes that can be used for graphene production besides the scotch tape and liquid phase sonication methods. For example, ball milling process is a common technique used to produce powder. The shear force acting laterally on graphite flakes in ball milling drives the exfoliation mechanism. Many studies have been reported demonstrating the use of both wet and dry ball milling process to produce graphene.[60-63] The ball milling method also suffers from the high defect density in the resulting graphene due to the high energy collision of grinding media similar to the liquid sonication based process,[64, 65] suggesting the process to be more suitable for the functionalized graphene production.[61, 62] Alternatively, fluid dynamics can be applied to mimic the shearing force of ball milling. Various ways to create the fluid movement (e.g., vortex from rotation,[66] pressure difference driven,[67] mixer driven,[68] etc.) have been reported. Fluid dynamic based methods, especially in mixer driven process, have high exfoliation efficiency compared to the liquid sonication and ball milling method, therefore beneficial to the industrialization of graphene product although sharing the common obstacle of graphene quality.

1.2.2 Bottom-up approach: synthesis

Chemical synthesis methods such as chemical vapor deposition (CVD) and epitaxial growth are promising approaches to high-quality graphene production on a larger scale. Synthesis methods generally requires more complicated equipment and have higher operational cost but provides high yield production of high-quality graphene while the platform can be easily scalable for mass production. In general, the growth mechanism of graphene involves the breakdown of precursor molecules/structure to free carbon atoms and recombination of carbon atoms into graphene. The growth of thin graphite film on silicon carbide was reported long before the rise of

CVD graphene process, and those early findings in the graphitization of the carbides surface eventually lead to the development of the epitaxial growth technique for the high quality single layer graphene.[69-72] Especially, epitaxial growth of graphene has attracted much attention from the semiconductor industry because of the possibility of wafer scale growth of single crystal graphene.[73-75] Growth of high quality single layer graphene on Si had been a challenge due to relatively high solubility and low diffusivity of carbon in Si, but recent development showed successful growth of single crystal graphene over wafer scale area using a hydrogen-terminated germanium buffer layer.[76] However, high-cost substrate materials, low yield, and complicated transfer process limit the widespread use of the method.

Chemical vapor deposition started in the 19th century and had been an established thin film deposition technique since 1950s. CVD process can produce high quality graphene comparable to the epitaxial growth while on various metal substrate that can be easily etched away to transfer the grown graphene onto new desired substrates. Therefore, CVD growth process gained its popularity since the first report in 2006.[77] Since then, Cu,[78] Ni,[79] and Ir[80] were used to demonstrate the CVD growth of graphene. Among the different catalytic metals, Cu became an excellent candidate for single layer graphene synthesis owing to its low carbon solubility and low cost. It was shown that the graphene film grown on copper foil was predominantly single layer (< 5% of double layer) and continuous across the metal surface steps and grain boundaries.[78]

During the CVD process of graphene growth, hydrocarbon precursors decompose to form carbon radicals in a hot zone. Then, the radicals undergo subsequent chemical reactions with the catalytic metal substrate. Even though the mechanism is not fully understood yet, a carbon isotope labeling study revealed different kinetic mechanisms for Ni and Cu during CVD growth of graphene.[81] In the case of Cu, the carbon source of graphene was found to be mainly on the surface

of the metal catalyst due to the negligible solubility of carbon in Cu. As the growth time increases, individual graphene crystals coalesce into a continuous polycrystalline graphene film on the surface of Cu. Therefore, graphene growth on Cu is preferentially monolayer and known to be surface mediated. In contrast, carbon sources diffuse into bulk Ni and the segregation process occurs until the concentration of carbon in the bulk metal reaches saturation. For this reason, a thin copper foil is often used for single layer graphene growth, and Ni is often used for multilayer graphene growth.

In addition to the effects of catalytic substrates, CVD growth condition and their effects were studied extensively to improve the quality of graphene such as number of layers, defect density, and crystallinity.[82-85] Roll-to-roll production of CVD graphene is demonstrated as well as large size single crystal graphene growth.[86-89] CVD is one of the reliable tools to produce high quality single layer graphene over a large area while versatile to be transferred onto various substrates; The CVD process was chosen to synthesize single layer graphene for this dissertation.

1.3 Characterization of graphene

Single layer graphene is almost transparent, but still can be seen easily when graphene is deposited on a SiO_2/Si surface. Raman spectroscopy can be used to probe many different properties of graphene, and detailed surface topology can be imaged using Atomic Force Microscope (AFM). In this section, frequently used characterization techniques of graphene are described with the emphasis on Raman spectroscopy of graphene.

1.3.1 Optical microscopy

Graphene absorbs 2.3% of incident light with negligible reflectance.[90] This relatively significant light absorption given its atomic thickness makes the imaging of graphene feasible under optical microscope. However, it is still generally challenging to distinguish graphene from its underlying substrate especially with untrained eyes. Instead of the transmission measurement, the visualization of graphene can be more easily done in reflectance measurement.[91] It has been shown that different light filter can be used to optimize the contrast of graphene up to ~ 12 % on the substrate regardless of oxide thickness.[92] With certain thickness of SiO_2 layer (e.g., ~90 nm or ~280 nm) on Si wafer, physical features of graphene can be easily examined using optical microscopy with white light.

1.3.2 Atomic force microscopy (AFM)

AFM is one of the scanning probe microscopy techniques that can be used to probe a wide range of properties of graphene. The initial report of successful separation of graphene by Novoselov and Geim used AFM to identify single layer and few layer graphene after optical screening.[4] Since then, AFM is widely used to identify the number of layers in exfoliated graphene samples owing to its sub-nanometer scale resolution of surface topographic imaging. In AFM, a probe is attached to a flexible cantilever, and a laser is focused on the back of cantilever. As the probe scans the sample surface, the cantilever bends due to the change of force between the surface and the probe. The bending causes a change in the reflected laser position. The reflected laser is detected by a position-sensitive detector and the movement of the tip is recorded. There are three basic modes of operation in AFM: contact mode, non-contact mode, and tapping mode. Contact

mode scans with the tip in close contact with the surface of the sample. Non-contact mode is used when the tip contact might alter or damage the sample. Tapping mode alternately places the tip in contact with the surface and lifts it off, combining contact mode and non-contact mode. Tapping mode was used to observe the morphology of CVD graphene in our study.

Scanning probe microscopy (SPM) techniques such as AFM are widely used to measure the physical dimensionality of nanoscale materials. By scanning the step of graphene on substrate, the thickness of graphene flake and ultimately the number of graphene layer can be estimated. However, the thickness measurement of the single layer graphene requires careful analysis. There had been a wide range of thickness values reported in the literature (from 0.4 nm to 1.7 nm)[93] considering the inter-plane spacing of graphite is only 0.335 nm.[94, 95] Possible variables such as interactions between AFM probe/graphene/underlaying substrate, adsorption of water layer, and sample preparation process are generally regarded as the contributing factors of the observed variation in the thickness measurements.

During the topographic scan, AFM can also provide the chemical information via phase contrast. In dynamic mode such as tapping or non-contact mode, AFM probe is brought close and oscillated normal to the sample surface. When the probe taps the surface, the oscillation amplitude gets reduced which is used to record the topology information. The phase of the oscillation also can be affected via probe and surface interaction. The phase shift occurs as the oscillation of the probe gets delayed, which can be caused by the change of adhesion or viscoelasticity of materials. Although the interpretation of phase shift is complicated due to various contributing factors especially with changing topology and should be analyzed carefully, phase contrast is one of the most commonly used techniques to characterize the composition of material surface. Functionalized area of graphene can be distinguished from its pristine area using phase contrast

image. In addition, various non-topographic modes of AFM such as magnetic force microscopy, Kelvin probe microscopy, force spectroscopy, nanoindentation, and thermal modes make AFM versatile tool to study a wide array of graphene properties.[28, 96-99]

1.3.3 Raman spectroscopy

Raman spectroscopy can be viewed as one of the essential and critically important characterization methods for graphene related research. It is a non-destructive analytical technique, and carbon materials have unique Raman signatures that have been studied extensively long before the graphene research came into the spotlight.[100-102] Starting with the number of graphene layer studies in 2006, Raman spectroscopy of graphene has been studied intensely to probe various properties.[103, 104]

The process of normal Raman scattering is caused by the incident photon promoting an electron to a virtual state instead of an excited electronic state. Therefore, incident photon energy does not need to be matched to the energy between ground and exited electronic states in order for Raman scattering to occur. Most of the time, the molecule is excited to a higher energy state (virtual state) and quickly relaxed without any nuclear movement. The emitted photon in this process is elastic and has same energy as the incident photon, and the process is called Rayleigh scattering. On rare occasions, nuclei move along with electrons, and the energy involved in the motion of nuclei is no longer negligible. This difference in energy results in a frequency change of the scattered photon, which is called inelastic Raman scattering. Depending on its initial energy state, inelastically scattered photon has a lower or higher frequency (energy) compared to the incident photon, and those scatterings are called Stokes and anti-Stokes, respectively. Since Stokes shift is more intense than anti-Stokes shift, typical Raman spectra uses the Stokes shift and uses

positive wavenumber by convention, plotting the intensity of the scattered light versus the energy shift, or "Raman shift", in cm^{-1} unit.

One of the major advantages of Raman compares to another vibrational spectroscopy, such as Infrared (IR) spectroscopy, is the photon interaction process noted above. IR spectroscopy involves the absorption of photons, and one of the unique optical properties of graphene is that graphene is spectrally flat with optical absorbance of 2.3 %. Moreover, vibrational motion that changes the polarizability will activate Raman scattering while changes in polarity of the molecule activates IR. Therefore, Raman spectroscopy is sensitive to highly symmetric structures without natural dipole moments, and graphene with its carbon-carbon bonds are a perfect fit to those conditions. Raman is also high-throughput compared to other high-resolution microscopic techniques. Therefore, Raman spectroscopy serves as an important analytical tool in wide range of graphene related research as well as throughout this dissertation projects.

For graphene, there are three major characteristic Raman peaks: the D peak (~1350 cm^{-1}), the G peak (~1580 cm^{-1}), and the 2D peak (~2700 cm^{-1}).[105] The G peak is associated with the doubly degenerate phonon mode corresponding to the bond stretching of all pairs of sp^2-hybridized carbon atoms.[106, 107] In fact, the G peak is the only peak coming from a normal first order Raman scattering process in graphene.[103] Similar bands resembling G peak are found in all polyaromatic hydrocarbons.[108] The D and 2D peak originate from a second order process.[103] The D peak requires disorder in the symmetry of graphene to be activated, and is absent in defect free graphene. The 2D peak is approximately twice the D peak frequency, but does not require any defect for its activation.[103] The 2D peak is sometimes referred to as G´ in the literatures, due to early studies mistakenly thought to be the overtone or related to G peak. In this dissertation, G, D, and 2D nomenclature is used.

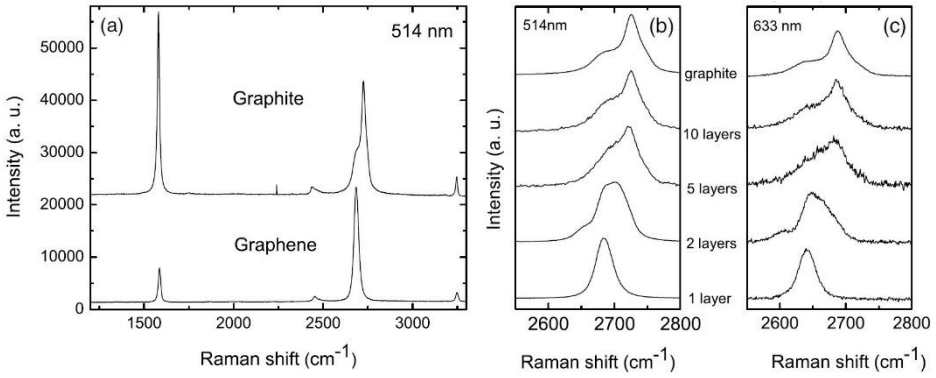

Figure 1.3 Raman spectra of graphene and graphite Comparison between graphene and graphite with 514 nm laser, rescaled to have similar 2D peak height. b) and c) Evolution of 2D peak as number of graphene layer changes using two different laser power 514 nm and 633 nm. Reprinted with permission from ref 103. Copyright 2006 by the American Physical Society.

The D and 2D peak undergo a significant change in its shape, position, and intensity depending on the number of graphene layer.[103] There are two components $2D_1$ and $2D_2$ in graphite 2D peak having approximately ¼ and ½ of G peak intensity, respectively. Figure 1.3 shows the change of the 2D peak as a function of the number of graphene layer.[103] Once graphene layers exceed more than 5, its Raman spectrum becomes almost indistinguishable from that of graphite. The change in the electronic band structure of graphene with the increase of its number of layers affects the 2D peak evolution. Therefore, Raman spectroscopy is widely used to confirm the number of graphene layer along with AFM topographic edge height scan. Moreover, different orientations of stacking multi-layer graphene should in principle be resulted in the significant electronic band structure that would be reflected in Raman spectrum.[109] For example, turbostratic (misoriented non-AB Bernal stacking) multi-layer graphene exhibit a single sharp 2D peak like single layer graphene.[110-112]

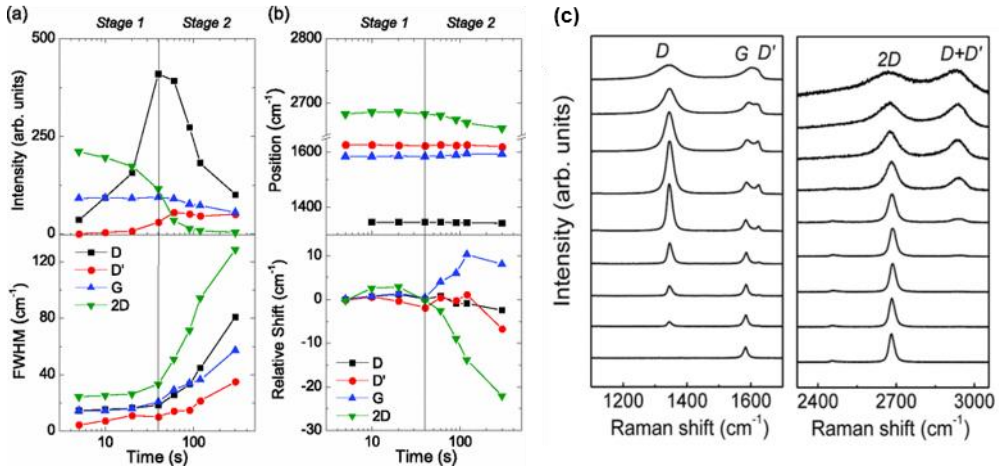

Figure 1.4 Raman spectrum evolution of the graphene disorder The epectrum evolution is represented in (a) intensity, FWHM, (b) position, and relative shift of the peak position of the D, D´, G, and 2D peaks as the defect concentration increases over time. (c) Raman spectra of oxidized graphene with increasing defect concentration from bottom to top. Laser power used was 2.41 eV. Reprinted with permission from ref 113. Copyright 2013 by the American Physical Society.

The quantification of defects, such as their density and type, is critical in graphene related studies since defects in sp^2 carbon structure can have significant impacts on their fundamental properties and ultimately for their future applications. Graphite disorder can be classified into three different stages proposed by Ferrari and Robertson.[114] Stage 1 is graphite symmetry broken into nanocrystalline graphite, and stage 2 is nanocrystalline graphite to low sp^3 amorphous carbon, and stage 3 is from low to high sp^3 amorphous carbon. In the case of graphene, earlier stages are mostly relevant owing to its limited dimensionality. At first, during the stage 1, D peak appears, and the intensity of the D peak (I(D)) increases as well as the ratio of D and G peak intensity (I(D)/I(G)). Following a D´ peak appears (~ 1620 cm^{-1}) and all peaks broaden with increase defect density. As disorder progresses, the D + D´ peak appears (~ 2940 cm^{-1}). In the second stage, the position of G peak (Pos(G)) shifts down toward ~ 1510 cm^{-1} and I(D)/I(G) decreases. Later, there are no longer

well resolved second order peaks only broad feature ranging from ~2300 to ~3200 cm^{-1}. Although Pos(G) is very useful to identify external factors such as doping, I(G) is relatively stable under the same laser excitation frequency.[115-117] Therefore, I(G) is often used as a reference to monitor the intensity change in other peaks. For example, as noted above, I(D) rapidly increases with the defect density of graphene, but I_G does not change significantly until the defect density reaches to certain point. Thus, I(D)/I(G) is often used to quantify the density of defects in graphene. As shown in Figure 1.4, I(D)/I(G) of graphene continuously increases until it reaches ~3 to 4 under the oxidation reaction.[118] The Tuinstra and Koenig relation,[106] which correlates the I(D)/I(G) with crystalline size of graphene, fails in the high disorder stage because with sp^2 rings become fewer, I_D decreases with respect to I(G). Therefore, increasing D peak indicates the defect density increase in graphene while it indicates more order in amorphous carbons. While Raman can be a great tool to quantify defects in graphene, one should keep in mind that some defects are not Raman-active and will be hard to be recognized in Raman spectroscopy. For example, perfect zigzag edges do not induce a D peak, but changes the shape of G peak that can be identified with the careful attention.[119, 120]

The Raman spectrum of graphene is sensitive to many perturbations that analysis should be made with careful considerations of many possible external parameters. One of external parameters is the doping condition of graphene. Graphene can be looked as entirely made out of surface area, thus interactions with the surroundings can have significant impacts on the electronic energy level of graphene. The effects of doping level on the Raman spectrum of graphene have been studied in great detail.[107, 121-125]

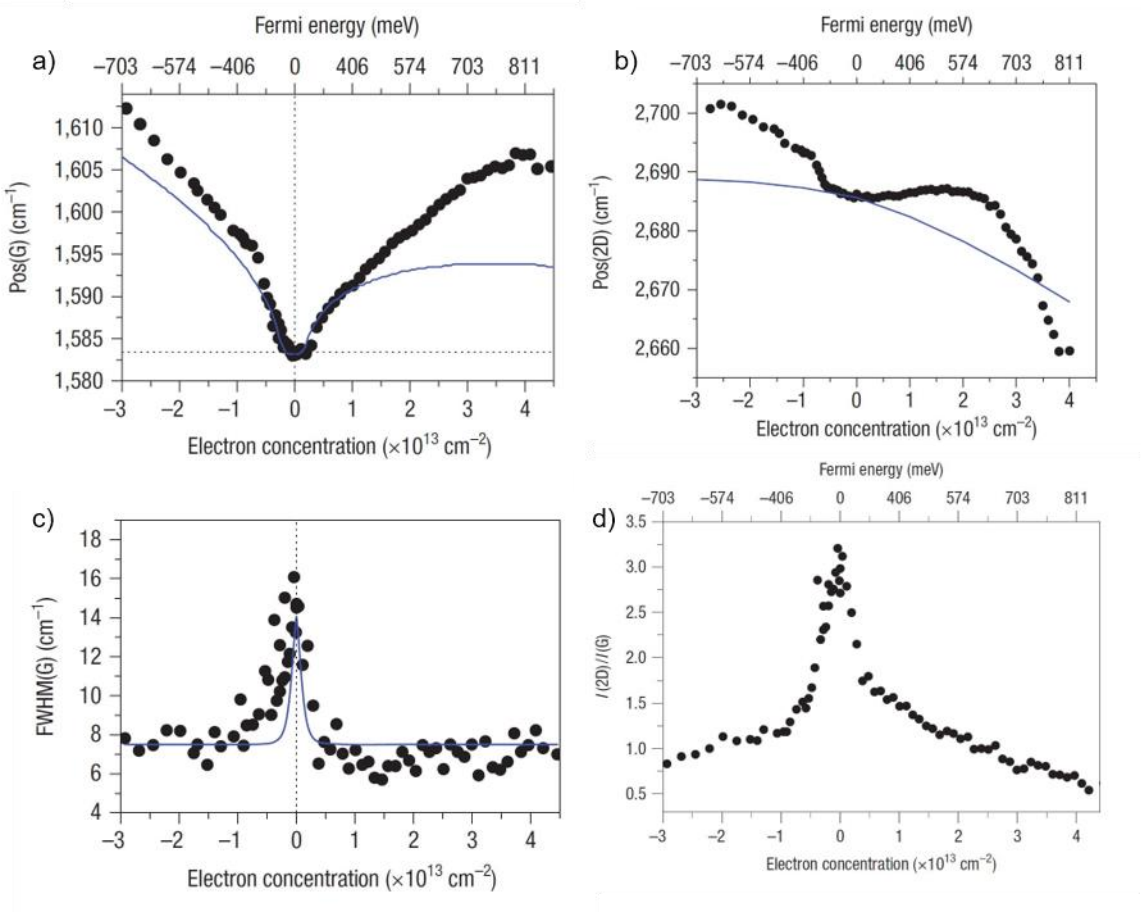

Figure 1.5 Raman spectra of graphene as a function of a gate voltage a) Position of the G peak, b) position of the 2D peak, c) FWHM of the G peak, and d) the ratio of the intensity of the 2D and G peak exhibit the dependence on the electron concentration. Reprinted with permission from ref [125]. Copyright 2008 by Nature Publishing Group.

As shown in Figure 1.5, Pos(G) upshifts, and the FWHM(G) decreases symmetrically as the charge charrier density increases. On the other hand, Pos(2D) shifts down as under large electron density. Even though Pos(2D) does not shift as much as Pos(G) especially near charge neutral point, the G and 2D peak can be used together to analyze whether graphene is doped by holes or electrons. The FWHM(G) also shows dependence on the electron concentration. I(2D)/I(G) also can be a good measure of the doping level of graphene, as the ratio decreases with

the increase of hole carrier density of graphene. The doping level can be shown in the defect related peaks of graphene too. The intensity of the D and D´ peaks decreases as doping level increases.[126]

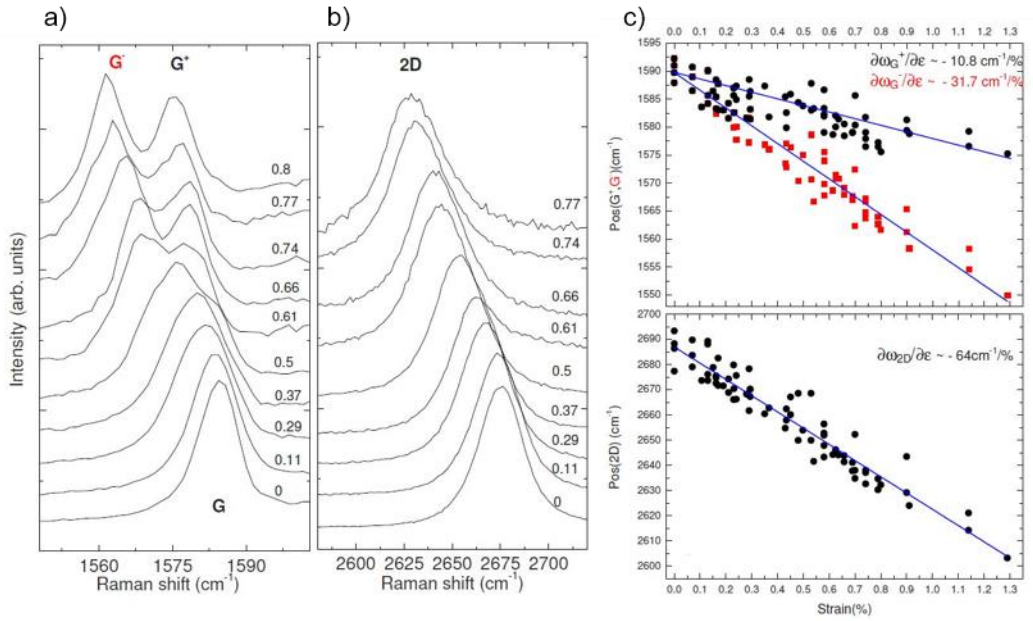

Figure 1.6 Raman spectra of graphene with uniaxial strain (a) G and (b) 2D peak measured with incident light polarized along the strain direction. (c) Peak positions of G^+, G^-, and 2D plotted as a function of applied strain. The blue lines are linear fit to the data and slope of the linear fit was -10.8, -31.7, and -64 cm^{-1}/% respectively. The doubly degenerate G peak splits in the subbands G^+ and G^- while 2D peak remains as a single band. Reprinted with permission from ref 127. Copyright 2009 by the American Physical Society.

A material is under strain when it is stretched or compressed out of its relaxed state. Usually, phonon softening occurs for a crystal when tensile strain is applied, and the opposite occurs with the compressive strain. The Grüneisen parameters describes the rate of those relationship, phonon softening as a function of strain.[128] The effects of strain on the Raman spectrum of graphene had been also reported.[127, 129-133] The doubly degenerate optical mode E_{2g} splits into two components as tensile strain is increased resulting in the splitting of the G peak into

two sub-bands as shown in Figure 1.6. In addition to the splitting, both G^+ and G^- subpeaks as well as 2D peak downshift with the tensile strain. The downshift is much more pronounced in the 2D peak. The uniaxial strain changes the relative positions of the Dirac cones,[134] as in return have significant impact on double resonance and triple resonance process in Raman scattering leading to additional shift of 2D peak as well as the peak broadening and splitting.[127, 131, 135] Interestingly, CVD graphene exhibited different behavior in G peak compared to the exfoliated graphene under strain. The G peak under compressive strain shift down in CVD graphene opposite to the upshift of exfoliated graphene, which was attributed to the polycrystalline nature of CVD graphene owing to its grain domain boundaries.[132] Due to the sensitivity of G and 2D peak of graphene towards both charge density and mechanical strain, the Raman spectrum of graphene should be carefully analyzed when doping and strain effects are co-existing. The correlation between Pos(G) and Pos(2D) can be used to separate the effects of charge and strain on Raman spectrum of graphene.[136]

1.3.4 Other surface analysis techniques

There are many other techniques available for the characterization of graphene. Scanning Electron Microscope (SEM) uses electron beam to interact with the surface of material and collect various information about the sample. Modern optical microscope can provide 1500 times of magnification with the spatial resolution limit of 0.2 μm.[137] This limited resolving power inherited from the wavelength of white light is solved in electron microscopy owing to the wavelength of accelerated electrons being much shorter. Similar to optical microscope and AFM, SEM has been used widely to investigate the topological surface information of graphene samples such as folding, tearing, wrinkles, etc. In addition, *in situ* SEM had been used to monitor the growth process of graphene.[138] In electron microscope family, transmission electron microscope (TEM) is also

widely used especially in atomic scale resolution. TEM transmits very high voltage electrons through the sample, making thin layer nature of graphene a good fit for TEM. High resolution TEM provides valuable atomic resolution imaging on the structural deviations of graphene from its pristine state.[139, 140] With the high resolution and electron diffraction patterns provided by TEM, the number of layers of graphene flake can be accurately counted from the edges as well as crystal orientations of graphene since the location of individual carbon atoms can be imaged.

X-ray photoelectron spectroscopy (XPS) is a standard surface analysis technique with approximately 5 nm average analysis depth. The chemical and structural information of the surface are obtained via X-ray and material interactions. During XPS analysis, the surface of the studied material is irradiated with a beam of X-rays, and electrons are ejected by a photoemission process. The kinetic energy difference between the ejected electrons and incident photon measures the electron binding energy of the surface atoms. The number of detected electrons is plotted as a function of the binding energy to provide quantitative information. Because atoms eject electrons having specific characteristic energy, elemental identification and quantification can be made. XPS has been also widely used for graphene and graphene related material to investigate various properties such as surface structural characteristics, chemical compositions, and electronic properties.[141-143]

Spectroscopic ellipsometry (SE) is another classical surface and thin film analysis technique that has wide range of analysis thickness from a few Angstroms to several tens of microns. Linearly polarized light is reflected off of a surface, and the change in the polarization of the light (often resulting in elliptical polarization, hence the name) is measured to model the thickness and optical properties of the thin film. SE is indirect and non-destructive that widely used in many optical and semiconductor thin film applications. With the single layer of graphene

measurement, unknown single layer model can be established and used to identify number of graphene layer in different samples. Moreover, the surface contamination of graphene from ambient air or in pure water of open container had been monitored using SE previously.[144, 145] With well-established model of SiO_2, thickness of SiO_2 on Si wafer can be also measured to control the uniformity of the substrate for graphene.

1.4 Chemistry of graphene

Graphene had attracted intense interest from wide range of disciplinary for over a decade. First, being a noble material while having such simple atomic structure as a building block of familiar carbon allotropes, fundamental solid-state physic and quantum physics studies has been progressing incredibly with this air-stable stand-along nanomaterial. With its unique electronic, physical, material properties, many possible application areas were studied intensively. To this date, 17 years after the start of gold rush, graphene and its hybrid/derivative materials are continuously being studied all over the world. Specifically in chemistry community, functionalization of graphene has been a great interest to fine-tune its electronic, chemical, and mechanical properties.[146-148] Graphene can be viewed as a double-sided surface which are widely open to various reactions; there are endless possibilities to tweak graphene via chemical modification, and especially accessibility is great while being a solid since everything is happening on the surface level. This giant aromatic-ring-containing molecule has intriguing properties such as extreme electrical conductivity and mechanical strength that can be engineered chemically and further incorporated into a composite material to contribute those beneficial properties. Full hydrogenation of graphene converts semi-metallic graphene into insulating graphane, a two-

dimensional hydrocarbon layer.[115, 149] Chemical doping of graphene can modify the carrier type and concentration while extremely high carrier concentration is feasible in graphene owing to its band structure, which could lead to exciting properties such as room temperature superconductivity and ferromagnetism.[150-152] With the scope of material extended to graphene derivatives and composites, implications of graphene chemistry are greater.

For the exciting future applications, understanding chemical reactivity of graphene is critical. In addition, as a fundamental building block of other carbon materials, gained understanding of graphene chemistry may further contribute to the chemistry of other carbon allotropes. In this dissertation, three major aspects of graphene are explored. First, environmental effects on graphene are studied. It is critical to understand how graphene interacts with ambient-found species for any in-air applications of graphene. Secondly, method to control and enhance the reactivity of graphene was developed to gain the understanding of graphene oxidation reaction and its enhancement. Then, inertness of graphene was evaluated to employ it as a catalyst to enhance other chemical reaction, specifically HER to demonstrate the usefulness of elastic mechanical modulation on graphene and its catalytic activities.

2.0 Environmental Effects on Graphene Doping via Static Gate Voltage

2.1 Introduction

The Fermi energy of graphene can be controlled by various doping methods. Especially, external electric field can be applied via gating, which could modulate carrier concentration without directly changing the electronic band structure of graphene. During electrical modulation, other external factors can contribute to the overall doping process of graphene such as underlaying substrate, oxygen-containing molecules, and other contaminations from the surrounding of the graphene device.

Adsorption greatly influence the properties of graphene because of its surface dominating two-dimensionality. The adsorption of small gas molecules such as H_2, O_2, CO, and NO_2, and their effects on graphene's electronic properties have been studied both theoretically and experimentally.[153-158] Those reports showed that the molecular adsorption can lead to either n-type or p-type doping of graphene. Electron acceptors, such as oxygen, are known to hole dope graphene (p-type), and NH_3 and CO act as donors to electron dope graphene (n-type).[156] Since the electrical conductivity depends on the charge carrier density, molecular adsorption can alter the electrical conductivity of graphene. The effects of adsorbates need to be well understood before graphene can be implemented especially under ambient conditions for wide range of practical applications in-air.

In addition to interaction with adsorbates from air, its interaction with substrate is another critical factor in impacting graphene chemistry. Unless graphene is fully suspended, the effects of underlying substrate on graphene should be considered. During graphene transfer to a wafer

substrate, charges can be trapped in the bulk oxide and graphene-oxide interface. Those trapped charges could act as external scattering centers and significantly suppress the charge mobility of graphene.[159] Charge trapping is also known to be responsible for the hysteresis observed in electrical measurements in graphene devices.[159-162] Moreover, strong interactions between graphene and substrate could ultimately modify the band structure of graphene. For example, a theoretical study predicted the opening of a small band gap in graphene by using oxygen-terminated SiO_2.[163]

Water can also play a significant part in graphene doping.[164-166] The interaction between an adsorbed water molecule and graphene is thought to be rather weak, and strong attractive forces between water molecules could form a water cluster that acts as a defect center in graphene.[167] A theoretical study showed that highly ordered water molecules can induce a strong electrostatic dipole moment causing local electrostatic fields, which interact with the substrate and result in graphene doping.[164] Also, a controlled gas exposure study showed the direct relationship between air exposure and SiO_2/Si substrate.[166] The results suggest charge transfer doping of graphene by an oxygen-water redox couple mechanism similar to that seen with diamond.[168]

Electrical control of molecular adsorption doping of graphene has been studied with many different molecules such as NO_2, NH_3,[169] H_2,[170] CO_2,[171] and piperidine.[172] Those results from recent studies show that the concentration of adsorbates on the surface of graphene can be modulated by external electric field. The controlled adsorption of oxygen using an applied external electric field was also demonstrated with bilayer graphene field-effect transistor (FET).[154] The oxygen adsorption was enhanced when bilayer graphene was electrically n-doped. A theoretical study suggested the diffusion of oxygen atoms on graphene also strongly depends on carrier density.[173] Therefore, it could be possible to further control the rate of reactions on the surface of

graphene using electrical modulation by tuning the concentration and diffusion of adsorbates simultaneously. In addition, the electrical control of the charge transfer between graphene and adsorbed molecules had been also demonstrated which could lead to fine-tune the electron-transfer (ET) based reactions.[154]

The adsorption process can help the electric modulation to achieve the desired Fermi level by having the same doping effect as the direction of the electric field applied to graphene. However, it also can counteract to reduce the overall doping density. Therefore, even though electrical modulation possesses great potential to tweak chemical reactions of graphene, the combined effects of applying an electric field to graphene exposed to its surroundings are challenging to control simultaneously and further studies are highly desired.

The effects of applying an external electric field have been studied by many researchers in order to modify electronic properties of graphene[4, 121, 174, 175] and other low dimensional systems.[176, 177] Graphene FET is a commonly used device to investigate the effects of the applied electric field and the fundamental electronic properties of graphene. Although top-gated graphene FETs have been reported with promising performances,[125, 178, 179] SiO_2/Si back-gated graphene FETs remain the most common configuration due to their simplicity. In general, graphene is transferred onto a SiO_2/Si wafer, and electron-beam lithography and standard lift-off procedure are performed to pattern graphene and deposit metal contacts to the device. Heavily doped Si is typically used as a back gate, and the dielectric layer lies between graphene and the bulk Si back gate. The source/drain metal contacts are deposited on the graphene surface.

Despite high performance devices has been demonstrated previously, complete control of the surrounding environment of graphene can be challenging with a graphene FET. In conventional FET devices, the charges from the substrate or gate are known to be trapped in the bulk oxide and

oxide interface during the operation. Analogous to Si-SiO_2 interface, the charge trapping effect at graphene-SiO_2 interface has been proposed.[180, 181] In addition, the typical graphene FET undergoes a long device fabrication process. Additional contamination can be introduced during the process and affect the performance of the graphene FET.[182-184] Moreover, most of electrical modulation of graphene FETs are done in vacuum, first to prevent device hysteresis on electric measurements, and secondly systematically study the effects of electric field with controlled exposure of target molecules. Also, most studies focus on the electric properties of graphene FETs such as conductance and mobility measurements which only requires the electric modulation to be done in very short time scale. A better understanding of the longer time scale effects is necessary to study the effects of electric modulation on the reaction kinetics. Also, in situ Raman spectroscopy has been scarcely used study the time dependence of the applied gate voltage.

The mechanism of hysteresis observed in graphene FETs is still not clear because many previous reports showed scattered results. First, very short time scale of ~100 μs was reported with interface charge trapping mechanism.[185, 186] In long time scale, the charge injection from graphene to interface was proposed using Kohlrausch stretched exponential function with a time scale of ~100 s.[187] The similar time scale of about 100 s was observed using Raman spectroscopy, but the different mechanism, the electrochemical doping of the O_2/H_2O redox couple, was proposed.

In this chapter, the effects of applied electric field on graphene were investigated focusing on long time scale using Raman spectroscopy. The change in Pos(G) in air and N_2 showed that aqueous oxygen electrochemical redox couple is unlikely to be the dominant mechanism. The decrease of Pos(G) in N_2 and Ar were fitted with the double exponential decay and the time constants (~20 s and ~200 s) were found under 3 MV/cm. In all gas environments, the shift in

Pos(G) was consistent with the charge trapping/de-trapping mechanism. However, the different time scale suggests more complex charge trap process.

2.2 Experimental

2.2.1 Graphene synthesis

Copper foil (25 μm thick, Alfa Aesar, item No.46365) was used for CVD growth of graphene. Cu foil was cut into approximately 1.5 cm × 6 cm strips and treated with electropolishing (EP).[188] In brief, copper foil is electrolyzed at 5 V for 30 s in phosphoric acid solution (500 ml of deionized water, 250 ml of phosphoric acid, 250 ml ethanol, 50 ml isopropyl alcohol, and 5 g of urea). Only polished anode copper foil was used for graphene growth. After EP treatment, anode copper foil was rinsed with deionized water twice. In some cases, copper foil was further treated with concentrated HCl for 15 s after EP. Copper foil treated with both EP and concentrated HCl did not have any significant effects on graphene compared to copper foil with EP only.

After thorough rinsing, copper was blow dried with a nitrogen gun and placed on the top of a quartz boat. The quartz boat with the copper foil was then inserted into the center of a 1-inch-diameter fused quartz tube furnace. The tube furnace was evacuated within 5 min to prevent further oxidation of the copper foil. After evacuation, the tube was back filled with $H_{2(g)}$ (2 standard cubic centimeters per minutes (sccm)) and annealed for 1 h at 1000 °C (annealing). The alternative annealing process was done at various higher temperatures (highest at 1060 °C) and extended time periods (up to 10 h). Different annealing temperatures and periods showed similar results in Raman spectroscopy and AFM. $CH_{4(g)}$ (20 sccm) was introduced after the annealing step for 30 min

(growth). H_2 flow and temperature during the growth were kept same. After the growth step, furnace was cooled to room temperature with the same gas flow as growth step for both H_2 and CH_4. Figure 2.1 shows the growth process summary. Graphene samples were stored in a clean glass petri dish until the transfer.

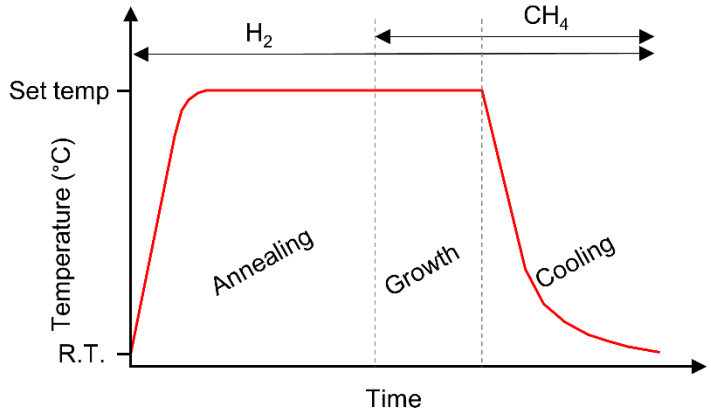

Figure 2.1 The CVD process of graphene synthesis Annealing period was varied between 1 h to 10 h depending on the system fluctuation such as received copper foil quality. Growth time was fixed to 30 min. Cooling time was ~2 h down to room temperature. H_2 and CH_4 flow rate was set to 2 sccm and 20 sccm respectively.

2.2.2 Graphene transfer

Graphene films were transferred on SiO_2/Si wafer using polymer based wet transfer technique.[189, 190] Poly(methyl methacrylate) (PMMA) and Poly(Bisphenol A carbonate) (PC) were used as supporting polymers. In a typical transfer, as grown graphene film on top of Cu foil was spin coated with 5 wt% PMMA (Aldrich, MW 996000) in anisole (Sigma-Aldrich, 99%) at 3400 rpm for 50 s 5 times or 1.5 wt% PC (Sigma-Aldrich, MW 45000) in chloroform (Sigma-Aldrich, 99.8%) at 3400 rpm for 30 s 3 times. Then the Cu foil was etched for 3 h in 0.1 M of aqueous

$(NH_4)_2S_2O_8$ solution (Sigma-Aldrich, 98%). After etching, polymer/graphene film was scooped out with a clean glass slide and transferred into a water bath multiple times to rinse off the etchant. After thorough rinsing, polymer/graphene film was placed on a SiO_2/Si wafer and spin dried at 5000 rpm for 5 min. Different drying methods such as drying extended time in air or in vacuum did not have significant impact on the Raman spectrum. In order to remove the supporting polymer layer, a second layer of PMMA was applied onto PMMA coated graphene following reported procedure.[191] PMMA solution (1.4%) was drop casted on the PMMA/graphene/SiO_2/Si sample and cured for 30 min at room temperature. Then the sample was placed in acetone bath for 1 h followed by another acetone bath or acetic acid (glacial) bath for 12 h. For PC removal, PC/graphene/SiO_2/Si sample was soaked in chloroform for 12 h. Once polymer supporting layer is removed, graphene was rinsed with isopropanol and gently blow dried with N_2.

2.2.3 Graphene device fabrication

Electrical connections were made on graphene side (top) and on Si side (bottom) by applying silver paste (SPI Supplies, 04969A-AB) as a conductive glue to attach copper wires. Unpolished bottom side of Si wafer was scratched off with a diamond tip to expose bulk Si layer. Highly doped Si layer of the bottom side of wafer served as a back-gate and connected to the positive terminal of the power source. Two different types of SiO_2/Si wafer were used throughout the study, wet thermal SiO_2 (University Wafer, 300 nm wet thermal oxide, P/B) and dry chlorinated thermal SiO_2 (Nova Electronic Materials, 300 nm dry chlorinated thermal oxide with forming gas annealing, P/B). After the fabrication, each sample was tested to confirm the applied voltage with 0.1 V of precision using a multimeter.

2.2.4 Raman spectroscopy

Micro-Raman spectra were obtained using a homemade Raman spectrometer with 532 nm CW single-longitudinal mode solid state laser and 40 × objective (NA: 0.60). The size of laser spot was approximately 1 μm, and laser power from 0.1 mW to 20 mW was used. The laser power was measured at the sample stage with the laser power meter. Obtained spectra were calibrated with standard naphthalene and processed with Igor pro 6.37 software. All graphene peaks were fitted with a single Lorentzian lineshape. A custom-made aluminum flow cells with a quartz window was used to host a graphene sample in a desired gas environment. The gas outlet of the flow cell was connected to an oil bubbler to prevent any air diffusion back into the flow cell. Graphene device was faced down against the quartz window, and flow cell was placed on the inverted Raman microscope sample stage. Figure 2.2 shows schematic image of graphene sample setup with Raman spectroscopy.

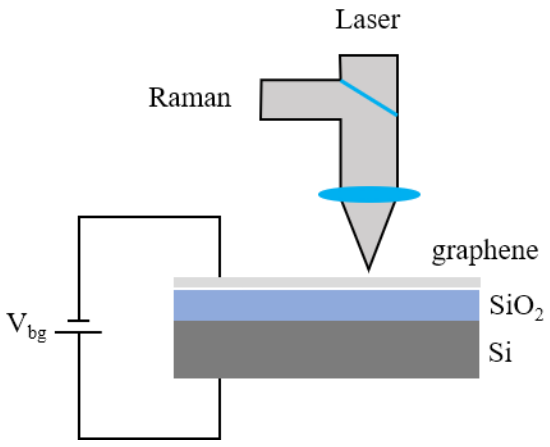

Figure 2.2 Schematic image of experimental setup Raman spectrometer and graphene sample with electric connection are shown. Heavily doped (p^{++}) Si was used as a back-gate (V_{bg}). Graphene and Si were connected to low and high terminals respectively.

2.2.5 Atomic force microscopy

Atomic force microscope images were obtained using SPM SmartSPM^{TM}-1000 Scanning Probe Microscope (AIST-NT, n/s HE002-H) with tapping mode and HQ:NSC15/AL BS AFM probes (MikroMasch, 325 kHz, 40 N/m).

2.2.6 Electrical modulation of graphene

Keithley 2614B SourceMeter SMU instrument (Keithley) was used to source and measure voltage and current. In brief, one set of terminals were used to source the chosen voltage ranging from -90 V to +80 V and measure voltage and current across the graphene/SiO_2/Si sample. The second set of terminals were attached on the separate electrical contacts to confirm the applied voltage across the sample. SMU instrument was controlled remotely via Keithley Test Script Builder software.

2.3 Results and discussion

2.3.1 CVD grown single layer graphene

Raman spectrum and AFM images were obtained to verify the quality of single layer graphene grown by CVD method. Typical Raman spectrum of single layer graphene in ambient condition is shown in Figure 2.3a. The D peak was not present suggesting graphene had very low defect density. Two prominent peaks, the G and 2D peak, were similar in intensity and positioned

at 1594.8 cm^{-1} and 2684.4 cm^{-1}, respectively. The graphene sample was a single layer, based on the sharp 2D peak without any sub-band feature. AFM image in Figure 2.3b shows the wrinkles which are known for CVD grown graphene due to the different thermal expansion between Cu substrate and graphene during the cooling process. No pin holes or cracks are observed.

Undoped single layer graphene has the 2D peak roughly 4 times more intense than the G peak.[103] The decreased intensity ratio I(2D)/I(G) with upshifted Pos(G) indicate prepared graphene sample was highly doped, and the upshifted Pos(2D) further shows that the graphene sample was hole doped which is commonly observed in samples measured in ambient. The relation between air exposure and hole doping of graphene can be verified by using different gas environment. Figure 2.3c shows clear change in Pos(G) during 9 h of moderate (~200 sccm) N_2 flow. The significant decrease of Pos(G) was observed overtime. This observation suggests the desorption of physisorbed molecules from the graphene surface which were responsible for hole doping. Overall change of Pos(G) can be fitted to an exponential decay. However, the decay of Pos(G) diverged from the first order kinetic model suggesting multiple types of doping molecules were desorbing from the graphene surface. Most of desorption occurred during the first couple of hours of N_2 flow, and the desorption process slowed down dramatically. However, the intrinsic Pos(G) for undoped graphene, ~1584cm^{-1}, could not be recovered even after 9 h of N_2 flow. The water residue with dissolved oxygen could take much longer time to be desorbed and be responsible for the remaining hole doping effect.

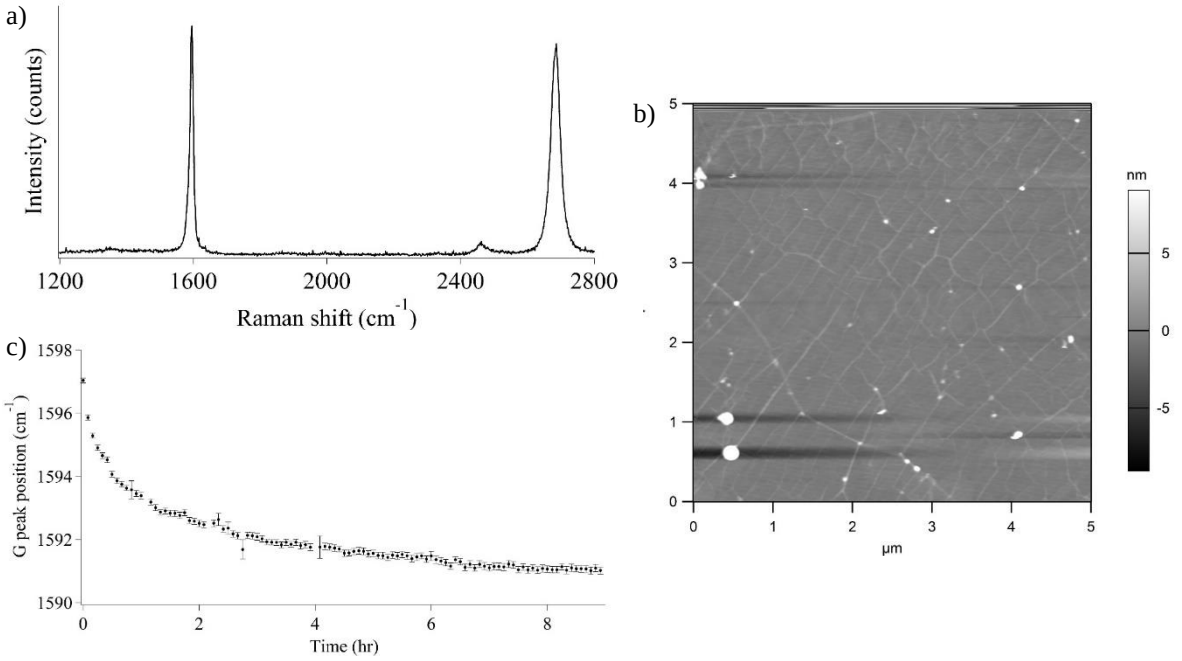

Figure 2.3 CVD grown single layer graphene a) Raman spectrum and b) AFM image of CVD grown single-layer graphene on SiO_2/Si in ambient. c) The effect of N_2 flow on the G peak position of graphene Raman spectrum.

2.3.2 Electrical doping in air and early N_2 environment

Raman spectroscopy can be a great tool to monitor the effects of electric doping on graphene. In general, negative (positive) back gate voltage introduces excess positive (negative) charge carriers on graphene resulting in hole (electron) or p-type (n-type) doping of graphene. However, in ambient condition, electron doping of graphene was not observed even with +80 V of back gating, which is the maximum voltage used in this study. The observation was consistent with heavily p-doped graphene as shown in previous section.

In order to investigate the proposed O_2/H_2O redox mechanism on the change of Pos(G) in more detail,[192] the electrical doping effects were monitored throughout the change of graphene

surrounding from air to N_2. If the change of Pos(G) is driven by the electrochemical charge transfer, the limited oxygen in N_2 should suppress the amount of charge transfer and reduce the change in Pos(G). Figure 2.4 shows the evolution of Pos(G) on the same location of graphene plotted as function of time with alternating polarity of applied electric field in air and early N_2 environment. Raman spectrum was taken every 10 s while each static voltage, 0 V, -80 V, and +80 V, was applied for 10 min. Different magnitude of gate voltage resulted in the different magnitude of electrical doping on graphene, but same general trends were observed. Due to possible inhomogeneity within a sample, direct comparison of Raman spectrum between different position of the sample was avoided.

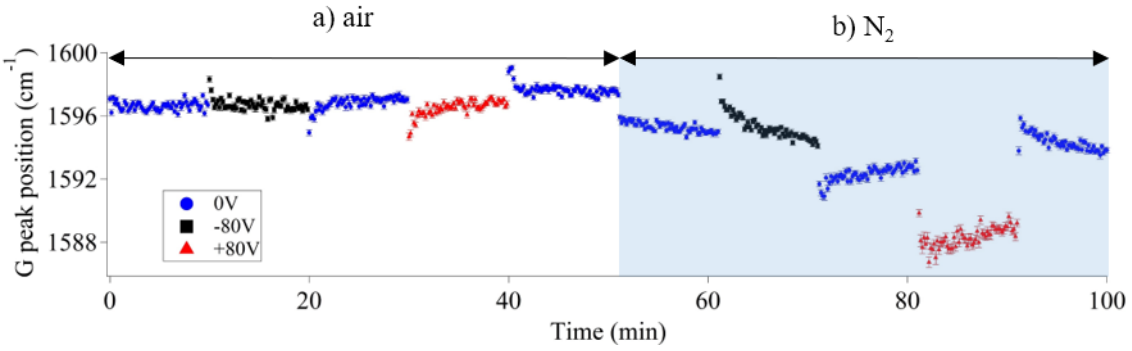

Figure 2.4 The G peak position of graphene under various electric field Each Raman spectrum was obtained with 10s of exposure time. Static gate voltage was held for 10 min a) in air and b) in nitrogen while Raman spectra were collected on the same location of graphene.

When negative gate voltage was applied in air, hole doping immediately upshifted Pos(G), suggesting an increase of total hole doping in graphene. This initially increased charge carrier density was decreased back as shown with gradual downshift of Pos(G) during the 10 min period (black square in Figure 2.4a). Since applied electric field was held constant throughout the duration of each value, the change of Fermi level of graphene reflected in Pos(G) suggested that the

decrease was related to the change in graphene and its surroundings. When the gate voltage was turned to 0 V (blue circle at 20 min), Pos(G) immediately downshifted as electrical p-doping was removed and upshifted gradually over time. Assuming graphene is significantly hole doped as shown by initial characterization in the previous section, positive gate voltage leads graphene to lower charge carrier concentration. Therefore, downshifted Pos(G) under the positive gate voltage can be explained with the overall graphene Fermi level being closer to its neutral point and upshifted back. Then, at following 0 V switch, Pos(G) shifted up and gradually downshifted.

The electrochemical doping of O_2/H_2O redox couple on graphene occurs due to the Fermi level of graphene higher than the electrochemical potential of the redox reaction as following.

At acidic conditions: $$O_2 + 4\,H^+ + 4\,e^- \leftrightarrow 2\,H_2O \quad (2.1)$$

At basic conditions: $$O_2 + 2\,H_2O + 4\,e^- \leftrightarrow 4\,OH^- \quad (2.2)$$

The electrochemical potentials of the electrons for this oxygen redox couple in Equation 2.1 and 2.2 are -5.66 eV at pH 0 and -4.83 eV at pH 14, respectively (relative to vacuum level, at 0.21 bar of partial pressure of O_2).[168] Assuming water is in equilibrium with air, slightly acidic (pH 6) condition can be used which corresponds to an electrochemical potential of -5.3 eV. The Fermi level of undoped graphene (~4.6 eV)[193] lies above the electrochemical potential of the solution. Hence, electrons can transfer out of graphene into an adsorbed water layer when graphene is exposed to humid air, and the observed hole doping of graphene in air is consistent with the mechanism.

The initial Pos(G) in air was 1596.5 cm^{-1}, corresponding to a doping induced shift of the Fermi level from the Dirac point of about -0.3 eV.[125] The resulted Fermi level of ~ -4.9 eV falls

within the electrochemical potential of the redox couple (from -4.83 eV to -5.66 eV with pH range14-0). Assuming the charge transfer between graphene and the redox couple reached equilibrium at the end of each 10 min of gate voltage, the observed change of Pos(G) in air can be explained with the O_2/H_2O redox couple mechanism. The observed Pos(G) under negative gate voltage corresponds to ~ -5 eV. The electron transfer from the O_2/H_2O redox couple to graphene could occur until a new equilibrium is established. Once gate voltage was turned off, the Fermi level of graphene was pushed up back to -4.9 eV and the electron transfer from graphene to the O_2/H_2O redox couple can occur. Similarly, positive gate voltage and followed 0 V would change the Fermi level of graphene and a new equilibrium can be reached.

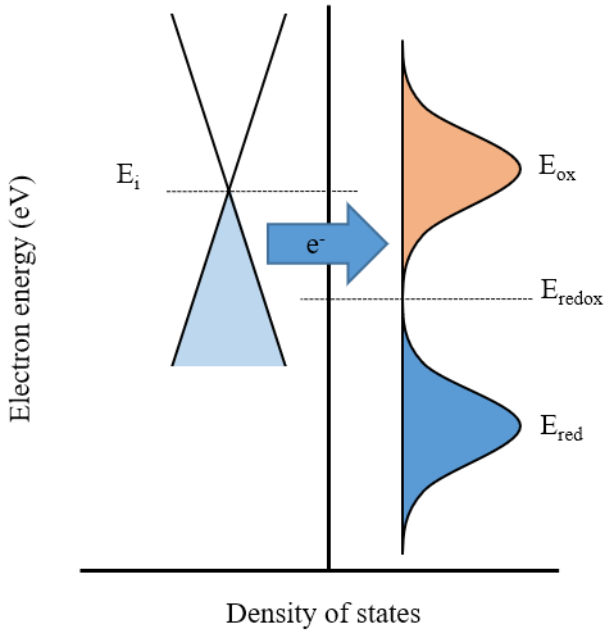

Figure 2.5 Schematic diagram of the electrochemical electron transfer doping process of graphene E_i is the Fermi level of graphene (-4.6 eV) and E_{redox} is the electrochemical potential of O_2/H_2O redox couple at pH 6 (-5.3 eV). The blue arrow shows the direction of electrons transfer from graphene into the solution.

However, the proposed electrochemical electron transfer mechanism did not agree well with data obtained in N_2 environment. The overall downshift of Pos(G) within 1 h of N_2 flow at the first 0 V in Figure 2.4b coincides with the desorption of physisorbed molecules observed in previous section. The shifting of Pos(G) did not stabilize within 10 min compared to air which reached its stable Pos(G) less than 3 min. The effects of on-going desorption process could be a major contributing factor for this slower kinetic observed in N_2 environment oppose to air. Still, some noticeable differences in Pos(G) shifting trend were observed in early stage of N_2 flow. First, the change of Pos(G) was more drastic under 10-min same voltage period. The previous O_2/H_2O redox couple study showed the dissolved oxygen is necessary for charge transfer to take place, and the significantly reduced change in pH was observed under N_2 environment.[168] The increased change in Pos(G) under N_2 does not coincide with the previous observation.

Another important change observed in N_2 was the different behavior in Pos(G) under positive gate voltage. As shown in Figure 2.4b, Pos(G) changes the direction of the shift (downshift and upshift) within the same positive gate voltage. This sudden change in the direction of Pos(G) cannot be explained with the electron transfer by the O_2/H_2O redox couple because only one direction will be thermodynamically favorable. The stable Pos(G) is expected once graphene is in equilibrium with water layer.

The overall spread of Pos(G) was significantly wider in N_2 compared to air. In N_2, the Pos(G) after 10 min of -80 V and +80 V were 1594.1 cm^{-1} and 1589.1 cm^{-1}, respectively. On the other hand, all the Pos(G) in air reached to 1596.8 ± 0.5 cm^{-1} after 10 min of each gate voltages. Despite same gating effect was used, electrical doping was not effective in air after 10 min of static hold of gating voltages. The effects of applied electric field on the adsorption of oxygen coincide with this observation. A study showed the enhanced adsorption of oxygen on bilayer graphene

with more positive back gate voltage.[154] Assuming similar adsorption trend with electrical modulation on single layer graphene, the amount of adsorbed oxygen is lowered by -80 V and increased by +80 V. Since the adsorbed oxygen hole dopes graphene, negative gate voltage electrically hole dopes while total amount of adsorbed oxygen decreases due to the applied electric field, resulting in the reduction of hope doping effect originated from the charge transfer of oxygen-containing species. Similarly, positive gate voltage electrically electron dopes graphene, but increased oxygen concentration adsorbed on the graphene surface increases the hole doping of graphene. Thus, in air or oxygen containing environments, the electrical doping effect is always reduced by the change in adsorbed oxygen concentration. With the reduced oxygen concentration in the flow cell, the Pos(G) between voltages in N_2 noticeably increased supporting the role of oxygen adsorption under the applied electric field.

2.3.3 Electrical doping in N_2

The effects of electrical doping on Pos(G) under N_2 environment was further investigated in more details. Raman spectra were taken on a fixed location in a series throughout different gas environments with three electric modulation values, off, -80 V, and +80 V. The off state (open circuit) was used instead of 0 V to make sure no external gate voltage was applied on graphene. The change in Pos(G) under the gate voltages is shown in Figure 2.6 with three different environments: air, N_2, and N_2 through water bubbler. N_2 environment was established by flowing N_2 for 2.5 h before the start of Raman measurements.

In air, the initial Pos(G) was 1587.4 cm^{-1}, much less upshifted compared to the initial Pos(G) in Figure 2.4a, which suggests the variation of initial doping level between the graphene samples. Pos(G) downshifted when it switched from electrical hole doping (-80 V) to neutral (off)

and from neutral (off) to electron doping (+80 V), still showing sufficiently high p-doping level of graphene. Also, the change in Pos(G) during each gate voltage was again showed that the electrical doping effect was reduced by an opposite doping effect.

Well established N_2 environment should have very limited concentration of oxygen and water; the only remaining ones could be trapped in between graphene and the substrate since graphene should be impermeable to all standard gasses. The initial Pos(G) at first off state was 1585.0 cm^{-1}, suggesting the graphene became nearly charge neutral. The positive back gate voltage resulted in upshift of Pos(G) in contrast to air, showing graphene is effectively electron doped by electrical modulation without heavy p-doping effect from adsorbates. Both positive and negative gate voltage upshifted Pos(G), but significant downshift was followed. This change in Pos(G) was again clearly enhanced in dry N_2 compared to air environment. N_2 with water showed small shift in Pos(G) within the same gate voltage similar to air, but the trend in Pos(G) was similar to early N_2 environment observed in the previous section.

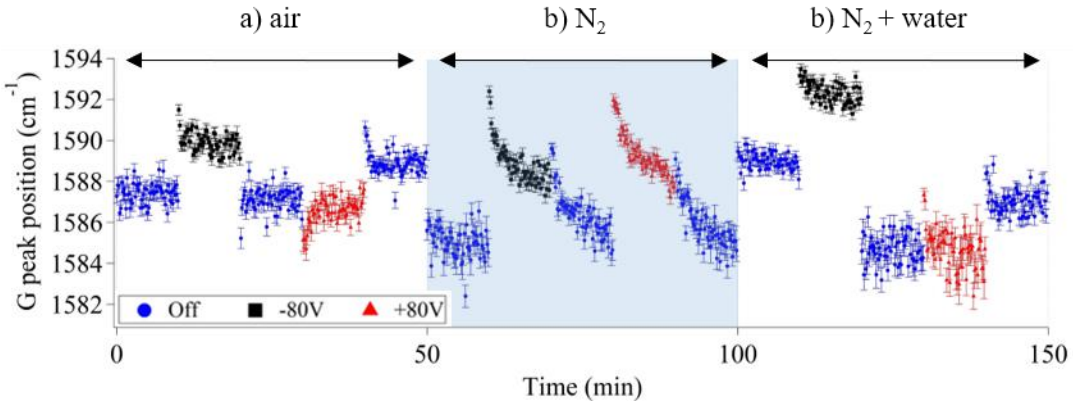

Figure 2.6 The G peak postion in dry and wet environment Raman spectrum were collected under the electric modulation in a) air, b) dry N_2, and c) wet N_2. N_2 flow was kept for 2.5 h before the dry N_2 measurement. Water bubbler was used to flow N_2 through for wet N_2.

Charge trapping is a well-known effect in dielectric materials under an applied electric field, and hysteretic behaviors in conductance measurement of graphene FETs were previously suggested to be originated from those trapped charges between the graphene-oxide interface.[161, 162] The change in Pos(G) under the applied electric field we observed is also in a good agreement with the proposed mechanism of trapped charges in graphene FETs. Figure 2.7 shows the schematic image of the charge trapping and de-trapping process.

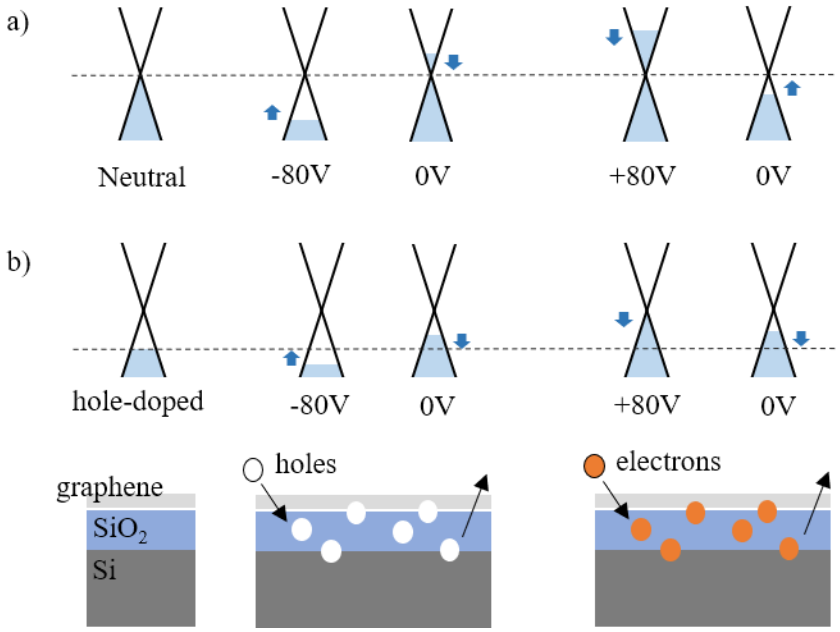

Figure 2.7 Schematic diagram of the dynamic Fermi level of graphene Dynamic change in graphene Fermi level under electric modulation and charge trapping and de-trapping mechanism in a) N_2 and b) in air. Negative (positive) gate-voltage hole (electron) dopes graphene but trapped electrons (holes) changes the net charge carrier density.

When N_2 environment is well established that the available dopants on the gas-graphene interface are negligible, Pos(G) should be at its minimum value near to neutral which corresponds to the first 10 min of N_2 measurements. When -80 V gate voltage was applied, graphene was electrically p-doped, and the Fermi level of graphene lies in the valence band of graphene. The

trapped negative charge carriers between graphene-SiO_2 interface can be accumulated to form a local electric field and decrease the overall electrical doping level. When the gate voltage was turned off after -80 V, Pos(G) was still upshifted compared to the initial Pos(G) (first off state) which could be explained with the trapped charge induced doping. Those trapped electron puddles would result in n-type doping of graphene. Pos(2D) and current leakage direction were consistent with the electron doping. The accumulated charge carriers gradually diffuse from the interface to eventually recover the initial Pos(G). Similarly, when graphene is n-doped by positive gate voltage, accumulated positive charge carriers under graphene could explain the diminishing electrical doping effect over time. The charge trapping mechanism can also explain the air environment with the significant hole doped initial Pos(G) as shown in Figure 2.7b.

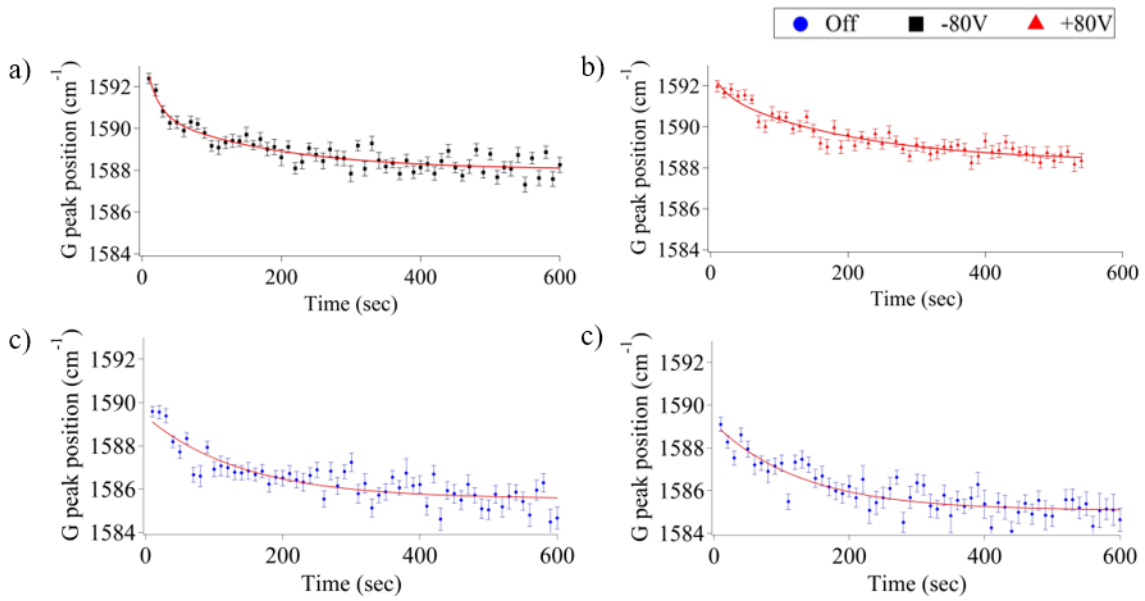

Figure 2.8 The kinetic of G peak position under applied electric field in N_2 Pos(G) as a funtion of time was fitted with a,b) double exponential model and c, d) single exponential model. Solid red lines represent the fitted values.

The fast change in the conductance measurement on graphene FETs was reported with two time constants of ~100 μs and ~2 ms by different researchers with the charge trapping mechanism.[185, 186, 194] The trapping site of the mechanism is often suggested to be at the graphene-oxide interface instead of oxide-Si or -bulk oxide interface due to the short time constants. On the other hand, the charge injection from graphene into the interface was proposed with the time constant of ~1000 s with stretching parameter, in order to include the distribution of time constants for different traps.[187] Recent study added another set of time constants ~1 s and ~20 s and proposed the graphene-oxide interface and bulk oxide trapping mechanism respectively.[195] In our study, the change in Pos(G) under N_2 showed a good agreement with the double exponential model when the gate voltage was applied. Figure 2.8 shows zoomed-in plot of N_2 environment with the model fit.

Table 2.1 Time constants of counter doping Double and single exponential fitting on each gate-voltage and off states under N_2 and Ar flow. Error on each coefficient indicates one standard deviation.

		Applied back-gate voltage			
		-80 V	Off	+80 V	Off
N_2	$\tau_{1\,(s)}$	15 ± 10	141 ± 28	20 ± 12	130 ± 23
	$\tau_{2\,(s)}$	171 ± 59		150 ± 43	
Ar	$\tau_{1\,(s)}$	16 ± 10	141 ± 38	10 ± 9	200 ± 43
	$\tau_{2\,(s)}$	291 ± 165		250 ± 67	

The longer time constant (~200 s) under applied gate voltage was more dominant than the first time constant (~20 s). When the applied electric field was turned off, single exponential model showed much improved fitting results compare to double or modified (stretched) single exponential model. The time constant found at off state (~150 s) was in similar time scale with the dominant time constant (~200 s) in the gate voltages. Different inert environment (Ar) also showed

consistent results with the similar time constants, suggesting the observed change in Pos(G) is not from unintentional contamination of N_2 source.

The common time constant component between off and on state of applied electric field suggests there might be a partially similar origin they share in both cases of the G peak drift, which also fits well with the charge trapping and de-trapping mechanism. The relatively longer time scale compared to the earlier studies can be attributed to the accumulation of charges trapped further into the bulk oxide instead of the nearer to the interface. When electric field is applied, the rate of diffusion of those trapped charges could be dampened by the coulombic forces between the trapped charges, explains the slower kinetic for charge trapping mechanism compared to the de-trapping mechanism of the off state. In addition, the short time constant was only well resolved when the electric field was applied externally. It is possible that different type of charge migrations (e.g., accumulation of the charges diffusing from bulk oxide to near interface) may become more pronounced under external electric field to be resolved into multiple mechanisms.

The different locations near and far from the metal contacts on graphene did not affect the result of time dependence of electric modulation. In addition, the donor type of molecules adsorbed on graphene, such as NH_3 or CO, could be responsible for the change in Pos(G) in air, but should be removed in N_2 environment. Since the shifting in Pos(G) is more prominent in N_2, the role of the adsorption of n-doping molecules on graphene should be negligible.

When N_2 was fed through water bubbler, the shift of Pos(G) during the static gate voltage hold was significantly reduced sharing the similarity to the air environment. This observation was in a good agreement with the previous study that the effect of water on the hysteresis of graphene FET is opposite to the charge trapping mechanism.[161] This advantageous effect on the applied electric field was explained with the capacitive gating induced by strong dipole moment of water.

Under the applied electric field, adsorbed water molecules on the top of graphene can be ordered to form dipole moments which will be oriented along the direction of the applied electric field. The local electric field near the dipoles draws more charge carriers into graphene which enhances the overall doping level of graphene. This positive effect of water induced local electric field could counter the trapped charge puddle effects observed, canceling the drift of Pos(G).

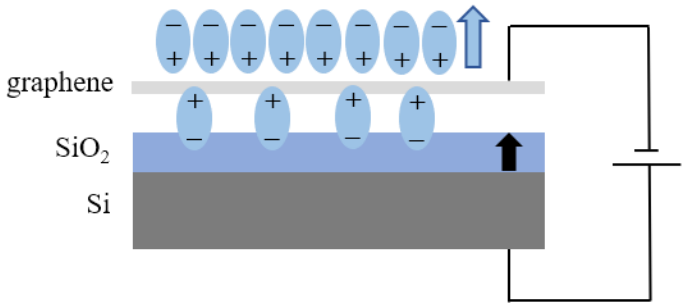

Figure 2.9 Diagram of water induced dipoles forming on the top surface of graphene Black arrow shows the direction of applied electric field and blue arrow is the direction of the dipoles enhancing the local electric field.

2.3.4 Long term effect

Interestingly, prolonged electric modulation showed overall change in doping level of graphene and eventually lead graphene to be electron doped when gate voltage was not applied. In Figure 2.10a, it is clearly shown that the effect of electrical n-doping was increased over time in N_2 environment (red arrow). The Pos(G) was initially ~1585 cm^{-1} after 1 h of N_2 flow, indicating nearly neutral graphene without adsorbate doping effect. While the increase in electron doping was clearly shown over time, the change in G peak under hole doping or off state were less pronounced. N_2 flow was kept for 10 h after the first cycled electrical modulation for 80 min, and

later trend on Pos(G) eventually shows overall n-doping graphene with decreased shift of Pos(G) under the negative gate voltage, as shown in Figure 2.10b-d.

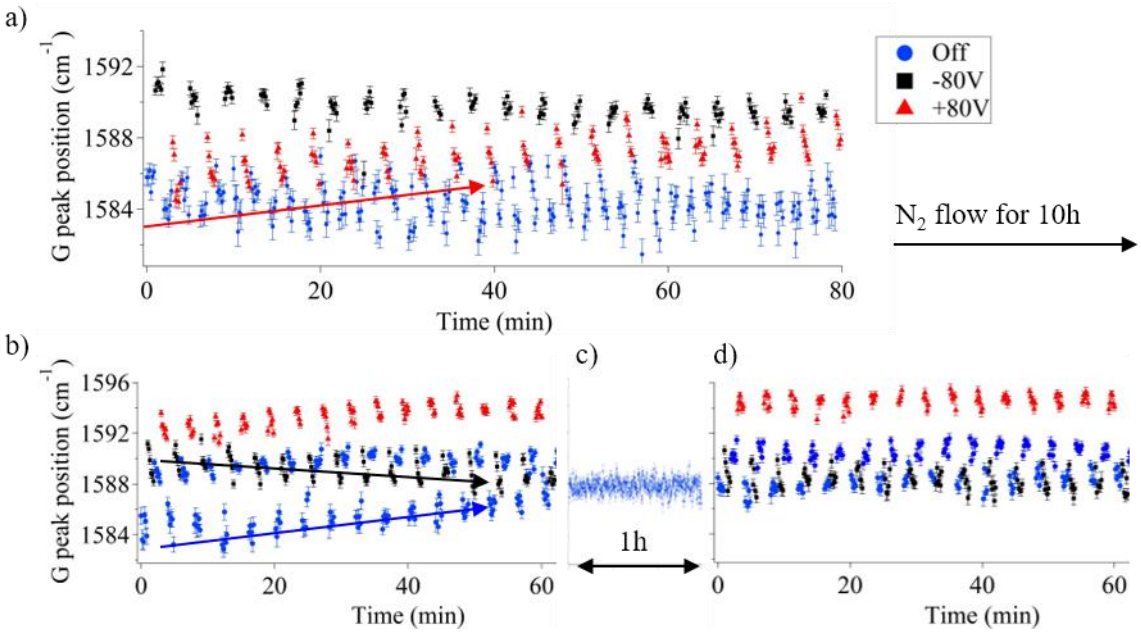

Figure 2.10 Long term effects of electrical modulation on graphene G peak position change under N_2. For each cycled electrical modulation noted as run, gate voltage was applied as in off, -80 V, off, and +80 V sequence for 80 min (1 min per voltage). First, a) run1 was obtained, then was kept on for 10 h. After the 10 h break, b) run2 was obtained followed by c) 1 h Raman without any applied gate voltage and d) run3 was obtained.

Unintentional n-doping adsorbates could exist but should not be significant since 10 h of N_2 flow without any electrical modulation (time between Figure 2.10a and Figure 2.10b) did not induce the significant change in n-doping level of graphene compared to the change observed during electrically cycled period. This n-doping behavior could be more strongly related to the electrical modulation. The n-type doping was stable for an hour without the applied gate voltage (Figure 2.10c).

Previous study showed the low work function of SiO_2 relative to graphene can lead to n-type behavior of graphene.[196] However, the studied graphene device was annealed at 200 °C for ~20 h in vacuum because room temperature vacuum is known to be ineffective for removing the adsorbates. Interestingly, n-type graphene in this experiment was observed under the room temperature with N_2 environment. The applied gate voltage over long period on SiO_2 could have affected the surface characteristic of SiO_2 and caused stronger interaction between graphene and SiO_2, resulting in n-type doping of graphene. Some trapped holes are known to fall into long-lived deep trap states near the interface during the transport process which can be stable for hours or even years, which could also be possible origin of the observation.

2.4 Conclusion and future directions

Electrical doping has significant advantage over chemical doping with *in-situ* controllability, while limited range of doping concentration could be a potential drawback for many applications. For the further development on the use of external electrical doping of graphene for its chemical reactions and related applications, understanding the behavior of graphene device in air is critical. The interactions between surroundings and charge carrier density of graphene could pave a new approach to enhance the effects of applied electric field. The change in Pos(G) showed that the electrical doping level of graphene is significantly reduced with the time constants ~20 s and ~200 s under statically applied gate voltage (±80 V). The time constants observed here were five orders of magnitude larger than previously reported values, and similar to the study proposed the O_2/H_2O redox couple mechanism. However, the observed change in Pos(G) in N_2

did not strongly support the redox mechanism. The change in Pos(G) was more in a good agreement with the charge trapping/de-trapping mechanism under both air and N_2.

Wet N_2 showed the mixed trend in Pos(G). The small shifting range of Pos(G) during same voltage hold was similar to the observation in air which could be explained via the capacitive gating effect of water. However, the similarity between wet N_2 and early N_2 environment suggests possible dissolved O_2 remaining in water. Additional investigation with more carefully designed various environments such as oxygen-free dry and wet conditions can be followed to confirm the water effect projected in the document. Further investigation on the sustainable n-type doping of graphene under prolonged electrical modulation could provide faster ways of graphene/oxide device preparation without extensive vacuum annealing.

3.0 Electric Field Effects on the Reactivity of Graphene

Part of this chapter was previously published and reprinted by permission from Kim, M. A.; Qiu, N.; Li, Z.; Huang, Q.; Chai, Z.; Du, S.; Liu, H., Electric Field Effect on the Reactivity of Solid State Materials: The Case of Single Layer Graphene. *Adv. Funct. Mater.* **2020**, 30 (13), 1909269.

Author Contributions: HL conceived the project and directed the experimental studies. MK and ZL designed and conducted experiments. NQ, QH, ZC, and SD carried out DFT calculations. The DFT results are included here to provide a comprehensive view of my experimental results. All authors discussed and commented on the manuscript.

3.1 Introduction

The charge state of a small molecule significantly impacts its electronic structure and hence its chemical reactivity. For example, aryl halides are very stable but upon accepting an electron, undergo rapid dehalogenation reaction; using charge transfer to alter molecular reactivity is also the underlying mechanism for many redox-mediated catalytic reactions.[197-200] In theory, the same charging-induced enhancement on the reactivity should also be observed in solid state materials, as long as a comparable level of charge density can be achieved. However, while it is easy to inject a single charge into a neutral small molecule to achieve charge density on the order of hundredths of *e*/atom, achieving the same level of charge density in bulk solid state materials are much more difficult due to the very small capacitance of macroscopic objects. As an example, to reach a charge

density of 0.01 *e*/atom for a graphite sphere of *ca*. 1.1 cm in radius (*ca.* 12 g in mass and 1.2 pF of capacitance) will require a voltage of *ca.* 8 x 10^{14} V, way beyond the reach of current technology.

In this chapter, we showed that charge doping of macroscopic-sized single layer graphene increases its reactivity towards oxygen, an effect analogue to those observed in small molecules. Graphene is electrically conductive and its 2D geometry allows simultaneous charge doping and chemical access to the charge-doped region;[201] charge doping levels on the order of 0.01 *e*/atom has been reported.[202] Enhancing the reactivity of carbon materials is desired in many applications in energy (*e.g.*, combustion),[203] transportation (*e.g.*, soot removal from diesel exhaust),[204] and chemical industry (*e.g.*, removal of coke deposit on catalysts).[205] Charge-doping enhancement of reactivity can be a new, orthogonal approach to compliment chemical-based catalysis currently used in these applications. This work is the first example of using charge doping to alter the reactivity of macroscopic-sized solid state material.

Chemical doping of graphene (*e.g.*, by nitrogen) and its use in electrocatalysis has been reported extensively in recent years.[206-214] In these cases, the chemically-doped graphene serves as a electrochemical catalyst, for example, to enhance the electrochemical reduction of oxygen. Electrically charge-doped catalyst had been also demonstrated previously, *e.g.*, by using an external bias to control catalytic activity of Pt on CO oxidation.[215] In addition, external electric field had been also applied to study its effect on wide range of chemical reactions.[216-218] In contrast to all these studies, the present work is unique in that it demonstrates that charge doping enhances the chemical reactivity of a solid state material (graphene) itself in a non-electrochemical environment, *i.e.*, the reactivity of graphene is enhanced without using a chemical catalyst.

Oxidation of graphene is an important reaction that many researchers are trying to better understand the reaction mechanism along with other carbon allotropes.[155, 219, 220] However, the

mechanism and chemistry of the oxidation process is still not clear and more detailed explanation is needed. Single layer graphene has been shown to be significantly more reactive to molecular O_2 than multi-layer graphene.[155] During oxidation, cracks are initiated along the line of epoxy groups, leading to an oxygen-driven unzipping process on the carbon network.[221, 222] Previous studies on the dependency of oxygen adsorption and diffusion[154, 173, 223] showed that the electric field can be used to modulate oxygen containing molecules on the surface of graphene. In addition, the unique semi-metal property of graphene could be a key to the bond strength modulation. If one can finely tune the surface interaction of graphene with the manipulation of the bond strength simply using electric field modulation, the oxidation reaction could also be controlled which could be a versatile tool to control the reactivity of the carbon material.

3.2 Experimental

3.2.1 Graphene synthesis

Graphene was grown on copper foils using a chemical vapor deposition (CVD) method previously reported.[78] Copper foil (25 μm thick, Alfa Aesar, item No.46365) was cut into approximately 1.5 cm × 6 cm strips and electropolished similar to the previously reported electropolishing method.[188] In brief, copper foil is electrolyzed with the current limit of 0.02 A for 1 h in phosphoric acid solution (500 ml of deionized water, 250 ml of phosphoric acid, 250 ml ethanol, 50 ml isopropyl alcohol, and 5 g of urea). Copper foil was used for both anode and cathode electrode, but only polished anode copper foil was used for graphene growth. After the electropolishing treatment, copper foil was thoroughly rinsed with deionized water, blow dried

with nitrogen gas, and placed on a quartz boat. The quartz boat with the copper foil was then inserted into the center of a 1-inch-diameter fused quartz tube furnace. The tube was pump down to the base pressure ~50 mTorr and back filled with H_2 (2 standard cubic centimeters per minutes (sccm)). The tube pressure with H_2 flow was maintained at ~100 mTorr. The furnace temperature was ramped to 1000 °C and annealed for 30 min. CH_4 (20 sccm, P_{total} ~500 mTorr) was introduced after the annealing step for 10 min (growth), and the furnace was cooled rapidly to room temperature with the same gas flow for both H_2 and CH_4. Graphene samples were stored in a clean glass petri dish until the transfer.

3.2.2 Graphene transfer

After the synthesis, graphene was transferred on to SiO_2/Si wafer using a wet transfer technique.[189] In a typical transfer, as grown graphene on top of Cu foil was spin coated with 5 wt% Poly(methyl methacrylate) (MW 996000, Aldrich) solution in anisole (99 %, Sigma-Aldrich). After the PMMA was coated on top of the graphene layer, the Cu foil was etched in fresh 0.1 M of aqueous ammonium persulfate solution (98 %, Sigma-Aldrich) for 3 h. Then, the PMMA/graphene film was scooped out with a clean glass slide and transferred into multiple water baths to rinse off the etchant. After thorough rinsing, the PMMA/graphene film was placed on a SiO_2/Si wafer with the graphene side in contact with the SiO_2 and spin dried at 5000 rpm for 5 min. To remove the PMMA support after drying, 1.4 % PMMA solution was drop casted on the PMMA/graphene/SiO_2/Si sample and cured for 30 min at room temperature.[189] Then the sample was placed in an acetone bath for 1 h followed by another acetone bath for 12 h. Once the PMMA layer is removed, the graphene surface was rinsed with isopropanol and gently blow dried with N_2.

3.2.3 Fabrication of back-gated graphene samples

Electrical connections were made on graphene (top) side and on Si side (bottom) by applying silver paste (SPI Supplies, 04969A-AB) as a conductive glue to attach copper wires. For the electrical connection to the Si wafer, the bottom side of the Si wafer was scratched off with a diamond tip to remove the surface oxide before the copper wire was glued with the silver paste. Highly doped bulk Si wafer served as a back gate and connected to the positive terminal of the power source. After the wiring, several random locations on the graphene sample were tested to confirm the electrical connectivity using a multimeter. Two different types of SiO_2/Si wafer were used throughout the study, wet thermal SiO_2 (University Wafer, 300 nm wet thermal oxide, P type/Boron) and dry chlorinated thermal SiO_2 (Nova Electronic Materials, 300 nm dry chlorinated thermal oxide with forming gas annealing, P/B). Both wafers showed similar results.

3.2.4 Raman spectroscopy

Schematic image of the experimental setup is shown in Figure 3.1a. A custom-built micro-Raman spectrometer with 532 nm CW single-longitudinal mode solid state laser and Nikon S Plan Fluor ELWD 40x objective (NA: 0.60, WD: 3.6-2.8 mm) was used in this study. The calculated size of the Gaussian laser beam waist at focus is 1 μm. The graphene was heated photothermally by the focused Raman laser, which ranges from 6 mW to 18 mW. The Raman spectra of the sample were obtained during the oxidation and when needed, by using a much lower laser power (< 1 mW) to eliminate photothermal heating effect. Laser power was measured at the sample stage before each experiment run. All obtained spectra were calibrated with Naphthalene spectrum and

processed with Igor pro 6.37 software. All graphene peaks were fitted with a single Lorentzian lineshape for analysis.

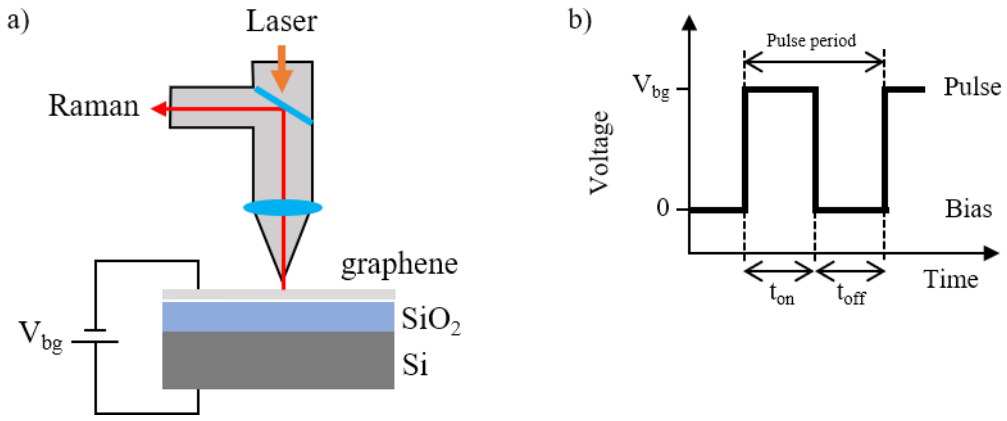

Figure 3.1 Experimental setup of laser induced oxidation of graphene with electrical modulation a) Schematic image of Raman spectrometer and graphene sample with electric connection. Heavily doped (p^{++}) Si was used as a back gate. b) The square waveform voltage modulation setting. The desired back gate voltage level (V_{bg}) was applied for t_{on}, pulse on-time, followed by t_{off}, pulse off-time. Bias level was set to 0 V for all pulsed modulation.

3.2.5 Back-gating of graphene

Keithley 2614B SourceMeter SMU instrument (Keithley) was used to source and measure voltage and current. In brief, one set of terminals were used to source the gate voltage ranging from -100 V to +100 V and measure the gate leakage current across the graphene/SiO_2/Si sample. The second set of terminals were attached on the separate electrical contacts on the device to confirm the desired gate voltage was applied on the sample. SMU instrument was controlled remotely via the Keithley Test Script Builder software.

When the steady gate-voltage was applied, electrical doping effect was significantly reduced within tens of seconds time scale (see Appendix A.1.6). This change in the doping level of graphene is consistent with the previously observed hysteretic behavior of graphene devices on the electric measurements, which was attributed to the charge trapping in the dielectric layer.[159-162, 181] To address this issue, the gate voltage was applied in a square wave form (Figure 3.1b). The desired back gate voltage level was applied for t_{on}, pulse on-time, followed by applying zero gate voltage for t_{off}, pulse off-time, and repeated throughout the experiment. The gating voltage of 0 V was applied during t_{off} served to relax and recover from the counter doping effects induced by charge trapping. The waveform frequency in the range of 0.02 – 2 Hz, duty cycle 33 – 50 %, and V_{bg} = -100 V – +100 V were used throughout the experiments.

3.3 Results and discussion

3.3.1 Preliminary results

The effect of electric modulation on the oxidation reaction of graphene has great potential to control the reaction without the present of catalysts or chemical modification of graphene. Thermal oxidation of graphene/Si sample using direct heating method is hard to maintain the electrical connections of wires at such elevated temperature. Most of solder material used in electrical connection melts at relatively low temperature, and pressuring method can easily damage the thin layer of SiO_2 physically. More importantly, dielectric strength of SiO_2 decreases as temperature increases. This temperature dependency significantly reduces the range of electric field that can be used to modulate the doping level of graphene electrically. Laser induced heating

on the other hand is only focused on the graphene surface of about 1 μm. Incident laser source can heat graphene, and the early breakdown of SiO_2 can be prevented with the efficient thermal dissipation throughout the bulk graphene device.

First, graphene on SiO_2/Si was heated with laser (3 mW) for 3 h without any external voltage applied. For laser induced heating, the laser source of Raman instrument was used to optically heat the graphene sample while also used to collect Raman spectrum. The temperature rises due to the laser irradiation and graphene was etched away as a result of oxidation. The integrated area intensity ratio between the Raman D peak and G peak, I(D)/I(G), of graphene is a convenient measure of defect density in graphene.[107, 117, 118] Our study focused on the early stage of graphene oxidation during which I(D)/I(G) is positively (but not linearly) correlated with the defect density. We note that at very high defect densities, the I(D)/I(G) could decrease with increasing defect density. Figure 3.2a and b show initial variation and the development of I(D)/I(G) between different samples during 3 h of laser heating. The second measurements of two different graphene samples (G4_2 and G5_2) were obtained after several external electric modulations were performed on graphene. The inconsistent variation between those second measurement results compared to the first runs suggests that the previous electric modulations done on graphene device do not have significant effects on the development of defect density. The I(D)/I(G) initially ranged from 0.02 to 0.07, and it scatters much widely from 0.05 to 0.31 after 3 h of laser heating showing significant variation between the graphene samples and different locations within the same sample.

Such large range of the overall change in I(D)/I(G) after 3 h of laser heating could be originated from many atomic scale variations such as aggregated local epoxy group or slightly higher local defect density contributing to different rate of oxidation reaction. The direct correlation between the amount of growth of I(D)/I(G) and underlaying conditions such as initial

defect density could not be resolved with the current result because the initial D peak intensities were almost negligible in most of measurements that the comparison was not reliable with the background noise. The second run of the sample G5 (G5_2) had the smallest initial I(D)/I(G) and resulted in the largest final I(D)/I(G) after 3h of laser heating (0.02 to 0.31). The effects of applied electric field on the development of defect density also did not show clear trend as shown in Figure 3.2c and d. After 2 h of laser oxidation of graphene, I(D)/I(G) was largest (0.38) under the gating voltage of -60 V, followed by -80 V, -40 V, 0 V, and -20 V. The variation between the graphene area being studied could have significant contribution to the I(D)/I(G) development, therefore should be eliminated to identify the interested contributing factors (*e.g.*, electrical doping) in defect density growth.

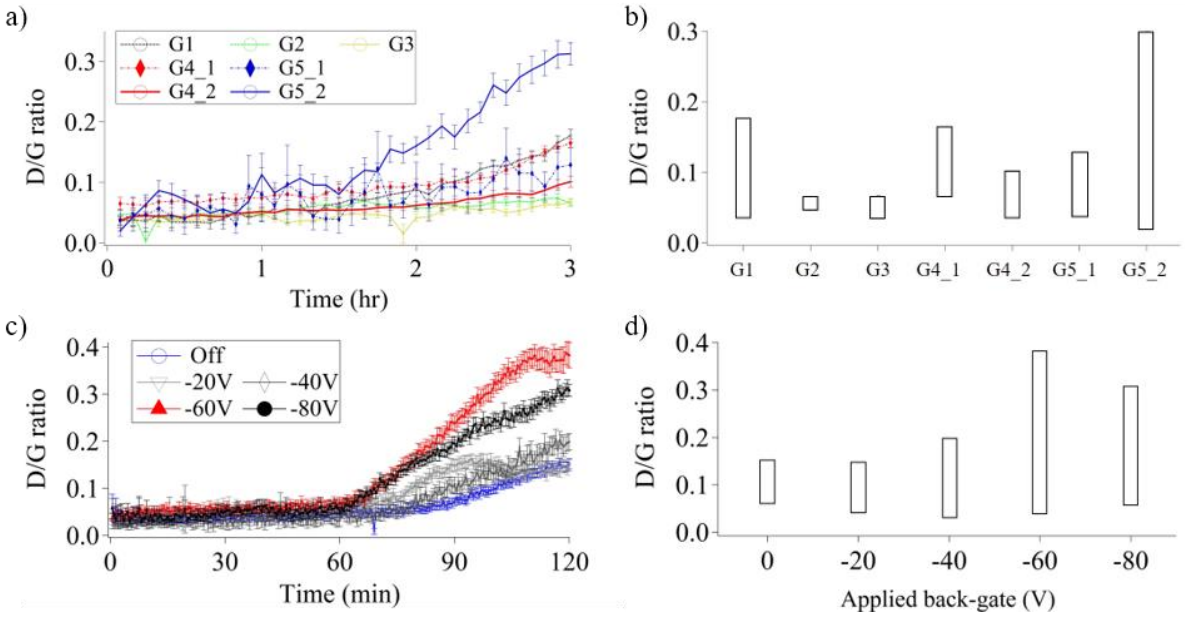

Figure 3.2 The development of I(D)/I(G) upon laser oxidation a) without electric modulation as function of time and b) initial to final I(D)/I(G) values shown in bar graph bottom to top, respectively. c) I(D)/I(G) change under negative back gate application (hole-doping of graphene) on different location of single sample as function of time and d) initial to final I(D)/I(G) shown in bar graph bottom to top, respectively.

In order to reduce the variability of graphene between the studied locations, same location laser heating was tested while the gate voltage (-90 V) was applied periodically (10 min) on and off. After each 10 min of oxidation under different voltage conditions, the graphene sample was set to rest for 20 min. Laser beam was blocked and the gate voltage was turned off during the break. Then, a Raman spectrum was taken with low laser power (~0.4 mW) before the next heating period in order to obtain the Raman spectrum at room temperature without residual electric doping effect. The effect of applied gate voltage was clearly shown in Figure 3.3a. When -90 V (black) was applied to graphene, Pos(G) was always higher compared to the previous off state position. However, the significant shift of Pos(G) was also observed as previously reported. Initial Pos(G) was 1587.0 cm^{-1} and dropped to 1584.9 cm^{-1} immediately when laser heating was started with off state possibly indicate the desorption of water or oxygen containing group on the surface due to the laser heating, or significant increase in temperature. The temperature could be calculated with the temperature dependency of Pos(G),[224] however, qualitative analysis can be inaccurate due to available ambient condition adsorbates on graphene effecting Pos(G).

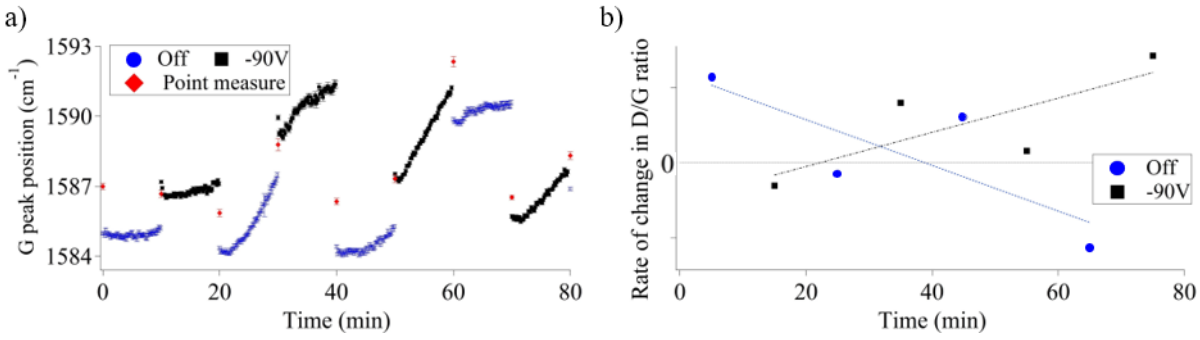

Figure 3.3 *in-situ* Raman spectra of laser induced graphene oxidation with gate voltage Single point Raman spectrum were obtained with relaxation period after every 10 min of high power laser oxidation under off and -90 V back gate application alternatively. a) G peak position during the oxidation and the after 20 min of break (point measure). b) The change in I(D)/I(G) calculated from the point measurements.

Figure 3.3b shows the change in I(D)/I(G) throughout the oxidation. Each data point represents the slope of I(D)/I(G) calculated from the two Raman spectrum at resting state before and after each oxidation period. Highest increment of I(D)/I(G) was ~ 0.3, from 0.28 to 0.57 during the -90 V oxidation. The maximum I(D)/I(G) was 0.57 after 80 min of laser heating indicates that graphene was still at very early stage of oxidation. The effects of electric modulation on oxidation of graphene could not be further analyzed in Figure 3.3 because of the I(D)/I(G) fluctuation throughout the 80 min oxidation. As negative slope of I(D)/I(G) change shown in Figure 3.3b, the decrease in I(D)/I(G) was measured during both off and -90 V doping conditions. It is possible to observe the decrease of the D peak intensity with the increase of charge carrier density of graphene. However, 20min of relaxation time should eliminate most of doping effects from the trapped charge doping. Since laser density filter was manually changed between heating and point measurements, the significant decrease of D peak intensity could have originated from the shift of laser beam during the experiment.

The oxidation reaction of graphene was monitored with the I(D)/I(G) and showed effective defect growth with the laser induced heating. However, the regional variation of the graphene samples significantly affects the rate of oxidation reaction, that the effects of electric modulation were yet to be resolved. The very large data collection could be done using automated system, and possibly overcome the regional variation of graphene samples, or the single location study can be used to eliminate the variables. *In-situ* Raman is a great tool to monitor both the electrical doping and defect formation during reactions, but careful experimental design should be practiced owing to its sensitivity and complex dependencies on various conditions.

3.3.2 Electric field effect on the photothermal oxidation of graphene

By maximizing electrical doping effect, we found that electrical back gating increases the rate of graphene oxidation by a factor of 2 – 3. The graphene sample was heated by a focused Raman laser beam (532 nm, 6 – 18 mW, *ca*. 1 μm focus spot) and the photothermal oxidation of graphene was characterized via *in-situ* Raman spectroscopy. The temperature within the laser focus was estimated to be *ca*. 240 ºC with 10 mW laser power by using the shift of the G peak following established methods.[224] The graphene was supported by a heavily doped Si wafer that has 300 nm thick of SiO_2 layer. The heavily doped Si and graphene forms a capacitor; its capacitance was measured to be 9.9 nF/cm^2. At 80 V of gate voltage, the amount of charge injected into graphene is calculated to be 4.9 x 10^{12} *e*/cm^2, or 1.3 x 10^{-3} *e*/atom.

In the absence of an applied gate voltage, graphene can be oxidized by O_2 under photothermal heating. The graphene area irradiated by 18 mW of laser for 1 h showed the increase in I(D)/I(G) and decrease in I(2D)/I(G) along with an upshift of Pos(G) in its Raman spectra (Figure 3.4a). These changes in the spectrum indicate an increased defect density with hole doping of graphene due to oxygen and/or the oxygen containing functional groups formed as a result of the oxidation reaction. These results mimic those reported for the thermal oxidation of graphene.[155] The laser illumination did not affect graphene outside of its focused area.

To probe the effect of gate-induced charge doping on the rate of oxidation, the photothermal heating of graphene was repeated with an applied gate voltage in square waveform. Each back gate voltage level (V_{bg}) was applied to induce electron doping (+80 V), hole doping (-80 V), and floating ground (0 V). The waveform of voltage on-time (t_{on}) and off-time (t_{off}) were 5 s and 10 s, respectively (see section 3.2.5 for details). Figure 3.4a shows the typical Raman spectra of the graphene before and after oxidation. The further increase in the D peak intensity under +80

V (red) signals the additional defect density in graphene compared to normal photothermal oxidation (blue). The I(D)/I(G) value after 1 hr of oxidation was noticeably larger with ±80 V of back gating than 0 V, suggesting the degree of oxidation was further proceeded under the electrical field modulation. In order to eliminate the variations originating from the transfer process, oxidation results from a single graphene/SiO_2/Si device (graphene area of 1 cm^2) were used in Figure 3.4b for comparison. This behavior was reproduced using multiple graphene/SiO_2/Si samples (Appendix A.1.1). The back gating itself (without laser heating) did not change the I(D)/I(G) and the light absorbance of the graphene/SiO_2/Si sample at the laser wavelength (532 nm); hence the efficiency and temperature of the photothermal heating (Appendix A.1.2 and Appendix A.1.3). Possible resistive heating was also negligible to affect the oxidation of graphene which is further discussed below.

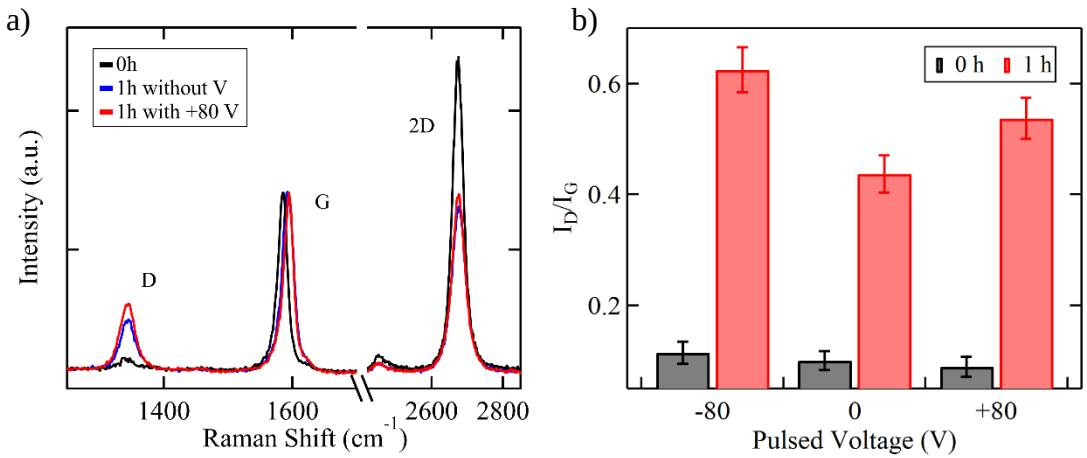

Figure 3.4 The Raman Spectrum of graphene with 1h oxidation The Raman spectrum of graphene a) before (0 h, black) and after the 1 h photothermal oxidation without (1 h, blue) and with +80 V gate voltage (1h, red), t_{on} = 5 s, and t_{off} = 10 s. Each spectrum was normalized to I(G). b) The 1h oxidation comparison between 0 V, +80 V, and -80 V. Each V_{bg} level was repeated four times to find the average and a standard deviation of I(D)/I(G).

To illustrate the effect of back gating on the oxidation kinetics, we observed the change in I(D)/I(G) of graphene during the oxidation while dynamically changing the back gating of graphene. Graphene was photothermally heated with 10 mW of laser power, and Raman spectra were collected every 10 s. Unlike Figure 3.4, here we vary the gate voltage throughout each oxidation experiment, at the same spot, thus completely eliminated potential contribution from the heterogeneity within a graphene/SiO_2/Si sample.

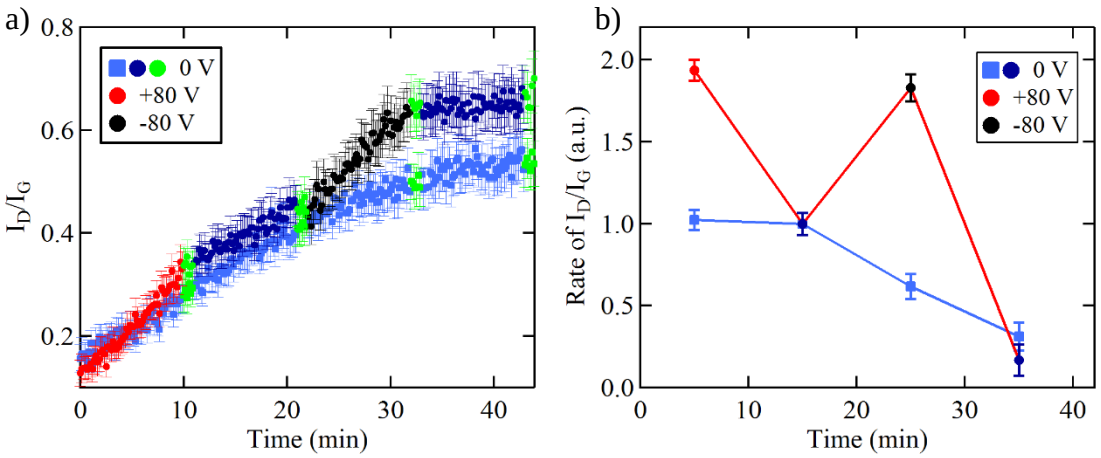

Figure 3.5 The photothermal oxidation of graphene as a function of time a) without back gating (0 V, light blue square) and with the gate voltages (±80 V, $t_{on} = t_{off} = 0.5$ s). b) The average rate of change in I(D)/I(G) calculated from linefit of each 10 min oxidation period (1 min break before and after 10 min oxidation inclusive) and normalized with respect to the second 10 min oxidation period.

Figure 3.5a compares two oxidation kinetics measured, one with and one without varying levels of back gating. In the absence of back gating (light blue square), I(D)/I(G) increases over time, but the rate of increase slows down as the oxidation progresses. Such slow decrease in the oxidation rate was previously reported for thermal oxidation.[225] In the varying back gating, each back gate voltage level was applied for 10 min chronologically (+80 V, 0 V, -80 V, and 0 V, t_{on} =

t_{off} = 0.5 s). In between every 10 min blocks, an additional 1 min of 0 V gate voltage period was inserted. Shown in Figure 3.5a, the I(D)/I(G) value increased rapidly for the first 10 min under +80 V of pulsed gate voltage (red, 1.21 ± 0.06 hr^{-1}) but noticeably slowed down in the second 10 min when no gating was applied (blue, 0.63 ± 0.07 hr^{-1}). When -80 V gate voltage was applied, the rate was increased again (black, 1.15 ± 0.08 hr^{-1}) and dropped again (blue, 0.10 ± 0.09 hr^{-1}) in the last 10 min with 0 V gate voltage. Figure 3.5b compares the relative rate of the I(D)/I(G) change in these two single-spot measurements. The rate of change in I(D)/I(G) was calculated by line-fitting each 10 min of reaction. When the rate was normalized with respect to the second 10 min period (both at 0 V), the rate of I(D)/I(G) under ±80 V pulsed voltage modulation was approximately 2 – 3 times higher of that without the back gating. Due to the dynamic reaction rate as shown in normal oxidation (light blue) and possible inhomogeneity within large graphene surface, quantitative comparison was avoided. Assuming the growth of defect is a direct result from the oxidation of graphene, the results in Figure 3.5 shows that the electrical back gating directly enhances the reactivity of graphene towards oxidation.

3.3.3 Magnitude of the back-gate voltage

If the observed enhancement of reactivity is due to the charge doping of graphene, one should expect that the degree of enhancement to be positively correlated to the charge doping density and hence the magnitude of the back gate voltage. This prediction was indeed verified in our experiments. Figure 3.6 shows the kinetics of several single-spot oxidations with varying back gate voltages similar to the case of Figure 3.5. Figure 3.6a and b show that +100 V produced a much higher enhancement of the oxidation compared to the +50 V case. Similar observations were made in experiments where the effect of different levels of gate voltages (0 V, 30 V, and 60 V in

Figure 3.6c, 50 V and 100 V in Figure 3.6d, and 0V, ±50 V and ± 100 V in Figure A.4) were directly compared within a single-spot oxidation. The enhancement effect of the back gating is most significant in the early stage of the oxidation but less pronounced after 40 min as can be seen in Figure 3.6c and Figure A.4. We again attribute this observation to the plateauing of I(D)/I(G) at the later stage of the oxidation (Figure 3.5a) due to the decrease in the rate of reaction with time and non-linear response of I(D)/I(G) to the defect density in graphene.

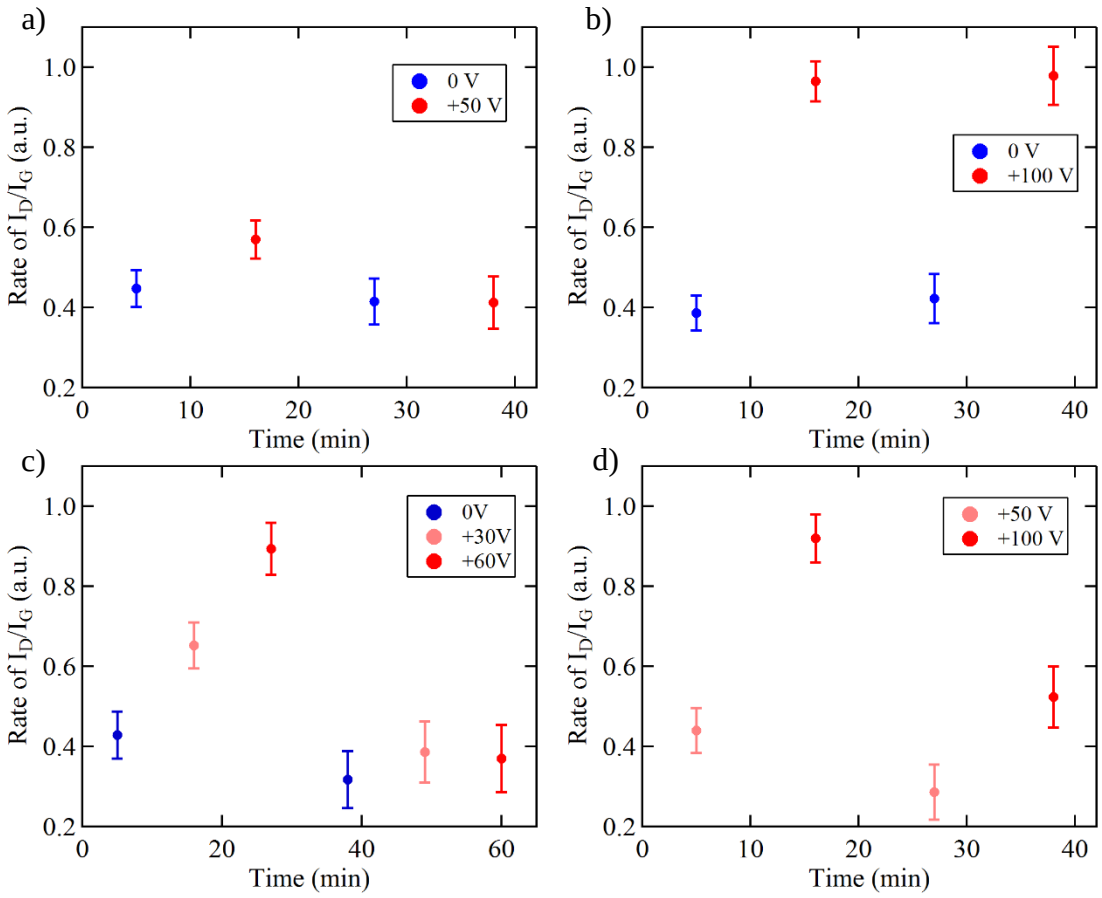

Figure 3.6 The change in the oxidation kinetic of graphene with the magnitude of back gate voltage The effect of gate voltage was compared between a) 0 V and +50 V, b) 0 V and +100 V, c) 0 V, +30 V, and +60 V, and d) 50 V and 100 V. The back gating level was changed every 10 min during the oxidations (t_{on} = t_{off} = 0.5 s).

3.3.4 Frequency of back-gate modulation

The frequency of the back gate waveform is an important factor in determining the enhancement of the graphene oxidation, with higher frequency produces faster graphene oxidation. Figure 3.7 shows the effect of back gate waveform having different periods ($t_{on} = t_{off}$ = 0.25 s, 2.5 s, and 25 s) but the same amplitude V_{bg} (+80 V) and duty cycle (50 %). During each oxidation, the frequency of the back gate voltage was varied every 10 min. As shown in Figure 3.7b, increasing the waveform frequency from 0.02 Hz to 2 Hz (decreasing the period from 50 s to 0.5 s) resulted in an increase of oxidation rate by almost 50%.

This result may seem counter-intuitive given that the duty cycles of the three waveforms are the same, and hence the total amount of time the sample was subject to the back gating are also the same. We attribute this frequency dependence to the local electric field near the graphene-SiO_2 interface. The gating hysteresis of graphene field effect transistors is well-known behavior that often ascribed to the trapped charges near the graphene-SiO_2 interface.[161, 162] The trapped charges can produce a local electric field that reduces the doping level in graphene, which is confirmed in our Raman measurement (see Appendix A.1.6 and Chapter 2).We reason that applying square wave allows most of the trapped charge to dissipate during the t_{off} period. Since graphene sample only experiences high doping level right after the transitions of the square wave (from off to on), increasing the frequency of the square wave gate voltage increases effective gating efficiency experienced by graphene. Accordingly, we found that under constant DC voltage gating, there was no obvious trend in the change of I(D)/I(G) after 1 h of photothermal oxidation (Figure A.5).

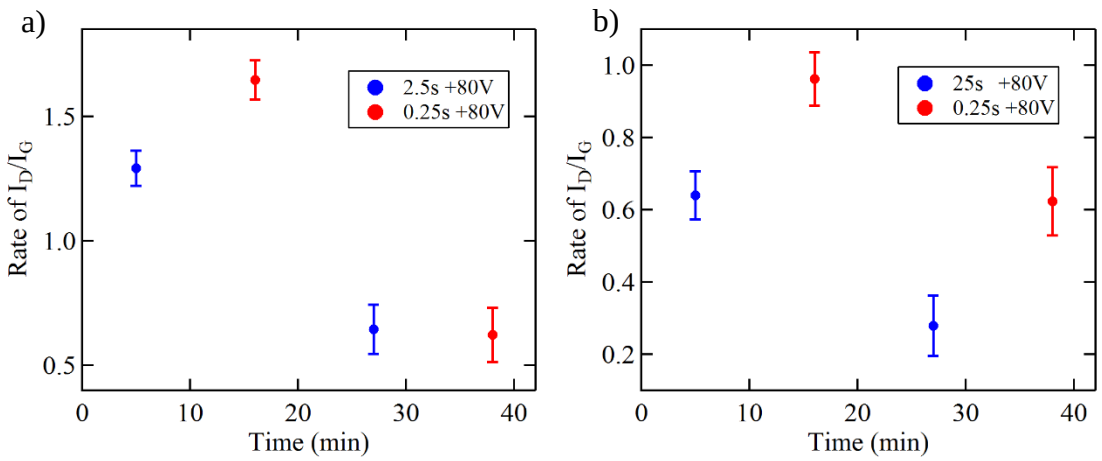

Figure 3.7 The effect of back gating frequency on the oxidation kinetic The effect of back gating frequency on the oxidation kinetic. The waveform period was compared between a) $t_{on} = t_{off}$ = 2.5 s and 0.25 s, and b) $t_{on} = t_{off}$ = 25 s and 0.25 s. The back gate voltage was fixed at +80 V while the period of waveform was changed every 10 min.

3.3.5 Theoretical study of the oxidation mechanism

Our results strongly suggest that the electric field-induced charge doping is responsible for the increases in the oxidation rate of graphene. Both positive and negative gate voltage increases the oxidation rate, and the enhancement is positively correlated with the magnitude of the gate voltage. These data are consistent with the idea that charge doping reduces the bond strength in graphene, resulting in an increased reactivity. Figure 3.8 illustrates this concept for the case of defect-free graphene. Here, both electron and hole doping results in a decrease of bond order in graphene, which could explain the enhancement of reactivity with both positive and negative gate voltages.

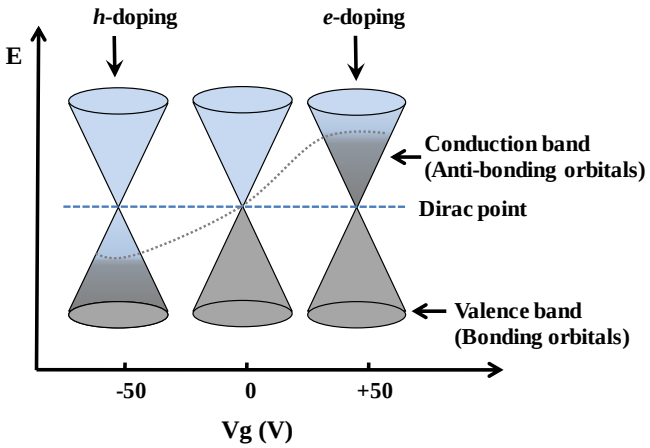

Figure 3.8 Band filling of graphene as a function of electrical charge doping The filled and empty bands are shown in grey and blue, respectively. The overall bond order of graphene decreases with hole-doping (electron-doping) due to a reduction (increase) of band filling.

While Figure 3.8 highlights the concept of charge-induced reactivity enhancement for pristine graphene, it does not capture the complexity of its oxidation process. Graphene oxidation involves formation of defects and functional groups, both would modify its electronic structure. To better understand the mechanism, we have modelled the oxidation of graphene under an electric field using density functional theory (DFT) calculations. Our calculation focuses on the change of activation barrier upon applying an electric field. Although DFT calculations are not expected to reproduce the absolute thermodynamic data, it is known to make good predictions on the trend and change of energetics upon small perturbation. [226]

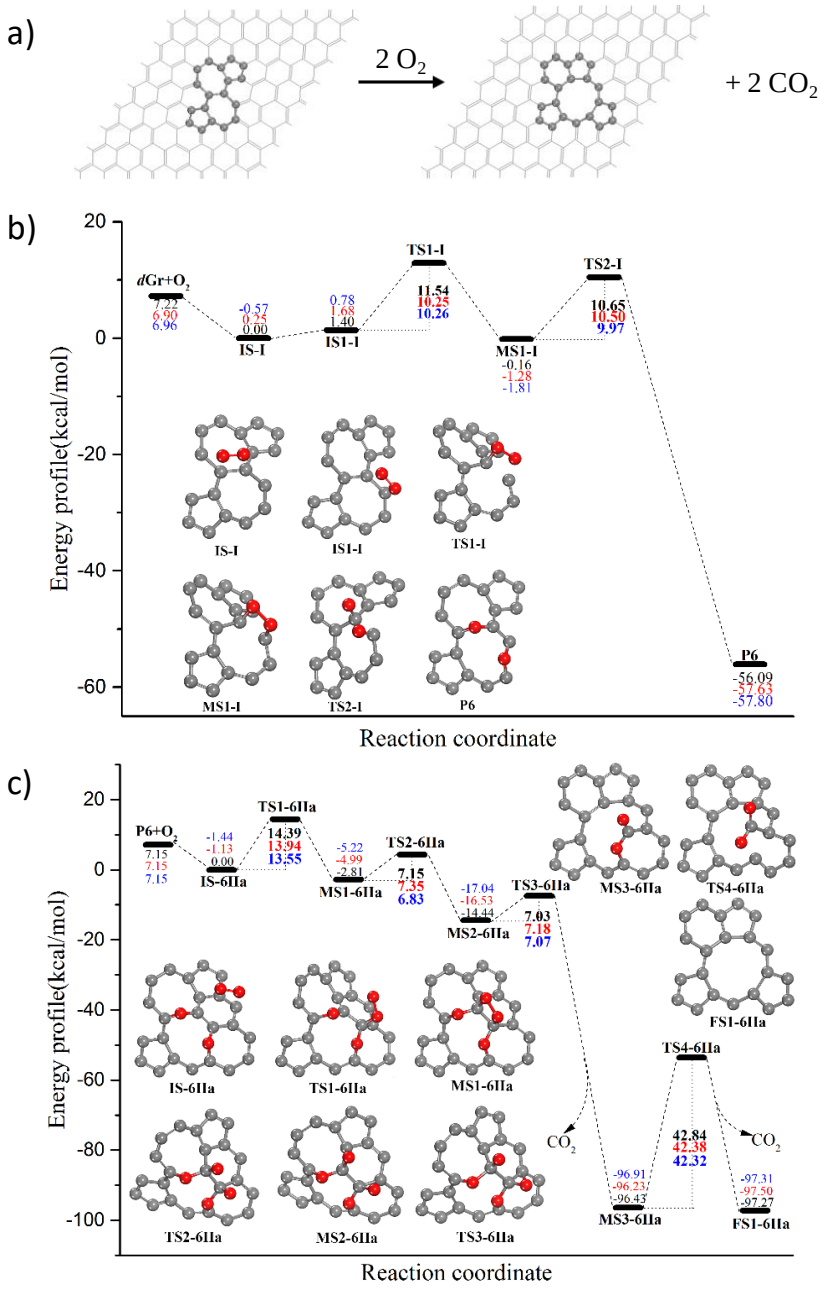

Figure 3.9 DFT calculation of the oxidation of graphene (a) Overall reaction modelled by the calculation, showing the 126-atom fragment of graphene and the highlighted (5-7-7-5) defect. Reaction coordinate of the graphene reacting with (b) the first O_2 and (c) second O_2. Only the structures near the reaction center is shown. Black and red spheres represent carbon and oxygen atoms, respectively. Values associated with transition states are barrier heights for the forward reaction. The energies values were calculated without (black), with positive (red) and negative (blue) electric field of 0.001 Hartree/Bohr or 0.514 V/nm.

We modelled the reaction of two O_2 molecules with a 126-atom fragment of graphene that contains a topological (5-7-7-5) defect. The reaction produces ethers and lactones, which then decarboxylate to release two CO_2 molecules (Figure 3.9a). Oxygen binding and decarboxylation processes are commonly accepted as key steps in the oxidation of graphitic carbons.[227] Among the 21 different reaction pathways we surveyed, the two shown in Figure 3.9b-c have the lowest apparent activation barriers (See Appendix A.4 for the other 19 reaction pathways). In this pathway, the first oxygen molecule binds to two carbon atoms within the (5-7-7-5) defect, producing a four-membered ring peroxide-like intermediate (IS1-I *via* TS1-I to MS1-I, E_a = 11.54 kcal/mol, E_a: activation energy), which then transforms to two ethers (MS1-I *via* TS2-I to P6, E_a = 10.65 kcal/mol, Figure 3.9b). The second oxygen molecule attacks the carbon-carbon bond between the two ether groups (IS-6IIa *via* TS1-6IIa to MS1-6IIa, E_a = 14.39 kcal/mol), forming another two epoxide groups (MS1-6IIa *via* TS2-6IIa to MS2-6IIa, E_a = 14.39 kcal/mol), which then transform to a lactone and release a CO_2 (MS2-6IIa *via* TS4-6IIa to MS3-6IIa, E_a = 7.03 kcal/mol). The lactone undergoes further decarboxylation to release the second CO_2 (*via* TS4-6IIa) with a much higher activation barrier of 42.84 kcal/mol (Figure 3.9c).

The adsorption of O_2 onto the graphene substrate (IS-I and IS1-I of Figure 3.9b and IS-6IIa of Figure 3.9c) shows asymmetric response to the electric field. The negative electric field elongates O-O bond length and increases adsorption energy while the positive electric field resulted in the opposite effect. These results are consistent with previous reports and can be explained by the field-induced charge redistribution between the π orbitals of graphene and the anti-bonding $2\pi^*$ orbital of O_2 molecule (Table A.1).[223, 228]

Table 3.1 Effect of electric field on the rate of graphene oxidation

Reaction	Electric Field (V/nm)	E_a (kcal/mol)	Relative reaction rate (513 K)
IS1-I to MS1-I	0	11.54	1
	+0.514	10.25	3.55
	-0.514	10.26	3.52
Overall rxn of Fig 3.9b	0		1
	+0.514		2.00
	-0.514		5.16
MS3-6IIa to FS1-6IIa	0	42.84	1
	+0.514	42.38	1.57
	-0.514	42.32	1.66
Overall rxn of Fig 3.9c	0		1
	+0.514		1.26
	-0.514		2.52

However, the overall kinetics of the reaction is not limited by the O_2 adsorption. Instead, the barriers associated with the formation of peroxide-containing intermediates (TS1-I and TS1-6IIa) and the desorption of CO_2 (TS4-6IIa) are the highest ones in the reaction. We found that these activation barriers are sensitive to an external electric field vertical to the graphene plane. The projected density of states of transition states TS1-I, TS1-6IIa, and TS2-I (Appendix A.5) show that the negative/positive external electric field promotes the electron transfer from C atoms to O atoms and improve the hybridizations between C P_z and O_2 1πu and/or 1πg* states, which indicates that the O-O bond is weakened and the C-O bonds are strengthened during the formation of peroxide intermediates and the subsequent ether intermediates. Table 3.1 lists the change of activation energy under +/- 0.514 V/nm of electric field for the two highest transition states in Figure 3.9b (TS1-I) and c (TS4-6IIa). From the changes in the activation barrier, we calculated the relative reaction rate at 513 K using transition state theory and also modelled the overall reaction

shown in Figure 3.9b-c using steady state approximation (See Appendix A for details). The electric field increases the rate of both the elementary reaction steps and the overall reactions, with an enhancement ratio ranging from 1.26 to 5.16 times. This theoretical prediction is within the same order of magnitude of our experimental results, which showed 2 - 3 times enhancement at *ca*. 0.07 V/nm. Notably, the DFT calculation showed that both positive and negative electric field enhances the reactivity, as we observed in the experiment.

3.3.6 Alternative mechanisms

Our data argues against electrochemical-based mechanisms. Graphitic carbon materials undergo electrochemical oxidation at high anodic potentials.[229-231] In our experiments, both positive (cathodic) and negative (anodic) back gate voltages increase the oxidation rate. In addition, electrochemical oxidation of graphite is not expected to be dependent on the frequency of the square wave. In our experiment, with the same duty cycle, the rate of oxidation increases at higher frequency of the back-gate voltage. These observations cannot be explained by electrochemical oxidation of graphene.

The high electric field could trap charges and generate reactive species (*e.g.*, radicals) at the graphene-SiO_2 interface. To rule out their contributions, we conducted a control experiment where a graphene was subject to the square wave modulate but without laser heating. We did not observe any increase of defect density of graphene (Figure A.6). In addition, with lower frequency square wave (up to DC gating), which favor charge trapping at the graphene-SiO_2 interface, we observed reduced enhancement of oxidation. These data argue against electrochemical-related mechanisms.

Many semiconductors, especially Si, exhibit doping dependent oxidation behavior. Si can also be oxidized using a conductive AFM tip, even under both anodic and cathodic conditions.[232] However, these effects were due to the band bending at the interface, which is a function of the doping and/or electric field. The overall mechanism is still electrochemical in nature. In our case, no oxidation was observed outside the laser focus, inconsistent with such mechanism.

Our result cannot be explained by resistive heating. The graphene area outside of laser focus did not show any noticeable change in their defect density despite the electrical modulation affecting the entire sample; this fact shows that the resistive heating itself, if any, was not significant enough to induce the thermal oxidation of graphene. Indeed, the capacitive current measured throughout the experiment was on the order of 10^{-8} A for a centimeter-sized graphene sample; the steady state leakage current is less than 1 nA. Even at the 10^{-5} W/cm^2 level of power density, the change in temperature of graphene due to the resistive heating of graphene/SiO_2 (300 nm)/Si wafer is on the order of 10^{-6} K (See Appendix A.1.4 for detailed calculation). Such a small temperature change should not affect the oxidation kinetics within the laser focus.

Finally, the enhanced oxidation we observed here is also mechanistically different from the electrochemical promotion of catalysis (EPOC) effect, also known as non-Faradaic electrochemical modification of catalytic activity (NEMCA).[233, 234] Similar to electrochemical oxidation of graphite, EPOC/NEMCA effect is only observed under anodic potentials. In addition, the EPOC/NEMCA effect requires a solid electrolyte substrate (*e.g.*, Yttria-stabilized zirconia) to produce activated oxygen species for the oxidation of molecules adsorbed on the solid electrolyte substrate. In contrast, the substrate used in our experiment is SiO_2, which is not expected to catalyze nor participate in the oxidation reaction.

3.4 Conclusion

In summary, we showed that back-gating increases the reactivity of graphene in gas-phase oxidation reaction. Using 300 nm SiO_2 as the dielectric, we observed increase of reactivity by 2 – 3 times in the presence of +/-80 V of back gate voltage, which corresponds to a charge doping density on the order of $1.3x10^{-3}$ *e*/atom. The enhancement cannot be explained by the electrochemical oxidation of graphene since both positive and negative gate voltages increase the oxidation rate while gating itself does not induce the oxidation of graphene. DFT calculation shows that an external electric field perpendicular to graphene, regardless of its direction, reduces the overall activation barrier for the reaction of oxygen with graphene to form peroxide-containing intermediates and the decarboxylation of lactones intermediates. Our results show that electrical-induced charge doping enhances reactivity of graphene in non-electrochemical reactions. This charge-doping enhancement of reactivity is an attractive alternative to the chemical-based catalysis and may be coupled with the latter to provide greater enhancement and real time control of chemical reactivity.

4.0 Enhanced Hydrogen Evolution Activity on Strained Graphene

Part of this chapter is being prepared for submission authored by Min A Kim, Dan C. Sorescu, Shigeru Amemiya, Kenneth D. Jordan, and Haitao Liu.

Author Contributions: HL conceived the project and directed the experimental studies. MK designed and conducted experiments. KDJ directed the theorical calculations. DCS carried out DFT calculations. The DFT results are included here to provide a comprehensive view of my experimental results. SA provided helpful discussion on electrochemical theory. All authors discussed and commented on the manuscript.

4.1 Introduction

Strain engineering has attracted great interest with the rise of 2D materials because mechanical modulation is more easily achievable with thin materials. Strain can be introduced indirectly using lattice mismatch between layers. The surface strain of a thin layered metal on a bulk substrate has been studied extensively for the development of epitaxial growth of thin layer materials. It has been shown that one can grow a thin layer metal on top of another metal that has a different lattice constant in order to have a strained surface.[235] The chemical properties of strained surfaces can differ significantly from their unstrained counterparts. For example, increase in oxygen adsorption has been observed on strained Ru surfaces.[236, 237] The effect of metal surface strain on their surface reactivity is of great interest in catalyst development. Specifically, the effect of strain on HER has been widely studied.[238-240] A major motivation of these studies is to find

alternative catalyst materials for HER that are cost efficient. Carbon materials have attracted considerable interest in this context.[241] Graphene is a particularly interesting target to probe the effect of extreme strain since it is strong and expected to withstand > 20% of tensile strain before fracture.[242] By comparison, most single crystalline metals in macroscopic samples can only sustain < 1% strain elastically. Therefore, graphene offers a unique test-bed to explore extreme modulations of catalytic activities using strain engineering. HER on graphene electrodes has been studied previously,[243, 244] and strain effects on the chemical reactivity of graphene itself have been studied and applied to functionalize graphene.[245, 246] However, the effects of strain on graphene towards HER activity as a electrochemical catalysts has not reported. Here, we show enhanced HER activity for strained graphene. In particular, we show that tensile/compressive strain on graphene increases/decreases the current density of HER. DFT calculations show increasing adsorption energy of hydrogen with increasing tensile strain, leading to a reduction of the activation barrier of HER.

4.2 Experimental

4.2.1 Graphene synthesis and transfer

Graphene was grown on copper foils using chemical vapor deposition (CVD) based on previously reported method.[78] Copper foil (No. 46986, Alfa Aesar) was cut into approximately 1.5 cm × 6 cm strips and electropolished similar to the previously reported electropolishing method.[188] In brief, copper foil is electrolyzed with the current limit of 0.5 A for 30 s (or optimized to have smooth polished surface of copper) in phosphoric acid solution (500 ml of deionized water, 250

ml of phosphoric acid, 250 ml ethanol, 50 ml isopropyl alcohol, and 5 g of urea). Copper foil was used for both anode and cathode electrode, but only polished anode copper foil was used for graphene growth. After the electropolishing treatment, copper foil was thoroughly rinsed with deionized water, blow dried with nitrogen gas, and placed into a 1-inch-diameter fused quartz tube furnace. The tube was pump down to the base pressure <50 mTorr and back filled with H_2 (2 standard cubic centimeters per minutes (sccm)). The tube pressure with H_2 flow was maintained at ~200 mTorr. The furnace temperature was ramped to 1050 °C and annealed for >1 h under H_2. CH_4 (0.4 sccm, P_{total} ~230 mTorr) was introduced after the annealing step for ~30 min (growth), and the furnace was cooled rapidly to room temperature with the same gas flow for both H_2 and CH_4. Above condition is the example of various optimized synthesis condition. Different ratio and flow rate of gas sources can be used as well as the furnace set temperature (1000 ºC – 1055 ºC), annealing time (1 h – 2 h, annealing time was measured from the start which includes the furnace to reach the set temperature ramp-up time. Typical ramp-up time for 1000 °C was about 20 min.), and growth time (< 30 min).

After the synthesis, graphene was transferred on to Polyethylene Terephthalate (PET, No. 365-144-58, Goodfellow) or SiO_2/Si wafer (thermal oxide, 300 nm, Addison Engineering) using a wet transfer technique.[189] In a typical transfer, as grown graphene on top of Cu foil was spin coated with 5 wt% Poly(methyl methacrylate) solution (PMMA, MW 996000, Aldrich) in anisole (99 %, Sigma-Aldrich). After the PMMA was coated on top of the graphene layer, the Cu foil was etched in fresh 0.1 M of aqueous ammonium persulfate solution (98 %, Sigma-Aldrich) for > 6 h. The PMMA/graphene film was scooped out with a clean glass slide and transferred into multiple water baths to rinse off the etchant and finally placed on the target substrate. Transferred samples were dried in air over night or spin dried at 5000 rpm for 4 min. Centrifugal force from the spin-drying

method did not have any noticeable added strain on the prepared graphene samples based on the Raman spectroscopy. PMMA layer was removed in an acetone bath for 1 h followed by another acetone bath for >6 h.

4.2.2 Raman spectroscopy

A custom-built micro-Raman spectrometer with 532 nm CW single-longitudinal mode solid state laser and Nikon S Plan Fluor ELWD 40x objective (NA: 0.60, WD: 3.6-2.8 mm) was used. The laser power was kept low (< 1 mW) to eliminate any photothermal heating effect unless noted to induce the laser heating (~ 25 mW). Laser power was measured at the sample stage before each experiment run. The 2D μ-Raman spectra were obtained using Horiba scientific XploRA PLUS with Olympus Microscope BX41 and 10x objective (NA:0.25, WD:10.6). The CW laser at 473nm (20-25mW) with 10 % density filter was used. All graphene peaks were fitted with a single Lorentzian lineshape. It should be noted that the effect of laser induced heating should be negligible in this chapter (unless noted otherwise) and does not affect the result of this chapter Raman result since both graphene and PDMS substrate have high transparency, and short exposure time was used (<10 s) with long blackout time (~30 s) between the Raman measurement. All obtained spectra were processed with Igor pro 6.37 software.

4.2.3 Electrochemical measurements

All electrochemistry measurements were performed using Reference 600 potentiostat from Gamry instruments. Ground was set to float for the potentiostat. Electrochemical three electrode cell was constructed using platinum wire as a counter electrode and silver/silver chloride as a

reference electrode. Graphene electrode was attached to copper wire using silver paste (#12686-15, Electron Microscopy Sciences). Any exposed silver paste and copper wire surface were insulated by using high-vacuum silicone grease (Dow Corning). Sulfuric acid (95.0-98.0 %, Sigma-Aldrich) and Potassium Hexacyanoferrate(II) trihydrate (≥99.95 %, Sigma-Aldrich) solutions were prepared with ultrapure water (18.2 MΩ) from the Barnstead MicroPure system (Thermo Scientific).

4.3 Results and discussion

4.3.1 Preliminary study

The mechanical strain on solid materials modifies their physical properties which can have effect on the chemical reactivity. The lattice structure distortion of graphene can alter the electronic structure; strain induced band gap engineering of graphene has been studied while applying large strain required to open up the band gap of graphene remains to be challenging.[247, 248] Unlike the band gap engineering, chemical activity of graphene can be much more sensitive due to its surface dominated nature. As a result, strain enhanced reactivity of graphene has been studied extensively.[245, 246, 249-253] For example, Bisset et al. has used a flexible substrate to strain CVD graphene to show the effect of mechanical strain on the functionalization of graphene.[246] The study showed not only the rate of activity increased up to 10 times with strain, it also acted as a catalyst for reactions that normally would not occur despite the poor strain transfer between the polymer substrate and graphene. Applied strain can be easily lost due to inefficient interfacial transfer mechanisms such as slippage. Also, transferred strain from the substrate is not distributed

homogeneously across the surface of graphene, which makes it difficult to determine the 'real' strain exerted on graphene.

This preliminary section summarizes the different methods used to apply mechanical strain on graphene and their effect on the chemical reactivity of graphene, specifically the electrochemical oxidation reaction of graphene. The oxidative etching reaction was electrochemically induced while graphene was under uniaxial/multiaxial strain. Electrochemical oxidative etching (EOE) of graphene can occur any aqueous electrochemical cell. Therefore, this preliminary study provides better understanding of the strain effects on graphene electrodes and its stability in typical electrochemical cell.

4.3.1.1 The transfer of graphene on the flexible substrates

Graphene grown on Cu foil was transferred to polydimethylsiloxane (PDMS, SYLGARD 184 Silicone Elastomer, Dow Corning) using three methods: hot-press, cure-on, and spin-coating. First, the PDMS mixture (10:1, the ratio of base polymer to crosslinker) was thoroughly mixed and degassed in vacuum for 30 min before use. In case of hot-press and spin-coating methods, PDMS block substrate was prepared separately by fully curing the PDMS mixture at 70 °C for 4 h or at room temperature for 24 h.

For hot-press method, a piece of graphene/Cu/graphene sample was attached on top of a PDMS block by pressing the stack of graphene/Cu/graphene/PDMS block with the heating strip for 30 min – 60 min in a vice. The temperature of heating strip was set to ~100 °C. Once graphene/Cu/graphene piece was attached to the PDMS block, Cu was etched in fresh 0.1 – 0.2 M of aqueous ammonium persulfate solution (ammonium persulfate, Sigma-Aldrich, 98%). The top graphene layer was removed first by wiping thoroughly with etchant soaked Kimwipe, and

Cu/graphene/PDMS block was floated on the etchant solution for >12 h (Cu face down). Obtained graphene/PDMS block sample was rinsed in the large water bath and dried in air before use.

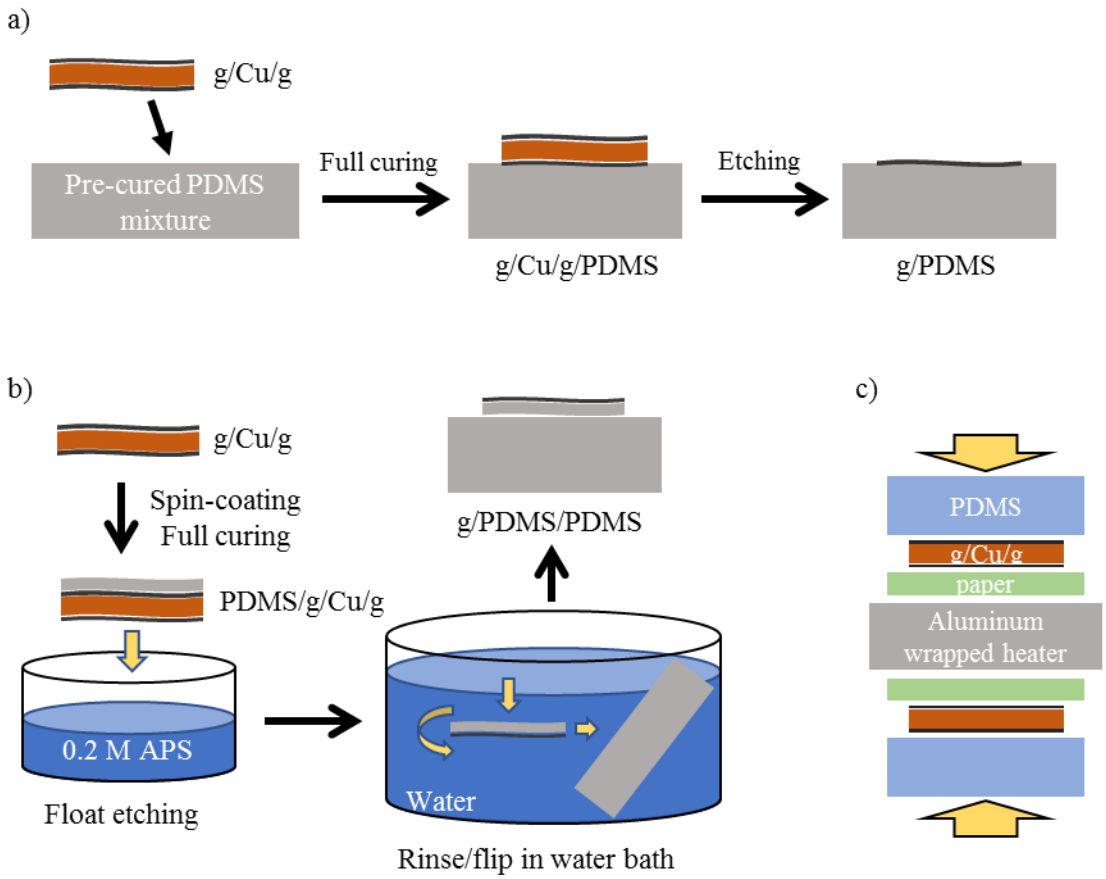

Figure 4.1 Graphene transfer process on PDMS a) Cure-on method, b) spin-coating method, and c) hot-press method.

Cure-on sample was prepared by carefully placing graphene/Cu/graphene on top of the PDMS mixture before the full curing process. In order to prevent the accidental sinking of graphene/Cu/graphene piece, the PDMS mixture was pre-cured slightly at 70 °C for 15 min. Fully cured graphene/Cu/graphene/PDMS block was processed further to remove top graphene layer and Cu same as hot-press method.

Similar to the common graphene transfer method with the supportive polymer layer, spin-coating method employed a thin layer of PDMS as a supporting layer of graphene during the transfer. First, the PDMS mixture was spin-coated on graphene/Cu/graphene at 2,000 – 3,000 rpm for 1 min. For the thinker coat, soft baking (at 70 °C for 15 min) was done between the spin-coating. The coated PDMS was fully cured at 70 °C for > 4 h. Two different supportive backplate was used, PDMS block and bubble plate. For a PDMS block assembly, Cu was etched in the etchant solution for >3 h before the assembly. After etching, PDMS coated graphene film was scooped out with a clean glass slide and floated on multiple water bath to rinse off the etchant. After thorough rinsing, PDMS/graphene film was flipped in a large water bath and scooped out with a PDMS block. Graphene/thin PDMS layer/PDMS block was dried in air before use. For the bubble plate, cured PDMS/graphene/Cu/graphene was first gently pressed onto the bubble plate and Cu was removed in fresh 0.1 M of aqueous ammonium persulfate solution (ammonium persulfate, Sigma-Aldrich, 98%). The bottom graphene layer was removed first by touching bottom graphene in the etchant and wiping thoroughly, then assembled bubble-plate/PDMS/graphene/Cu was floated on the etchant solution for > 4 h to fully dissolve Cu. Assembly was carefully removed from the etchant solution and floated on multiple water bath to rinse off the etchant. After thorough rinsing, graphene/PDMS/bubble-plate was dried in air before use. The transfer of graphene on PET substrate was done on following typical wet transfer method using sacrificial PMMA layer as noted in section 4.2.1.

4.3.1.2 Devices for the mechanical strain application

All devices were custom-made to apply different types of mechanical strain on graphene. First, three different versions of pushing devices were machined to the design sketch shown in Figure 4.2a, b, and c. Those ‘push-up’ devices stretch the disk-shaped samples through the circular

opening cover in multi-directional/axial motion. A treaded rod is fixed at the bottom center of the devices to push up and down the sample by vertical motion. Push-up version 1 has tread size 7/8-9 of moving rod to travel 2.8 mm per revolution. Push-up version 2 has low profile to fit under Horiba scientific XploRA PLUS Raman measurements. It also has moving rod with finer thread size of ¼-28 which reduce the travel distance to 0.9 mm per revolution. Push-up version 3 has free-spinning part to improve the substrate distortion due to rotational motion of moving rod. Dome shaped top of free-spinning part has radius of 2.6 inches. The moving rod thread is M20 × 1.5, traveling 1.5 mm per revolution.

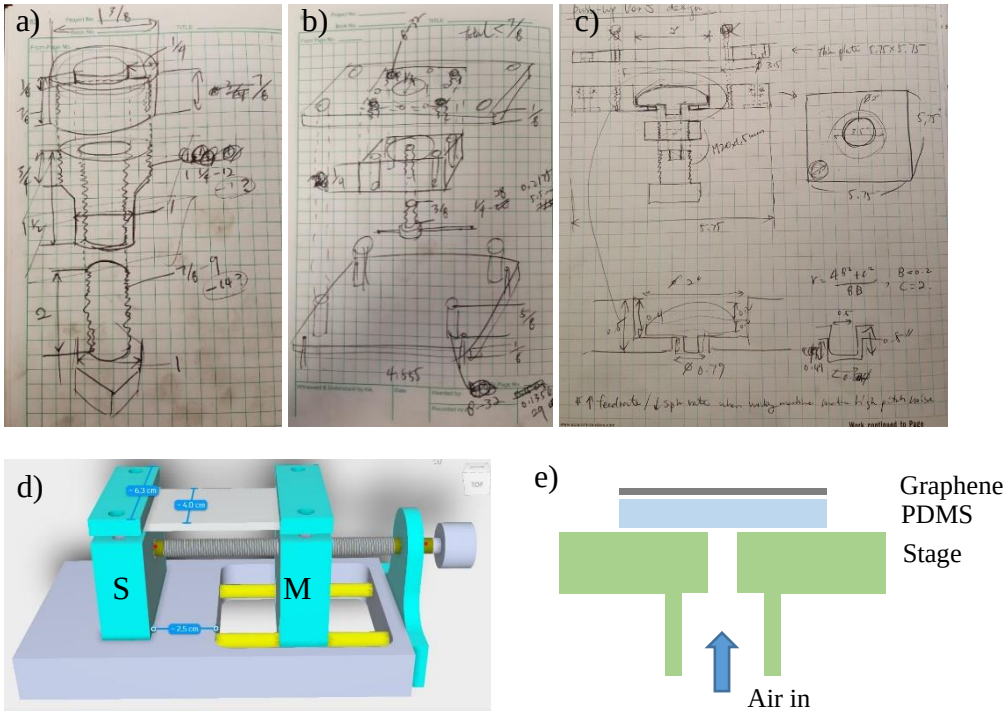

Figure 4.2 Devise designs for mechanical strain application Parts sketch of push-up a) version 1, b) version 2, and c) version 3 devices. d) The 3D model sketch of the uniaxial stretching device. Left block (S) is stationary and right block (M) travels along the rails (yellow bar on the sketch) driven by the rotation of threaded rod (M8-1.00). e) Schematic drawing of bubble plate for graphene/PDMS stretching.

In addition, uniaxial stretching device was made with M8-1.00 threaded rod which has 1 mm traveling distance per rotation of knob. Sample loading space was designed to load maximum width of 4 cm and minimum length of 5 cm for secure clamp holding. One end of stretcher was fixed stationary, and other end was designed to travel along the sliding rails. The uniaxial stretcher 3D design sketch is shown in Figure 4.2d. Bubble-plate was custom-made to apply positive mechanical strain on graphene. Schematic of bubble plate is shown in Figure 4.2e. The top opening to PDMS had 0.292 inches in diameter, and bottom opening was 0.2 inches in diameter for the tube connection. All the joints were sealed with parafilm.

4.3.1.3 Stretching behavior of graphene on PDMS

First, Raman spectrum was taken to verify the graphene on PDMS. All Raman signature peaks of graphene are all identifiable with PDMS Raman signal as shown in Figure 4.3a. However, low I(D) cannot be resolved due to strong PDMS peaks. When the PDMS substrate is stretched (1%) uniaxially, Pos(2D) showed upshifting trend with larger variation. The upshift of Pos(2D) could be explained with the compression of graphene. It is well-known that the stretching motion also compresses a material in a direction transverse to the direction of stretching due to the Poisson effect. The Poisson effect on the PDMS material having significant contraction in the direction perpendicular to the stretching direction could explain the upshifting of Pos(2D).

Compression of PDMS substrate from the uniaxial stretching can be significantly reduced when strain is multidirectional. Push-up devices were designed to gain better control of the mechanical strain motion on graphene. The Raman peak shift of graphene under multidirectional mechanical strain is shown in Figure 4.4. When graphene is under the strain, Pos(G) and Pos(2D) provide a great indication of mechanical strain on graphene. It is known that both the G and 2D peak downshift as graphene is stretched.[127, 129] However, the G peak in case of polycrystalline

graphene was found to shift up under the positive strain (stretching) due to the effect of domain boundaries.[132]

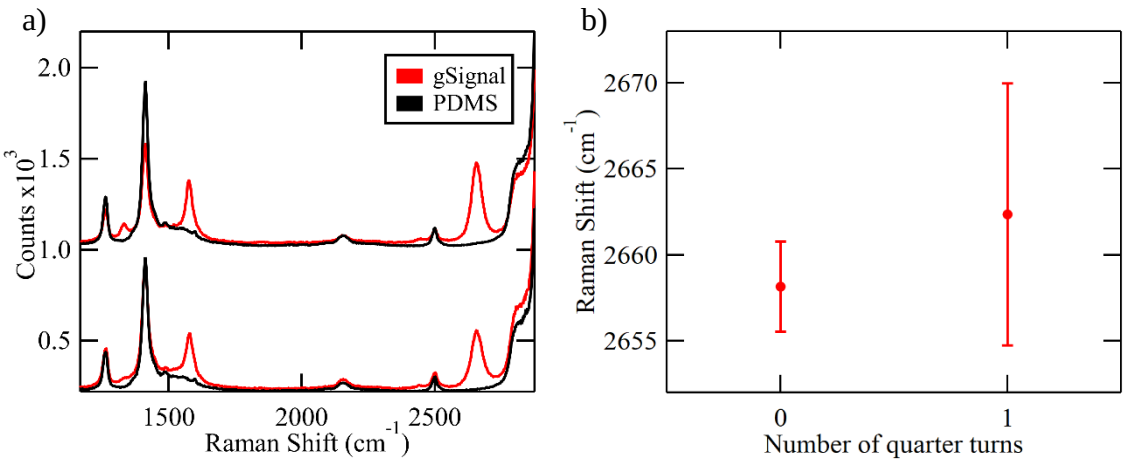

Figure 4.3 Raman spectrum of graphene on PDMS a) Graphene signature shown in red line and bulk PDMS signal in black line. Distinct D peak shown in top red spectra and not shown in bottom red spectra. b) The 2D peak position of graphene with and without the mechanical stress. A quarter turn of stretcher knob was equivalent to 1% uniaxial stretching of PDMS substrate.

With push-up version 1 device, two distinct behaviors of the peak shifting were observed: downshift of Pos(G) and Pos(2D) until a threshold, and zigzag shift. Those behaviors shown in Figure 4.4 suggest that the mechanical motion of pushing up the PDMS substrate successfully applied tensile strain on graphene. The unison downshift of Pos(G) and Pos(2D) indicates that the laser irradiated area (~ 1μm diameter, where Raman scattering is collected in return) is likely much smaller compared to average individual grain size of polycrystalline CVD graphene sample used. Pos(2D) as a function of positive strain (+, CW turn of the moving rod) shifted down until the third turn at 2655 cm^{-1}, then shifted back close to the initial position which indicates graphene was under tensile strain and released to relax back.

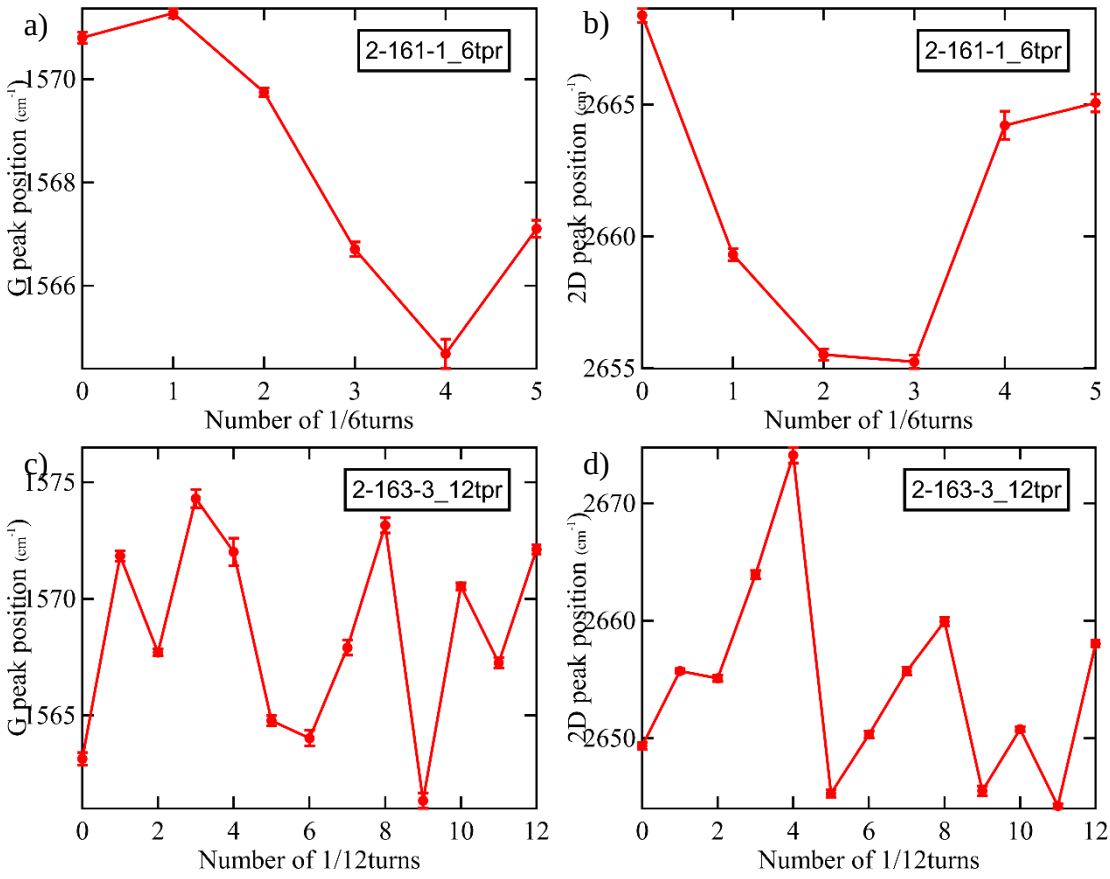

Figure 4.4 The G and 2D peak under multi-directional stretching strain The G peak (a and c) and the 2D peak (b and d) change as a function of strain applied to the PDMS substrate. Separate graphene/PDMS samples were used for a,b) and c,d). Positive turn indicates the clock-wise turn of treaded rod which moves the rod upward vertically.

Another behavior observed with the multi-directional stretching was repeated up/down shifting of both the G and 2D peak position. This observation can be explained with the slippage of graphene on the surface of PDMS substrate. Interestingly, the initial Pos(2D) without any strain was at 2650 cm^{-1}, which was close to the minimum Pos(2D) observed throughout the stretching indicating graphene is under the maximum tensile strain before any stretching motion is applied. Since the surface interaction between graphene and PDMS substrate should remain same, the maximum tensile strain that can be transferred to graphene before slipping should be also

consistent if other interface variables are absent (*e.g.*, trapped contaminants), resulting in limited range of Pos(2D) and Pos(G).

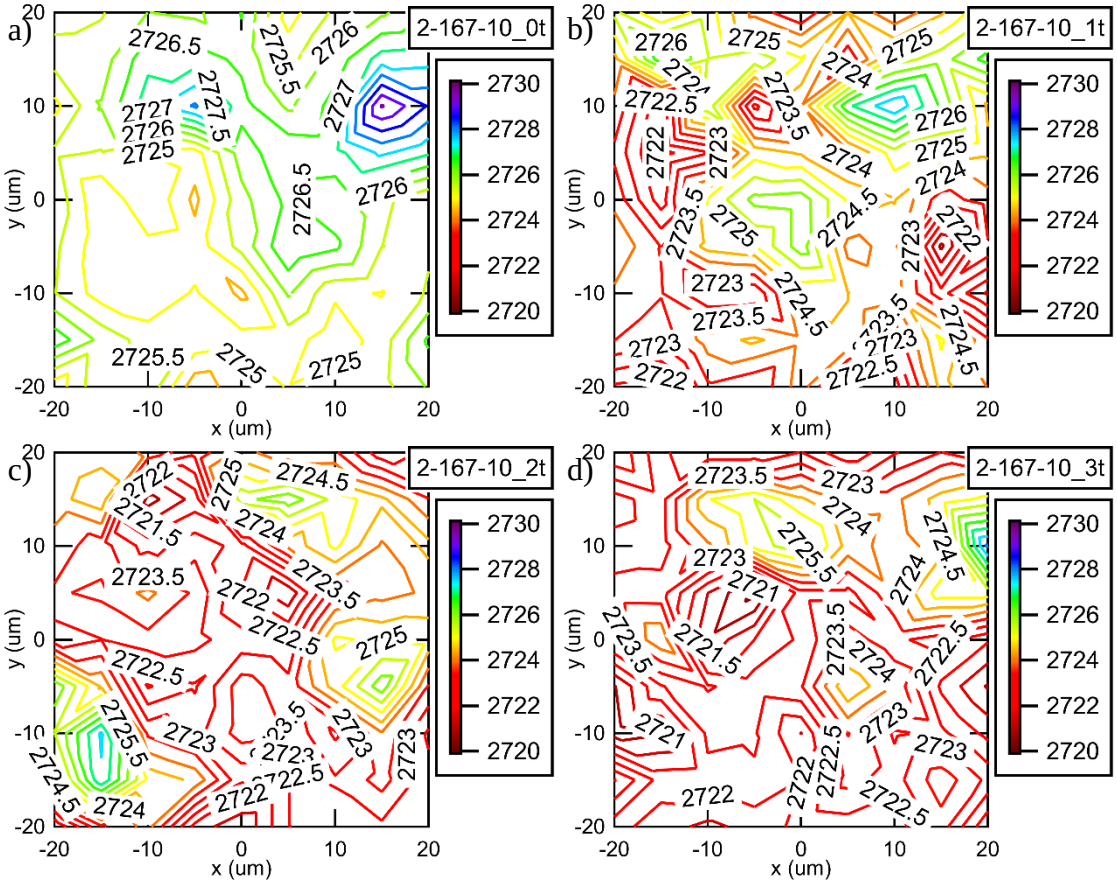

Figure 4.5 The 2D Raman map of graphene under multi-directional stretching strain The contour image of Pos(2D) over 20×20 μm^2 area of graphene a) as initial state without strain, with b) +1 quarter turn, c) +2 quarter turns, and d) +3 quarter turns of the moving rod. The push-up version 2 was used. Positive turn indicates the clock-wise turn of treaded rod which moves the rod upward vertically.

The 2D Raman map before and after the multi-directional stretching strain using push-up version 2 device is shown in Figure 4.5. The initial Pos(2D) shows slight variation (~ 5 cm^{-1}) over the mapped area (20 μm × 20 μm) which was reasonable due to the roughness of PDMS substrate and inherited roughness from the copper substrate in case of the cure-on method samples.

As shown in Figure 4.5, Pos(2D) downshifted progressively as sample was stretched further with each positive turn. The contour map representation clearly shows that the red color (lower Pos(2D)) collectively occupied larger area with more turns. However, the average Pos(2D) between the turns only shifted slightly due to applied strain being too small. The average change in Pos(2D) from initial to 3 turns was 3 cm^{-1}. With the reported Pos(2D) shift on CVD grown graphene was -72.3 cm^{-1}/%,[132] graphene was under 0.04 % tensile strain. The approximated PDMS substrate stretching amount using push-up version 2 was 0.06 %, 0.25 %, and 0.57 % after 1 turn, 2 turns, and 3 turns, respectively. Assuming 10 % of strain being transferred from PDMS to graphene, only 0.06 % of tensile strain will be exerted on graphene after 3 turns which is well within the order of magnitude agreement with the experimental value obtained here. Despite amount of strain being small, the 2D Raman map again supported that the multi-directional strain on PDMS substrate using push-up devices applies tensile strain on graphene. Unlike uniaxial stretcher, moving rods pushes up the substrate and stretches uniformly in every direction to reduce the compressive counter motions of PDMS substrate. It should be noted that the area monitored by the 2D mapping was only approximately maintained with the microscopic image. The small shift between the mapping was expected due to the manual stretching process of the device, therefore direct comparison of regional change between each image should be avoided.

Since the mechanical strain application requires the physical deformation of prepared graphene samples, graphene can be damaged while applying strain unintentionally. Additional 2D Raman maps of graphene under tensile strain were collected with larger grating in order to better resolve the D peak. Unfortunately, the intense signal from PDMS near 1400 cm^{-1} significantly hinders the accuracy of the D peak area. This interference results in large scattering of I(D)/I(G) shown in Figure 4.6. The height ratio of D to G peak provided better precision. The D/G height

ratio did not increase neither after tensile strain was applied or removed, suggesting that the strain did not cause additional damage on graphene itself. However, it should be noted that because of relatively stronger PDMS signal intensity compared to graphene, small intensity D peak cannot be resolved, thus corresponding low defect density developed on graphene cannot be detected via Raman.

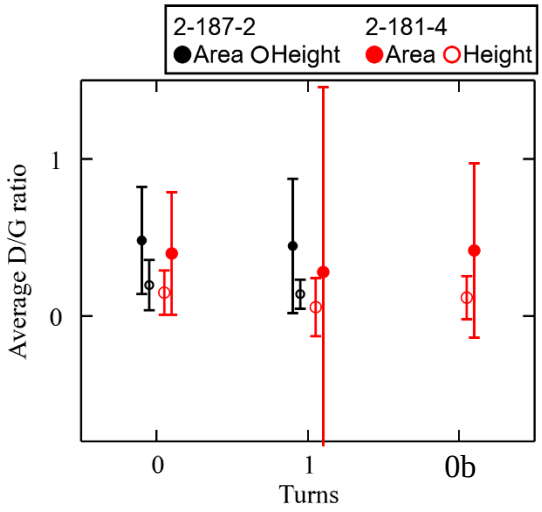

Figure 4.6 The D to G peak ratio under different strain conditions Two graphene/PDMS samples in separate 2D Raman mapping measurement shown in black and red markers. I(D)/I(G) was calculated both using peak area (closed circle) and peak height (open circle). Error bar is one standard deviation of Raman spectrums. The push-up version 2 was used. The turn 0b indicates the sample was back to 0 turn after the 1 turn stretch.

4.3.1.4 Electrochemical oxidative etching of graphene/PDMS

Graphene can be electrochemically oxidized when high anodic potential is applied. Constant voltage was applied between graphene and reference electrode (Ag/AgCl) to induce electrochemical oxidative etching (EOE) of graphene, and current was monitored over time. As expected, measured current was decreased rapidly and eventually flattened to negligible response.

Raman spectrum of graphene before and after EOE was shown in Figure 4.7a. Significant intensity of D peak had been developed after EOE. However, there was still large G peak signal present suggesting graphene is still on the surface of PDMS but partially oxidized.

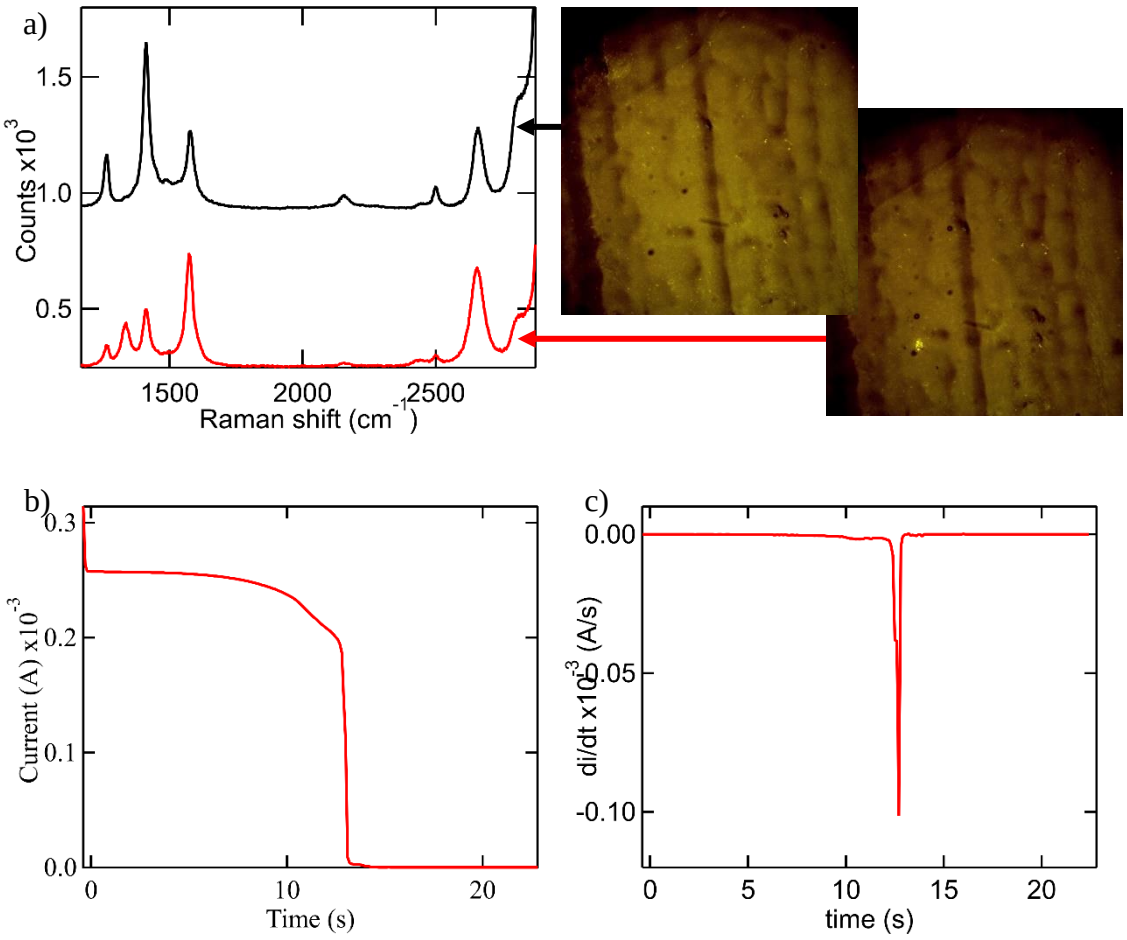

Figure 4.7 The electrochemical oxidative etching (EOE) of graphene a) Raman spectrum of graphene on PDMS before (black) and after (red) EOE under constant 2 V with 10 µL of 1 M KCl. Optical images of corresponding graphene surface is shown. b) Measured current-time of graphene/PDMS under EOE at 3 V. c) Derivative of current in b) with respect to time.

Repeated EOE on graphene/PDMS samples often showed a sudden drop of current as time progresses until the current was less than 1 µA when the current measurement was no longer

reliable due to the potential drop in the cell from unstable electrical connection. When graphene is oxidized, it loses its electrical conductivity and could lead to the disconnection of the cell circuit. Therefore, EOE was stopped when the current measurement leveled to 1 µA for the consistency of the data analysis. The time corresponding to the cut off condition was noted as a cut time, the time graphene electrode took to complete EOE and lost sufficient electrical conductivity. As shown in Figure 4.7b and c, single large drop can be easily found in the minima of current derivative with the high voltage used in the experiment. The time corresponding to this sharp current drop is noted as drop time.

Graphene electrode can be regenerated if the oxidation reaction was reversible. As shown in Figure 4.8a, the negative current (red) is measured at 10 s when the potential (black) on graphene against Ag/AgCl was set back to 0 V. This negative current corresponds to the reduction current which was not observed after 60 s of EOE (Figure 4.8b). Therefore, the defected graphene after EOE is likely gone under the irreversible oxidation reaction and cannot be reduced back once the current reached near the cut off value (1 µA).

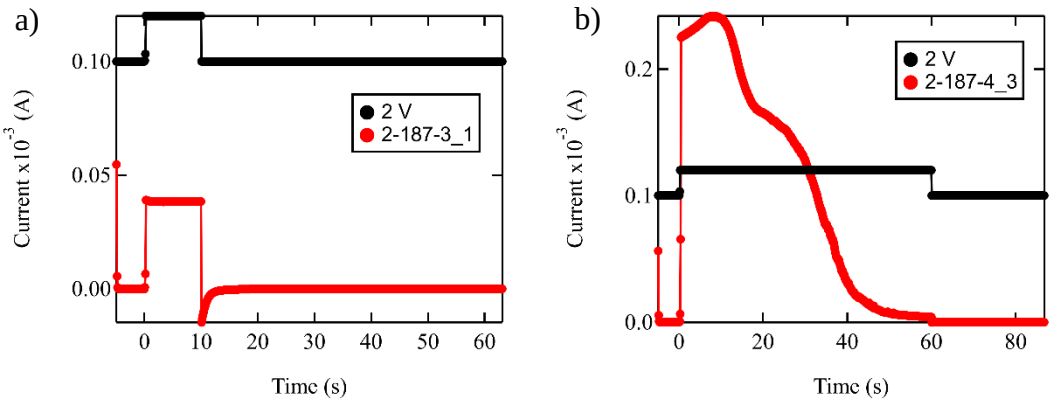

Figure 4.8 The regeneration of graphene electrode a) Spontaneous reduction of graphene electrode at 0 V after 10 s of EOE at 2 V. b) Irreversibly oxidized graphene after 60 s of EOE at 2 V. All potentials are against Ag/AgCl reference electrode.

4.3.1.5 Effects of PDMS uniaxial stretching on graphene EOE

Despite many attempts on the graphene transfer to PDMS substrate using different transfer methods, transferring very large area of graphene in a pristine condition onto the soft surface of PDMS remains to be a challenging problem. To reduce the variation between each run and increase the sampling size to observe general trend, reduced electrolyte volume was used to limit the area of graphene surface being studied. While widely distributed, three different sets of EOE using different volume of electrolyte showed consistent trend of decreasing total charge collected during EOE as the uniaxial stretching of PDMS substrate progressed. The drop time trend was also observed; the length of EOE was increased as the uniaxial strain on PDMS increased.

If we assume the dominant strain exerted on graphene from PDMS substrate uniaxial stretching is compressive, Figure 4.9 suggests that the compression of graphene electrode decreases the total collected charges during EOE while it increases the life-span of graphene electrode. Decreased total collected charges could suggest that the electrochemically active site of graphene area could be blocked or became less accessible due to compression, therefore reduces graphene EOE resulting in longer lasting graphene electrode.

When graphene sheet tear and crack under stress, surface area of graphene being studied could be changed. Decrease of total collected charges coincides with the loss of graphene surface area. However, decreased graphene area cannot explain the increased EOE duration.

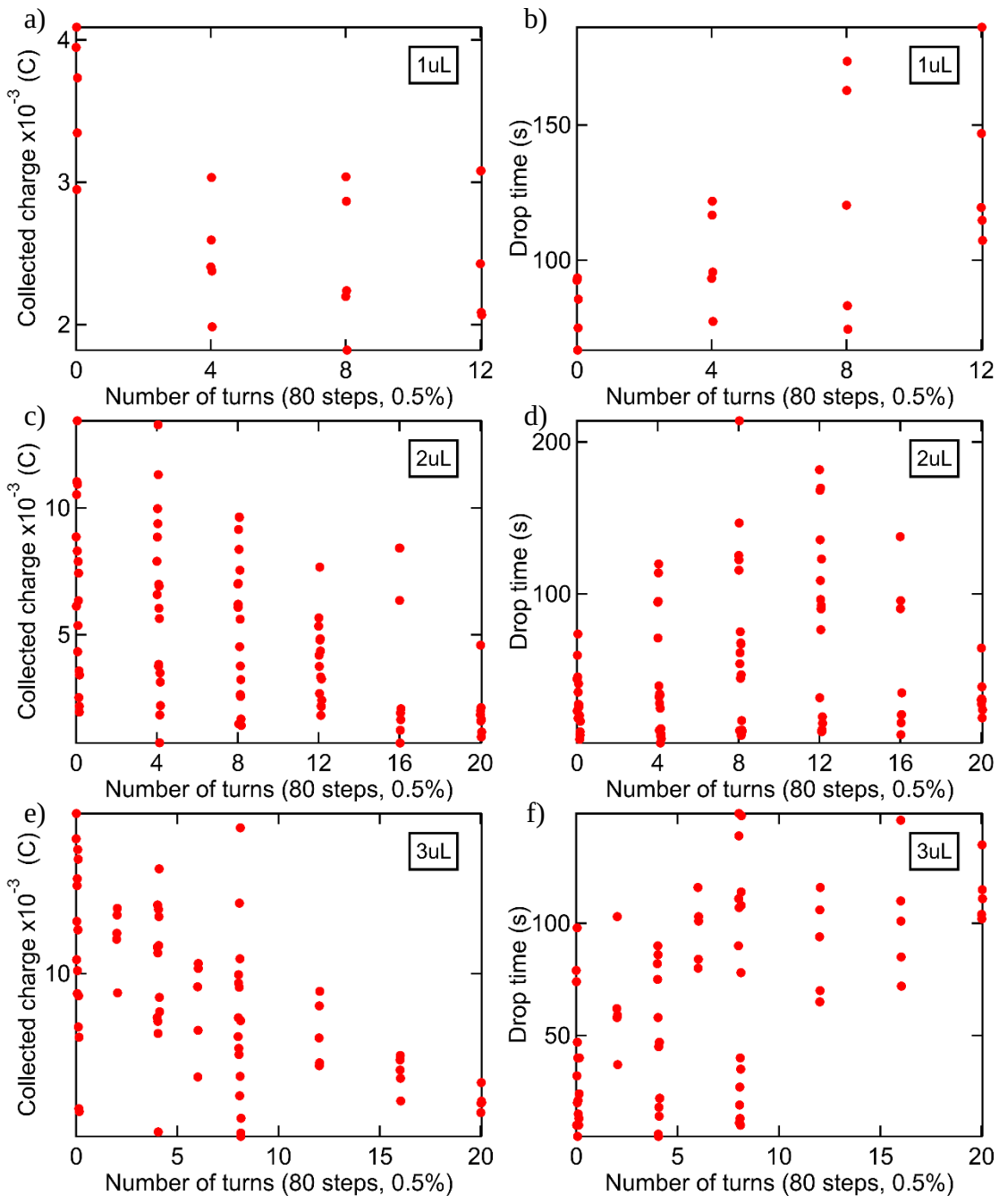

Figure 4.9 EOE of graphene on PDMS under uniaxial strain EOE at 3 V with different volume of electrolyte. Total collected charge and drop time at 1 uL (a,b), 2 uL (c,d), and 3 uL (e,f). Collected charge was calculated area of measured current vs time from 0 s to drop time. Each turn stretched 0.5% of PDMS substrate.

4.3.1.6 Location and mechanical modulation effects

Locational variation within a graphene sample did not show any concerns. Location was numbered from 0 to 6 from left to right side of graphene surface, where the location 0 was closest to the copper wire connection. The second line (L2) of locations were added to increase the distance from the electrical connection. EOE results were scattered and did not present a clear dependency on the distance from the electrical connection.

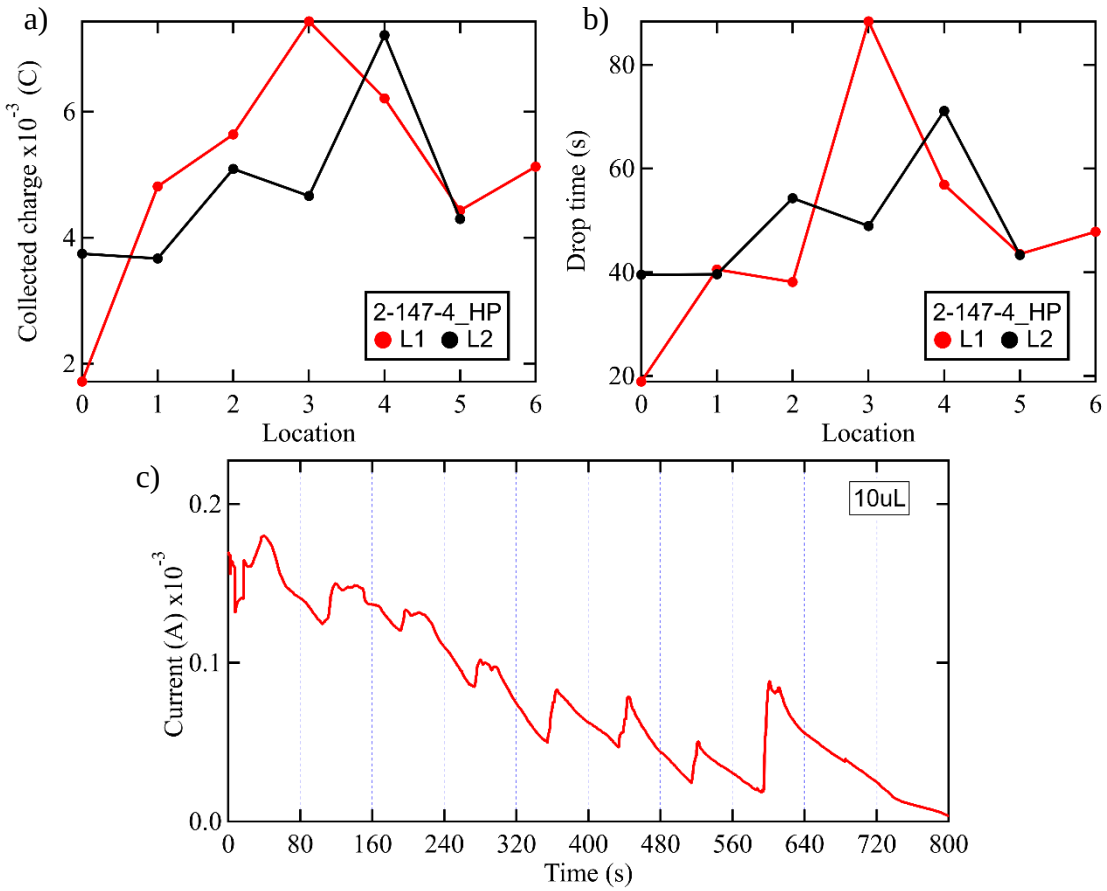

Figure 4.10 Locational control of graphene EOE Graphene on PDMS was uniaxially stretched while EOE at 3 V was done on a,b) different location of single sample and c) same location with dynamically modulated stretching. Line 1 (L1) was closer to the electrical connection of graphene than line 2 (L2). Collected charge was calculated area of measured current vs time from 0 s to drop time. Volume of electrolyte was 1 uL for a) and b), 10 uL for c).

When PDMS was dynamically stretched while *in situ* chronoamperometry on graphene was measured, it clearly showed there was an abrupt change in the current measurement in response to the stretching mechanism (Figure 4.10c). Uniaxial stretching and relaxing were repeated every 80 s with 5 s hold before the strain direction change. Current decreased while PDMS was stretched uniaxially and sharply increased during 5 s hold, decreasing back from local maximum current during the relaxing motion. Larger background change, overall decrease of current, is expected since EOE is in effect throughout the experiment. The initial decrease of current coincides with the compressive strain on graphene observed under static measurements. Interestingly, when exerted strain on PDMS was being held, the current sharply increased as if system was trying to recover its initial state. This observation could suggest that the adhesion of graphene on PDMS is not significant enough to maintain the exerted force on graphene. Graphene could be debulked out from the PDMS surface to release its compressive strain which could explain the increased current direction. Repeated measured current behavior corresponding to the mechanical modulation implies the correlation between those two parameters.

4.3.1.7 EOE under tensile strain – multi-axial stretching of PDMS

In order to control the mechanical strain on graphene/PDMS with minimum passion effect, EOE was repeated on graphene/PDMS with multi-directional stretching using push-up version 2 device. Figure 4.11 shows the initial current measured when EOE was started without any applied strain in comparison to the multi-directional tensile strain. The initial current was noticeably and consistently increased under tensile strain. On the other hand, the cut time was reduced with the stretching, with one sample of exception.

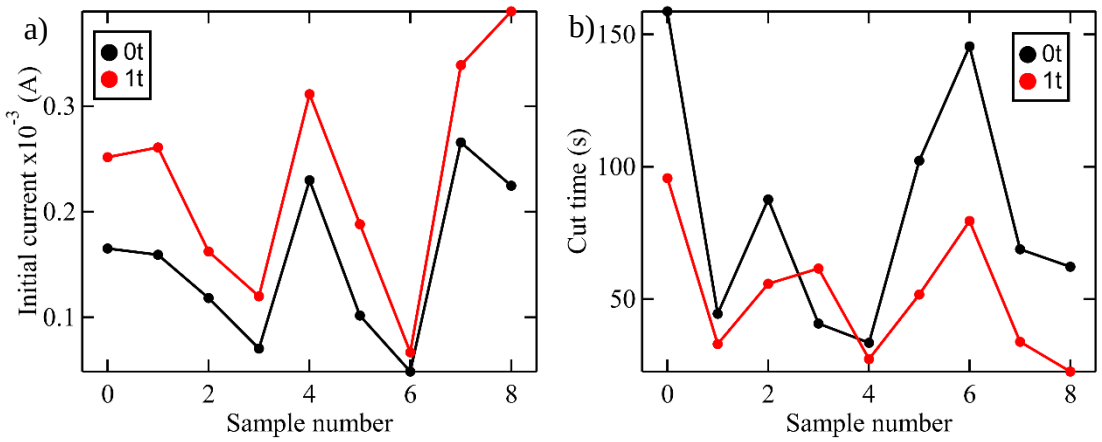

Figure 4.11 EOE of graphene with multi-directional strain a) The initial current measured at the start of EOE and b) the cut time (time electrode took to complete EOE) were measured without the strain first (0t, black) and with 1 quarter turn stretch (1t, red) using 9 different samples. Cut time was calculated that the current measurement leveled to 1 μA. After the cut time, current measurement became unstable due to the damage of graphene electrode. The push-up version 2 was used. Positive turn indicates the clock-wise turn of treaded rod which moves the rod upward vertically.

The surface area of graphene under 1 μL electrolyte used in this study was approximately 1.5 mm^2. For the complete oxidation of carbon within the area, total charge of ~ 3.5x10^{-5} C is needed. Therefore, the magnitude of initial current (10^{-4} A) clearly shows that the majority of initial current is a result of electrochemical reaction of electrolyte, not the oxidative etching of graphene electrode. It is well-known that the catalytic reactivity of graphene can be enhanced by chemical doping of graphene.[206, 208, 209] Since the mechanical strain also alters the electronic structure of graphene, one can hypotheses the change in the catalytic activity under strain similar to the chemical doping effect. The result shown in Figure 4.11a agrees with this hypothesis that the enhancing catalytic behavior of graphene electrode for the electrochemical system can be induced via mechanical strain.

The cut time on the other hand provides the information on the graphene electrode itself. The cut time was recorded at the time when electrical connection of the cell was degraded to the point that intended potential cannot be held; graphene had lost most of its electrical contact from the cell circuit. Figure 4.11b shows the general decrease in the cut time suggesting the lifetime of graphene electrode got shortened under tensile strain. Enhanced oxidation of graphene under strain is in a good agreement with our hypothesis. Under mechanical strain, the electronic structure of graphene can be altered as well as the physical distance between carbon atoms itself also changes. Stretching graphene could lower the C-C bond breaking activation energy, enhancing oxidative etching of graphene.

It should be noted that during early repetition of graphene EOE under varying degree of tensile strain, the correlation between electrochemical measurements and incremental applied strain was not easily duplicated. Large distribution of scattered electrochemical measurement results between different graphene samples made the statistical comparison challenging. Among possible reasons for such inconsistent response, the integrity of graphene electrode was questioned. The edges of graphene electrode are more likely lifted off from PDMS surface compared to the center area when the surface of PDMS moves under strain. Therefore, by increasing the physical size of graphene electrode and only focusing on the center area, the chance of having graphene without cracks and holes under the electrolytes. The center of large graphene electrode sample (~ $4cm^2$) showed expected trend in the change of electrochemical measurements responds to the applied tensile strain (Figure 4.12). The sudden change in the direction of both current and cut time was observed as tensile strain progressed which fits well with the slippage of graphene on PDMS.

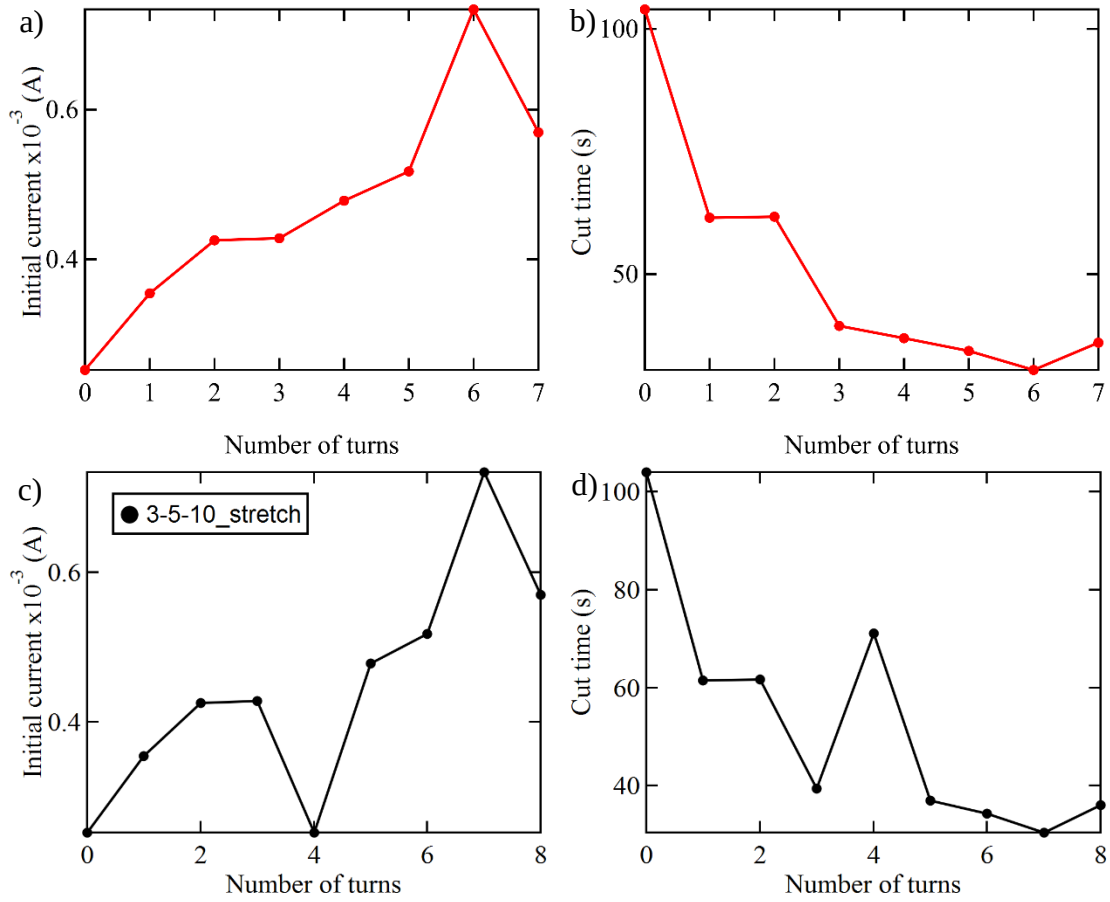

Figure 4.12 EOE of graphene under various amount of tensile strain The initial current flow (left column) and the cut time (right column) using the center area of large graphene electrode. Two different samples (sample1 in red, a,b and sample2 in black, c,d) were repeated. The push-up version 3 was used.

EOE of graphene with tensile strain was further repeated. At a glance, the initial current decreases while cut time increases which was opposite to the observed trend. However, closer look shows that the initial current was originally increased and start to decrease soon after first 1-2 turns of tensile strain. If we assume that the sudden directional change in current/cut time response is due to the slipping graphene, the true strain on graphene diminishes and graphene is back to relaxed state.

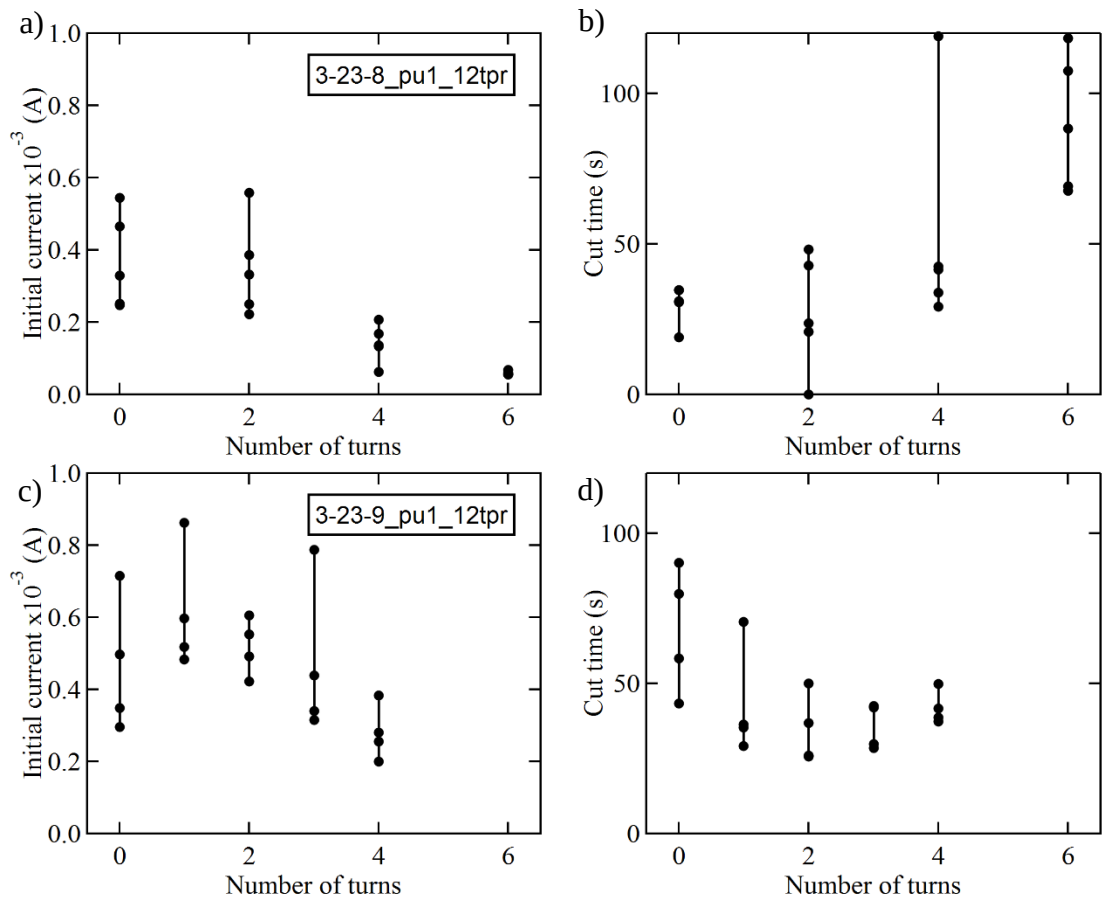

Figure 4.13 Reproduced graphene EOE trend The initial current flow (left column) and the cut time (right column) of two different samples (sample1 in a,b and sample2 in c,d). The push-up version 3 was used.

In order to confirm the tensile strain effect, slippage of graphene should be avoided. The bubble-plate method is used apply small strain while minimum friction is excreted on the sample since it expands the graphene/PDMS film by pumping air. EOE result with bubble-plate method confirmed the increase in initial current and decrease of cut time when graphene/PDMS was stretched using small volume of air. Interestingly, deflated bubble to relax graphene showed similar results as stretched graphene/PDMS suggesting the mechanical strain used in this experiment deformed the state of graphene/PDMS irreversibly.

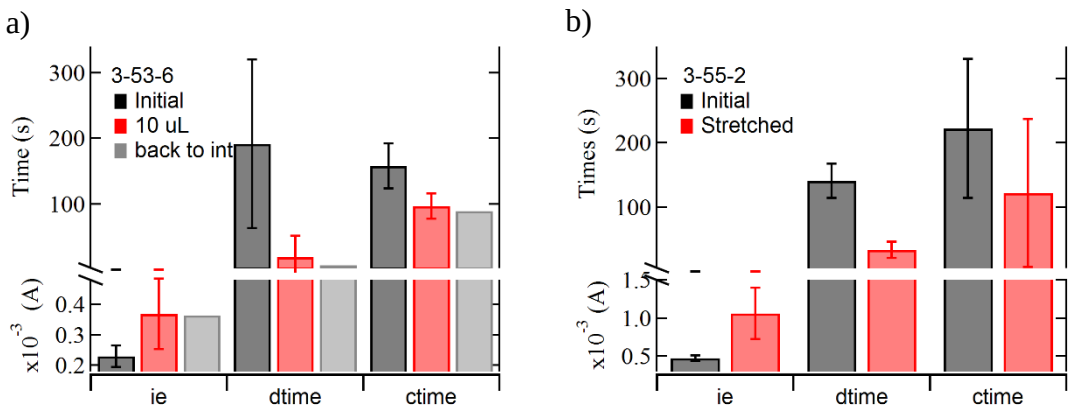

Figure 4.14 EOE of graphene using bubble-up method to apply tensile strain a) Graphene/PDMS was oxidized before (black), while (red), and after (gray) stretched with 10 µL air. b) graphene/PDMS was oxidized before (black) and while (red) stretched using unknown amount of air.

4.3.1.8 EOE under compressive strain – multi-axial stretching of PDMS

Based on the blue shift trend of Raman spectrum of graphene under uniaxial stretching of PDMS substrate and known large Poisson's ratio of PDMS (~ 0.5),[254, 255] the overall force exerted on graphene via uniaxial PDMS stretching was suggested to be compressive. To confirm the effects of compressive strain on graphene, push-up device was used. The block PDMS substrate was loaded on the push-up version 1 device and pushed to stretch out to form dome shape. Spin-coated PDMS/graphene sample was floated on the large water bath to be gently pressed by the stretched block PDMS into water. Assembled sample was ordered in graphene/coated PDMS/pre-stretched block PDMS. As the moving rod of push-up device travels downward (-, CCW direction turning), stretched block PDMS substrate contracts back to its initial form. This shrinking surface area of block PDMS substrate exerts compressive strain on graphene.

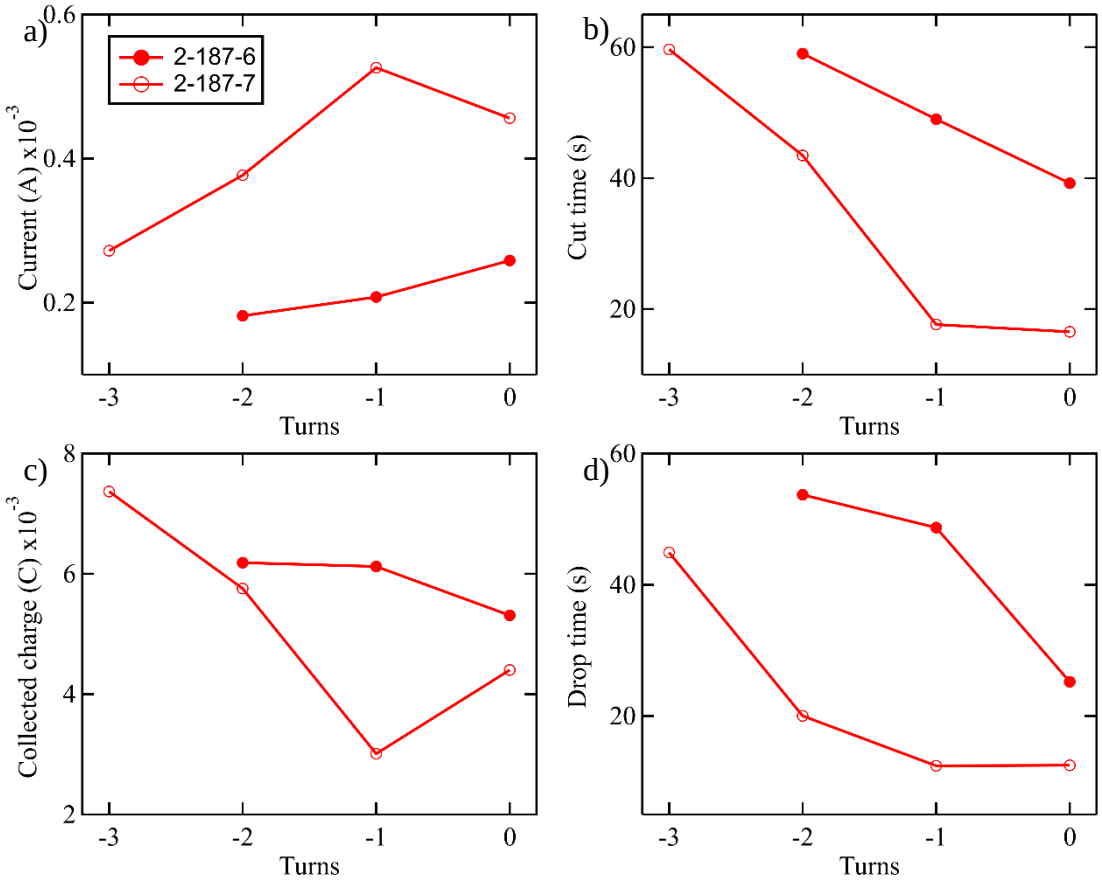

Figure 4.15 EOE of graphene under compressive strain a) The initial current flow, b) the cut time, c) the overall collected charges throughout EOE until the cut time, and d) the drop time were collected using two separate samples (red filled and unfilled dots). The drop time was calculated that current drops significantly at the end of EOE (dI/dt minimum). The push-up version 1 was used. Negative turn indicates the counter clock wise turn of treaded rod which moves the rod downward vertically.

When the compressive strain was applied on graphene, the initial current was decreased and cut time was increased which coincides with the trend observed in the uniaxial stretching confirming the compressive nature in uniaxial stretching. Moreover, current increase and cut time decrease are opposite to the observed trend in tensile strain. Figure 4.15 shows two separate samples exhibit similar trend on initial current, cut time, total collected charge, and drop time. As the compressive strain increased, initial current was decreased suggesting the catalytic activity of

graphene was suppressed under the compression. The cut time of EOE got progressively longer after each negative turn, suggesting that electrochemical oxidation of graphene could be slowed down by compressive strain. The total collected charges also showed increasing trend similar to the cut time as a function of negative strain which indicates the electrochemical reaction of the electrolyte is the dominant contributor to the measured current. Despite the reduced catalytic activity of graphene under compressive strain, prolonged life-time of graphene electrode overall resulted in more productive electrochemical reaction system.

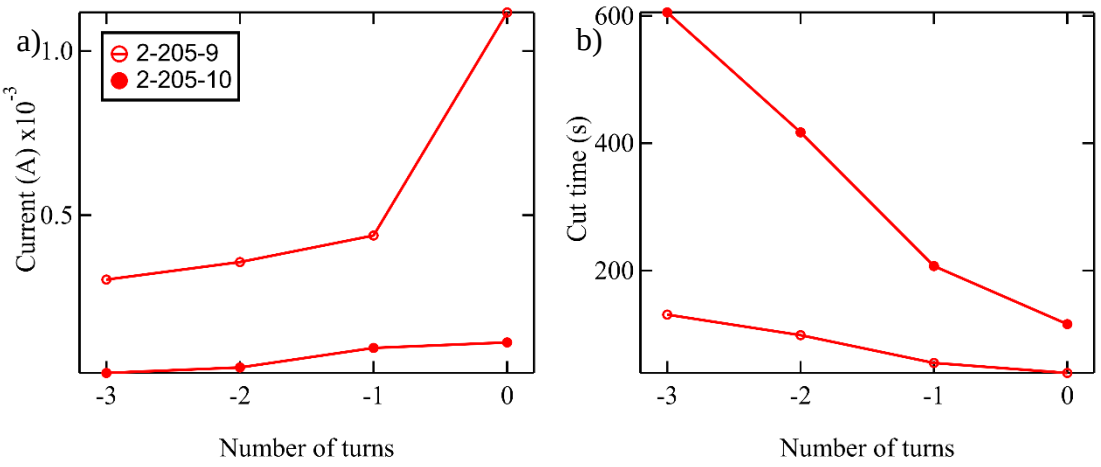

Figure 4.16 EOE of graphene under compressive strain duplicated a) The initial current flow and b) the cut time collected using two separate samples (red filled and unfilled dots). Duplicated experiment of Figure 4.15. The drop time was calculated that current drops significantly at the end of EOE (dI/dt minimum). The push-up version 1 was used. Negative turn indicates the counter clock wise turn of treaded rod which moves the rod downward vertically.

4.3.1.9 EOE under tensile strain – bending of PET

To increase the adhesion of graphene and stability throughout the transfer process, polyethylene terephthalate (PET) was substituted as a flexible substrate. PET is much stiffer plastic

having lesser elasticity compared to the fully cured PDMS. The stability of graphene transfer drastically increases in trade of less flexible physical property of PET. Typical wet transfer method via PMMA supporting layer can be used for PET substrate owing to the compatibility of wider range organic solvents on PET. The details on graphene on PET can be found in section 4.2.1.

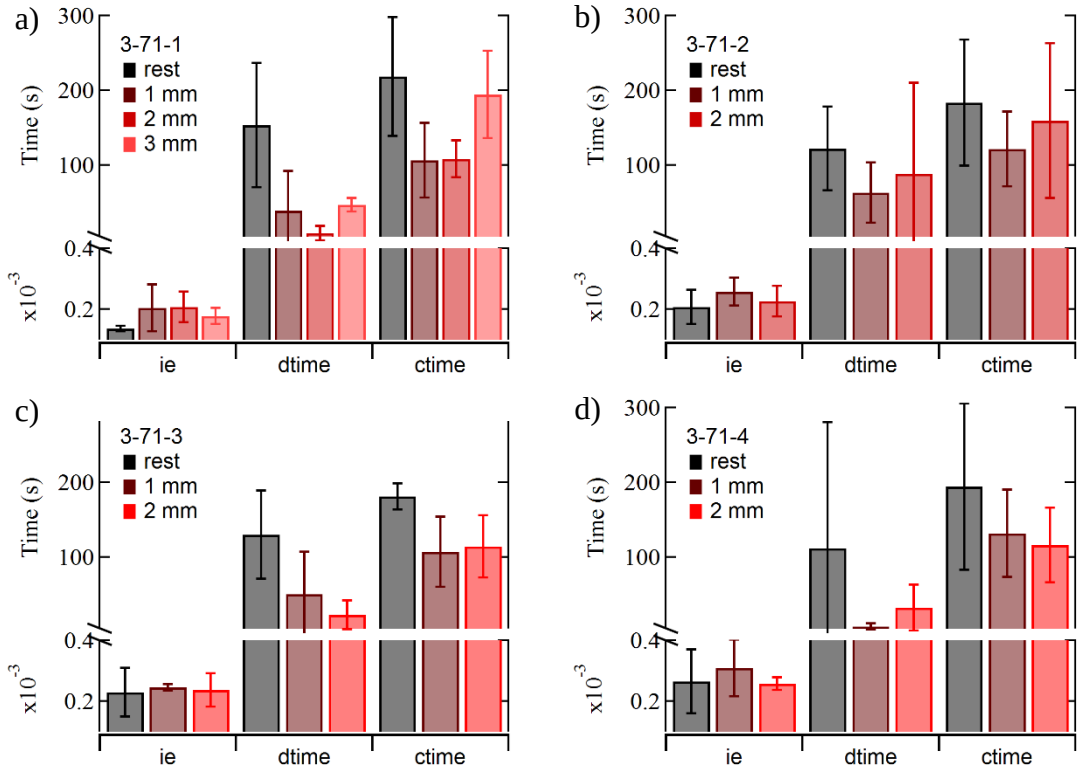

Figure 4.17 EOE of graphene on PET with tensile strain via bending PET substrate Graphene/PET was oxidized before (black) and while (red and dark red) being stretched using substrate bending device. The initial current flow (ie), drop time (dtime), and cut time (ctime) were collected using four separate samples. The drop time was calculated that current drops significantly at the end of EOE (dI/dt minimum).

The disadvantage of PET is the significant interference of its Raman signal with graphene signatures. Strong intensity near 1200 – 1300 cm^{-1} from PET makes the D peak of graphene pretty

much undetectable. Strong G peak presence can be resolved on the shoulder of PET peak with multi-layer graphene but challenging with single layer graphene. The 2D peak of graphene is well-resolved and always present that can be used to probe the strain on graphene. Raman spectrum of graphene on PET can be found in the following section 4.3.2.

The results of EOE on graphene/PET showed consistent trend throughout the experiments (Figure 4.17). The increase in initial current (ie) and decrease in cut time (ctime) were observed as PET substrate was bent in order to induce the tensile strain on graphene, and trend was repeated throughout all four individual samples of graphene/PET. Moreover, inversion of the change (from increase to decrease) was also persisted when graphene was stretched further. Overall, the consistent trend observed in initial current and cut time is in good agreement with the PDMS results.

4.3.1.10 Summary and future directions

In summary, the effects of mechanical strain on electrochemical oxidative etching (EOE) of graphene electrode were observed. The decrease in measured current and increase in the duration of EOE were found when graphene electrode was subjected under the compressive strain. The compressive force on graphene was achieved via both uniaxial stretching and multi-directional contracting of PDMS substrate. The current and duration of EOE indicates reduced catalytic activity of graphene electrode while graphene is less susceptible from the oxidation reaction. In comparison, at least during very early stage of tensile strain application, stretched graphene showed increased initial current and decreased cut time; tensile strain promotes both the catalytic activity of graphene and reactivity of graphene itself. These observed results were consistent throughout different tensile strain application methods: multi-directional stretching of PDMS, inflation of PDMS film using bubble-plate, and bending of PET substrate.

The low precision remains as a main challenge to find the significance in the findings. Establishing transfer method to reliably obtain large enough homogeneous area of graphene is critical since optical and Raman spectroscopic characterization of transferred graphene quality is more challenging with polymer substrates. The adhesion strength of graphene on PDMS is not favorable due to large difference in their surface energy. PET substrate provides much more reliable preparation of graphene samples and better controlled mechanical strain application. However, sacrificial PMMA layer used during the transfer contaminates the surface which could interfere with the interested electrochemical activities.

Alternatively, the internal standard method could be developed to normalize the experimental fluctuation using CV of well-known electrochemical system on graphene. Moreover, signal can be amplified to improve signal to noise ratio. Achieving large strain application via clamping graphene and stretching directly is mechanically challenging problem to solve. In recent collaborative work, we developed graphene fiber solely made from single sheet of graphene and demonstrated its strength in macroscale. The adaptation of graphene fiber could provide a new insight into the electrochemical reactivity of graphene under extreme mechanical strain.

EOE requires high potential to induce graphene oxidation within reasonable period of time (minutes) which inevitably producing many other electrochemical reactions in the cell. On the other hand, graphene oxidation can be negligible with the low enough potential while still studying available electrochemical species. The effects of strain on the catalytic activity of graphene towards other electrochemical system are evidenced in EOE of graphene, and further investigated in detail in following sections confirming the mechanical modulation can be a great tool to control the catalytic activities of graphene.

4.3.2 Mechanical strain on graphene

Tensile and compressive strain was applied to graphene supported on a flexible polymeric substrate. For this purpose, the graphene sample was transferred first to a polyethylene terephthalate (PET) substrate using a wet transfer method. In order to apply mechanical strain to graphene, the substrate was physically bent in either the outward or inward directions, leading to an applied tensile or compressive strain to graphene, respectively (Figure 4.18).

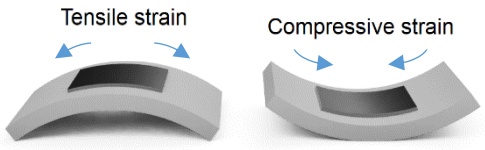

Figure 4.18 Schematics of strain application on a graphene/PET sample Graphene (black) is placed on top of the PET substrate (gray). The PET substrate is bent outward/inward to induce tensile/compressive strain on the graphene.

The amount of mechanical strain applied to graphene via bending of the PET substrate was measured using Raman spectroscopy. Typical Raman spectra of graphene on PET are shown in Figure 4.19 along with the Raman spectrum of the PET substrate and of graphene on a SiO_2/Si substrate. The Raman spectrum of graphene has three major peaks: the D peak at ~1350 cm^{-1}, the G peak at ~1580 cm^{-1}, and the 2D peak at ~2700 cm^{-1}.[103] The 2D peak is sensitive to the mechanical strain.[103, 127, 129, 131] A previous study of a graphene layer grown by chemical vapor deposition (CVD) showed that a strain of 1% results in a -72.3 cm^{-1} shift of the 2D peak.[132] We use the same Raman spectral dependency on strain when evaluating the change of strain in our sample.

A zero strain % (ε) was assigned to unbent PET supported samples while for the strained samples, the experimentally measured strain % was obtained relative to the unbent samples. Due

to possible charge doping from the substrate/environments,[122] the initial amount of strain on an individual graphene/PET sample cannot be accurately measured based on the Raman 2D peak. The Raman spectrum of the PET substrate has several strong features below 1800 cm^{-1}, which hinders the analysis of the D and G peak regions. The maximum strain % applied to graphene throughout the experiment was ~ ±0.3 %. The absolute strain % of graphene can vary between samples since the assigned zero strain condition could differ.

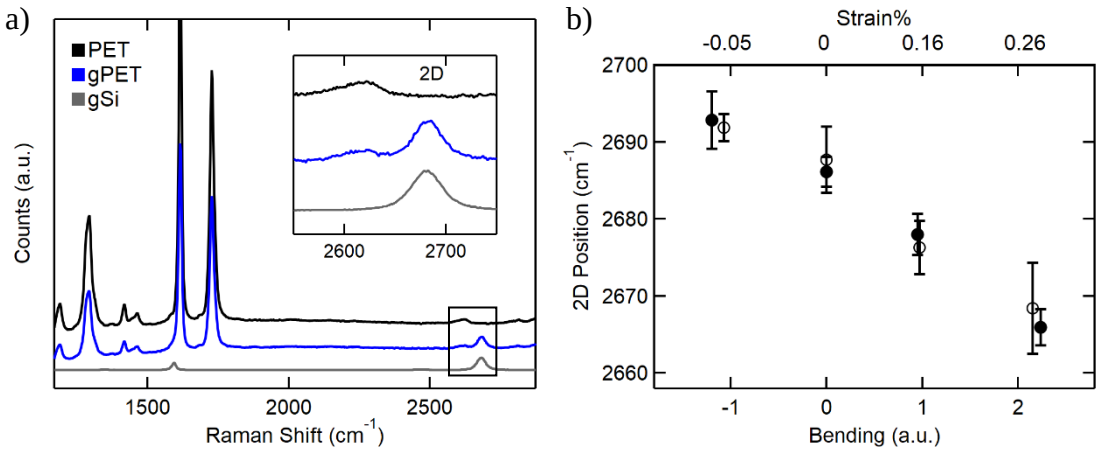

Figure 4.19 Raman spectra of graphene/PET (a) Raman spectra of PET substrate, graphene on PET, and graphene on Si wafer (from top to bottom). Insert shows a zoomed region of the PET peak at ~2620 cm^{-1} and the graphene 2D peak at ~2685 cm^{-1}. (b) The position of the 2D peak of graphene with the bending amount of the substrate expressed in arbitrary units (a.u.) on the bottom axis. Top axis shows the corresponding graphene strain % calibrated from the 2D peak position shift. Two sets of Raman measurements (filled/empty symbols) are represented showing good reproducibility in the Raman data, in response to the applied strain.

4.3.3 The effects of strain on graphene hydrogen evolution reaction (HER)

The effects of strain on the measured current in HER can be determined using current-time measurements (Figure 4.20). The current was measured at a fixed potential (-0.5 V vs. Ag/AgCl) while the strain conditions were changed periodically. The apparent area of graphene was optically measured to calculate the current density (J). Tensile strains of 0, 0.17, and 0.25 % were applied. Each strain was applied and held for a period of 20 s.

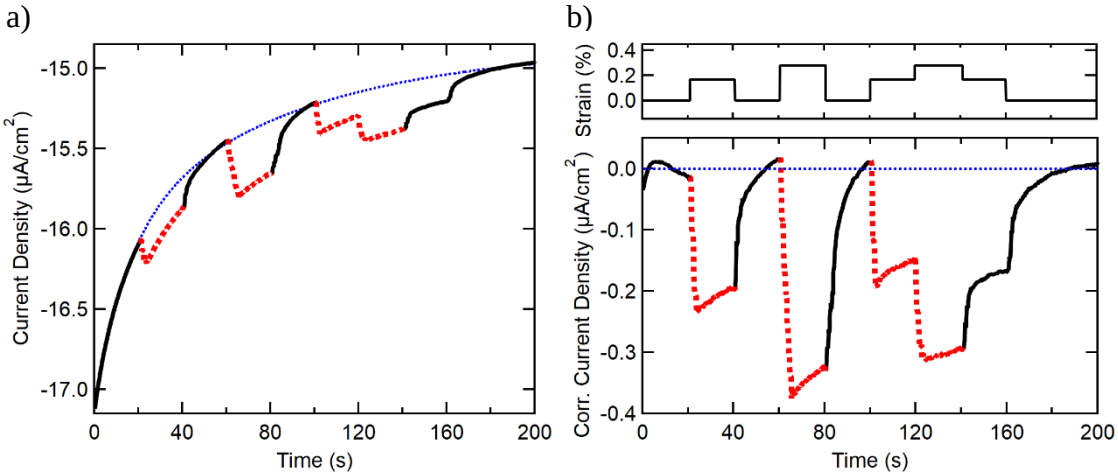

Figure 4.20 Measured current density of HER vs. time Current measurement as a function of time under constant potential (-0.5 V vs Ag/AgCl). a) Change in current density under tensile strain (dotted red). The overall shift of the current density is shown by a blue dotted line which was fitted with an exponential function over the range of values at zero strain%. b) Time variation of the current density with the background subtracted out (lower panel). Strain modulation sequence applied (upper subpanel). Note that a dip in the current density curve corresponds to an increase in the cathodic current.

We observed a significant background drift in the current density, especially at the early stage of the experiment. This background drift of current density (dotted blue curve) varies between electrode samples, possibly due to non-uniform surface conditions of large area graphene

(e.g., contaminants, defect density, grain size, etc.). For example, we previously showed that HOPG surface slowly adsorbs hydrocarbon contaminants in water, reducing its double layer capacitance and electrochemical activity.[145, 256-258] The contaminants on the graphene surface can be also lifted off from the surface as H_2 gas bubbles form on the surface of graphene during HER. Nevertheless, despite the background drift of the current density throughout the measurements, a sharp change in current density is observed in response to the change in the applied strain (Figure 4.20a). A similar current response to the applied strain with negligible background drift is shown in Figure B.1.

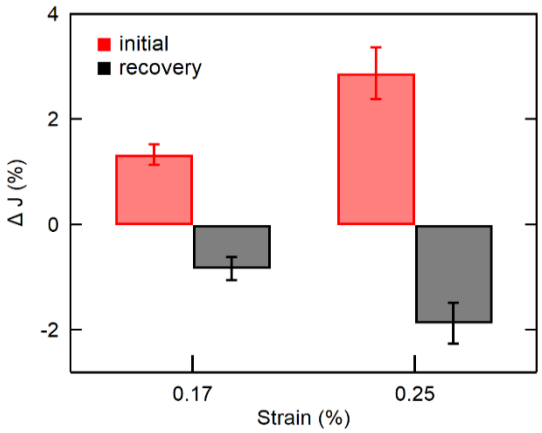

Figure 4.21 The average change in current density The current density change (ΔJ) under different amounts of tensile strain and recovery. There is a positive correlation between the strain and current change. The average increase in current under each strain is shown as positive change (initial). The average decrease in current upon the relaxation of each strain is shown as negative change (recovery).

The change in the current density (ΔJ) with strain can be visualized more clearly with the background subtracted out as shown in Figure 4.20b. Sharp and fast increase of the current density is seen under tensile strain. The magnitude of ΔJ was affected by the degree of strain%; larger tensile strain leads to larger ΔJ. Recovery of the current density (solid black) is clearly seen upon

the relaxation of tensile strain. Interestingly, the kinetic behavior of the current density upon relaxation was slower compared to the change during the stretched period despite the absolute value of rate of change in strain% remaining the same (manual bending and unbending action was done in the same speed). This slower change in current during the relaxation was also observed when compressive strain was applied (Figure B.2). The removal of applied tensile strain results in a compressive directional force similar to that taking place upon application of a compressive strain.

The average percentage change in current density is shown in Figure 4.21. The effects of strain on HER current were collected repeatedly (24 times for 0.17 % and 8 times for 0.25 % tensile strain values) using multiple graphene electrodes. The change in current density values (ΔJ) were obtained from the difference between the current density before ($J_\circ$) and after (J_s) each strain application and expressed in percent variation relative to $J_\circ$. Because current density always increases with the tensile strain, initial ΔJ is positive ($J_s - J_\circ > 0$). The average initial ΔJ was 1.3 ± 0.2 % for 0.17 % tensile strain and 2.9 ± 0.5 % for 0.25 % tensile strain. Recovery of the current density was found from the change of current density upon the relaxation ($J_{\circ'}$) from the strained state (J_s) and expressed in percent variation relative to J_s. The recovery ΔJ ($J_{\circ'} - J_s < 0$) was averaged 64 % of initial ΔJ under tensile strain. Slow kinetic of current recovery after negative directional strain change might require a much longer time to reach equilibrium than the holding period used in the study, resulting in a lower estimate in the percent recovery. The surface of the graphene electrode could also partially undergo irreversible changes during initial HER with tensile strain and cause a smaller recovery amount. For example, polymer residues on the graphene surface can be removed curing HER via H_2 gas bubble forming between graphene and polymer interface or graphene can rupture if H_2 gas forms between graphene and supporting substrate.[244]

Although such bubble formation was never visibly observed under the conditions used in this study, it is possible that HER could introduce additional defects over time, increasing activity with increased defect density (if defects are favored) or/and electrode area increase due to tear/lift of the graphene film from the substrate making observed strain-current effect pseudo-reversible.

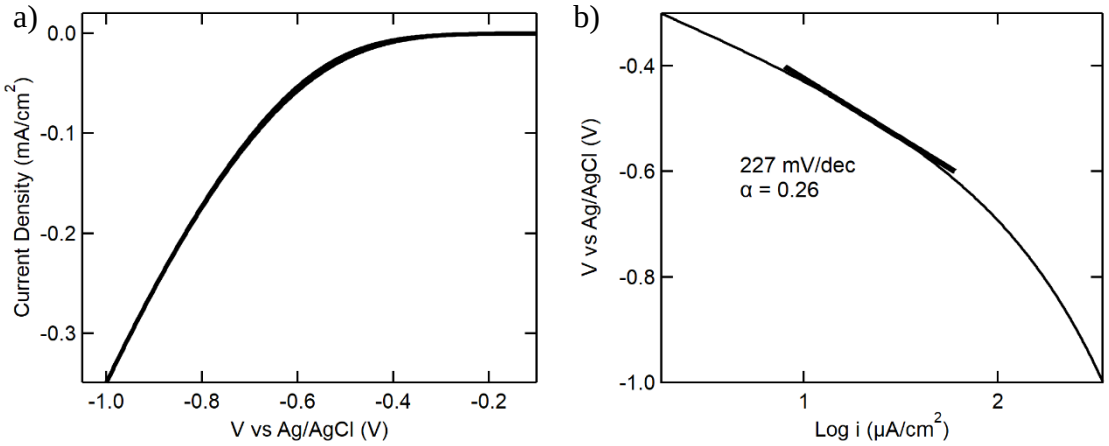

Figure 4.22 Cyclic voltammetry on graphene/PET a) Cyclic voltammetry on graphene electrode in 0.5 M H_2SO_4. b) Tafel plot. All CVs were collected at scan rate of 0.1 V/s.

A typical cyclic voltammetry (CV) measurement on graphene electrode in 0.5 M H_2SO_4 is shown in Figure 4.22. The onset potential of HER was at around -0.4 V vs. Ag/AgCl. Increase in HER current under the tensile strain was also observed in CV measurements (Figure B.3). The background drift observed in current-time measurement also persisted in the CV measurement, as a result, the effect of strain was less obvious due to the longer CV sampling interval. At -0.5 V, the Tafel slope and the transfer coefficient were 227 mV/decade and 0.26, respectively. The Tafel plot shows significant change in its slope depending on the potential. The Tafel slope increases as potential becomes more negative. The Tafel slope of ~690 mV/decade in the potential region lower than -0.8 V is found to be three times larger than the one of ~230 mV/decade around -0.5 V. The

change of the Tafel slope by a factor of 3 at more negative potentials has been predicted theoretically when the Heyrovsky reaction is the rate-determining step.[259] It is generally accepted that HER occurs in following reaction steps:

Volmer	$M + H^+ + e^- \rightleftharpoons M-H$	(4.1)
Heyrovsky	$M-H + H^+ + e^- \rightleftharpoons H_2$	(4.2)
Tafel	$2(M-H) \rightleftharpoons 2M + H_2$	(4.3)

where M denotes an available adsorption site on the electrocatalyst surface.

The change of the Tafel slope observed here suggests that HER on graphene electrode used in this study proceeds through the Volmer-Heyrovsky pathway. However, the absolute values of Tafel slopes are much larger than those theoretically calculated (120, 40, and 30 mV/decade for the rate determining steps of Volmer, Heyrovsky, and Tafel respectively). Various Tafel slopes of graphene electrode have been reported previously, ranging from 147 mV/decade to 234 mV/decade.[243, 244] The use of different substrates in the different studies could be the reason the variation in the different reported values of the Tafel slope of graphene. The effects of underlaying substrates on the electronic properties of graphene such as substrate induced doping of graphene are well-known.

The measured HER current reflects the kinetics of H^+ reduction on the electrode surface when the concentration of H^+ near the surface has not been depleted. The current density is very low (< 1 mA/cm^2) for 1 M of H^+, suggesting that the diffusion of H^+ to the electrode surface has negligible effects on the current. Therefore, the observed current change should be independent of the changes in surface roughness (e.g., flattening wrinkles under tensile strain) and geometry (e.g.,

curved shape due to the bending motion). Based on the pseudo-reversible response of the current as a function of applied strain, we believe that strain-induced damage (e.g., new defects, change of surface area) on graphene is not a major cause of the current change we observed because they should result in irreversible change in the current. With the small strain% values used in our experiments, the adsorption site is also unlikely to be changed. This analysis leaves the strain-induced change of adsorption energy at the relevant site as the most likely mechanism to explain our data. The density of the accessible active sites could also change due to the flattening of the graphene surface under tensile strain, slowing down the electron-transfer kinetics of graphene which will negatively impact the net change in the current.

4.3.4 Theoretical results

To provide a molecular scale understanding of the experimental results, we have calculated the adsorption energy of H atoms on graphene as a function of strain using density functional theory (DFT) and explored the possibility that variations in H atom adsorption energies on strained graphene are responsible for the observed changes in current density. The calculations employ 3D periodic slab models and were done using the dispersion-corrected PBE-D3[260] density functional. As demonstrated by Davidson *et al.*,[261] when compared with other exchange-correlation functionals, PBE-D3 was found to provide the closest agreement to experimental data for physisorption energy of H on graphite. In this work we assume that this improved performance of PBE-D3 functional is transferrable to the case of chemisorption properties of H on graphite. Additional details of the computational setup used are provided in Computational Methods section.

The first objective of the computational investigations was to determine the adsorption energy of an H atom in the case of unstrained graphene and its dependence on coverage with a

focus on the low coverage limit. Both these aspects are detailed in Figure 4.23. The dependence of the adsorption energy on coverage was established using a set of hexagonal supercells ranging from (2x2) to (8x8) in which a single H atom is adsorbed on unstrained graphene surface. This set of supercells allows to investigate a decrease in coverage from 1/8 ML in the case of the (2x2) supercell, to (1/50) ML for the (5x5) case, and further down to 1/128 ML for the (8x8) supercell.

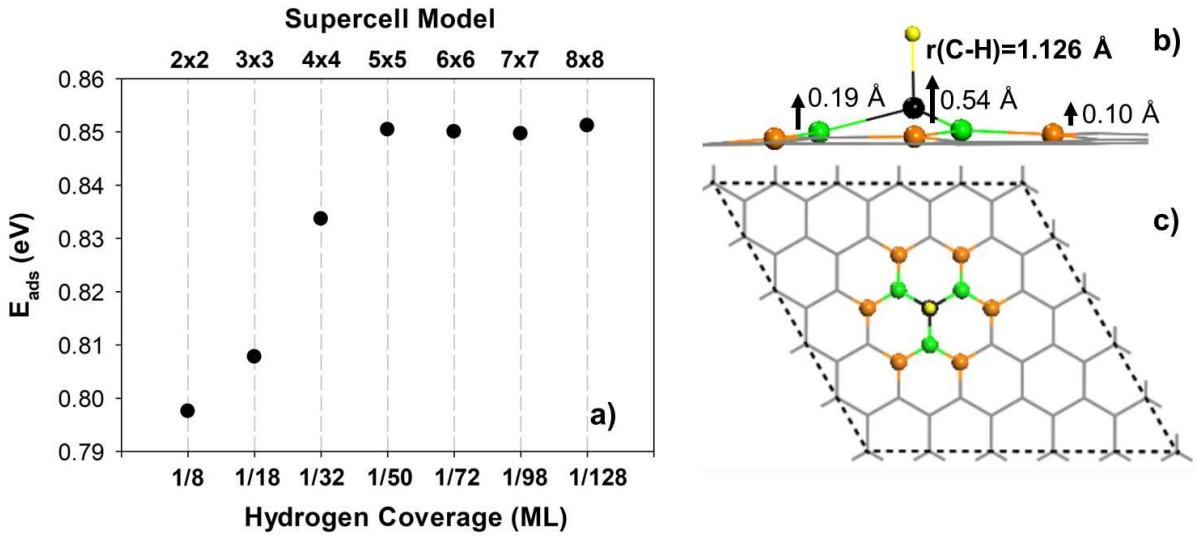

Figure 4.23 The dependence of the H adsorption energy on the surface coverage (a) Variation with coverage of H adsorption energy on graphene at different coverages. The sum of energies of the bare graphene and of an isolated H atom was taken as the reference. Panels (b) and (c) indicate side and top views of the H adsorption configuration on-top a C site in the case of the (5x5) supercell model. In panel b) the upward displacements of the C atom to which the H is bonded (black colored) and its first (represented in green) and second (represented in brown) nearest neighbors are indicated. The H atom is shown with a yellow ball in panels b and c.

From the data in Figure 4.23a, it can be seen that increase in supercell size leads to an increase in adsorption energy for the case of supercells ranging from (2x2) to (5x5) followed by a plateau in adsorption energies for supercells with larger lateral sizes. Based on this dependence it can be concluded that for the case of (5x5) supercell and the larger size supercells investigated,

there is a minimal contribution of lateral interactions to H adsorption. The adsorption energy of 0.85 eV determined in this study for the case of the (5x5) supercell using PBE-D3 functional is comparable but slightly higher than the value of 0.84 eV reported by Casolo *et al*.[262] based on PBE functional without inclusion of long-range dispersion corrections. We also note that in Figure 4.23a the adsorption energy is expressed relative to the energy of the H atom. Positive adsorption energies correspond to stable configurations. For convenience, the same adsorption energy expressed relative to the energy of molecular H_2 (1/2 $E(H_2)$) is provided in Figure B.4. Relative to the sum of energies for the bare graphene molecule and H_2 molecule, the adsorption energy of atomic H on graphene is found to be a negative value, indicating an endothermic character for adsorption relative to the selected reference state.

Details of the binding configuration of the H atom in the (5x5) supercell are shown in Figure 4.23b from which it is seen that H adsorbs on-top of a C atom with a CH bond length of 1.126 Å. Adsorption takes place with sizable upward displacement of the C atom to which the H atom is bound (represented as a black ball in Figure 4.23b as well as its first and second nearest neighbors (shown as green and orange balls in Figure 4.23b and c. For the C atom to which the H atom is bound this displacement is calculated to be of 0.54 Å. A similar displacement of 0.59 Å was reported by Casolo *et al*.[262] for the case of H binding on graphene in a (5x5) supercell.

The second objective of the computational investigations was to determine the dependence of the H adsorption energy on the amount of surface strain. Motivated by the independence of the H adsorption energy on lateral interactions for the case of the (5x5) supercell identified above, we selected this supercell (or supercells with similar sizes as described below) for these calculations. In order to evaluate the variation of the adsorption energy for different levels of tensile strain applied to the graphene lattice two different supercell models have been considered as detailed in

Figure B.5. The first one corresponds to a (5x5) hexagonal supercell with a single H atom adsorbed on-top a carbon site, similar to that depicted in Figure 4.23c. Details of this model, the system of axes used and directions for lattice expansions are provided in Appendix B.3 Figure B.5a. Specifically, a first type of lattice expansion was taken along a zigzag crystallographic direction conveniently chosen to be parallel to the selected Cartesian Ox axis (see Figure B.5a) and hereafter denoted as (Zg,x). The second stretch direction was also taken along a zigzag direction but rotated 60° relative to (Zg,x) and hereafter denoted as (Zg,d) (see Figure B.5a). In our hexagonal supercell setup model having (**u**1,**u**2) as hexagonal unit vectors, lattice elongations along the (Zg,x) direction involve tensile strain applied only along $\mathbf{u}_1$ hexagonal direction while extension of the lattice along (Zg,d) direction involves simultaneous tensile strains of equal sizes along both $\mathbf{u}_1$ and $\mathbf{u}_2$ hexagonal directions. The second model considered (see Figure B.5b) consists of an orthogonal (5x3) supercell with axes parallel to Cartesian Ox and Oy axes and oriented along the zigzag and armchair crystallographic directions, respectively. In this case, the tensile strain was applied only along Oy direction which was taken to be parallel to the armchair crystallographic direction, and hereafter indicated with the (Arm,y) acronym.

A summary of the results corresponding to variation of H adsorption energy on graphene for the case of lattices expanded along (Zg,x), (Arm,y) and (Zg,d) directions is presented in Figure 4.24. Lattice elongations up to 5% are considered. As shown in this Figure 4.24, for each of the three directions considered, stretching the graphene lattice leads to increase in the H adsorption energy. Individual energy changes however were found to depend on the displacement type. Specifically, for (Zg,x) and (Arm,y) displacements which involve elongations only along Cartesian Ox and Oy axes, respectively, the calculated adsorption energy values are practically superimposed and have similar overall variations. In contradistinction, the expansion along (Zg,d)

direction which involves simultaneous stretches of similar sizes along both $\mathbf{u}_1$ and $\mathbf{u}_2$ hexagonal directions leads to larger adsorption energy changes. In fact, it can be seen that adsorption energy for a given displacement along (Zg,d) direction is almost equal to the one along either (Zg,x) or (Arm,y) directions but at a displacement twice as large as the one considered for (Zg,d) direction. These results indicate not only an increase in adsorption energy of H with lattice expansion but they also demonstrate that when involving simultaneous displacements along $\mathbf{u}_1$ and $\mathbf{u}_2$ hexagonal axes, the effect on adsorption energies is practically twice that for single axis displacement (Zg,x) of an equal amount.

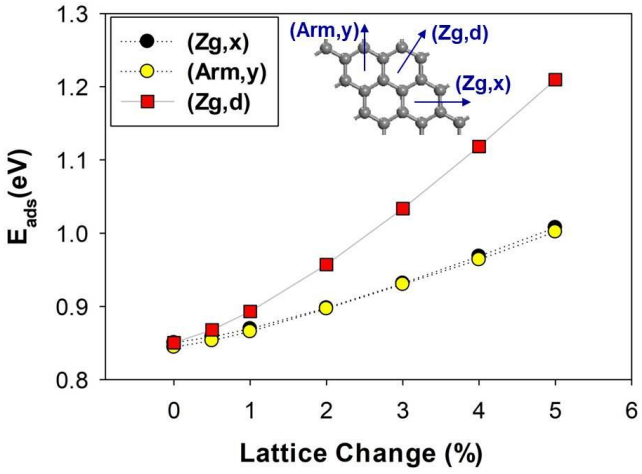

Figure 4.24 Variation of the H adsorption energy on graphene lattice elongation Lattice elongations up to 5% are considered. Three elongations along the zigzag (Zg,x), (Zg,d) and armchair (Arm,y) crystallographic directions are shown in black, red, and yellow markers respectively.

Graphene lattice expansion induces changes not only on the adsorption energy of H but also on its binding distance and vibrational properties. In particular, consistent with the increase in adsorption energy, the H atom is pulled closer to the graphene surface, as can be seen in Figure

B.6a where a systematic decrease in r(C-H) bond distance is observed with increasing amount of lattice stretch. These modifications take place with a corresponding blue shift of the ν(C-H) stretch vibration as shown in Figure B.6b.

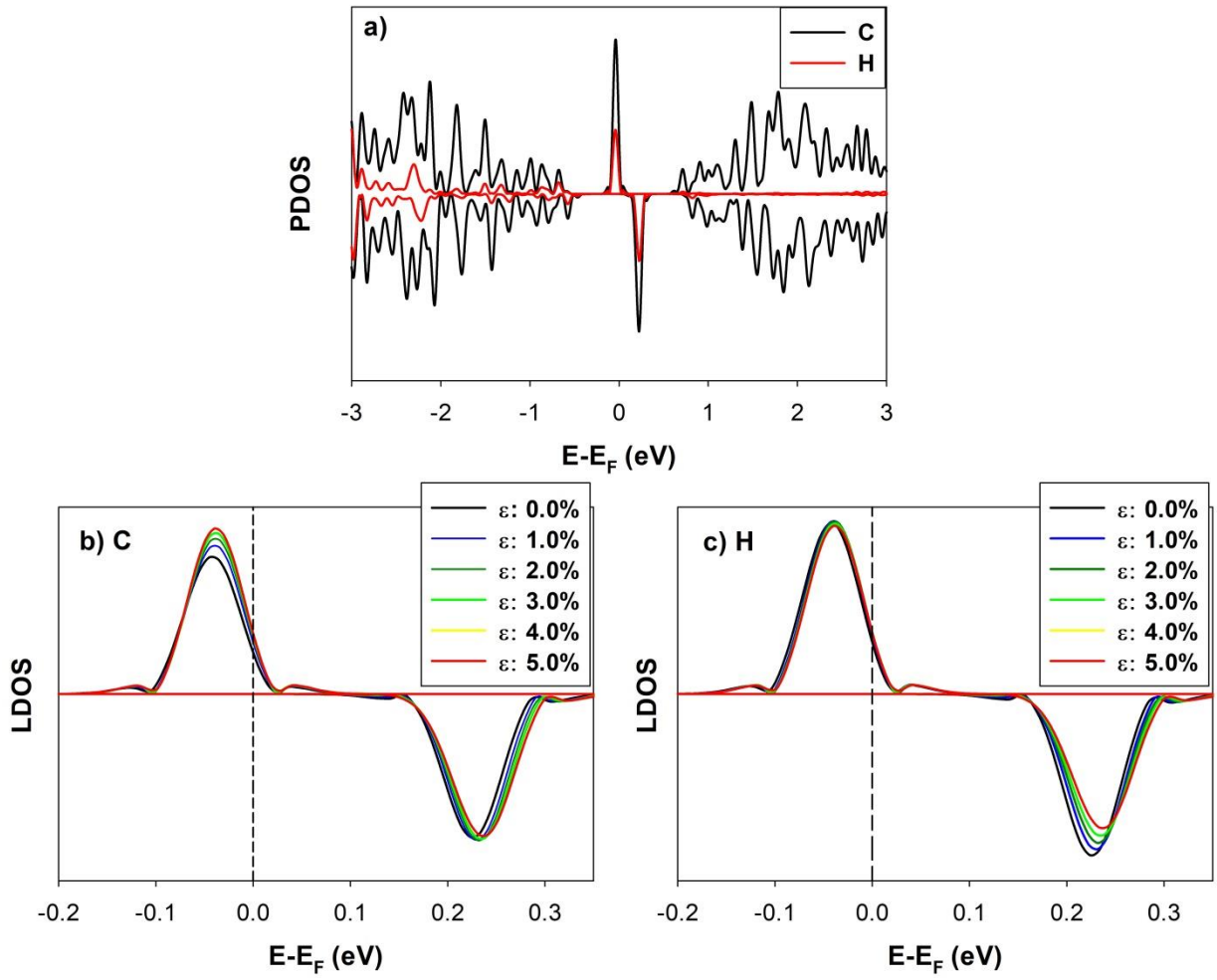

Figure 4.25 Projected density of states (PDOS) of C and H atom (a) PDOS for the graphene C atoms and the adsorbed H atom in the case of un-stretched lattice. Details of the local density of states (LDOS) for the case of the bonding C atom and the H adsorbate as function of the lattice strain (ε) along (Zg,x) direction expressed in percentage form are detailed in panels (b) and (c), respectively.

Additionally, there are also changes in electronic properties of the system. Specifically, as seen in Figure 4.25a upon H adsorption on the graphene surface a new peak is observed in the density of states near the Fermi level originating from hybridization of C (2s) and C(2p) orbitals and associated mixing with H(1s). Stretching of the graphene lattice along (Zg,x) direction leads to an increase in electronic density corresponding to the occupied states of the C atom engaged in the CH bond just below the Fermi level. The electronic property modifications also extend to the work function of the system which increases with amount of lattice deformation (see Figure B.7) as well as the p-band center (ε_p) of the graphene substrate which is shifted closer toward the Fermi level (see Figure B.8), indicating a catalytically more active system.

For the bare graphene surface our measured Raman results from Figure 4.19 showed a red shift of the 2D peak with applied tensile stress. We have performed a similar theoretical analysis of vibrational frequencies shifts for the same range of stress values as determined experimentally. The calculated value of the in-plane D vibration of graphene changes from 1363 cm^{-1} for the unstretched lattice to 1358 cm^{-1} and 1355 cm^{-1} for the lattice stretched by 0.17% and 0.25%, respectively. When scaled by a 0.985 factor recommended for the PBE functional,[263] the second order overtones of these vibrations become 2685.1, 2675.2 and 2669.3 cm^{-1}, respectively These values can be compared with experimental results for the graphene 2D values in Figure 4.19. At zero strain, a very good agreement within 2.9 cm^{-1} is found between the calculated and experimental 2D frequency values. This agreement is maintained upon strain increase, with the calculated frequencies being within 2.3 cm^{-1} of the experimental values of 2673 cm^{-1} at 0.17% and 2667 cm^{-1} at 0.25% tensile strains, respectively.

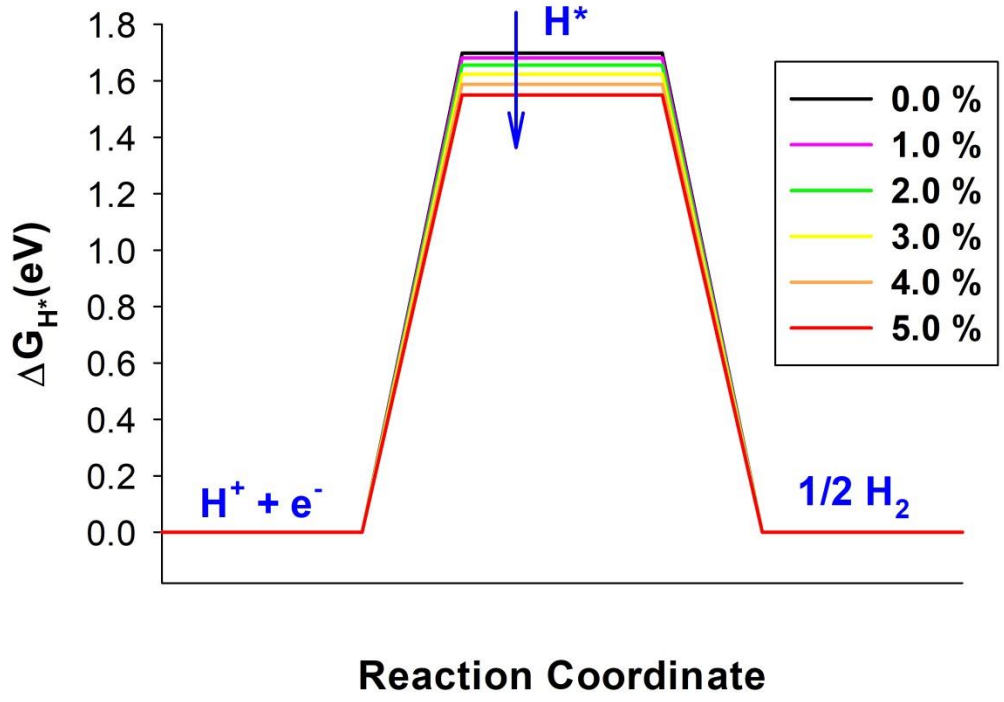

Figure 4.26 Variation of free energy ΔG_{H^*} (eV) The free energy for reaction * + H^+ + e^- ↔ H* on graphene at equilibrium (U=0) and standard conditions under different lattice expansions along (Zg,x) direction.

A final aspect investigated is the influence of the enhanced bonding between H and graphene as a result of tensile strain upon HER. This reaction is generally described by a stepwise mechanism[264] which involves in the initial step a proton-coupled electron transfer reaction (Volmer reaction, see Eq.(4.1)) leading to adsorption of H on the electrocatalyst surface. In a subsequent step, desorption of molecular H_2 takes place via a Heyrovsky reaction (Eq.(4.2)) or a Tafel reaction (Eq.(4.3)). Independent of atomistic details of the mechanism involved, computational evaluation of the thermochemistry for reaction corresponding to atomic hydrogen bonding to the surface has proven to be a useful tool to compare HER activity of different catalysts.[265] In this work we followed a similar procedure and evaluate the free energy (ΔG_{H^*}) for bonding reaction of H on graphene by including the adsorption energy changes (ΔE_H), the

corresponding vibrational zero point energy (ΔZPE), entropic ($T\Delta S_H$) and the integrated heat capacity up to 298 K ($\Delta H_{0\rightarrow 298.15}$) corrections. The list of this set of corrections is detailed in Table B.2. The corresponding calculated free energy diagram for hydrogen evolution on graphene surface under tensile strain is shown in Figure 4.26 for the case of lattice deformations along (Zg,x) direction, while similar results obtained for deformations along (Zg,d) are illustrated in Figure B.9.

Ideal electrocatalysts for the HER reaction should have ΔG_{H^*} values as close as possible to zero. From this perspective, as seen in Figure 4.26, the bare unstretched graphene presents a relatively high and positive ΔG_{H^*} value, indicating a small HER activity. Relevant for the experimental results reported in this work is the fact that computational results in Figure 4.26 and Figure B.10 demonstrate a systematic decrease in ΔG_{H^*} values when graphene lattice is stretched in the range 0-5 %. In particular, when considering the range of small elongations (0-0.25) % along (Zg,x) which encompasses the experimental strain range considered in this work, a fitted dependency of the calculated free energies changes from Table B.2a of the form $\Delta G(\varepsilon)(eV)=1.698621 - 0.001970\ \varepsilon - 0.03000\ \varepsilon^2$ was determined, where ε represents the amount of lattice strain expressed in percentage form. The drop in ΔG_{H^*} values as shown in Figure 4.26 will lead to an increase in HER activity and of the measured current density similar to our experimental findings. The increase in current density can be obtained based on the general relationship between the exchanged current and ΔG_{H^*} value as obtained by Kurapati *et.al.*[264] Following their work, the corresponding change of reaction rate at equilibrium is found to be proportional to $e^{\left(-\frac{\Delta G_{H^*}}{2RT}\right)}$. Based on this expression, one can estimate current density increases of 2.4% and 4.7% for lattice expansions of 0.17%, and 0.25%, respectively. Both of these theoretical estimates compare reasonably well with the measured current density increases determined in this study, which are 1.3 ± 0.2 % and 2.9 ± 0.5 % with 0.17 % and 0.25 % tensile strain, respectively.

Possible reasons for the slight overestimation of the current density increase in calculations relative to the corresponding measured values might be the polycrystalline nature of graphene composed of large flakes in experiments and an anisotropic stress distribution. Stress anisotropy can be due to several factors including the flatness degree of the PET support and functional chemical groups existent on the support which can modify the coupling of PET support and graphene leading to an initial localized stress on graphene or possible slippage or inefficient strain transfer from the substrate. Additionally, the edge effects of graphene flakes and the quality of graphene layer itself can bring their own contributions as different types of surface defects can also modify the local stresses.

4.4 Conclusion

In summary, our combined experimental and computational analysis demonstrates that adsorption energy of H on graphene is enhanced by applying tensile strain which in turn leads to a drop in the associated free energy change corresponding to HER. The calculated variation in ΔG_{H^*} correlates well with the shift in the C p-band center of graphene (see Figure B.10), demonstrating again the usefulness of this descriptor for correlating catalytic activity with electronic structure properties.[266] Furthermore, the good overall agreement between the calculated and measured current density variations with amount of tensile strain support the interpretation that the increase in the H adsorption energy on graphene with stretching is responsible for the observed changes in HER reactivity. Graphene can sustain up to 20% of strain, much larger than the values considered here, without breaking. Thus, strain engineering offers a promising approach to enhance the electrocatalytic activity of carbon-based materials.

Appendix A Supplementary Information on Effect of Electric Field on Graphene Oxidation

Adapted from the Supporting Information of the published work presented in Chapter 3, Kim, M. A.; Qiu, N.; Li, Z.; Huang, Q.; Chai, Z.; Du, S.; Liu, H., Electric Field Effect on the Reactivity of Solid State Materials: The Case of Single Layer Graphene. *Adv. Funct. Mater.* 2020, 30 (13), 1909269.

Appendix A.1 Additional experimental data

Appendix A.1.1 Effect of back gating after 1 hour oxidation of graphene

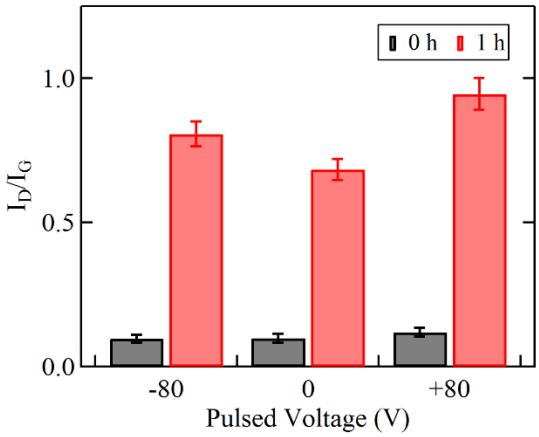

Figure A.1 The I(D)/I(G) value comparison after the 1h oxidation The average I(D)/I(G).after 1 h of laser induced oxidation under different gate voltage conditions. Each V_{gb} level, 0 V, +80 V, and -80 V was repeated four times to find the average and a standard deviation of I(D)/I(G).

The 1 h oxidation comparison with and without an applied gate voltage was reproduced using separate graphene sample. Experimental conditions were kept same. Figure A.1 shows results similar to Figure 3.4b in the main text. The I(D)/I(G) after 1 h of oxidation was larger with ±80 V of back gating which shows an increased progress of the oxidation compared to the oxidation without applied electric field (0 V).

Appendix A.1.2 The effect of back gating on I(D)/I(G)

The charge doping has significant effects on the Raman fingerprint of graphene. The width of G peak and the intensity of D peak change with the charge density of graphene,[121, 122, 126] which could potentially alter the integrated intensity ratio used in this study.

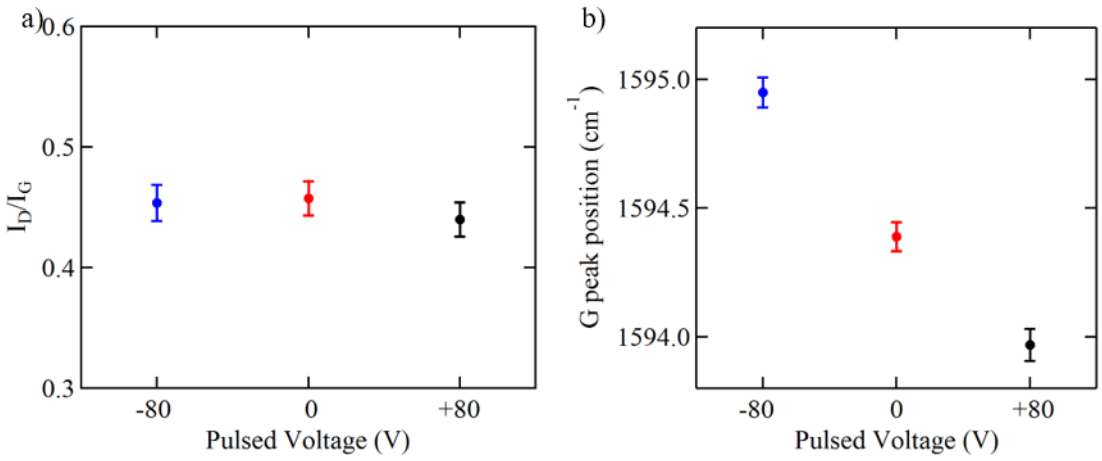

Figure A.2 The waveform gate voltage effect on Raman spectroscopy Raman spectrum were collected on a oxidized graphene with low laser power (<1 mW) to prevent further laser induced oxidation. a) comparison of I_D/I_G and b) G peak position under -80 V (blue), 0 V (red), and +80 V (black) pulsed gate voltages (t_{on} = t_{off} = 0.25 s).

To rule out this possibility, the effect of gate voltage modulation was compared on the oxidized location in order to confirm the consistency of I(D)/I(G). First, graphene sample was oxidized under laser irradiation (~ 12 mW) for 1.5 h. After the oxidation, Raman spectrums were obtained on the same location of the graphene sample while applying pulsed gate voltages, 0 V, +80 V and -80 V. The laser power was kept low (< 1 mW) to prevent any additional thermal oxidation induced by the laser. I(D)/I(G) were consistent between all conditions, with and without the pulsed gate voltages, showing electrical modulation used in the study does not alter the results on I(D)/I(G) values (Figure A.2a). On the other hand, the G peak shows the expected effect of electrical doping as the peak position shifts with the applied square waveform gate voltage (Figure A.2b).

Appendix A.1.3 Laser absorbance test under back gating

The optical absorption of solid can be affected by an electric field due to the relationship between absorption coefficient and dielectric constant, a phenomenon known as the Franz-Keldysh effect. The change in the light absorbance could increase/decrease the resulting temperature of irradiated graphene sample area and alter the oxidation results.

We found that the electric field we used does not impact the optical adsorption of graphene. To demonstrate this fact, we measured the absolute intensity of reflected laser light by the graphene samples. The light source was the same laser used in the study. Figure A.3 shows the raw intensity counts of reflected 532 nm laser with 2 s of integration time. The change in the reflected light spectrums did not show any dependency on the electrical modulation used in the study. The observed fluctuation throughout the spectrums can be attributed to the fluctuation of incident light source.

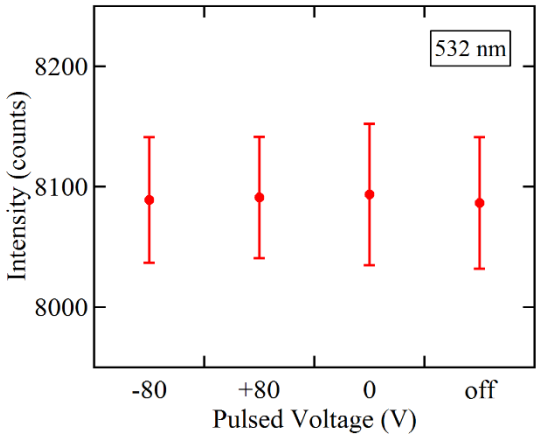

Figure A.3 The waveform gate voltage effect on the laser absorbance The reflected laser (532 nm) intensity counts under square-waveform back gating (t_{on} = t_{off} = 0.25 s). Each spectrum was obtained with 2 s exposure time. The change in the reflectance is ca.1%.

Appendix A.1.4 The effect of Joule heating

The resistive heating from the electrical modulation used in this study could be the additional heat source of the thermal oxidation. However, unoxidized area of graphene outside the laser focus suggests that the additional heat from Joule heating is not significant enough to induce the graphene oxidation itself. Capacitive current measured throughout the experiment was < 100 nA. We estimate the average temperature change on our typical graphene/SiO_2/Si sample using the thermal resistance of our device R_t :[267]

$$\Delta T = PR \approx PR_t$$

$$R_t = R_B + R_{OX} + R_{Si}$$

$$R_B = \frac{1}{hA} \ , \qquad R_{OX} = \frac{t_{OX}}{\kappa_{OX} A} \ , \qquad R_{Si} = \frac{1}{2\kappa_{Si} A^{1/2}}$$

With the thermal conductance of graphene and SiO_2 boundary h = 10^8 $W \cdot m^{-2} \cdot K^{-1}$,[268] the thermal conductance of SiO_2 and Si wafer (R_{OX} and R_{Si} respectively), and the area of graphene A, the thermal resistance of graphene on 300 nm SiO_2/Si wafer was estimated to be in order of 10^{-1} $K \cdot W^{-1}$. Assuming average current of 100 nA at 100 V, the temperature change of our graphene/SiO_2/Si sample due to Joule heating is in order of 10^{-6} K.

Appendix A.1.5 Additional data on the effect of magnitude of back-gating on the oxidation kinetics

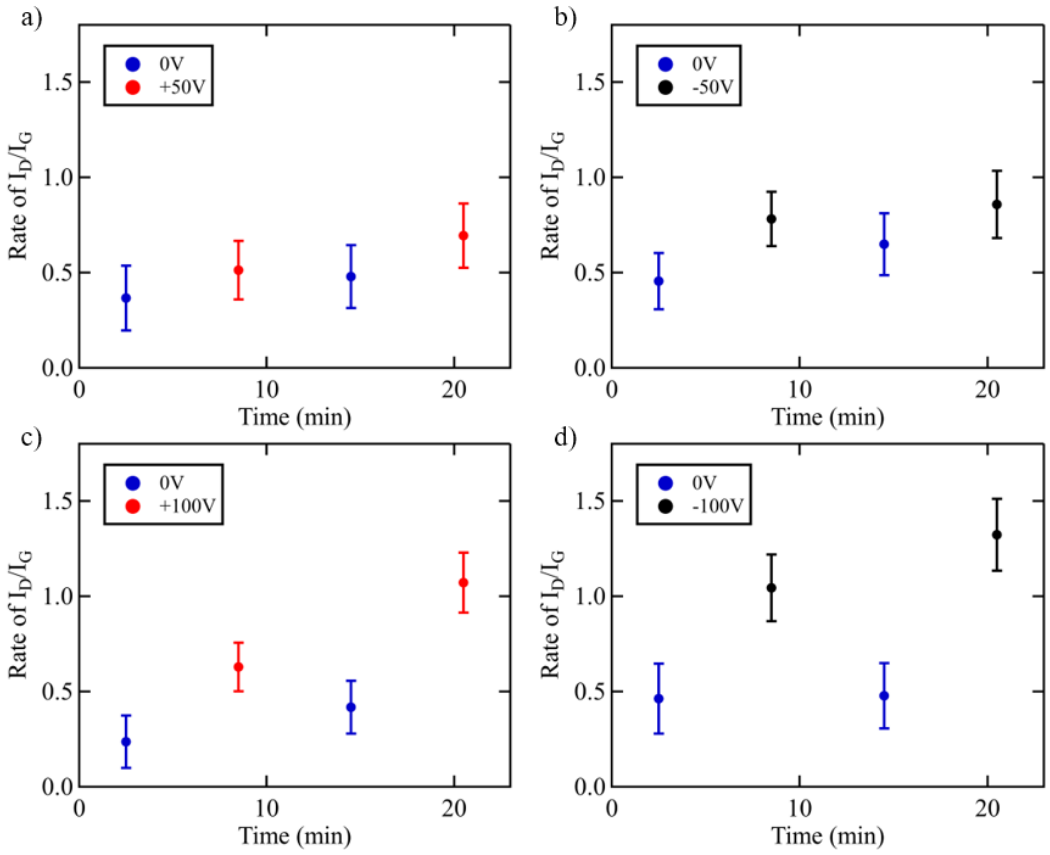

Figure A.4 The change in the oxidation kinetic of graphene with various back gate voltage magnitudes The back gating level was changed every 5 min during the oxidations (t_{on} = t_{off} = 0.5 s). The effect of gate voltage was compared between a,b) 0 V and ±50 V, and c,d) 0 V and ± 100 V.

Appendix A.1.6 Effect of frequency of the back-gate

To understand the effect of back gate frequency on the oxidation, we probed the true electric field experienced by the graphene during oxidation. To do so, we eliminate the oxidation reaction induced by laser and monitored the shift of G peak as a function of time after a constant (non-waveform) gate voltage was applied to graphene (Figure A.5a). The laser source was kept low (<1 mW) throughout the experiment. Both electron and hole doping shift the G peak to higher wavenumbers thus from the shift of G peak, one can probe the charge doping level of graphene, which is directly related to the electric field it experiences.[121, 122]

Our graphene sample is naturally hole-doped due to the surface interactions of graphene and air adsorbates/substrate.[122, 269] Upon applying a negative gate voltage, the electric field will further inject holes into graphene, thus shifting the G peak to even higher wavenumbers, which was indeed observed. However, the G peak shifts back to its original position within 20 s – 30 s, even under the applied gate voltage. Upon switching off the gate bias, another shift in the G peak position was observed, this time in the opposite direction, followed by a gradual shift to the steady state position. Similar behaviors were observed when a positive gate voltage was applied and switched off. These observations can be attributed to the charge trapping/de-trapping near the graphene-SiO_2 interface as discussed in detail in chapter 2. The trapped charge produces an electric field that counters the effect of back gating. This effect has been extensively studied due to its contribution to the gating hysteresis of graphene field effect transistors.[161, 162] Our data shows that the electric field experienced by graphene is transient, with a half-life of 10 s – 20 s in our experiments.

With these control experiments, the effect of waveform frequency can be understood. The graphene sample only experiences high doping level during the transitions of the square wave.

Therefore, increasing the frequency of the square wave gate voltage increases effective gating efficiency experienced by graphene. Accordingly, we found that under constant DC gating, there was no obvious trend in the change of I(D)/I(G) after 1 h of photothermal oxidation (Figure A.5b). It should be noted that due to the frequent failure of graphene samples owing to dielectric breakdown induced by the steady voltage, larger number of samples were used which increased the variability of graphene surface being studied.

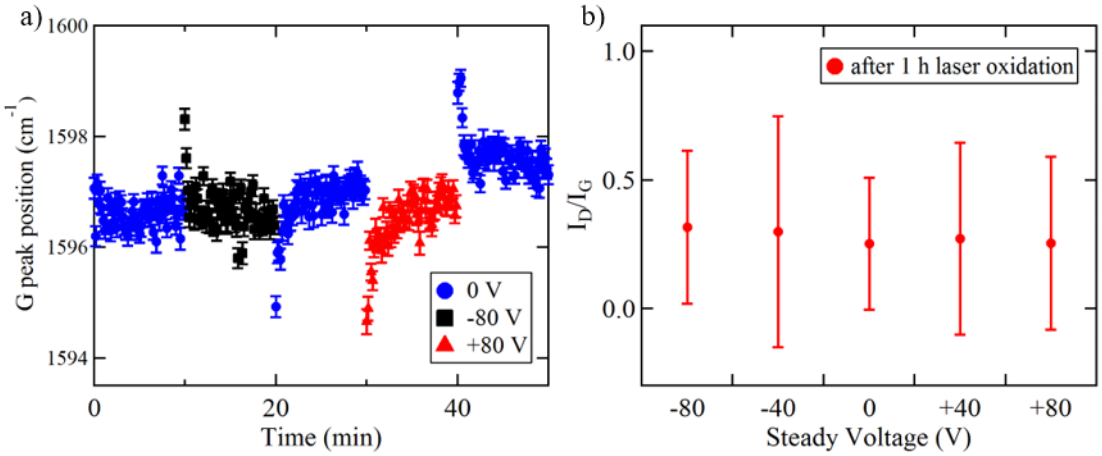

Figure A.5 The effects of static electric field on the graphene and its oxidation a) The G peak position of graphene in air as a function of time. Each back gate voltage (0 V, -80 V, and +80 V) were applied for 10 min. Raman spectrum was obtained with low laser power (<1 mW) to prevent the oxidation. b) The diminished photothermal oxidation enhancement effect under the constant back gating.

Appendix A.1.7 Contribution of electrochemical based reactions

Various reactive species can be formed under high electric field which could potentially react with graphene and contribute to the additional oxidation of graphene. For example, decomposition of CO_2 had been demonstrated using non-thermal plasma; highly reactive radicals

produced under high voltage allow thermodynamically unfavorable reaction in ambient conditions.[270] When the electrical modulation used in this study was applied without laser, the defect density of graphene remained same. As shown in Figure A.6, change in I(D) was negligible after electrical modulation when the photothermal oxidation was avoided. This stability of graphene suggests the increased oxidation reaction rate we observed in this study was not due to the electrochemically triggered mechanism at ambient condition. In addition, the enhancement effect was significant only under high frequency square wave, which minimizes the accumulation of trapped species at the interface between graphene and dielectric substrate. We did not observe clear electric modulation effect under DC voltage, which is expected to favor accumulation of trapped species at graphene-dielectric interface. These results suggest that the oxidation was not modulated by certain reactive species or trapped species produced by the electric field.

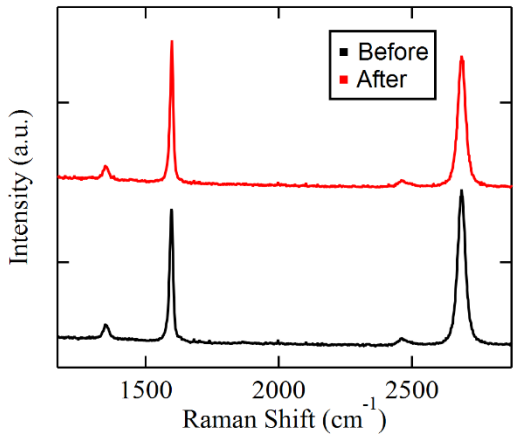

Figure A.6 The effect of square waveform modulation on graphene Raman spectra were obtained before and after the 2 h of back gating (±80 V, $t_{on} = t_{off} = 0.5$ s) on the same location. Laser power was kept low (<0.5 mW) to prevent the photothermal heating of graphene.

Appendix A.2 Density functional theory (DFT) calculation

All calculations were performed with DMol^3 package[271, 272] using spin-polarized density functional theory (DFT) and linear combination of atomic orbitals, which could provide more accurate results of the effects of the charging and external electric field on graphene than those of plane wave basis sets.[273] The generalized gradient approximation (GGA) with Perdew, Burke and Ernzerhof (PBE) functional was employed as the exchange-correlation functional.[260] The effect of long-range van der Waals (vdW) interactions based on the PBE method was included explicitly by using the empirical correction scheme of Grimme.[274] The double numerical plus polarization function was chosen for the basis set, and the real-space global orbital cutoff radius was set as high as 4.6 Å in the calculations. During the structural optimization, the convergence criteria in energy, force, and displacement were set to be 10^{-5} Ha (1 Ha=627.51 kcal/mol), 0.002 Ha/Å, and 0.005 Å, respectively. Linear synchronous transit/quadratic synchronous transit (LST/QST) method[275] was used to search the transition state (TS) geometries and nudged elastic band (NEB) method[276] was also performed to confirm the transition states connecting the relevant reactants and products. Periodic boundary conditions with a supercell of topological defected graphene with 126 carbon atoms placed along *x* and *y* directions were chosen in the calculations. The vacuum layer thickness of 16.0 Å was considered to avoid the image interactions. The Brillouin zone integrations were performed with Monkhorst-Pack scheme and a 3 × 3 × 1 *k*-point sampling for the geometric optimizations and a 6 × 6 × 1 *k*-point were used to calculate the electronic properties. The external electric field was applied along the *z* direction, which is taken as positive if it is parallel to *z*-axis and vice versa.

The adsorption energy of oxygen molecules adsorbed on topological defected graphene was defined as the following equation, where $E_{dGr+nO2}$, E_{dGr} and E_{O2} are the total energies of the

O_2-adsorbed topological defected graphene, the isolated topological defected graphene and an O_2 molecule, respectively.

$$E_{ad} = \left(E_{dGr+nO_2} - \left(E_{dGr} + nE_{O_2}\right)\right)\Big/ n$$

Appendix A.3 Micro kinetic model for O_2 oxidation on graphene

a) The most favorable reaction pathway for oxidation of the first O_2 molecule on graphene which is shown in Figure 3.9b and Figure A.7 is modelled as the following processes:

1. O_2 + *d*Gr $\underset{k_{-1}}{\overset{k_1}{\longleftrightarrow}}$ IS1-I
2. IS1-I $\underset{k_{-2}}{\overset{k_2}{\longleftrightarrow}}$ MS1-I
3. MS1-I $\xrightarrow{k_3}$ P6

The adsorption of the first O_2 molecule on graphene, Reaction 1 (see Table A.2 for the numbering of the reactions), is assumed to be in equilibrium as

$$k_1 p\left(\mathrm{O}_2\right)\theta_{d\mathrm{Gr}} = k_{-1}\theta_{\mathrm{IS1\text{-}I}}$$

$$\theta_{\mathrm{IS1\text{-}I}} = \frac{k_1}{k_{-1}} p\left(\mathrm{O}_2\right)\theta_{d\mathrm{Gr}} = K_1 p\left(\mathrm{O}_2\right)\theta_{d\mathrm{Gr}}$$

where

$$K_1 = \exp\left(-\frac{\Delta G_1}{k_B T}\right) = \exp\left(\frac{-\left(\Delta E_1 - T\Delta S_{\mathrm{O}_2}\right)}{k_B T}\right)$$

θ_i is the fraction of graphene substrate *i* in all graphene substrates, ΔE_1 is the adsorption energy of O_2 on graphene, ΔS_{O2} represents the entropy change involved in O_2 adsorption and is equal to -221.32 J/(mol·K) at 513 K.

For Reaction 2 and Reaction 3, the rate constants k_2, k_{-2} and k_3 can be calculated based on transition state theory as the following:

$$k_2 = \frac{k_B T}{h} \exp\left(\frac{-\Delta G_2^{\neq}}{k_B T}\right) = \frac{k_B T}{h} \exp\left(\frac{-\left(E_{a,2} - T\Delta S_2^{\neq}\right)}{k_B T}\right)$$

$$k_{-2} = \frac{k_B T}{h} \exp\left(\frac{-\Delta G_{-2}^{\neq}}{k_B T}\right) = \frac{k_B T}{h} \exp\left(\frac{-\left(E_{a,-2} - T\Delta S_{-2}^{\neq}\right)}{k_B T}\right)$$

and

$$k_3 = \frac{k_B T}{h} \exp\left(\frac{-\Delta G_3^{\neq}}{k_B T}\right) = \frac{k_B T}{h} \exp\left(\frac{-\left(E_{a,3} - T\Delta S_3^{\neq}\right)}{k_B T}\right)$$

$E_{a,2}$, $E_{a,-2}$ and $E_{a,2}$ are the activation energies of the forward and reverse reaction of Reaction 2 and Reaction 3, contribution from $\Delta S^{\neq}_2$, $\Delta S^{\neq}_{-2}$ and $\Delta S^{\neq}_3$ are neglected as they are almost 0.

Next, the fraction of MS1-I is calculated by the steady state approximation:

$$\frac{d\theta_{\text{MS1-I}}}{dt} = k_2\theta_{\text{IS1-I}} - k_{-2}\theta_{\text{MS1-I}} - k_3\theta_{\text{MS1-I}} = 0$$

$$\theta_{\text{MS1-I}} = \frac{k_2}{k_{-2} + k_3}\theta_{\text{IS1-I}} = \frac{k_2}{k_{-2} + k_3} K_1 p\left(\text{O}_2\right)\theta_{d\text{Gr}}$$

The sum of fraction of *d*Gr, IS1-I, MS1-I and P6 should be equal to 1. Then, θ_{P6} can be derived from θ_{dGr}:

$$\theta_{d\text{Gr}} + \theta_{\text{IS1-I}} + \theta_{\text{MS1-I}} + \theta_{\text{P6}} = 1$$

$$\theta_{\text{P6}} = 1 - \frac{k_{-2} + k_3 + \left(k_2 + k_3 + k_{-2}\right) K_1 p\left(\text{O}_2\right)}{k_{-2} + k_3}\theta_{d\text{Gr}}$$

The formation rate of ether P6 can be calculated at the conditions of T = 513 K and $P(O_2)$ = 0.21 bar as the following:

$$r_{\mathrm{P6}} = \frac{d\theta_{\mathrm{P6}}}{dt} = k_3\theta_{\mathrm{MS1\text{-}I}} = \frac{k_2k_3}{k_{-2}+k_3}K_1p\left(\mathrm{O}_2\right)\theta_{d\mathrm{Gr}}$$

$$\theta_{d\mathrm{Gr}} = \exp\left(-\frac{k_2k_3K_1p\left(\mathrm{O}_2\right)}{k_{-2}+k_3+\left(k_2+k_3+k_{-2}\right)K_1p\left(\mathrm{O}_2\right)}t\right)$$

$r_{\mathrm{P6}} = 0.0208\exp\left(-0.0208t\right)\ \ s^{-1}$ when F = 0 V/nm;

$r_{\mathrm{P6}} = 0.0416\exp\left(-0.0416t\right)\ \ s^{-1}$ when F = 0.514 V/nm;

$r_{\mathrm{P6}} = 0.107\exp\left(-0.107t\right)\ \ s^{-1}$ when F = -0.514 V/nm.

and the maximum formation rate of P6 can be obtain when t = 0s:

$r_{\mathrm{P6,max}} = 0.0208\ s^{-1}$ when F = 0 V/nm;

$r_{\mathrm{P6,max}} = 0.0416\ s^{-1}$ when F = 0.514 V/nm;

$r_{\mathrm{P6,max}} = 0.107\ s^{-1}$ when F = -0.514 V/nm;

Therefore, the apparent rate constant for the formation of P6 can be obtained at T = 513 K and $P(\mathrm{O}_2)$ = 0.21bar:

$k_{a,\mathrm{P6}} = \frac{k_2k_3}{k_{-2}+k_3}K_1 = 0.0989\ s^{-1}$ when F = 0 V/nm;

$k_{a,\mathrm{P6}} = 0.198\ s^{-1}$ when F = 0.514 V/nm;

$k_{a,\mathrm{P6}} = 0.511\ s^{-1}$ when F = -0.514 V/nm.

b) The most favorable reaction pathway for the reaction of the second O_2 molecule on graphene which is shown in Figure 3.9c and Figure A.9 is modelled as the following steps:

4. P6 + O_2 $\xleftrightarrow[k_{-4}]{k_4}$ IS-6IIa
5. IS-6IIa $\xleftrightarrow[k_{-5}]{k_5}$ MS1-6IIa
6. MS1-6IIa $\xleftrightarrow[k_{-6}]{k_6}$ MS2-6IIa
7. MS2-6IIa $\xrightarrow{k_7}$ MS3-6IIa + CO_2
8. MS3-6IIa $\xrightarrow{k_8}$ FS1-6IIa + CO_2

Here, the Reaction 4 is in kinetic equilibrium as

$$k_4 p(\mathrm{O_2})\theta_{\mathrm{P6}} = k_{-4}\theta_{\mathrm{IS\text{-}6IIa}}$$

$$\theta_{\mathrm{IS\text{-}6IIa}} = K_4 p(\mathrm{O_2})\theta_{\mathrm{P6}}$$

$$K_4 = \exp\left(\frac{-\Delta G_4}{k_B T}\right) = \exp\left(\frac{-\left(\Delta E_4 - T\Delta S_{\mathrm{O_2}}\right)}{k_B T}\right)$$

where ΔE_4 is the adsorption energy of the second O_2 adsorbed on P6 and ΔS_{O2} represents the entropy change involved in the second O_2 adsorption.

For Reactions 5-8, the rate constants k_i can be obtained from equation below:

$$k_i = \frac{k_B T}{h}\exp\left(\frac{-\Delta G_i^{\neq}}{k_B T}\right) = \frac{k_B T}{h}\exp\left(\frac{-\left(E_{a,i} - T\Delta S_i^{\neq}\right)}{k_B T}\right)$$

where $E_{a,i}$ are the activation energies of the forward and reverse reactions of Reaction i, $\Delta S^{\neq}_i$ are almost equal to 0.

By applying the steady state approximation, the fractions of intermediates MS1-6IIa and MS2-6IIa can be calculated:

$$\frac{d\theta_{\mathrm{MS1\text{-}6IIa}}}{dt} = k_5\theta_{\mathrm{IS\text{-}6IIa}} - k_{-5}\theta_{\mathrm{MS1\text{-}6IIa}} - k_6\theta_{\mathrm{MS1\text{-}6IIa}} + k_{-6}\theta_{\mathrm{MS2\text{-}6IIa}} = 0$$

$$\frac{d\theta_{\mathrm{MS2\text{-}6IIa}}}{dt} = k_6\theta_{\mathrm{MS1\text{-}6IIa}} - k_{-6}\theta_{\mathrm{MS2\text{-}6IIa}} - k_7\theta_{\mathrm{MS2\text{-}6IIa}} = 0$$

$$\theta_{\text{MS1-6IIa}} = \frac{k_5\left(k_7 + k_{-6}\right)}{k_{-5}k_7 + k_{-5}k_{-6} + k_6k_7}\theta_{\text{IS-6IIa}} = \frac{k_5\left(k_7 + k_{-6}\right)}{k_{-5}k_7 + k_{-5}k_{-6} + k_6k_7}K_4 p\left(\text{O}_2\right)\theta_{\text{P6}}$$

$$\theta_{\text{MS2-6IIa}} = \frac{k_5k_6}{k_{-5}k_7 + k_{-5}k_{-6} + k_6k_7}\theta_{\text{IS-6IIa}} = \frac{k_5k_6}{k_{-5}k_7 + k_{-5}k_{-6} + k_6k_7}K_4 p\left(\text{O}_2\right)\theta_{\text{P6}}$$

The formation rate of the first CO_2 molecule can be calculated as the following:

$$r_{\text{CO}_2,1} = \frac{d\theta_{\text{MS3-6IIa}}}{dt} = -k_8\theta_{\text{MS3-6IIa}} + k_7\theta_{\text{MS2-6IIa}}$$

$$\theta_{\text{MS3-6IIa}} = \frac{C}{k_8\left(k_8 - B\right)}\left(k_8 - B - Ak_8\exp\left(-Bt\right) + \left(Ak_8 - k_8 + B\right)\exp\left(-k_8t\right)\right)$$

where

$$A = \frac{k_{-2} + k_3 + \left(k_2 + k_3 + k_{-2}\right)K_1 p\left(\text{O}_2\right)}{k_{-2} + k_3}$$

$$B = \frac{k_2k_3K_1 p\left(\text{O}_2\right)}{k_{-2} + k_3 + \left(k_2 + k_3 + k_{-2}\right)K_1 p\left(\text{O}_2\right)}$$

$$C = \frac{k_5k_6k_7}{k_{-5}k_7 + k_{-5}k_{-6} + k_6k_7}K_4 p\left(\text{O}_2\right)$$

Then, we can obtain the formation rate of the first and second CO_2 molecules:

$$r_{\text{CO}_2,1} = \frac{ABC}{k_8 - B}\exp\left(-Bt\right) - \frac{C\left(Ak_8 - k_8 + B\right)}{k_8 - B}\exp\left(-k_8t\right)$$

$$r_{\text{CO}_2,2} = \frac{d\theta_{\text{FS1-6IIa}}}{dt} = k_8\theta_{\text{MS3-6IIa}}$$

$$r_{\text{CO}_2,2} = C - \frac{ACk_8}{k_8 - B}\exp\left(-Bt\right) + \frac{C\left(Ak_8 - k_8 + B\right)}{k_8 - B}\exp\left(-k_8t\right)$$

Therefore, the overall formation rate of CO_2 molecules can be calculated at the conditions of T=513 K and $P(O_2)$=0.21bar:

$$r_{\text{CO}_2,\text{s}} = r_{\text{CO}_2,1} + r_{\text{CO}_2,2} = C - AC\exp\left(-Bt\right) = C\theta_{\text{P6}} = \frac{k_5k_6k_7}{k_{-5}k_7 + k_{-5}k_{-6} + k_6k_7}K_4 p\left(\text{O}_2\right)\theta_{\text{P6}}$$

$$r_{CO_2,s} = \frac{k_5 k_6 k_7}{k_{-5}k_7 + k_{-5}k_{-6} + k_6 k_7} K_4 p(O_2)\left(1 - \frac{k_{-2} + k_3 + (k_2 + k_3 + k_{-2}) K_1 p(O_2)}{k_{-2} + k_3}\theta_{dGr}\right)$$

$r_{CO_2,s} = 5.10\times10^{-3} - 5.10\times10^{-3}\exp(-0.0208t)\ \ s^{-1}$ when F = 0 V/nm;

$r_{CO_2,s} = 6.43\times10^{-3} - 6.43\times10^{-3}\exp(-0.0416t)\ \ s^{-1}$ when F = 0.514 V/nm;

$r_{CO_2,s} = 0.0128 - 0.0128\exp(-0.107t)\ \ s^{-1}$ when F = -0.514 V/nm.

and the maximum formation rate of CO_2 can be obtain when $t\rightarrow\infty$:

$r_{CO_2,s,max} = 5.10\times10^{-3}\ s^{-1}$ when F = 0 V/nm;

$r_{CO_2,s,max} = 6.43\times10^{-3}\ s^{-1}$ when F = 0.514 V/nm;

$r_{CO_2,s,max} = 0.0128\ s^{-1}$ when F = -0.514 V/nm.

The apparent rate constant for the CO_2 formation based on P6 can be obtained at T = 513 K and $P(O_2)$ = 0.21bar:

$$k_{a,CO_2,s} = \frac{k_5 k_6 k_7}{k_{-5}k_7 + k_{-5}k_{-6} + k_6 k_7} K_4$$

Because of $k_6 >> k_{-6}$ and $k_6 >> k_{-5}$,

$k_{a,CO_2,s} \approx k_5 K_4 = 0.0243\ s^{-1}$ when F = 0 V/nm;

$k_{a,CO_2} = 0.0306\ s^{-1}$ when F = 0.514 V/nm;

$k_{a,CO_2} = 0.0611\ s^{-1}$ when F = -0.514 V/nm.

In other words, the formation of CO_2 based on P6 is governed by the Reactions 4 and 5.

Appendix A.4 Additional reaction pathways surveyed by DFT calculations

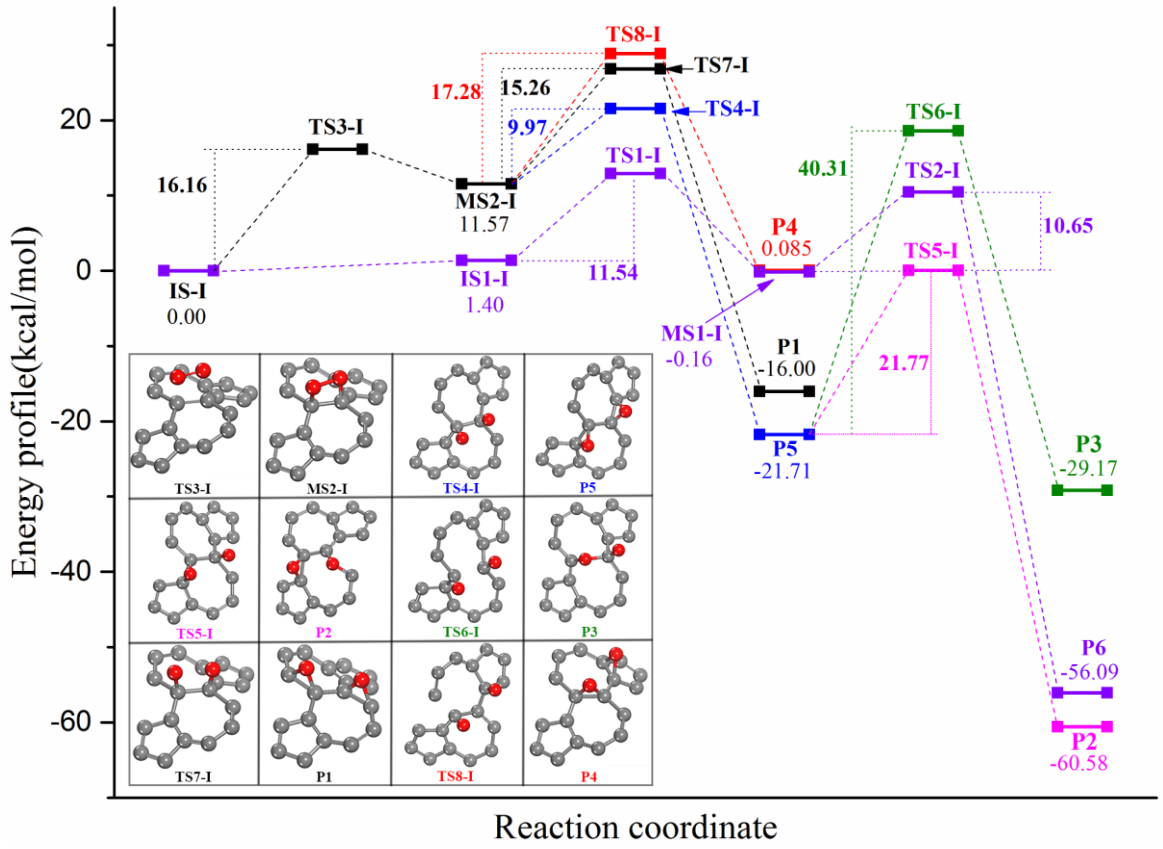

Figure A.7 Three alternative reaction pathways Reaction pathways for the reaction of the 126-atom fragment of graphene with one O_2 to produce P2 or P3. The reaction pathway that produces P6 is also shown for comparison.

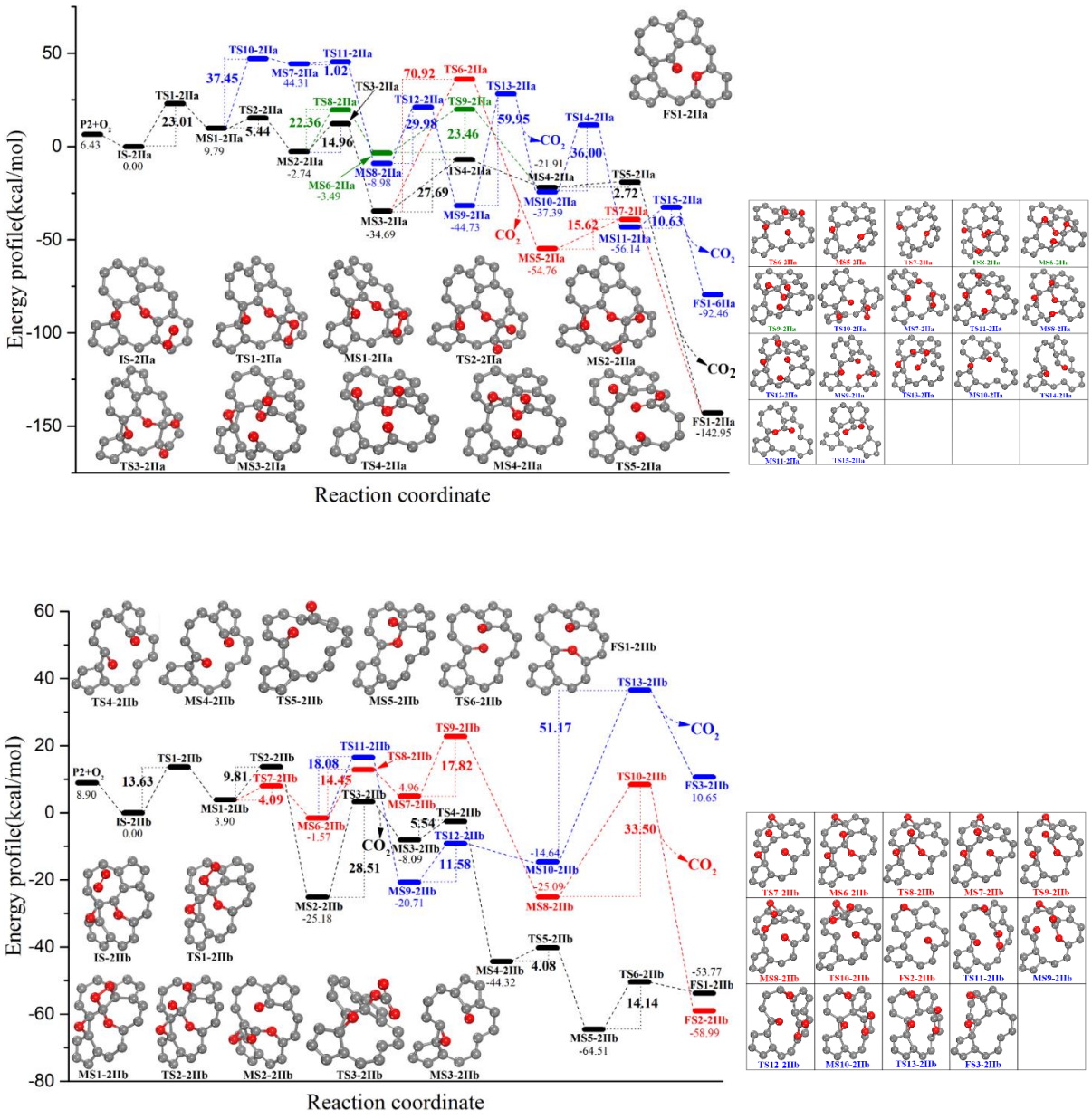

Figure A.8 Seven possible reaction pathways of P2 reacting with the second O_2 The O_2 attacks the carbon bond to the right (Top panel) or the top (Bottom panel) of the ether group in P2.

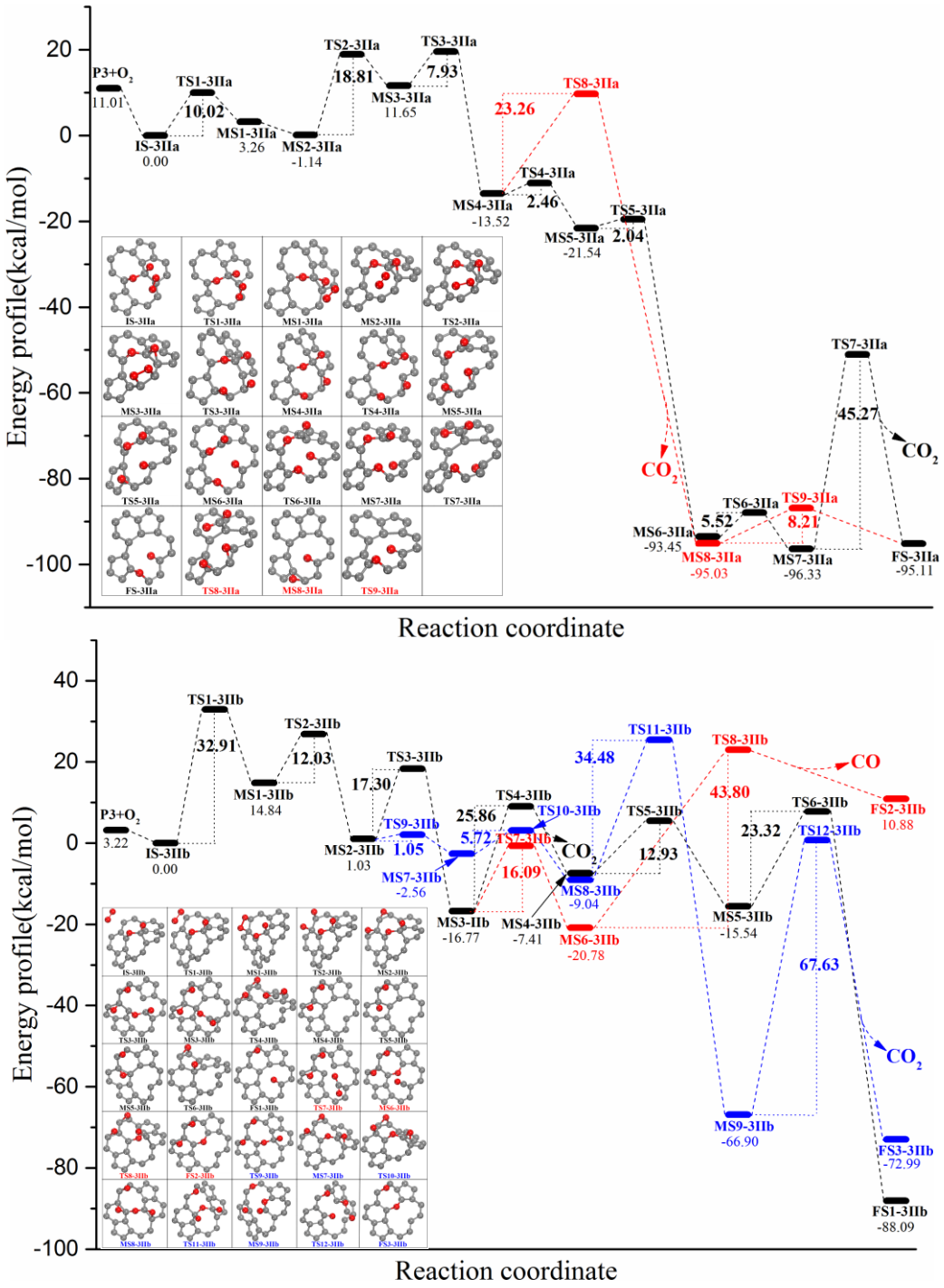

Figure A.9 Five possible reaction pathways of P3 reacting with the second O_2 The O_2 attacks the carbon bond to the right (Top panel) or the left (Bottom panel) of the ether group in P3.

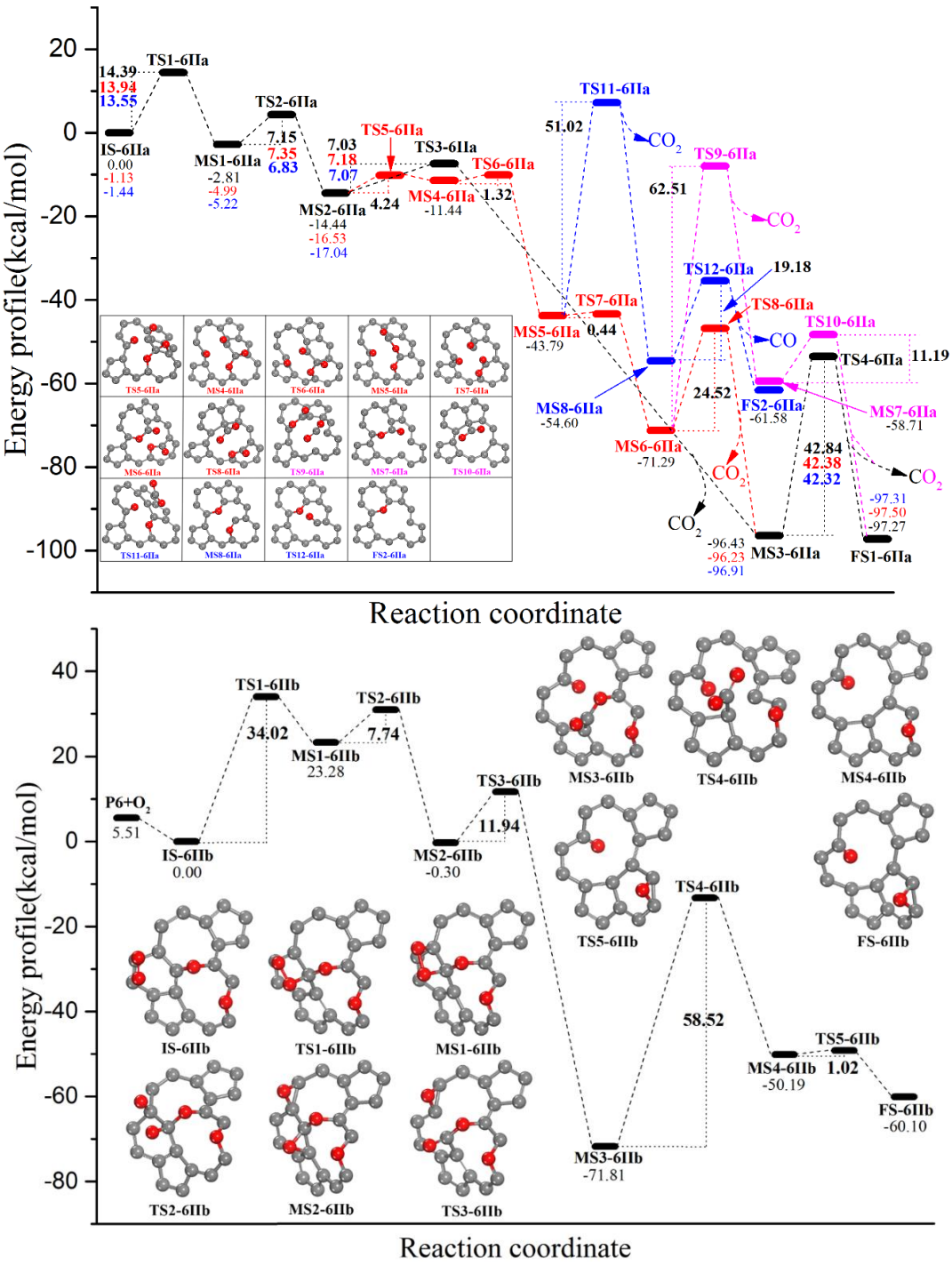

Figure A.10 Four other reaction pathways of P6 reacting with the second O_2 Here, the second O_2 attacks the carbon atoms on the right (Top panel) or left (Bottom panel) side of the ether groups in P6. The black colored reaction pathway that produces FS1-6IIa is also shown on the top panel for comparison.

Table A.1 O-O bond lengths (l_{O-O} (Å)) and mulliken atomic charges (Q_{O2} (*e*)) The transition states IS-I, IS1-I (Figure 3.9b) and IS-6IIa (Figure 3.9c) in the presence of electric fields (V/nm).

		F=+0.514	*F*=0	*F*=-0.514
IS-I	l_{O-O}	1.248	1.250	1.252
	Q_{O2}	-0.138	-0.154	-0.170
IS1-I	l_{O-O}	1.246	1.248	1.251
	Q_{O2}	-0.136	-0.154	-0.170
IS-6IIa	l_{O-O}	1.247	1.248	1.249
	Q_{O2}	-0.142	-0.150	-0.159

Appendix A.5 Effect of electric field on the transition states

Figure A.11 shows the electronic local density of states projected onto O atoms of O_2 molecule and the C atoms which will react with the O atoms to form the peroxide-containing intermediates in transition states TS1-I (a) and TS1-6IIa (b) under applied electric fields. As shown in Figure A.11 and Figure A.12, the O_2 molecule reacted with graphene mainly from the interaction between C P_z states and O_2 $1\pi_u$ and $1\pi_g^*$ states. In the presence of a negative/positive electric field, it is clear that the O_2 $1\pi_g^*$orbitals near the Fermi level for the TS1-I structure are broadened, which can be identified from the PDOS contribution of O_2 $1\pi_g^*$ orbitals at the Fermi level in the insert of Figure A.11a. The $1\pi_g^*$orbitals are also more involved with C P_z orbitals, weakening the O-O bond. Moreover, the hybridization between C P_z and $1\pi_u$ states at ~-8 eV are enhanced to stabilize the transition state. As compared to TS1-I structure, the overlapping between C P_z and $1\pi_u$ states in

the energy range from -3 to -8 eV for TS1-6IIa (Figure A.11b) is significantly enhanced though the interaction between C P_z and O_2 $1\pi_g^*$ states is slightly weakened at ~-0.5 eV.

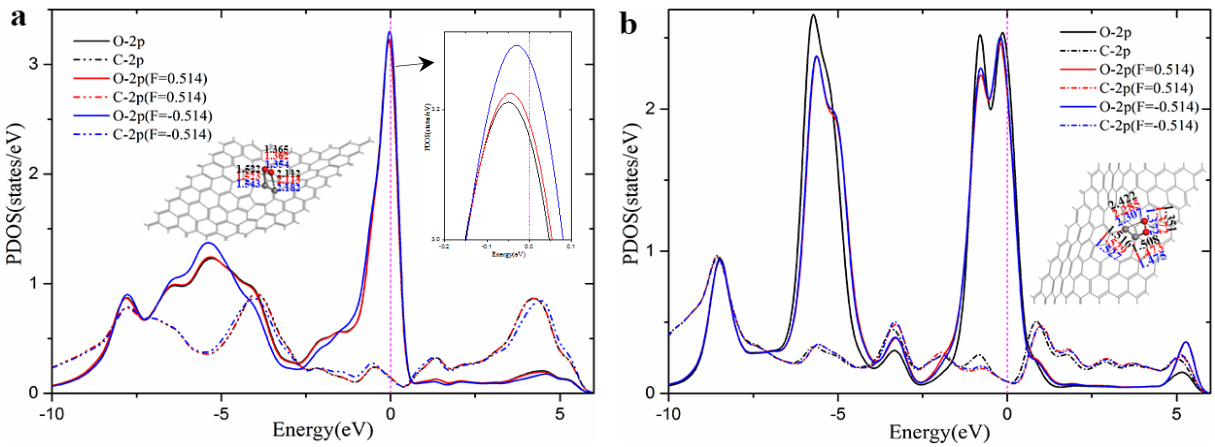

Figure A.11 Projected density of states (PDOS) of O and C atoms O atoms of O_2 molecule and C atoms below the O atoms in transition states TS1-I (a) and TS1-6IIa (b) under applied electric fields.

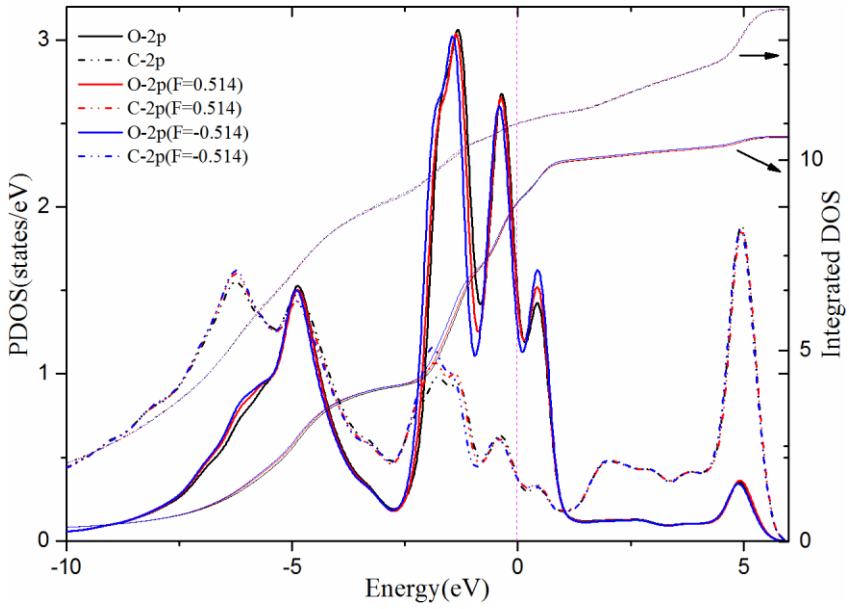

Figure A.12 Projected DOS and integrated DOS of O atoms and C atoms O atoms of O_2 molecule and C atoms below the O atoms in transition state TS2-I under applied electric fields.

Table A.2 Effect of electric field on the oxidation rate of graphene

Reaction		**Electric Field (V/nm)**	***E*a (kcal/mol)**	**Relative Reaction Rate at 513 K**
Reaction 1 $O_2 + dGr \underset{k_{-1}}{\overset{k_1}{\longleftrightarrow}} IS1\text{-}I$	K_1	0	0	1
		+0.514		0.55
		-0.514		2.57
Reaction 2 $IS1\text{-}I \underset{k_{-2}}{\overset{k_2}{\longleftrightarrow}} MS1\text{-}I$	k_2	0	11.54	1
		+0.514	10.25	3.55
		-0.514	10.26	3.52
Reaction 3 $MS1\text{-}I \xrightarrow{k_3} P6$	k_3	0	10.65	1
		+0.514	10.50	1.15
		-0.514	9.97	1.93
Reaction 4 $P6 + O_2 \underset{k_{-4}}{\overset{k_4}{\longleftrightarrow}} IS\text{-}6IIa$	K_4	0	0	1
		+0.514		0.81
		-0.514		1.10
Reaction 5 $IS\text{-}6IIa \underset{k_{-5}}{\overset{k_5}{\longleftrightarrow}} MS1\text{-}6IIa$	k_5	0	14.39	1
		+0.514	13.94	1.56
		-0.514	13.55	2.30
Reaction 6 $MS1\text{-}6IIa \underset{k_{-6}}{\overset{k_6}{\longleftrightarrow}} MS2\text{-}6IIa$	k_6	0	7.15	1
		+0.514	7.35	0.82
		-0.514	6.83	1.36
Reaction 7 $MS2\text{-}6IIa \xrightarrow{k_7} MS3\text{-}6IIa + CO_2$	k_7	0	7.03	1
		+0.514	7.18	0.87
		-0.514	7.07	0.96
Reaction 8 $MS3\text{-}6IIa \xrightarrow{k_8} FS1\text{-}6IIa + CO_2$	k_8	0	42.84	1
		+0.514	42.38	1.57
		-0.514	42.32	1.66

Furthermore, it can be readily identified that the significant redshift of C P_z states and O_2 $1\pi_u$ and $1\pi_g^*$ states in TS2-I structure under a negative/positive electric field as depicted in Figure A.12, which contributes to the stabilization of the transition state. The hybridizations which come from the C P_z states interacted with O_2 $1\pi_g^*$ states at ~-2 eV and $1\pi_u$ states at ~-5 eV are enhanced. From the above analysis, both negative and positive external electric field enhances the hybridizations between C P_z and O_2 $1\pi_u$ and/or $1\pi_g$* states, which weakens the O-O bond and strengthens the C-O bonds during the formation of peroxide intermediates and the subsequent ether intermediates. Table A.2 lists the change of activation energy and corresponding calculated relative reaction rate at 513 K under +/- 0.514 V nm^{-1} of electric field for all 8 transition states in the most favorable reaction pathway modeled in Appendix A.3. The highest activation barriers (reaction 2 and 8 with the first and second O_2 molecule, respectively) are sensitive to an external electric field vertical to the graphene plane and discussed in section 3.3.5.

Appendix B Supplementary Information on Enhanced Hydrogen Evolution Activity on Strained Graphene

Part of this appendix is being prepared for supporting information of submission authored by Min A Kim, Dan C. Sorescu, Shigeru Amemiya, Kenneth D. Jordan, and Haitao Liu.

Appendix B.1 Additional experimental data

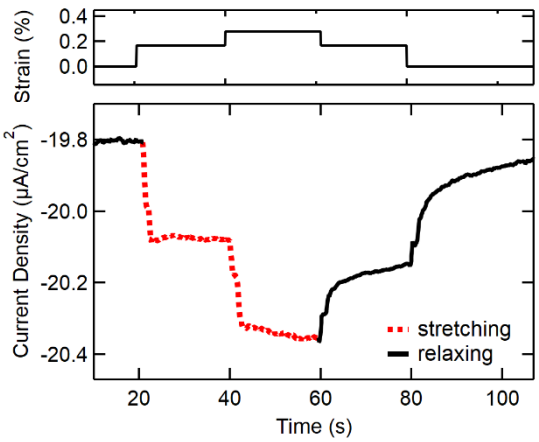

Figure B.1 Measured current density of HER with negligible background Time variation of the current density under constant applied potential (-0.5 V vs Ag/AgCl).without any background subtraction (lower panel). Tensile strain was applied (modulation sequence is shown in upper subpanel). Same tensile strain dependency of the current density is shown without any background subtraction resembling Figure 4.20b in the main text. HER current increases under tensile strain and decreases back upon the removal of strain.

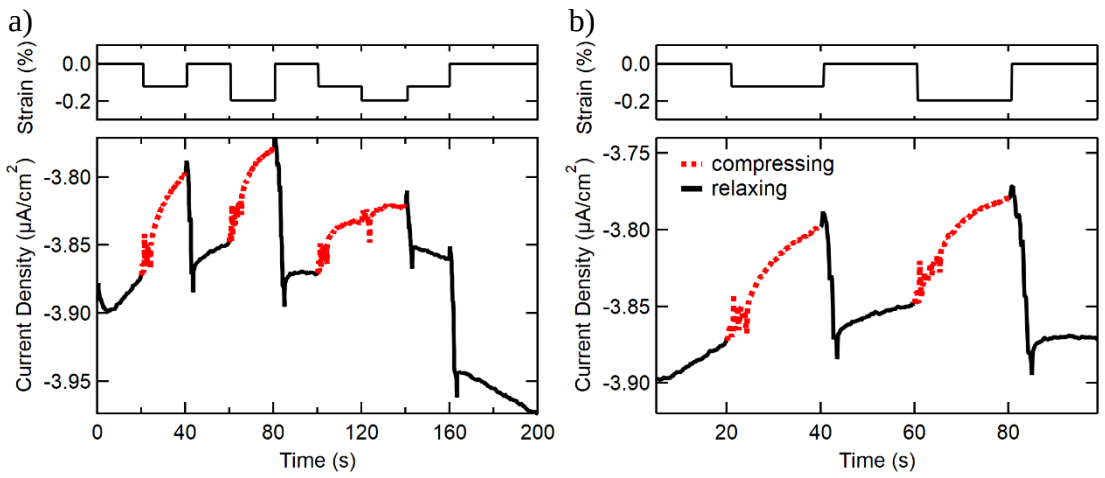

Figure B.2 Measured current density of HER under compressive strain Current measurement as a function of time with constant potential (-0.5 V vs Ag/AgCl). Compressive strain was applied (modulation sequence is shown in upper subpanel). Current was decreased slowly with compression(dotted red). Relaxing (positive directional strain change) resulted in fast increase of current density.

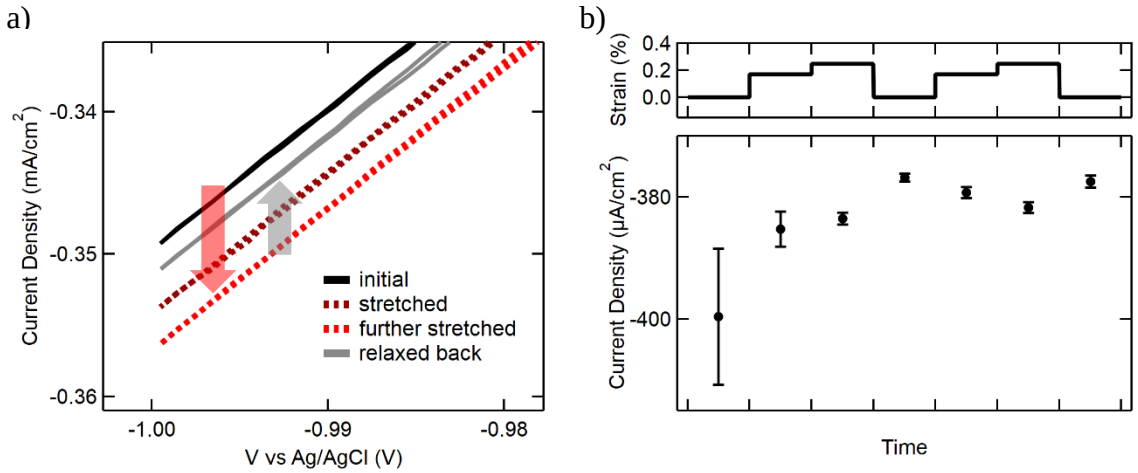

Figure B.3 Cyclic voltammetry (CV) on graphene electrode CV under different strain conditions in 0.5 M H_2SO_4. a) Zoom-in CV near -1 V. b) Average change in current density at -1 V shown as a function of time with varied strain% (0, 0.17, 0.25 %). All CVs were collected at scan rate of 0.1 V/s.

Appendix B.2 Computational methods

Adsorption of H on bare and stretched graphene has been analyzed using plane-wave spin-polarized DFT calculations with 3D periodic boundary conditions using the Vienna Ab Initio Simulation Package (VASP).[277, 278] The Perdew-Becke-Ernzerhof (PBE)[260] exchange-correlation functional corrected to include long-range van der Waals interactions using the D3 method of Grimme[274] with Becke-Johnson damping[279] has been used together with projector augmented wave (PAW) potentials of Blöch.[280, 281] The calculations also included dipole corrections as implemented in the VASP code.[282] A cutoff energy of 1000 eV was used to expand the plane-wave basis set. The adsorption energy per H atom was determined using expression $E_{ads} = [(nE_{(H^*)}+E_{(slab)})-E_{(slab+nH^*)}]/n$, where n represents the number of H* atoms adsorbed on the surface in the supercell employed, $E_{(slab)}$ is the energy of the isolated slab and $E_{(slab+nH^*)}$ is the energy of the adsorbate/slab system. In the case of adsorption energies referenced with respect to H in atomic form, $E_{(H^*)}$ is taken to be the spin-polarized energy of a single H atom, while for adsorption energies referenced relative to molecular H_2, $E_{(H^*)}$ was taken to be ½ $E(H_2)$ for the optimized H_2 molecule. Positive adsorption energies obtained using the above formulas correspond to stable configurations.

The majority of calculations were performed using two different supercell models detailed in Figure B.5. The first one (Figure B.5a) consists of a 5x5 hexagonal supercell with (**u**1,**u**2) cell versors taken along zigzag crystallographic directions of graphene while the second model (Figure B.5b) consists of a 5x3 orthogonal supercell with corresponding x and y cell directions taken along the zigzag (x) and armchair (y) directions. In both cases, a vacuum width of 16 Å in the direction perpendicular to the graphene surface was used to minimize the interactions with adjacent slabs. The dependence of adsorption energies on coverage was investigated using a set of hexagonal supercells ranging in size from 2x2 to 8x8. For the 5x5 hexagonal and 5x3 orthogonal supercells

a (7x7x1) Monkhorst Pack[283] k-point grid was used to sample the Brillouin zone while for the (2x2)-(8x8) set of supercells the k-point grid sizes were scaled as indicated in Table B.1.

The free energy changes corresponding to the hydrogen evolution reaction in acidic media at different stretching values of the graphene sheet were evaluated by including zero-point energy (ZPE), entropic and thermal corrections as detailed in Table B.2. Evaluation of ZPE corrections was done by including contributions from the adsorbed H atom and from the bonding C atom and its first and second nearest neighbors. The free energy of $H^+ + e^-$ was taken to be that of ½ H_2 and the free energy of adsorbed H* was evaluated with respect to energy of $1/_2H_2$.

Appendix B.3 Additional computational data

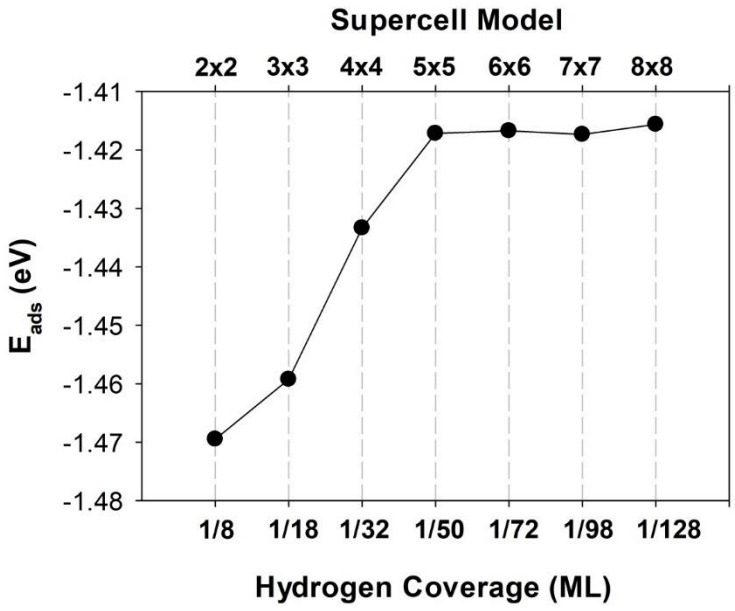

Figure B.4 Variation with coverage of H adsorption energy on graphene Adsorption energy is evaluated in this case function of energy of a single H_2 molecule, $E_{ads} = [(n/2)E_{(H2)}+E_{(slab)}-E_{(slab+nH^*)}]/n$, where n represents the number of H atoms adsorbed on the surface, $E_{(H2)}$ is the energy of optimized H_2 molecule, $E_{(slab)}$ is the energy of the isolated slab and $E_{(slab+nH^*)}$ is the energy of the adsorbate/slab system.

Table B.1 List of Monkhorst-Pack k-point grids Grid values used in calculations for supercells of different sizes on graphene surface.

Supercell	k-point grid
2x2	16x16x1
3x3	10x10x1
4x4	8x8x1
5x5	7x7x1
6x6	5x5x1
7x7	5x5x1
8x8	5x5x1

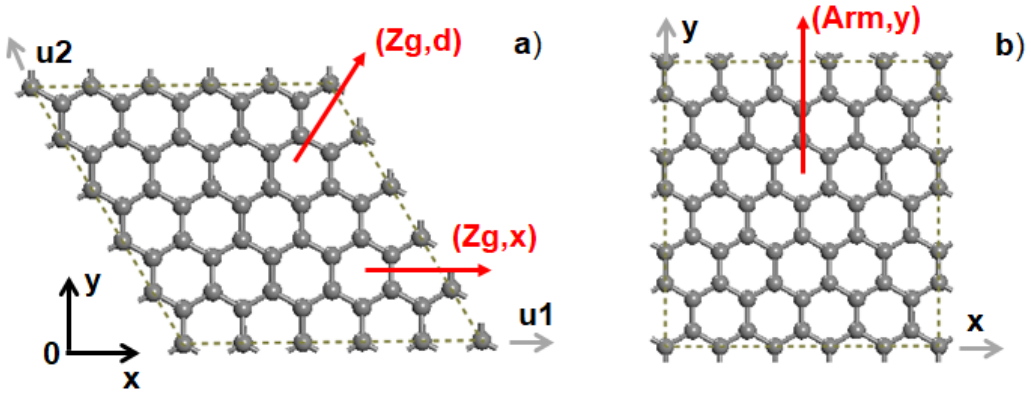

Figure B.5 Supercell cells used in calculations (a) the 5x5 hexagonal supercell cell used in calculations to determine the dependence of adsorption energy on lattice extension. Lattice extensions were taken along armchair crystallographic directions (Zg,x) and (Zg,d), respectively. Relative to the (yOx) Cartesian system of axes used, (Zg,x) direction is parallel to Ox axis while (Zg,d) is rotated by 60° relative to (Zg,x) direction. (**u**1,**u**2) denote the versor directions of the hexagonal cell. (b) the (5x3) orthogonal supercell used to investigate lattice expansion along the (Arm,y) direction, taken to be parallel to Cartesian Oy axis.

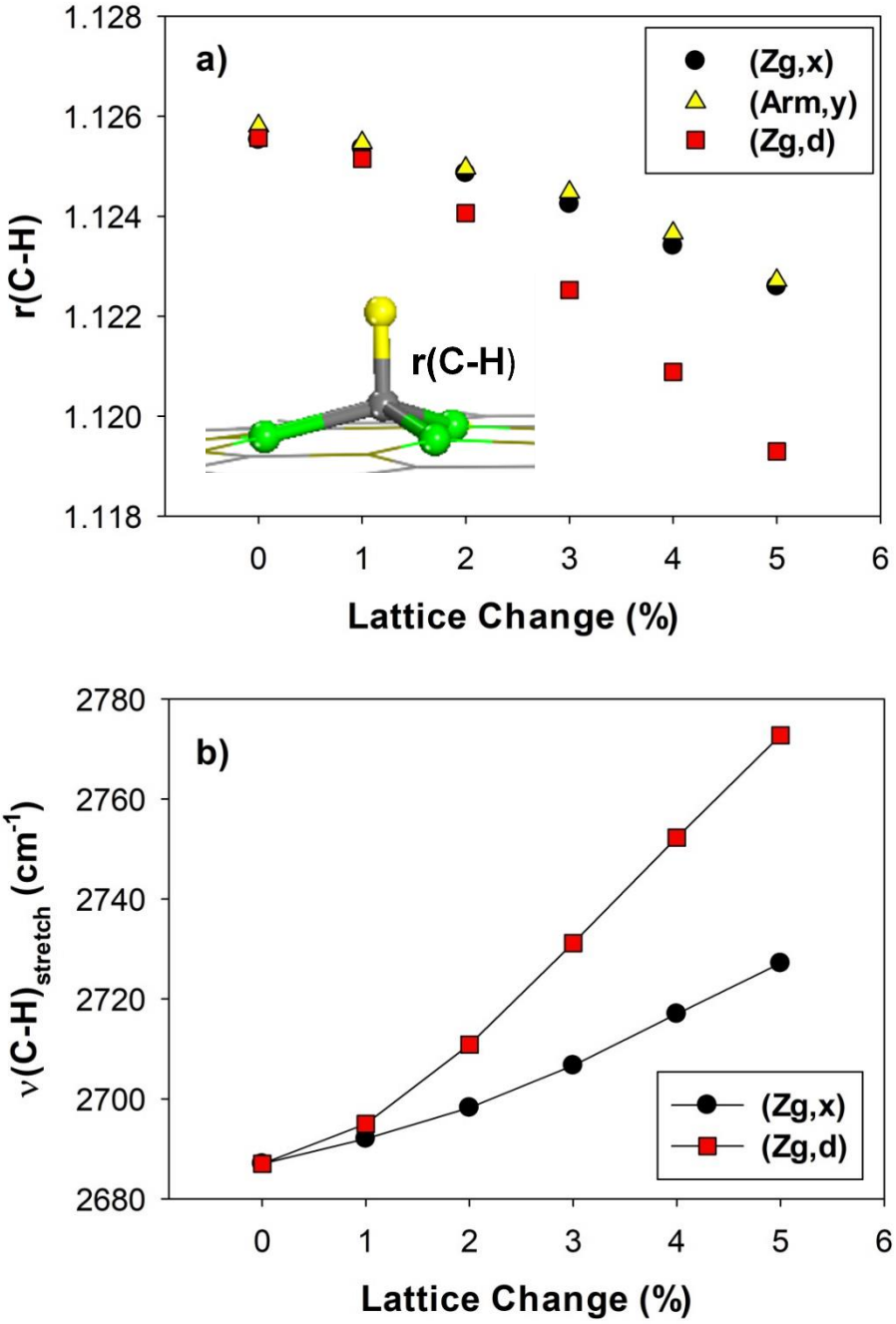

Figure B.6 Variation of C-H bond under lattice expansion (a) r(C-H) bond distance and (b) ν(C-H)$_{stretch}$ vibrational frequency with lattice expansion along different crystallographic directions.

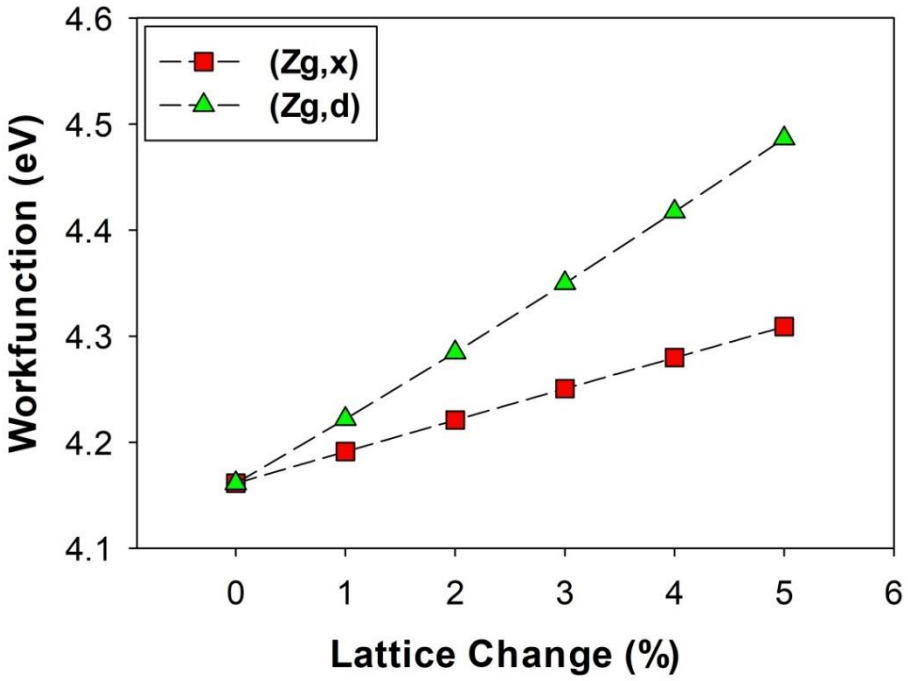

Figure B.7 Variation of the workfunction for adsorbed H Adsorbed H atom on graphene in a (5x5) supercell at different lattice elongations along (Zg,x) and (Zg,d) crystallographic directions.

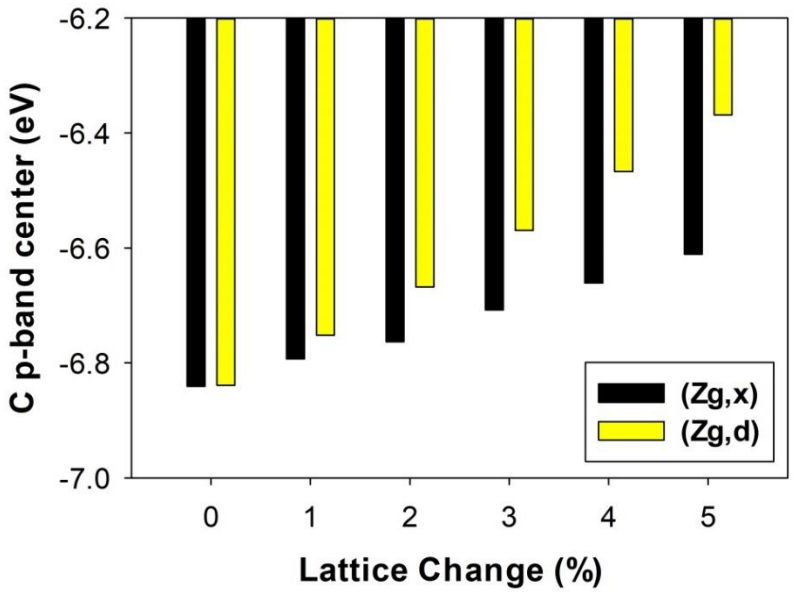

Figure B.8 Variation of C p-band center Upon lattice expansion along different crystallographic directions.

Table B.2 Calculated free energies of H adsorption reaction The free energies of reaction, zero point energy corrections, enthalpic and entropic contributions to the free energies.

H_2(g)	ΔZPE (eV)	Δ $H_{vib\ 0\rightarrow 298.15}$(eV)	Δ (TS)(eV)
	0.27284	0.08992	0.40309

a) Displacement along (Zg,x)

Lattice Disp. (%)	ΔZPE (eV)	Δ $H_{vib\ 0\rightarrow 298.15}$(eV)	Δ (TS)(eV)	ΔG (eV)
0.0	0.1288551	-0.0382633	-0.1914602	1.6986212
0.17	0.1293681	-0.0383686	-0.1916006	1.6974193
0.25	0.1294504	-0.0383537	-0.1915678	1.6962537
1.0	0.1309759	-0.0382496	-0.1913268	1.6817023
2.0	0.1332553	-0.0381588	-0.1911378	1.6555435
3.0	0.1350490	-0.0380830	-0.1910043	1.6235495
4.0	0.1365985	-0.0380098	-0.1908934	1.5881914
5.0	0.1378147	-0.0379238	-0.1907720	1.5501821

b) Displacement along (Zg,d)

Lattice Disp. (%)	ΔZPE (eV)	Δ $H_{vib\ 0\rightarrow 298.15}$(eV)	Δ (TS)(eV)	ΔG (eV)
0.0	0.1288551	-0.0382633	-0.1914602	1.6986212
1.0	0.1337798	-0.0382072	-0.1912123	1.6607740
2.0	0.1372252	-0.0380713	-0.1909814	1.6000445
3.0	0.1402519	-0.0379687	-0.1908647	1.5266971
4.0	0.1426632	-0.0377748	-0.1905729	1.4441804
5.0	0.1450584	-0.0376154	-0.1903402	1.3551424

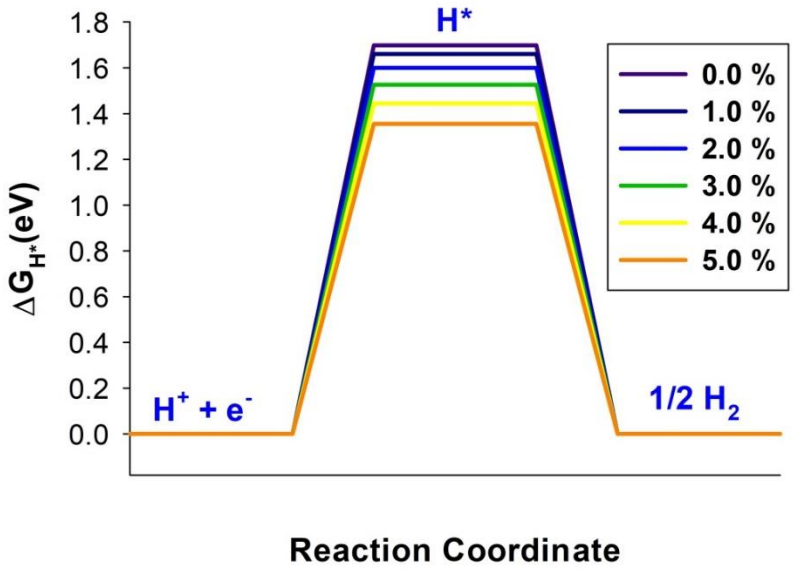

Figure B.9 Variation of free energy ΔG_{H^*} at equilibrium (U=0) For reaction * + H^+ + e^- ↔ H* on graphene and standard conditions under different lattice expansions along (Zg,d) direction.

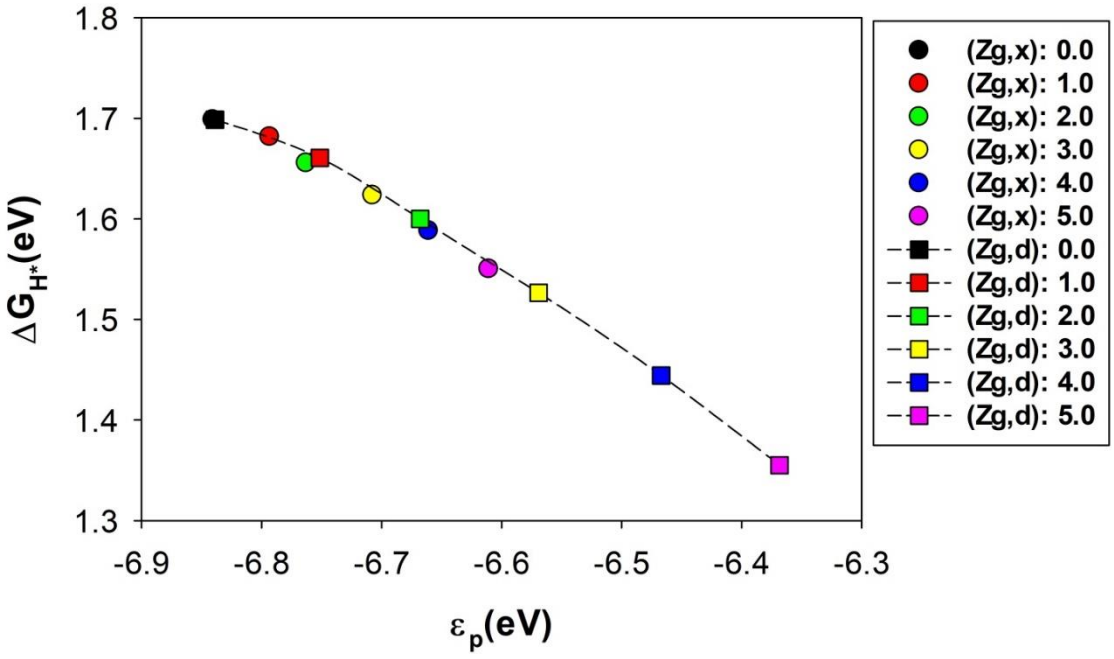

Figure B.10 Variation of the free energy ΔG_{H^*} with corresponding p-band center For reaction * + H^+ + e^- ↔ H* on graphene at different stretching levels along (Zg,x) and (Zg,d) directions.

Bibliography

1. Feynman, R. P., There's Plenty of Room at the Bottom. *Engineering and Science* **1960,** *23* (5), 22-36.
2. Kroto, H. W.; Heath, J. R.; O'Brien, S. C.; Curl, R. F.; Smalley, R. E., C60: Buckminsterfullerene. *Nature* **1985,** *318* (6042), 162-163.
3. Iijima, S., Helical microtubules of graphitic carbon. *Nature* **1991,** *354* (6348), 56-58.
4. Novoselov, K. S.; Geim, A. K.; Morozov, S. V.; Jiang, D.; Zhang, Y.; Dubonos, S. V.; Grigorieva, I. V.; Firsov, A. A., Electric field effect in atomically thin carbon films. *Science* **2004,** *306* (5696), 666-669.
5. Brodie, B. C., On the Atomic Weight of Graphite. *Phil. Trans. R. Soc.* **1859,** *149*, 249-259.
6. Ruess, G.; Vogt, F., Höchstlamellarer Kohlenstoff aus Graphitoxyhydroxyd. *Monatshefte für Chemie und verwandte Teile anderer Wissenschaften* **1948,** *78* (3), 222-242.
7. Boehm, H. P.; Clauss, A.; Fischer, G. O.; Hofmann, U., Das Adsorptionsverhalten sehr dünner Kohlenstoff-Folien. *Z. anorg. allg. Chem.* **1962,** *316* (3-4), 119-127.
8. Boehm, H. P.; Setton, R.; Stumpp, E., Nomenclature and terminology of graphite intercalation compounds. *Carbon* **1986,** *24* (2), 241-245.
9. Boehm, H. P.; Setton, R.; Stumpp, E., Nomenclature and terminology of graphite intercalation compounds (IUPAC Recommendations 1994). *Pure and applied chemistry* **1994,** *66* (9), 1893-1901.
10. Seibert, K.; Cho, G. C.; Kütt, W.; Kurz, H.; Reitze, D. H.; Dadap, J. I.; Ahn, H.; Downer, M. C.; Malvezzi, A. M., Femtosecond carrier dynamics in graphite. *Phys. Rev. B* **1990,** *42* (5), 2842-2851.
11. Ebbesen, T. W.; Hiura, H., Graphene in 3-dimensions: Towards graphite origami. *Adv. Mater.* **1995,** *7* (6), 582-586.
12. Lu, X.; Yu, M.; Huang, H.; Ruoff, R. S., Tailoring graphite with the goal of achieving single sheets. *Nanotechnology* **1999,** *10* (3), 269-272.
13. Gan, Y.; Chu, W.; Qiao, L., STM investigation on interaction between superstructure and grain boundary in graphite. *Surface Science* **2003,** *539* (1), 120-128.
14. Viculis, L. M.; Mack, J. J.; Kaner, R. B., A chemical route to carbon nanoscrolls. *Science* **2003,** *299* (5611), 1361.
15. Horiuchi, S.; Gotou, T.; Fujiwara, M.; Asaka, T.; Yokosawa, T.; Matsui, Y., Single graphene sheet detected in a carbon nanofilm. *Applied Physics Letters* **2004,** *84* (13), 2403-2405.
16. Shioyama, H., Cleavage of graphite to graphene. *Journal of Materials Science Letters* **2001,** *20* (6), 499-500.

17. Lovell, A. C. B., Electrical Conductivity of Thin Films of Rubidium on Glass Surfaces. *Nature* **1936,** *137* (3464), 493-494.

18. Venables, J. A.; Spiller, G. D. T.; Hanbucken, M., Nucleation and growth of thin films. *Reports on Progress in Physics* **1984,** *47* (4), 399-459.

19. Blakely, J. M.; Kim, J. S.; Potter, H. C., Segregation of Carbon to the (100) Surface of Nickel. *Journal of Applied Physics* **1970,** *41* (6), 2693-2697.

20. Grant, J. T.; Haas, T. W., A study of Ru(0001) and Rh(111) surfaces using LEED and Auger electron spectroscopy. *Surface Science* **1970,** *21* (1), 76-85.

21. Van Bommel, A. J.; Crombeen, J. E.; Van Tooren, A., LEED and Auger electron observations of the SiC(0001) surface. *Surface Science* **1975,** *48* (2), 463-472.

22. Rosei, R.; De Crescenzi, M.; Sette, F.; Quaresima, C.; Savoia, A.; Perfetti, P., Structure of graphitic carbon on Ni(111): A surface extended-energy-loss fine-structure study. *Phys. Rev. B* **1983,** *28* (2), 1161-1164.

23. McConville, C. F.; Woodruff, D. P.; Kevan, S. D.; Weinert, M.; Davenport, J. W., Electronic structure of the (2 x 2)C *p* 4*g* carbidic phase on Ni{100}. *Phys. Rev. B* **1986,** *34* (4), 2199-2206.

24. Land, T. A.; Michely, T.; Behm, R. J.; Hemminger, J. C.; Comsa, G., STM investigation of single layer graphite structures produced on Pt(111) by hydrocarbon decomposition. *Surface Science* **1992,** *264* (3), 261-270.

25. Nagashima, A.; Nuka, K.; Satoh, K.; Itoh, H.; Ichinokawa, T.; Oshima, C.; Otani, S., Electronic structure of monolayer graphite on some transition metal carbide surfaces. *Surface Science* **1993,** *287-288*, 609-613.

26. Terai, M.; Hasegawa, N.; Okusawa, M.; Otani, S.; Oshima, C., Electronic states of monolayer micrographite on TiC(111)-faceted and TiC(410) surfaces. *Applied Surface Science* **1998,** *130-132*, 876-882.

27. Forbeaux, I.; Themlin, J. M.; Debever, J. M., Heteroepitaxial graphite on 6*H*-SiC (0001): Interface formation through conduction-band electronic structure. *Phys. Rev. B* **1998,** *58* (24), 16396-16406.

28. Lee, C.; Wei, X. D.; Kysar, J. W.; Hone, J., Measurement of the elastic properties and intrinsic strength of monolayer graphene. *Science* **2008,** *321* (5887), 385-388.

29. Xie, S.; Li, W.; Pan, Z.; Chang, B.; Sun, L., Mechanical and physical properties on carbon nanotube. *Journal of Physics and Chemistry of Solids* **2000,** *61* (7), 1153-1158.

30. Yu, M.-F.; Files, B. S.; Arepalli, S.; Ruoff, R. S., Tensile Loading of Ropes of Single Wall Carbon Nanotubes and their Mechanical Properties. *Phys. Rev. Lett.* **2000,** *84* (24), 5552-5555.

31. Yu, M.-F.; Lourie, O.; Dyer, M. J.; Moloni, K.; Kelly, T. F.; Ruoff, R. S., Strength and Breaking Mechanism of Multiwalled Carbon Nanotubes Under Tensile Load. *Science* **2000,** *287* (5453), 637-640.

32. Mak, K. F.; Sfeir, M. Y.; Wu, Y.; Lui, C. H.; Misewich, J. A.; Heinz, T. F., Measurement of the Optical Conductivity of Graphene. *Phys. Rev. Lett.* **2008,** *101* (19), 196405.

33. Kuzmenko, A. B.; van Heumen, E.; Carbone, F.; van der Marel, D., Universal Optical Conductance of Graphite. *Phys. Rev. Lett.* **2008,** *100* (11), 117401.

34. Ando, T.; Zheng, Y.; Suzuura, H., Dynamical Conductivity and Zero-Mode Anomaly in Honeycomb Lattices. *Journal of the Physical Society of Japan* **2002,** *71* (5), 1318-1324.

35. Bunch, J. S.; Verbridge, S. S.; Alden, J. S.; van der Zande, A. M.; Parpia, J. M.; Craighead, H. G.; McEuen, P. L., Impermeable atomic membranes from graphene sheets. *Nano Letters* **2008,** *8* (8), 2458-2462.

36. Balandin, A. A.; Ghosh, S.; Bao, W.; Calizo, I.; Teweldebrhan, D.; Miao, F.; Lau, C. N., Superior Thermal Conductivity of Single-Layer Graphene. *Nano Letters* **2008,** *8* (3), 902-907.

37. Balandin, A. A., Thermal properties of graphene and nanostructured carbon materials. *Nature Materials* **2011,** *10* (8), 569-581.

38. Bolotin, K. I.; Sikes, K. J.; Jiang, Z.; Klima, M.; Fudenberg, G.; Hone, J.; Kim, P.; Stormer, H. L., Ultrahigh electron mobility in suspended graphene. *Solid State Communications* **2008,** *146* (9–10), 351-355.

39. Zhang, Y. B.; Tan, Y. W.; Stormer, H. L.; Kim, P., Experimental observation of the quantum Hall effect and Berry's phase in graphene. *Nature* **2005,** *438* (7065), 201-204.

40. Moser, J.; Barreiro, A.; Bachtold, A., Current-induced cleaning of graphene. *Applied Physics Letters* **2007,** *91* (16), 163513.

41. Geim, A. K.; Novoselov, K. S., The rise of graphene. *Nature Materials* **2007,** *6* (3), 183-191.

42. Castro Neto, A. H.; Guinea, F.; Peres, N. M. R.; Novoselov, K. S.; Geim, A. K., The electronic properties of graphene. *Reviews of Modern Physics* **2009,** *81* (1), 109-162.

43. Das Sarma, S.; Adam, S.; Hwang, E. H.; Rossi, E., Electronic transport in two-dimensional graphene. *Reviews of Modern Physics* **2011,** *83* (2), 407-470.

44. Wallace, P. R., THE BAND THEORY OF GRAPHITE. *Phys. Rev.* **1947,** *71* (9), 622-634.

45. Gierz, I.; Riedl, C.; Starke, U.; Ast, C. R.; Kern, K., Atomic Hole Doping of Graphene. *Nano Letters* **2008,** *8* (12), 4603-4607.

46. Li, D.; Windl, W.; Padture, N. P., Toward Site-Specific Stamping of Graphene. *Adv. Mater.* **2009,** *21* (12), 1243-1246.

47. Jayasena, B.; Melkote, S. N., An Investigation of PDMS Stamp Assisted Mechanical Exfoliation of Large Area Graphene. *Procedia Manufacturing* **2015,** *1*, 840-853.

48. Jayasena, B.; Subbiah, S., A novel mechanical cleavage method for synthesizing few-layer graphenes. *Nanoscale Research Letters* **2011,** *6* (1), 95.

49. Chen, J.; Duan, M.; Chen, G., Continuous mechanical exfoliation of graphene sheets via three-roll mill. *J. Mater. Chem.* **2012,** *22* (37), 19625-19628.

50. Dreyer, D. R.; Park, S.; Bielawski, C. W.; Ruoff, R. S., The chemistry of graphene oxide. *Chemical Society Reviews* **2010,** *39* (1), 228-240.

51. Hernandez, Y.; Nicolosi, V.; Lotya, M.; Blighe, F. M.; Sun, Z.; De, S.; McGovern, I. T.; Holland, B.; Byrne, M.; Gun'Ko, Y. K.; Boland, J. J.; Niraj, P.; Duesberg, G.; Krishnamurthy, S.; Goodhue, R.; Hutchison, J.; Scardaci, V.; Ferrari, A. C.; Coleman, J. N., High-yield production of graphene by liquid-phase exfoliation of graphite. *Nature Nanotechnology* **2008,** *3* (9), 563-568.

52. Nicolosi, V.; Chhowalla, M.; Kanatzidis, M. G.; Strano, M. S.; Coleman, J. N., Liquid Exfoliation of Layered Materials. *Science* **2013,** *340* (6139).

53. Cravotto, G.; Cintas, P., Sonication-Assisted Fabrication and Post-Synthetic Modifications of Graphene-Like Materials. *Chemistry – A European Journal* **2010,** *16* (18), 5246-5259.

54. Ciesielski, A.; Samorì, P., Graphene via sonication assisted liquid-phase exfoliation. *Chemical Society Reviews* **2014,** *43* (1), 381-398.

55. Flint, E. B.; Suslick, K. S., The Temperature of Cavitation. *Science* **1991,** *253* (5026), 1397-1399.

56. McNamara, W. B.; Didenko, Y. T.; Suslick, K. S., Sonoluminescence temperatures during multi-bubble cavitation. *Nature* **1999,** *401* (6755), 772-775.

57. Suslick, K. S.; Flannigan, D. J., Inside a Collapsing Bubble: Sonoluminescence and the Conditions During Cavitation. *Annual Review of Physical Chemistry* **2008,** *59* (1), 659-683.

58. Polyakova, E. Y.; Rim, K. T.; Eom, D.; Douglass, K.; Opila, R. L.; Heinz, T. F.; Teplyakov, A. V.; Flynn, G. W., Scanning Tunneling Microscopy and X-ray Photoelectron Spectroscopy Studies of Graphene Films Prepared by Sonication-Assisted Dispersion. *ACS Nano* **2011,** *5* (8), 6102-6108.

59. Skaltsas, T.; Ke, X.; Bittencourt, C.; Tagmatarchis, N., Ultrasonication Induces Oxygenated Species and Defects onto Exfoliated Graphene. *J. Phys. Chem. C* **2013,** *117* (44), 23272-23278.

60. Zhao, W.; Fang, M.; Wu, F.; Wu, H.; Wang, L.; Chen, G., Preparation of graphene by exfoliation of graphite using wet ball milling. *J. Mater. Chem.* **2010,** *20* (28), 5817-5819.

61. Jeon, I.-Y.; Shin, Y.-R.; Sohn, G.-J.; Choi, H.-J.; Bae, S.-Y.; Mahmood, J.; Jung, S.-M.; Seo, J.-M.; Kim, M.-J.; Wook Chang, D.; Dai, L.; Baek, J.-B., Edge-carboxylated graphene nanosheets via ball milling. *Proceedings of the National Academy of Sciences* **2012,** *109* (15), 5588-5593.

62. Jeon, I.-Y.; Choi, H.-J.; Jung, S.-M.; Seo, J.-M.; Kim, M.-J.; Dai, L.; Baek, J.-B., Large-Scale Production of Edge-Selectively Functionalized Graphene Nanoplatelets via Ball Milling and Their Use as Metal-Free Electrocatalysts for Oxygen Reduction Reaction. *J. Am. Chem. Soc.* **2013,** *135* (4), 1386-1393.

63. León, V.; Rodriguez, A. M.; Prieto, P.; Prato, M.; Vázquez, E., Exfoliation of Graphite with Triazine Derivatives under Ball-Milling Conditions: Preparation of Few-Layer Graphene via Selective Noncovalent Interactions. *ACS Nano* **2014,** *8* (1), 563-571.

64. Ong, T. S.; Yang, H., Effect of atmosphere on the mechanical milling of natural graphite. *Carbon* **2000,** *38* (15), 2077-2085.

65. Xing, T.; Li, L. H.; Hou, L.; Hu, X.; Zhou, S.; Peter, R.; Petravic, M.; Chen, Y., Disorder in ball-milled graphite revealed by Raman spectroscopy. *Carbon* **2013,** *57*, 515-519.

66. Chen, X.; Dobson, J. F.; Raston, C. L., Vortex fluidic exfoliation of graphite and boron nitride. *Chemical Communications* **2012,** *48* (31), 3703-3705.

67. Yi, M.; Li, J.; Shen, Z.; Zhang, X.; Ma, S., Morphology and structure of mono- and few-layer graphene produced by jet cavitation. *Applied Physics Letters* **2011,** *99* (12), 123112.

68. Paton, K. R.; Varrla, E.; Backes, C.; Smith, R. J.; Khan, U.; O'Neill, A.; Boland, C.; Lotya, M.; Istrate, O. M.; King, P.; Higgins, T.; Barwich, S.; May, P.; Puczkarski, P.; Ahmed, I.; Moebius, M.; Pettersson, H.; Long, E.; Coelho, J.; O'Brien, S. E.; McGuire, E. K.; Sanchez, B. M.; Duesberg, G. S.; McEvoy, N.; Pennycook, T. J.; Downing, C.; Crossley, A.; Nicolosi, V.; Coleman, J. N., Scalable production of large quantities of defect-free few-layer graphene by shear exfoliation in liquids. *Nature Materials* **2014,** *13* (6), 624-630.

69. Berger, C.; Song, Z.; Li, T.; Li, X.; Ogbazghi, A. Y.; Feng, R.; Dai, Z.; Marchenkov, A. N.; Conrad, E. H.; First, P. N.; de Heer, W. A., Ultrathin Epitaxial Graphite: 2D Electron Gas Properties and a Route toward Graphene-based Nanoelectronics. *J. Phys. Chem. B* **2004,** *108* (52), 19912-19916.

70. Berger, C.; Song, Z.; Li, X.; Wu, X.; Brown, N.; Naud, C.; Mayou, D.; Li, T.; Hass, J.; Marchenkov, A. N.; Conrad, E. H.; First, P. N.; de Heer, W. A., Electronic Confinement and Coherence in Patterned Epitaxial Graphene. *Science* **2006,** *312* (5777), 1191-1196.

71. de Heer, W. A.; Berger, C.; Wu, X.; First, P. N.; Conrad, E. H.; Li, X.; Li, T.; Sprinkle, M.; Hass, J.; Sadowski, M. L.; Potemski, M.; Martinez, G., Epitaxial graphene. *Solid State Communications* **2007,** *143* (1), 92-100.

72. Emtsev, K. V.; Bostwick, A.; Horn, K.; Jobst, J.; Kellogg, G. L.; Ley, L.; McChesney, J. L.; Ohta, T.; Reshanov, S. A.; Röhrl, J.; Rotenberg, E.; Schmid, A. K.; Waldmann, D.; Weber, H. B.; Seyller, T., Towards wafer-size graphene layers by atmospheric pressure graphitization of silicon carbide. *Nature Materials* **2009,** *8* (3), 203-207.

73. Sutter, P., Epitaxial graphene: How silicon leaves the scene. *Nature Materials* **2009,** *8* (3), 171-172.

74. Nie, S.; Wofford, J. M.; Bartelt, N. C.; Dubon, O. D.; McCarty, K. F., Origin of the mosaicity in graphene grown on Cu(111). *Phys. Rev. B* **2011,** *84* (15), 155425.

75. Riedl, C.; Coletti, C.; Starke, U., Structural and electronic properties of epitaxial graphene on SiC(0 0 0 1): a review of growth, characterization, transfer doping and hydrogen intercalation. *Journal of Physics D: Applied Physics* **2010,** *43* (37), 374009.

76. Lee, J.-H.; Lee, E. K.; Joo, W.-J.; Jang, Y.; Kim, B.-S.; Lim, J. Y.; Choi, S.-H.; Ahn, S. J.; Ahn, J. R.; Park, M.-H.; Yang, C.-W.; Choi, B. L.; Hwang, S.-W.; Whang, D., Wafer-Scale Growth of Single-Crystal Monolayer Graphene on Reusable Hydrogen-Terminated Germanium. *Science* **2014,** *344* (6181), 286-289.

77. Somani, P. R.; Somani, S. P.; Umeno, M., Planer nano-graphenes from camphor by CVD. *Chemical Physics Letters* **2006,** *430* (1-3), 56-59.

78. Li, X. S.; Cai, W. W.; An, J. H.; Kim, S.; Nah, J.; Yang, D. X.; Piner, R.; Velamakanni, A.; Jung, I.; Tutuc, E.; Banerjee, S. K.; Colombo, L.; Ruoff, R. S., Large-Area Synthesis of High-Quality and Uniform Graphene Films on Copper Foils. *Science* **2009,** *324* (5932), 1312-1314.

79. Reina, A.; Jia, X. T.; Ho, J.; Nezich, D.; Son, H. B.; Bulovic, V.; Dresselhaus, M. S.; Kong, J., Large Area, Few-Layer Graphene Films on Arbitrary Substrates by Chemical Vapor Deposition. *Nano Letters* **2009,** *9* (1), 30-35.

80. Coraux, J.; N'Diaye, A. T.; Busse, C.; Michely, T., Structural coherency of graphene on Ir(111). *Nano Letters* **2008,** *8* (2), 565-570.

81. Li, X. S.; Cai, W. W.; Colombo, L.; Ruoff, R. S., Evolution of Graphene Growth on Ni and Cu by Carbon Isotope Labeling. *Nano Letters* **2009,** *9* (12), 4268-4272.

82. Mattevi, C.; Kim, H.; Chhowalla, M., A review of chemical vapour deposition of graphene on copper. *J. Mater. Chem.* **2011,** *21* (10), 3324-3334.

83. Munoz, R.; Gomez-Aleixandre, C., Review of CVD Synthesis of Graphene. *Chemical Vapor Deposition* **2013,** *19* (10-12), 297-322.

84. Zhang, Y.; Zhang, L. Y.; Zhou, C. W., Review of Chemical Vapor Deposition of Graphene and Related Applications. *Accounts of Chemical Research* **2013,** *46* (10), 2329-2339.

85. Lee, H. C.; Liu, W. W.; Chai, S. P.; Mohamed, A. R.; Aziz, A.; Khe, C. S.; Hidayah, N. M. S.; Hashim, U., Review of the synthesis, transfer, characterization and growth mechanisms of single and multilayer graphene. *RSC Advances* **2017,** *7* (26), 15644-15693.

86. Bae, S.; Kim, H.; Lee, Y.; Xu, X. F.; Park, J. S.; Zheng, Y.; Balakrishnan, J.; Lei, T.; Kim, H. R.; Song, Y. I.; Kim, Y. J.; Kim, K. S.; Ozyilmaz, B.; Ahn, J. H.; Hong, B. H.; Iijima, S., Roll-to-roll production of 30-inch graphene films for transparent electrodes. *Nature Nanotechnology* **2010,** *5* (8), 574-578.

87. Wu, Y. M. A.; Fan, Y.; Speller, S.; Creeth, G. L.; Sadowski, J. T.; He, K.; Robertson, A. W.; Allen, C. S.; Warner, J. H., Large Single Crystals of Graphene on Melted Copper Using Chemical Vapor Deposition. *ACS Nano* **2012,** *6* (6), 5010-5017.

88. Hao, Y. F.; Bharathi, M. S.; Wang, L.; Liu, Y. Y.; Chen, H.; Nie, S.; Wang, X. H.; Chou, H.; Tan, C.; Fallahazad, B.; Ramanarayan, H.; Magnuson, C. W.; Tutuc, E.; Yakobson, B. I.; McCarty, K. F.; Zhang, Y. W.; Kim, P.; Hone, J.; Colombo, L.; Ruoff, R. S., The Role of Surface Oxygen in the Growth of Large Single-Crystal Graphene on Copper. *Science* **2013,** *342* (6159), 720-723.

89. Zhou, H. L.; Yu, W. J.; Liu, L. X.; Cheng, R.; Chen, Y.; Huang, X. Q.; Liu, Y.; Wang, Y.; Huang, Y.; Duan, X. F., Chemical vapour deposition growth of large single crystals of monolayer and bilayer graphene. *Nature Communications* **2013,** *4*.

90. Nair, R. R.; Blake, P.; Grigorenko, A. N.; Novoselov, K. S.; Booth, T. J.; Stauber, T.; Peres, N. M. R.; Geim, A. K., Fine Structure Constant Defines Visual Transparency of Graphene. **2008,** *320* (5881), 1308-1308.

91. Abergel, D. S. L.; Russell, A.; Fal'ko, V. I., Visibility of graphene flakes on a dielectric substrate. *Applied Physics Letters* **2007,** *91* (6), 063125.

92. Blake, P.; Hill, E. W.; Neto, A. H. C.; Novoselov, K. S.; Jiang, D.; Yang, R.; Booth, T. J.; Geim, A. K., Making graphene visible. **2007,** *91* (6), 063124.

93. Shearer, C. J.; Slattery, A. D.; Stapleton, A. J.; Shapter, J. G.; Gibson, C. T., Accurate thickness measurement of graphene. *Nanotechnology* **2016,** *27* (12), 125704-125704.

94. Bacon, G. E., The interlayer spacing of graphite. *Acta Crystallographica* **1951,** *4* (6), 558-561.

95. Franklin, R. E., The structure of graphitic carbons. *Acta Crystallographica* **1951,** *4* (3), 253-261.

96. Giesbers, A. J. M.; Zeitler, U.; Neubeck, S.; Freitag, F.; Novoselov, K. S.; Maan, J. C., Nanolithography and manipulation of graphene using an atomic force microscope. *Solid State Communications* **2008,** *147* (9), 366-369.

97. Yan, L.; Punckt, C.; Aksay, I. A.; Mertin, W.; Bacher, G., Local Voltage Drop in a Single Functionalized Graphene Sheet Characterized by Kelvin Probe Force Microscopy. *Nano Letters* **2011,** *11* (9), 3543-3549.

98. Kumar, R.; Varandani, D.; Mehta, B. R., Nanoscale interface formation and charge transfer in graphene/silicon Schottky junctions; KPFM and CAFM studies. *Carbon* **2016,** *98*, 41-49.

99. Jia, P.; Chen, W.; Qiao, J.; Zhang, M.; Zheng, X.; Xue, Z.; Liang, R.; Tian, C.; He, L.; Di, Z.; Wang, X., Programmable graphene nanobubbles with three-fold symmetric pseudo-magnetic fields. *Nature Communications* **2019,** *10* (1), 3127.

100. Ferrari, A. C.; Robertson, J., Resonant Raman spectroscopy of disordered, amorphous, and diamondlike carbon. *Phys. Rev. B* **2001,** *64* (7).

101. Reich, S.; Thomsen, C., Raman spectroscopy of graphite. *Phil. Trans. R. Soc. A.* **2004,** *362* (1824), 2271-2288.

102. Dresselhaus, M. S.; Dresselhaus, G.; Saito, R.; Jorio, A., Raman spectroscopy of carbon nanotubes. *Physics Reports-Review Section of Physics Letters* **2005,** *409* (2), 47-99.

103. Ferrari, A. C.; Meyer, J. C.; Scardaci, V.; Casiraghi, C.; Lazzeri, M.; Mauri, F.; Piscanec, S.; Jiang, D.; Novoselov, K. S.; Roth, S.; Geim, A. K., Raman spectrum of graphene and graphene layers. *Physical Review Letters* **2006,** *97* (18).

104. Gupta, A.; Chen, G.; Joshi, P.; Tadigadapa, S.; Eklund, P. C., Raman scattering from high-frequency phonons in supported n-graphene layer films. *Nano Letters* **2006,** *6* (12), 2667-2673.

105. Vidano, R. P.; Fischbach, D. B.; Willis, L. J.; Loehr, T. M., Observation of Raman band shifting with excitation wavelength for carbons and graphites. *Solid State Communications* **1981,** *39* (2), 341-344.

106. Tuinstra, F.; Koenig, J. L., Raman Spectrum of Graphite. *The Journal of Chemical Physics* **1970,** *53* (3), 1126-1130.

107. Ferrari, A. C., Raman spectroscopy of graphene and graphite: Disorder, electron-phonon coupling, doping and nonadiabatic effects. *Solid State Communications* **2007,** *143* (1-2), 47-57.

108. Castiglioni, C.; Tommasini, M.; Zerbi, G., Raman spectroscopy of polyconjugated molecules and materials: confinement effect in one and two dimensions. *Phil. Trans. R. Soc. A.* **2004,** *362* (1824), 2425-2459.

109. Latil, S.; Meunier, V.; Henrard, L., Massless fermions in multilayer graphitic systems with misoriented layers: Ab initio calculations and experimental fingerprints. *Phys. Rev. B* **2007,** *76* (20), 201402.

110. Lespade, P.; Marchand, A.; Couzi, M.; Cruege, F., Caracterisation de materiaux carbones par microspectrometrie Raman. *Carbon* **1984,** *22* (4), 375-385.

111. Poncharal, P.; Ayari, A.; Michel, T.; Sauvajol, J. L., Raman spectra of misoriented bilayer graphene. *Phys. Rev. B* **2008,** *78* (11), 113407.

112. Shallcross, S.; Sharma, S.; Kandelaki, E.; Pankratov, O. A., Electronic structure of turbostratic graphene. *Phys. Rev. B* **2010,** *81* (16), 165105.

113. Eckmann, A.; Felten, A.; Verzhbitskiy, I.; Davey, R.; Casiraghi, C., Raman study on defective graphene: Effect of the excitation energy, type, and amount of defects. *Phys. Rev. B* **2013,** *88* (3), 035426.

114. Ferrari, A. C.; Robertson, J., Interpretation of Raman spectra of disordered and amorphous carbon. *Phys. Rev. B* **2000,** *61* (20), 14095-14107.

115. Elias, D. C.; Nair, R. R.; Mohiuddin, T. M. G.; Morozov, S. V.; Blake, P.; Halsall, M. P.; Ferrari, A. C.; Boukhvalov, D. W.; Katsnelson, M. I.; Geim, A. K.; Novoselov, K. S., Control of Graphene's Properties by Reversible Hydrogenation: Evidence for Graphane. *Science* **2009,** *323* (5914), 610-613.

116. Ryu, S.; Han, M. Y.; Maultzsch, J.; Heinz, T. F.; Kim, P.; Steigerwald, M. L.; Brus, L. E., Reversible Basal Plane Hydrogenation of Graphene. *Nano Letters* **2008,** *8* (12), 4597-4602.

117. Cancado, L. G.; Jorio, A.; Ferreira, E. H.; Stavale, F.; Achete, C. A.; Capaz, R. B.; Moutinho, M. V.; Lombardo, A.; Kulmala, T. S.; Ferrari, A. C., Quantifying defects in graphene via Raman spectroscopy at different excitation energies. *Nano Letters* **2011,** *11* (8), 3190-6.

118. Eckmann, A.; Felten, A.; Mishchenko, A.; Britnell, L.; Krupke, R.; Novoselov, K. S.; Casiraghi, C., Probing the Nature of Defects in Graphene by Raman Spectroscopy. *Nano Letters* **2012,** *12* (8), 3925-3930.

119. Casiraghi, C.; Hartschuh, A.; Qian, H.; Piscanec, S.; Georgi, C.; Fasoli, A.; Novoselov, K. S.; Basko, D. M.; Ferrari, A. C., Raman Spectroscopy of Graphene Edges. *Nano Letters* **2009,** *9* (4), 1433-1441.

120. Sasaki, K.-i.; Yamamoto, M.; Murakami, S.; Saito, R.; Dresselhaus, M. S.; Takai, K.; Mori, T.; Enoki, T.; Wakabayashi, K., Kohn anomalies in graphene nanoribbons. *Phys. Rev. B* **2009,** *80* (15).

121. Yan, J.; Zhang, Y.; Kim, P.; Pinczuk, A., Electric field effect tuning of electron-phonon coupling in graphene. *Phys. Rev. Lett.* **2007,** *98* (16), 166802.

122. Casiraghi, C.; Pisana, S.; Novoselov, K. S.; Geim, A. K.; Ferrari, A. C., Raman fingerprint of charged impurities in graphene. *Applied Physics Letters* **2007,** *91* (23), 3.

123. Malard, L. M.; Pimenta, M. A.; Dresselhaus, G.; Dresselhaus, M. S., Raman spectroscopy in graphene. *Physics Reports-Review Section of Physics Letters* **2009,** *473* (5-6), 51-87.

124. Basko, D. M.; Piscanec, S.; Ferrari, A. C., Electron-electron interactions and doping dependence of the two-phonon Raman intensity in graphene. *Phys. Rev. B* **2009,** *80* (16), 10.

125. Das, A.; Pisana, S.; Chakraborty, B.; Piscanec, S.; Saha, S. K.; Waghmare, U. V.; Novoselov, K. S.; Krishnamurthy, H. R.; Geim, A. K.; Ferrari, A. C.; Sood, A. K., Monitoring dopants by Raman scattering in an electrochemically top-gated graphene transistor. *Nature Nanotechnology* **2008,** *3* (4), 210-215.

126. Bruna, M.; Ott, A. K.; Ijas, M.; Yoon, D.; Sassi, U.; Ferrari, A. C., Doping Dependence of the Raman Spectrum of Defected Graphene. *ACS Nano* **2014,** *8* (7), 7432-7441.

127. Mohiuddin, T. M. G.; Lombardo, A.; Nair, R. R.; Bonetti, A.; Savini, G.; Jalil, R.; Bonini, N.; Basko, D. M.; Galiotis, C.; Marzari, N.; Novoselov, K. S.; Geim, A. K.; Ferrari, A. C., Uniaxial strain in graphene by Raman spectroscopy: G peak splitting, Gruneisen parameters, and sample orientation. *Phys. Rev. B* **2009,** *79* (20), 205433/1-205433/8.

128. Grimvall, G. r., *Thermophysical properties of materials*. North-Holland: Amsterdam ;, 1986.

129. Ni, Z. H.; Yu, T.; Lu, Y. H.; Wang, Y. Y.; Feng, Y. P.; Shen, Z. X., Uniaxial Strain on Graphene: Raman Spectroscopy Study and Band-Gap Opening. *ACS Nano* **2008,** *2* (11), 2301-2305.

130. Yu, T.; Ni, Z.; Du, C.; You, Y.; Wang, Y.; Shen, Z., Raman Mapping Investigation of Graphene on Transparent Flexible Substrate: The Strain Effect. *The Journal of Physical Chemistry C* **2008,** *112* (33), 12602-12605.

131. Huang, M.; Yan, H.; Chen, C.; Song, D.; Heinz, T. F.; Hone, J., Phonon softening and crystallographic orientation of strained graphene studied by Raman spectroscopy. *Proceedings of the National Academy of Sciences* **2009,** *106* (18), 7304-7308.

132. Bissett, M. A.; Izumida, W.; Saito, R.; Ago, H., Effect of Domain Boundaries on the Raman Spectra of Mechanically Strained Graphene. *ACS Nano* **2012,** *6* (11), 10229-10238.

133. Zabel, J.; Nair, R. R.; Ott, A.; Georgiou, T.; Geim, A. K.; Novoselov, K. S.; Casiraghi, C., Raman Spectroscopy of Graphene and Bilayer under Biaxial Strain: Bubbles and Balloons. *Nano Letters* **2012,** *12* (2), 617-621.

134. Pereira, V. M.; Castro Neto, A. H.; Peres, N. M. R., Tight-binding approach to uniaxial strain in graphene. *Phys. Rev. B* **2009,** *80* (4).

135. Yoon, D.; Son, Y.-W.; Cheong, H., Strain-dependent splitting of the double-resonance Raman scattering band in graphene. *Phys. Rev. Lett.* **2011,** *106* (15), 155502-155502.

136. Lee, J. E.; Ahn, G.; Shim, J.; Lee, Y. S.; Ryu, S., Optical separation of mechanical strain from charge doping in graphene. *Nature communications* **2012,** *3* (1), 1-8.

137. Chen, X.; Zheng, B.; Liu, H., Optical and digital microscopic imaging techniques and applications in pathology. *Analytical Cellular Pathology* **2011,** *34* (1-2), 5-18.

138. Takahashi, K.; Yamada, K.; Kato, H.; Hibino, H.; Homma, Y., In situ scanning electron microscopy of graphene growth on polycrystalline Ni substrate. *Surface science* **2012,** *606* (7-8), 728-732.

139. Robertson, A. W.; Warner, J. H., Atomic resolution imaging of graphene by transmission electron microscopy. *Nanoscale* **2013,** *5* (1), 479-493.

140. Banhart, F.; Kotakoski, J.; Krasheninnikov, A. V., Structural Defects in Graphene. *ACS Nano* **2011,** *5* (1), 26-41.

141. Siokou, A.; Ravani, F.; Karakalos, S.; Frank, O.; Kalbac, M.; Galiotis, C., Surface refinement and electronic properties of graphene layers grown on copper substrate: An XPS, UPS and EELS study. *Applied Surface Science* **2011,** *257* (23), 9785-9790.

142. Artyushkova, K.; Kiefer, B.; Halevi, B.; Knop-Gericke, A.; Schlogl, R.; Atanassov, P., Density functional theory calculations of XPS binding energy shift for nitrogen-containing graphene-like structures. *Chemical communications* **2013,** *49* (25), 2539-2541.

143. Al-Gaashani, R.; Najjar, A.; Zakaria, Y.; Mansour, S.; Atieh, M. A., XPS and structural studies of high quality graphene oxide and reduced graphene oxide prepared by different chemical oxidation methods. *Ceramics International* **2019,** *45* (11), 14439-14448.

144. Kozbial, A.; Li, Z.; Sun, J.; Gong, X.; Zhou, F.; Wang, Y.; Xu, H.; Liu, H.; Li, L., Understanding the intrinsic water wettability of graphite. *Carbon* **2014,** *74*, 218-225.

145. Hurst, J. M.; Li, L.; Liu, H., Adventitious hydrocarbons and the graphite-water interface. *Carbon* **2018,** *134*, 464-469.

146. Plutnar, J.; Pumera, M.; Sofer, Z., The chemistry of CVD graphene. *J. Mater. Chem. C* **2018,** *6* (23), 6082-6101.

147. Yu, W.; Sisi, L.; Haiyan, Y.; Jie, L., Progress in the functional modification of graphene/graphene oxide: a review. *RSC Advances* **2020,** *1* (26), 15328-15345.

148. Loh, K. P.; Bao, Q. L.; Ang, P. K.; Yang, J. X., The chemistry of graphene. *J. Mater. Chem.* **2010,** *20* (12), 2277-2289.

149. Sofo, J. O.; Chaudhari, A. S.; Barber, G. D., Graphane: A two-dimensional hydrocarbon. *Phys. Rev. B* **2007,** *75* (15).

150. Csányi, G.; Littlewood, P. B.; Nevidomskyy, A. H.; Pickard, C. J.; Simons, B. D., The role of the interlayer state in the electronic structure of superconducting graphite intercalated compounds. *Nature Physics* **2005,** *1* (1), 42-45.

151. Wang, Y.; Huang, Y.; Song, Y.; Zhang, X.; Ma, Y.; Liang, J.; Chen, Y., Room-Temperature Ferromagnetism of Graphene. *Nano Letters* **2009,** *9* (1), 220-224.

152. Esquinazi, P. D.; Precker, C. E.; Stiller, M.; Cordeiro, T. R. S.; Barzola-Quiquia, J.; Setzer, A.; Böhlmann, W., Evidence for room temperature superconductivity at graphite interfaces. *Quantum Studies: Mathematics and Foundations* **2018,** *5* (1), 41-53.

153. Schedin, F.; Geim, A. K.; Morozov, S. V.; Hill, E. W.; Blake, P.; Katsnelson, M. I.; Novoselov, K. S., Detection of individual gas molecules adsorbed on graphene. *Nature Materials* **2007,** *6* (9), 652-5.

154. Sato, Y.; Takai, K.; Enoki, T., Electrically Controlled Adsorption of Oxygen in Bilayer Graphene Devices. *Nano Letters* **2011,** *11* (8), 3468-3475.

155. Liu, L.; Ryu, S. M.; Tomasik, M. R.; Stolyarova, E.; Jung, N.; Hybertsen, M. S.; Steigerwald, M. L.; Brus, L. E.; Flynn, G. W., Graphene oxidation: Thickness-dependent etching and strong chemical doping. *Nano Letters* **2008,** *8* (7), 1965-1970.

156. Leenaerts, O.; Partoens, B.; Peeters, F. M., Adsorption of H_2O, NH_3, CO, NO_2, and NO on graphene: A first-principles study. *Phys. Rev. B* **2008,** *77* (12), 6.

157. Wehling, T. O.; Novoselov, K. S.; Morozov, S. V.; Vdovin, E. E.; Katsnelson, M. I.; Geim, A. K.; Lichtenstein, A. I., Molecular doping of graphene. *Nano Letters* **2008,** *8* (1), 173-177.

158. Tang, S. B.; Cao, Z. X., Adsorption of nitrogen oxides on graphene and graphene oxides: Insights from density functional calculations. *The Journal of Chemical Physics* **2011,** *134* (4).

159. Chen, J.-H.; Jang, C.; Xiao, S.; Ishigami, M.; Fuhrer, M. S., Intrinsic and extrinsic performance limits of graphene devices on SiO_2. *Nature Nanotechnology* **2008,** *3* (4), 206-209.

160. Joshi, P.; Romero, H. E.; Neal, A. T.; Toutam, V. K.; Tadigadapa, S. A., Intrinsic doping and gate hysteresis in graphene field effect devices fabricated on SiO_2 substrates. *Journal of Physics-Condensed Matter* **2010,** *22* (33), 6.

161. Wang, H. M.; Wu, Y. H.; Cong, C. X.; Shang, J. Z.; Yu, T., Hysteresis of Electronic Transport in Graphene Transistors. *ACS Nano* **2010,** *4* (12), 7221-7228.

162. Liao, Z. M.; Han, B. H.; Zhou, Y. B.; Yu, D. P., Hysteresis reversion in graphene field-effect transistors. *The Journal of Chemical Physics* **2010,** *133* (4), 044703.

163. Shemella, P.; Nayak, S. K., Electronic structure and band-gap modulation of graphene via substrate surface chemistry. *Applied Physics Letters* **2009,** *94* (3), 032101/1-032101/3.

164. Wehling, T. O.; Lichtenstein, A. I.; Katsnelson, M. I., First-principles studies of water adsorption on graphene: The role of the substrate. *Applied Physics Letters* **2008,** *93* (20).

165. Cho, S. B.; Lee, S.; Chung, Y. C., Water Trapping at the Graphene/Al_2O_3 Interface. *Japanese Journal of Applied Physics* **2013,** *52* (6), 4.

166. Levesque, P. L.; Sabri, S. S.; Aguirre, C. M.; Guillemette, J.; Siaj, M.; Desjardins, P.; Szkopek, T.; Martel, R., Probing charge transfer at surfaces using graphene transistors. *Nano Letters* **2011,** *11* (1), 132-7.

167. Berashevich, J.; Chakraborty, T., Tunable band gap and magnetic ordering by adsorption of molecules on graphene. *Phys. Rev. B* **2009,** *80* (3), 4.

168. Chakrapani, V.; Angus, J. C.; Anderson, A. B.; Wolter, S. D.; Stoner, B. R.; Sumanasekera, G. U., Charge Transfer Equilibria Between Diamond and an Aqueous Oxygen Electrochemical Redox Couple. *Science* **2007,** *318* (5855), 1424-1430.

169. Singh, A. K.; Uddin, M. A.; Tolson, J. T.; Maire-Afeli, H.; Sbrockey, N.; Tompa, G. S.; Spencer, M. G.; Vogt, T.; Sudarshan, T. S.; Koley, G., Electrically tunable molecular doping of graphene. *Applied Physics Letters* **2013,** *102* (4), 043101.

170. Cab, C.; Medina-Esquivel, R.; Acosta, C.; Mendez-Gamboa, J.; Penunuri, F.; Tapia, A., Influence of Electric Field in the Adsorption of Atomic Hydrogen on Graphene. *Advances in Condensed Matter Physics* **2015**.

171. Muruganathan, M.; Sun, J.; Imamura, T.; Mizuta, H., Electrically Tunable van der Waals Interaction in Graphene Molecule Complex. *Nano Letters* **2015,** *15* (12), 8176-8180.

172. Solis-Fernandez, P.; Okada, S.; Sato, T.; Tsuji, M.; Ago, H., Gate-Tunable Dirac Point of Molecular Doped Graphene. *ACS Nano* **2016,** *10* (2), 2930-2939.

173. Suarez, A. M.; Radovic, L. R.; Bar-Ziv, E.; Sofo, J. O., Gate-Voltage Control of Oxygen Diffusion on Graphene. *Phys. Rev. Lett.* **2011,** *106* (14), 4.

174. Castro, E. V.; Novoselov, K. S.; Morozov, S. V.; Peres, N. M. R.; Dos Santos, J.; Nilsson, J.; Guinea, F.; Geim, A. K.; Castro Neto, A. H., Biased bilayer graphene: Semiconductor with a gap tunable by the electric field effect. *Phys. Rev. Lett.* **2007,** *99* (21).

175. Yu, Y. J.; Zhao, Y.; Ryu, S.; Brus, L. E.; Kim, K. S.; Kim, P., Tuning the Graphene Work Function by Electric Field Effect. *Nano Letters* **2009,** *9* (10), 3430-3434.

176. O'Keeffe, J.; Wei, C.; Cho, K., Bandstructure modulation for carbon nanotubes in a uniform electric field. *Applied Physics Letters* **2002,** *80* (4), 676-678.

177. Li, Y.; Rotkin, S. V.; Ravaioli, U., Electronic Response and Bandstructure Modulation of Carbon Nanotubes in a Transverse Electrical Field. *Nano Letters* **2003,** *3* (2), 183-187.

178. Kim, S.; Nah, J.; Jo, I.; Shahrjerdi, D.; Colombo, L.; Yao, Z.; Tutuc, E.; Banerjee, S. K., Realization of a high mobility dual-gated graphene field-effect transistor with Al_2O_3 dielectric. *Applied Physics Letters* **2009,** *94* (6).

179. Ohno, Y.; Maehashi, K.; Yamashiro, Y.; Matsumoto, K., Electrolyte-Gated Graphene Field-Effect Transistors for Detecting pH Protein Adsorption. *Nano Letters* **2009,** *9* (9), 3318-3322.

180. Wang, R.; Wang, S.-N.; Zhang, D.-D.; Li, Z.-J.; Fang, Y.; Qiu, X.-H., Control of Carrier Type and Density in Exfoliated Graphene by Interface Engineering. *ACS Nano* **2011,** *5* (1), 408-412.

181. Lafkioti, M.; Krauss, B.; Lohmann, T.; Zschieschang, U.; Klauk, H.; von Klitzing, K.; Smet, J. H., Graphene on a Hydrophobic Substrate: Doping Reduction and Hysteresis Suppression under Ambient Conditions. *Nano Letters* **2010,** *10* (4), 1149-1153.

182. Pirkle, A.; Chan, J.; Venugopal, A.; Hinojos, D.; Magnuson, C. W.; McDonnell, S.; Colombo, L.; Vogel, E. M.; Ruoff, R. S.; Wallace, R. M., The effect of chemical residues on the physical and electrical properties of chemical vapor deposited graphene transferred to SiO_2. *Applied Physics Letters* **2011,** *99* (12), 3.

183. Robinson, J. P.; Schomerus, H.; Oroszlany, L.; Fal'ko, V. I., Adsorbate-Limited Conductivity of Graphene. *Phys. Rev. Lett.* **2008,** *101* (19), 4.

184. Kumar, K.; Kim, Y. S.; Yang, E. H., The influence of thermal annealing to remove polymeric residue on the electronic doping and morphological characteristics of graphene. *Carbon* **2013,** *65*, 35-45.

185. Kalon, G.; Shin, Y. J.; Truong, V. G.; Kalitsov, A.; Yang, H., The role of charge traps in inducing hysteresis: Capacitance-voltage measurements on top gated bilayer graphene. *Applied Physics Letters* **2011,** *99* (8).

186. Lee, Y. G.; Kang, C. G.; Jung, U. J.; Kim, J. J.; Hwang, H. J.; Chung, H. J.; Seo, S.; Choi, R.; Lee, B. H., Fast transient charging at the graphene/SiO_2 interface causing hysteretic device characteristics. *Applied Physics Letters* **2011,** *98* (18).

187. Liu, Z.; Bol, A. A.; Haensch, W., Large-scale graphene transistors with enhanced performance and reliability based on interface engineering by phenylsilane self-assembled monolayers. *Nano letters* **2010,** *11* (2), 523-528.

188. Chen, S. S.; Ji, H. X.; Chou, H.; Li, Q. Y.; Li, H. Y.; Suk, J. W.; Piner, R.; Liao, L.; Cai, W. W.; Ruoff, R. S., Millimeter-Size Single-Crystal Graphene by Suppressing Evaporative Loss of Cu During Low Pressure Chemical Vapor Deposition. *Advanced Materials* **2013,** *25* (14), 2062-2065.

189. Li, X. S.; Zhu, Y. W.; Cai, W. W.; Borysiak, M.; Han, B. Y.; Chen, D.; Piner, R. D.; Colombo, L.; Ruoff, R. S., Transfer of Large-Area Graphene Films for High-Performance Transparent Conductive Electrodes. *Nano Letters* **2009,** *9* (12), 4359-4363.

190. Wood, J. D.; Doidge, G. P.; Carrion, E. A.; Koepke, J. C.; Kaitz, J. A.; Datye, I.; Behnam, A.; Hewaparakrama, J.; Aruin, B.; Chen, Y. F.; Dong, H.; Haasch, R. T.; Lyding, J. W.; Pop, E., Annealing free, clean graphene transfer using alternative polymer scaffolds. *Nanotechnology* **2015,** *26* (5).

191. Barin, G. B.; Song, Y.; Gimenez, I. D.; Souza, A. G.; Barretto, L. S.; Kong, J., Optimized graphene transfer: Influence of polymethylmethacrylate (PMMA) layer concentration and baking time on graphene final performance. *Carbon* **2015,** *84*, 82-90.

192. Xu, H.; Chen, Y. B.; Zhang, J.; Zhang, H. L., Investigating the Mechanism of Hysteresis Effect in Graphene Electrical Field Device Fabricated on SiO_2 Substrates using Raman Spectroscopy. *Small* **2012,** *8* (18), 2833-2840.

193. Barone, V.; Hod, O.; Scuseria, G. E., Electronic structure and stability of semiconducting graphene nanoribbons. *Nano Letters* **2006,** *6* (12), 2748-2754.

194. Lee, Y. G.; Kang, C. G.; Cho, C.; Kim, Y.; Hwang, H. J.; Lee, B. H., Quantitative analysis of hysteretic reactions at the interface of graphene and SiO_2 using the short pulse I-V method. *Carbon* **2013,** *60*, 453-460.

195. Mao, D. C.; Wang, S. Q.; Peng, S. A.; Zhang, D. Y.; Shi, J. Y.; Huang, X. N.; Asif, M.; Jin, Z., The two timescales in the charge trapping mechanism for the hysteresis behavior in graphene field effect transistors. *Journal of Materials Science-Materials in Electronics* **2016,** *27* (9), 9847-9852.

196. Romero, H. E.; Shen, N.; Joshi, P.; Gutierrez, H. R.; Tadigadapa, S. A.; Sofo, J. O.; Eklund, P. C., n-Type Behavior of Graphene Supported on Si/SiO_2 Substrates. *ACS Nano* **2008,** *2* (10), 2037-2044.

197. Johansson, C. C.; Colacot, T. J., Metal-Catalyzed α-Arylation of Carbonyl and Related Molecules: Novel Trends in C-C Bond Formation by C-H Bond Functionalization. *Angew. Chem. Int. Ed.* **2010,** *49* (4), 676-707.

198. Narayanam, J. M.; Stephenson, C. R., Visible light photoredox catalysis: applications in organic synthesis. *Chemical Society Reviews* **2011,** *40* (1), 102-113.

199. Narayanam, J. M.; Tucker, J. W.; Stephenson, C. R., Electron-transfer photoredox catalysis: development of a tin-free reductive dehalogenation reaction. *J. Am. Chem. Soc.* **2009,** *131* (25), 8756-8757.

200. Nicewicz, D. A.; MacMillan, D. W., Merging photoredox catalysis with organocatalysis: the direct asymmetric alkylation of aldehydes. *Science* **2008,** *322* (5898), 77-80.

201. Ohta, T.; Bostwick, A.; Seyller, T.; Horn, K.; Rotenberg, E., Controlling the electronic structure of bilayer graphene. *Science* **2006,** *313* (5789), 951-954.

202. Crowther, A. C.; Ghassaei, A.; Jung, N.; Brus, L. E., Strong Charge-Transfer Doping of 1 to 10 Layer Graphene by NO2. *ACS Nano* **2012,** *6* (2), 1865-1875.

203. Senneca, O., Oxidation of Carbon: What We Know and What We Still Need to Know. *Energy Procedia* **2017,** *120*, 62-74.

204. Fino, D.; Bensaid, S.; Piumetti, M.; Russo, N., A review on the catalytic combustion of soot in Diesel particulate filters for automotive applications: From powder catalysts to structured reactors. *Applied Catalysis A: General* **2016,** *509*, 75-96.

205. Siddiqui, M. R. H.; Holmes, S.; He, H.; Smith, W.; Coker, E. N.; Atkins, M. P.; Kozhevnikov, I. V., Coking and regeneration of palladium-doped $H_3PW_{12}O_{40}/SiO_2$ catalysts. *Catalysis Letters* **2000,** *66* (1-2), 53-57.

206. Shao, Y. Y.; Zhang, S.; Engelhard, M. H.; Li, G. S.; Shao, G. C.; Wang, Y.; Liu, J.; Aksay, I. A.; Lin, Y. H., Nitrogen-doped graphene and its electrochemical applications. *J. Mater. Chem.* **2010,** *20* (35), 7491-7496.

207. Denis, P. A., Chemical Reactivity of Lithium Doped Monolayer and Bilayer Graphene. *J. Phys. Chem. C* **2011,** *115* (27), 13392-13398.

208. Geng, D. S.; Chen, Y.; Chen, Y. G.; Li, Y. L.; Li, R. Y.; Sun, X. L.; Ye, S. Y.; Knights, S., High oxygen-reduction activity and durability of nitrogen-doped graphene. *Energy & Environmental Science* **2011,** *4* (3), 760-764.

209. Zhang, L. P.; Xia, Z. H., Mechanisms of Oxygen Reduction Reaction on Nitrogen-Doped Graphene for Fuel Cells. *J. Phys. Chem. C* **2011,** *115* (22), 11170-11176.

210. Denis, P. A., Chemical Reactivity of Electron-Doped and Hole-Doped Graphene. *J. Phys. Chem. C* **2013,** *117* (8), 3895-3902.

211. Ferrighi, L.; Datteo, M.; Di Valentin, C., Boosting Graphene Reactivity with Oxygen by Boron Doping: Density Functional Theory Modeling of the Reaction Path. *J. Phys. Chem. C* **2014,** *118* (1), 223-230.

212. Denis, P. A.; Huelmo, C. P., Structural characterization and chemical reactivity of dual doped graphene. *Carbon* **2015,** *87*, 106-115.

213. Tian, Y.; Liu, Y. J.; Zhao, J. X.; Ding, Y. H., High stability and superior catalytic reactivity of nitrogen-doped graphene supporting Pt nanoparticles as a catalyst for the oxygen reduction reaction: a density functional theory study. *RSC Advances* **2015,** *5* (43), 34070-34077.

214. Wu, J. J.; Rodrigues, M. T. F.; Vajtai, R.; Ajayan, P. M., Tuning the Electrochemical Reactivity of Boron- and Nitrogen-Substituted Graphene. *Adv. Mater.* **2016,** *28* (29), 6239-6246.

215. Baker, L. R.; Hervier, A.; Kennedy, G.; Somorjai, G. A., Solid-state charge-based device for control of catalytic carbon monoxide oxidation on platinum nanofilms using external bias and light. *Nano Letters* **2012,** *12* (5), 2554-2558.

216. Aragonès, A. C.; Haworth, N. L.; Darwish, N.; Ciampi, S.; Bloomfield, N. J.; Wallace, G. G.; Diez-Perez, I.; Coote, M. L., Electrostatic catalysis of a Diels–Alder reaction. *Nature* **2016,** *531*, 88.

217. Ciampi, S.; Darwish, N.; Aitken, H. M.; Diez-Perez, I.; Coote, M. L., Harnessing electrostatic catalysis in single molecule, electrochemical and chemical systems: a rapidly growing experimental tool box. *Chemical Society Reviews* **2018,** *47* (14), 5146-5164.

218. Shaik, S.; Ramanan, R.; Danovich, D.; Mandal, D., Structure and reactivity/selectivity control by oriented-external electric fields. *Chemical Society Reviews* **2018,** *47* (14), 5125-5145.

219. Brukh, R.; Mitra, S., Kinetics of carbon nanotube oxidation. *J. Mater. Chem.* **2007,** *17* (7), 619-623.

220. Surwade, S. P.; Li, Z.; Liu, H., Thermal Oxidation and Unwrinkling of Chemical Vapor Deposition-Grown Graphene. *J. Phys. Chem. C* **2012,** *116* (38), 20600-20606.

221. Li, Z. Y.; Zhang, W. H.; Luo, Y.; Yang, J. L.; Hou, J. G., How Graphene Is Cut upon Oxidation? *J. Am. Chem. Soc.* **2009,** *131* (18), 6320-6321.

222. Radovic, L. R., Active Sites in Graphene and the Mechanism of CO_2 Formation in Carbon Oxidation. *J. Am. Chem. Soc.* **2009,** *131* (47), 17166-17175.

223. Zhang, T.; Xue, Q. Z.; Shan, M. X.; Jiao, Z. Y.; Zhou, X. Y.; Ling, C. C.; Yan, Z. F., Adsorption and Catalytic Activation of O_2 Molecule on the Surface of Au-Doped Graphene under an External Electric Field. *J. Phys. Chem. C* **2012,** *116* (37), 19918-19924.

224. Calizo, I.; Balandin, A. A.; Bao, W.; Miao, F.; Lau, C. N., Temperature dependence of the Raman spectra of graphene and graphene multilayers. *Nano Letters* **2007,** *7* (9), 2645-2649.

225. Mitoma, N.; Nouchi, R.; Tanigaki, K., Photo-oxidation of graphene in the presence of water. *J. Phys. Chem. C* **2013,** *117* (3), 1453-1456.

226. Peng, X.; Wei, Q.; Copple, A., Strain-engineered direct-indirect band gap transition and its mechanism in two-dimensional phosphorene. *Phys. Rev. B* **2014,** *90* (8), 085402.

227. Lee, S. M.; Lee, Y. H.; Hwang, Y. G.; Hahn, J. R.; Kang, H., Defect-induced oxidation of graphite. *Phys. Rev. Lett.* **1999,** *82* (1), 217-220.

228. Mitoma, N.; Nouchi, R., Gate-controlled ultraviolet photo-etching of graphene edges. *Applied Physics Letters* **2013,** *103* (20).

229. Willsau, J.; Heitbaum, J., The influence of Pt-activation on the corrosion of carbon in gas diffusion electrodes—A dems study. *Journal of Electroanalytical Chemistry and Interfacial Electrochemistry* **1984,** *161* (1), 93-101.

230. Gewirth, A. A.; Bard, A. J., In Situ Scanning Tunneling Microscopy of the Anodic Oxidation of Highly Oriented Pyrolytic Graphite Surfaces. *J. Phys. Chem.* **1988,** *92* (20), 5563-5566.

231. Reiser, C. A.; Bregoli, L.; Patterson, T. W.; Jung, S. Y.; Yang, J. D.; Perry, M. L.; Jarvi, T. D., A reverse-current decay mechanism for fuel cells. *Electrochemical and Solid-State Letters* **2005,** *8* (6), A273-A276.

232. Krernmer, S.; Teichert, C.; Kuchar, F. In *Topographical modification of silicon oxide using a conducting atomic-force microscope*, Proceedings of the 2001 1st IEEE Conference on Nanotechnology. IEEE-NANO 2001 (Cat. No.01EX516), 30-30 Oct. 2001; 2001; pp 162-167.

233. Vayenas, C. G.; Bebelis, S.; Pliangos, C.; Brosda, S.; Tsiplakides, D., *Electrochemical activation of catalysis: promotion, electrochemical promotion, and metal-support interactions*. Springer Science & Business Media: 2001.

234. Vayenas, C.; Bebelis, S.; Neophytides, S., Non-Faradaic electrochemical modification of catalytic activity. *J. Phys. Chem.* **1988,** *92* (18), 5083-5085.

235. Flynn, C. P., Strain-Assisted Epitaxial Growth of New Ordered Compounds. *Physical Review Letters* **1986,** *57* (5), 599-602.

236. Gsell, M.; Jakob, P.; Menzel, D., Effect of substrate strain on adsorption. *Science* **1998,** *280* (5364), 717-720.

237. Mavrikakis, M.; Hammer, B.; Norskov, J. K., Effect of strain on the reactivity of metal surfaces. *Phys. Rev. Lett.* **1998,** *81* (13), 2819-2822.

238. Kitchin, J.; Nørskov, J. K.; Barteau, M.; Chen, J., Modification of the surface electronic and chemical properties of Pt (111) by subsurface 3d transition metals. *The Journal of Chemical Physics* **2004,** *120* (21), 10240-10246.

239. Kitchin, J. R.; Norskov, J. K.; Barteau, M. A.; Chen, J. G., Role of strain and ligand effects in the modification of the electronic and chemical properties of bimetallic surfaces. *Phys. Rev. Lett.* **2004,** *93* (15).

240. Kibler, L. A.; El-Aziz, A. M.; Hoyer, R.; Kolb, D. M., Tuning reaction rates by lateral strain in a palladium monolayer. *Angew. Chem. Int. Ed.* **2005,** *44* (14), 2080-2084.

241. Li, J.; Zhao, Z.; Ma, Y.; Qu, Y., Graphene and Their Hybrid Electrocatalysts for Water Splitting. *ChemCatChem* **2017,** *9* (9), 1554-1568.

242. Lee, C.; Wei, X.; Kysar, J. W.; Hone, J., Measurement of the Elastic Properties and Intrinsic Strength of Monolayer Graphene. *Science* **2008,** *321* (5887), 385-388.

243. Xie, A.; Xuan, N.; Ba, K.; Sun, Z., Pristine Graphene Electrode in Hydrogen Evolution Reaction. *ACS Appl. Mater. Interfaces* **2017,** *9* (5), 4643-4648.

244. Garcia-Miranda Ferrari, A.; Brownson, D. A. C.; Banks, C. E., Investigating the Integrity of Graphene towards the Electrochemical Hydrogen Evolution Reaction (HER). *Scientific Reports* **2019,** *9* (1), 15961.

245. Boukhvalov, D. W.; Son, Y. W., Covalent Functionalization of Strained Graphene. *ChemPhysChem* **2012,** *13* (6), 1463-1469.

246. Bissett, M. A.; Konabe, S.; Okada, S.; Tsuji, M.; Ago, H., Enhanced Chemical Reactivity of Graphene Induced by Mechanical Strain. *ACS Nano* **2013,** *7* (11), 10335-10343.

247. Pu, H. H.; Rhim, S. H.; Hirschmugl, C. J.; Gajdardziska-Josifovska, M.; Weinert, M.; Chen, J. H., Strain-induced band-gap engineering of graphene monoxide and its effect on graphene. *Phys. Rev. B* **2013,** *87* (8).

248. Gui, G.; Morgan, D.; Booske, J.; Zhong, J.; Ma, Z., Local strain effect on the band gap engineering of graphene by a first-principles study. *Applied Physics Letters* **2015,** *106* (5), 53113.

249. Cretu, O.; Krasheninnikov, A. V.; Rodriguez-Manzo, J. A.; Sun, L. T.; Nieminen, R. M.; Banhart, F., Migration and Localization of Metal Atoms on Strained Graphene. *Phys. Rev. Lett.* **2010,** *105* (19).

250. Low, T.; Guinea, F., Strain-Induced Pseudomagnetic Field for Novel Graphene Electronics. *Nano Letters* **2010,** *10* (9), 3551-3554.

251. Wang, B.; Puzyrev, Y.; Pantelides, S. T., Strain enhanced defect reactivity at grain boundaries in polycrystalline graphene. *Carbon* **2011,** *49* (12), 3983-3988.

252. Wu, Q. Z.; Wu, Y. P.; Hao, Y. F.; Geng, J. X.; Charlton, M.; Chen, S. S.; Ren, Y. J.; Ji, H. X.; Li, H. F.; Boukhvalov, D. W.; Piner, R. D.; Bielawski, C. W.; Ruoff, R. S., Selective surface functionalization at regions of high local curvature in graphene. *Chemical Communications* **2013,** *49* (7), 677-679.

253. Oliva-Leyva, M.; Naumis, G. G., Tunable dichroism and optical absorption of graphene by strain engineering. *2D Materials* **2015,** *2* (2), 025001.

254. Johnston, I. D.; McCluskey, D. K.; Tan, C. K. L.; Tracey, M. C., Mechanical characterization of bulk Sylgard 184 for microfluidics and microengineering. *Journal of Micromechanics and Microengineering* **2014,** *24* (3), 35017.

255. Pritchard, R. H.; Lava, P.; Debruyne, D.; Terentjev, E. M., Precise determination of the Poisson ratio in soft materials with 2D digital image correlation. *Soft Matter* **2013,** *9* (26), 6037-6045.

256. Tolman, N. L.; Mukai, J. M.; Wang, S.; Zito, A.; Luo, T.; Liu, H., The effect of physical adsorption on the capacitance of activated carbon electrodes. *Carbon* **2019,** *150*, 334-339.

257. Chen, R.; Balla, R. J.; Li, Z.; Liu, H.; Amemiya, S., Origin of Asymmetry of Paired Nanogap Voltammograms Based on Scanning Electrochemical Microscopy: Contamination Not Adsorption. *Anal. Chem.* **2016,** *88* (16), 8323-8331.

258. Chen, R.; Nioradze, N.; Santhosh, P.; Li, Z.; Surwade, S. P.; Shenoy, G. J.; Parobek, D. G.; Kim, M. A.; Liu, H.; Amemiya, S., Ultrafast Electron Transfer Kinetics of

Graphene Grown by Chemical Vapor Deposition. *Angew. Chem. Int. Ed.* **2015,** *54* (50), 15134-15137.

259. Shinagawa, T.; Garcia-Esparza, A. T.; Takanabe, K., Insight on Tafel slopes from a microkinetic analysis of aqueous electrocatalysis for energy conversion. *Scientific Reports* **2015,** *5* (1), 13801.

260. Perdew, J. P.; Burke, K.; Ernzerhof, M., Generalized gradient approximation made simple. *Phys. Rev. Lett.* **1996,** *77* (18), 3865-3868.

261. Davidson, E. R. M.; Klimeš, J.; Alfè, D.; Michaelides, A., Cooperative Interplay of van der Waals Forces and Quantum Nuclear Effects on Adsorption: H at Graphene and at Coronene. *ACS Nano* **2014,** *8* (10), 9905-9913.

262. Casolo, S.; Løvvik, O. M.; Martinazzo, R.; Tantardini, G. F., Understanding adsorption of hydrogen atoms on graphene. *The Journal of Chemical Physics* **2009,** *130* (5), 054704.

263. Computational Chemistry Comparison and Benchmark DataBase. Precomputed vibrational scaling factors. https://cccbdb.nist.gov/vibscalejust.asp (accessed March 25, 2021).

264. Kurapati, N.; Buoro, R. M.; Amemiya, S., Perspective—Beyond the Century-Long Paradigm of Hydrogen Electrochemistry through the Laviron–Amatore Paradox. *Journal of The Electrochemical Society* **2020,** *167* (14), 146514.

265. Hinnemann, B.; Moses, P. G.; Bonde, J.; Jørgensen, K. P.; Nielsen, J. H.; Horch, S.; Chorkendorff, I.; Nørskov, J. K., Biomimetic Hydrogen Evolution: MoS_2 Nanoparticles as Catalyst for Hydrogen Evolution. *J. Am. Chem. Soc.* **2005,** *127* (15), 5308-5309.

266. Nilsson, A.; Pettersson, L. G. M.; Hammer, B.; Bligaard, T.; Christensen, C. H.; Nørskov, J. K., The electronic structure effect in heterogeneous catalysis. *Catalysis Letters* **2005,** *100* (3), 111-114.

267. Dorgan, V. E.; Bae, M.-H.; Pop, E., Mobility and saturation velocity in graphene on SiO_2. *Applied Physics Letters* **2010,** *97* (8), 082112.

268. Chen, Z.; Jang, W.; Bao, W.; Lau, C. N.; Dames, C., Thermal contact resistance between graphene and silicon dioxide. *Applied Physics Letters* **2009,** *95* (16), 161910.

269. Ryu, S.; Liu, L.; Berciaud, S.; Yu, Y. J.; Liu, H. T.; Kim, P.; Flynn, G. W.; Brus, L. E., Atmospheric Oxygen Binding and Hole Doping in Deformed Graphene on a SiO_2 Substrate. *Nano Letters* **2010,** *10* (12), 4944-4951.

270. Tu, X.; Whitehead, J. C., Plasma-catalytic dry reforming of methane in an atmospheric dielectric barrier discharge: Understanding the synergistic effect at low temperature. *Applied Catalysis B: Environmental* **2012,** *125*, 439-448.

271. Delley, B., An All-Electron Numerical-Method for Solving the Local Density Functional for Polyatomic-Molecules. *The Journal of Chemical Physics* **1990,** *92* (1), 508-517.

272. Ryzhkov, M. V.; Ivanovskii, A. L.; Delley, B., Geometry, electronic structure and energy barriers of all possible isomers of Fe_2C_3 nanoparticle. *Theoretical Chemistry Accounts* **2008,** *119* (4), 313-318.

273. Topsakal, M.; Gurel, H. H.; Ciraci, S., Effects of Charging and Electric Field on Graphene Oxide. *J. Phys. Chem. C* **2013,** *117* (11), 5943-5952.

274. Grimme, S., Semiempirical GGA-type density functional constructed with a long-range dispersion correction. *Journal of Computational Chemistry* **2006,** *27* (15), 1787-1799.

275. Halgren, T. A.; Lipscomb, W. N., The synchronous-transit method for determining reaction pathways and locating molecular transition states. *Chemical Physics Letters* **1977,** *49* (2), 225-232.

276. Henkelman, G.; Jonsson, H., Improved tangent estimate in the nudged elastic band method for finding minimum energy paths and saddle points. *The Journal of Chemical Physics* **2000,** *113* (22), 9978-9985.

277. Kresse, G.; Furthmüller, J., Efficiency of ab-initio total energy calculations for metals and semiconductors using a plane-wave basis set. *Computation Materials Science* **1996,** *6* (1), 15-50.

278. Kresse, G.; Furthmüller, J., Efficient iterative schemes for ab initio total-energy calculations using a plane-wave basis set. *Phys. Rev. B* **1996,** *54* (16), 11169-11186.

279. Grimme, S.; Ehrlich, S.; Goerigk, L., Effect of the Damping Function in Dispersion Corrected Density Functional Theory. *Journal of Computational Chemistry* **2011,** *32* (7), 1456-1465.

280. Blöchl, P. E., Projector augmented-wave method. *Phys. Rev. B* **1994,** *50*, 17953.

281. Kresse, G.; Joubert, D., From ultrasoft pseudopotentials to the projector augmented-wave method. *Phys. Rev. B* **1999,** *59* (3), 1758-1775.

282. Neugebauer, J.; Scheffler, M., Adsorbate-substrate and adsorbate-adsorbate interactions of Na and K adlayers on Al(111). *Phys. Rev. B* **1992,** *46*, 16067.

283. Monkhorst, H. J.; Pack, J. D., Special points for Brillouin-zone integrations. *Phys. Rev. B* **1976,** *13*, 5188-5192.